Novel Inorganic materials for hydrogen evolution reaction in electrochemical water splitting

Roberta Moca

Submitted in fulfilment of the requirements for the

Degree of Doctor of Philosophy

School of Chemistry

College of Science and Engineering

University of Glasgow

September 2019

Abstract

Sunlight is the most abundant renewable source of energy available on earth, providing an amount more than several hundred times sufficient to satisfy human's need. However, it is diffusive and inconsistent over time, leading to problems related to its harvesting and storage. Devices able to perform splitting of water by the use of sunlight can be used to overcome these problems by producing hydrogen, which is an excellent fuel. Nevertheless, those devices need to be cheap to produce, and therefore an investment in research of earth abundant electrocatalysts for water splitting is necessary to make them available in a larger scale. This thesis focussed on the development of new inorganic catalysts for the half-reaction responsible for hydrogen production known as hydrogen evolution reaction. The prepared catalysts were morphologically characterized by the use of various techniques and their performances were then probed electrochemically.

The first synthesis carried out was the preparation of Co-doped molybdenum sulphide materials by hydrothermal synthesis. This catalyst exhibited a disordered structure, however it could be probed by Raman spectroscopy.

The second project was to investigate the role of replacing nickel with molybdenum within the Ni_2P structure. A $Mo_xNi_{2-x}P$ series were prepared using the solid-state method, where nickel was selectively substituted. Optimisation of the method allowed the synthesis of phase pure materials by time programmed reduction. Finally, the potential of the nitride class as hydrogen evolution reaction catalysts was investigated with the synthesis of a ternary nitride using a modified Pechini method.

In general, all the prepared materials exhibited good electrochemical performances in acidic media, while the overall performance in basic media was lower. It was possible to deposit the Co-doped molybdenum sulphide in a semi-transparent film on a Fluorine-doped SnO_2 substrate without the use of any binder. The material exhibited good electrochemical performance in acid media in line with what was already reported in the literature. The compounds belonging to the $Mo_xNi_{2-x}P$ series were successfully synthesised and showed enhanced catalytic performance proportional to the number of molybdenum within the formula. All the prepared compounds showed a high stability of the performance over time in acidic media. Moreover, the used synthesis strategy had the advantage of being easy to perform, opening up to the possibility of being scaled up for industrial

purposes. The obtained ternary nitride exhibited great performance in acidic media if compared to most of the nitrides already reported in the literature. The high activity was tentatively attributed to the zero state of the nickel within the structure. Further theoretical studies, however, will be needed to fully understand the reason behind this enhanced activity.

In conclusion, all the catalysts reported in this work showed good electrochemical performance in acidic media similar to what was already reported in the literature, with the additional synthetic advantage of being simple and cheap to produce.

List of Contents

List of Tables

List of Figures

Acknowledgements and declaration

I would like to thank my supervisor, Dr Alexey Ganin for offering me the possibility to work in his research group at the University of Glasgow for his help provided throughout my PhD.

I would like to thank Dr. Isolda Roger Barba and Dr. Mark Symes, who have carried out the gas analysis measurements as well as the electrochemical measurements of the Co-doped molybdenum sulphide project (Chapter 3). A particular acknowledgement goes to Dr. Isolda Roger Barba, who spent the time to teach me the electrochemical basics and trained me to measure the Tafel slopes by multi potential sweeps voltammetry. Moreover, I would like to thank Mr. Michael Began for having supervised me during the AAS and UV/vis measurements and Mr. Jim Gallagher for having assisted me during the SEM analysis. X-ray photoelectron spectra of Chapter 3 were collected by the National EPSRC XPS Users' service at the University of Newcastle.

For the work reported in Chapter 5, I would like to acknowledge Angela Daisley and Professor Justin Hargreaves for having collaborated with me and synthesised the Ni_2Mo_3N material, which I have characterized electrochemically and morphologically.

A particular thank goes also to all the students, which I had the honour to supervise in all those years at Glasgow University: Manel Chettibi, Lee Brown, Laura Aguerri and Ramandeep Dosanjh

I hope I have been a good supervisor and you have learned from me as much as I did by teaching you.

Special thanks goes to Professor Serena Corr for her support and encouragement during my studies.

Finally, I would like to thank all the people, which I have shared time with during my PhD and have contributed to make my time at Glasgow University more enjoyable. Michael, thanks for all the time that we have spent together during my PhD (coffees, lunches and soon). Cailean, thanks for having corrected my English. We share this experience together from the first day and it seems very strange to me that we will not sit at the same desk anymore. Jake, thanks you for the sushi dinners that we have shared at crazy times. Jessica, thanks for your help in the lab but also for your cheerful attitude towards life and making everyone feel

welcome. Irene, thanks for the priceless advices during your time in the group. James, thanks for having shared with me the biscuits and cakes from your engineering students, I do not know if you did it to not gain weight but it was indeed appreciated. To Liudvika and Youyi which have just joined the group; I wish you good luck for your studies and future. Last but not least, thanks Florian for proofreading my thesis, I would not have managed to finish this work in time if it wasn't for you.

Ai miei genitori e a mio fratello, grazie ai quali sono la persona che sono e ai quali posso dire solo un sincero grazie.

"The real voyage of discovery consists not in seeking new landscapes, but in having new eyes"

Marcel Proust

Abbreviations

AAS Atomic absorption spectroscopy

AC alternative current

AE auxiliary electrode

AFM Atomic Force Microscopy

BSE backscattered electrons

C_{dl} double-layer capacitance

CE counter electrode

CP chronopotentiometry

CPE constant phase element

C_s specific capacitance for a smooth planar surface

CV cyclic voltammetry

DC direct current

DFT density functional theory

ECPB electron-coupled proton buffer

EDX Energy-Dispersive X-ray spectroscopy

EIS Electrochemical impedance spectroscopy

ESCA electrochemically active surface area

F faraday constant

FTO fluorine doped tin oxide

GC glassy carbon

GC Gas chromatography

HDS hydrogen desulfurization

HER hydrogen evolution reaction

HT Hydrothermal synthesis

ICSD International Centre for Diffraction Data

ITO iodium tin oxide

j Current density

j_o Exchange current density

LSV linear sweep voltammetry technique

MWCNT multiwalled carbon nanotubes

NHE Normal Hydrogen Electrode

OER oxygen evolution reaction

PDS programmable divergent slits

POM polyoxometalate

R resistor

Rct charge transfer resistance

RDS rate determining step

Ref reference

RGO reduced graphene oxides

RHE Reversible Hydrogen Electrode

rpm rotation per minute

Rs solvent resistance

RTMS real time multiple strip detector

SCE saturated calomel electrode

SE secondary electrodes

SEM Scanning Electron Microscopy

STM scanning tunnelling microscope

TMDs Transition metal dichalcogenides

TOF The turnover frequency

TPR time programmed reduction

UPS Ultraviolet Photoelectron microscopy

UV-VIS Ultraviolet-visible

VdW Van der Waals forces

WE working electrode

XRD X-ray diffraction

XPS X-Ray Photoelectron Spectroscopy

η Overpotential

Author's declaration

I declare that, except where explicit reference is made to the contribution of others, this dissertation is the result of my own work and has not been submitted for any other degree at the University of Glasgow or any other institution.

Roberta Moca

Date: September 2019

1 Introduction

Renewable energy sources have always been an appealing alternative to fossil fuels to satisfy the rising energy demand. However, the lack of constancy over time has made them less competitive than more traditional energy sources. Solar radiation is the most promising source of energy and it can be stored in a hydrogen chemical bond to ensure constant energy availability over time. Hydrogen is then produced by a water splitting reaction into electrochemical or photoelectrochemical electrolysers with the use of catalysts that allow performing both semi-reactions efficiently.

The use of earth abundant elements as catalysts could make it possible to scale up industrially those devices, leading to the use of hydrogen as a useful alternative for the future.

This chapter will give a brief background overview to better understand this thesis's contribution on the matter of finding new effective, cheap and available catalysts for hydrogen production. After having introduced the overall water splitting reaction, the focus will move on to the half-reaction responsible for hydrogen evolution reaction (HER), defining the criteria for a good HER catalyst. The chapter will introduce the three inorganic classes further investigated in the experimental chapters. The discussion will be particularly focussed on their specific characteristics, properties and common applications. Finally, the electrochemical and photoelectrochemical electrolysers will be introduced, describing the challenges that still need to be resolved before becoming a valuable alternative for energy production.

1.1 The importance of renewable energies

Enormous interest has been sparked in the use of renewable energies like geothermal, wind, tidal or solar as a valuable alternative to fossil fuel. In particular, the amount of solar energy irradiated to the earth is 3×10^{24} J per annum and it covers 10 000 times the annual global consumption required, which is estimated by the International Energy Agency in 2012 to be 1.56×10^5 TWh per annum.[1]

Figure 1-1 Left: Image of the Solar Impulse2.[2] Right: MS Turnanor PlanetSolar.[3]

Because of its enormous potential together with its worldwide availability, a lot of projects have been developed using solar light as an alternative source of energy. An example is the solar powered airplane named Solar impulse2 (Figure 1.1), whose energy is collected by over 17 000 solar cells on the wings and covers the amount necessary to power its electric motors.[4] Another alternative way to use the solar power is shown in Figure 1.1, where the MS Turnanor PlanetSolar with its 512 m^2 of solar panels collects solar energy charging eight tons of lithium-ion battery.[5] This battery is so efficient that it covers on its own the power needed for the navigation of the boat for up to 72 hours when the batteries are fully charged. [6]

An attempt to use solar panels to cover a large area was done in the Netherlands in 2014 with the construction of a 70-metre cycle path made with a silicon solar cell. [7] This was the first instance where the use of solar cells was applied in a large scale. The cells were translucent to allow sunlight to pass through and resistant to permit the use on a bicycle lane.

1.2   Hydrogen as a source of energy

Solar radiation is a valuable source of energy capable to satisfy on its own the rising energy demand on planet earth. However, its inconstant availability comes with the necessity to store the radiation, allowing the re-use.[8,9,10] Molecules like hydrogen can help to overcome this problem using their chemical bond as an energy storage that can be release back when needed.[8,11]

A photoelectrochemical reaction can be used to split the water in order to obtain hydrogen from sunlight. (Equation 1.1) There are several advantages of using hydrogen as a fuel source, like the possibility of utilising the energy stored when needed with the production of only clean water as final product. [12]Moreover, its use will help to reduce carbon dioxide emission into the atmosphere in the long term.[13]

$$H_2O \rightarrow O_2 + 2H_2 \qquad (1.1)$$

Hydrogen is the molecule used as a fuel with the highest energy density [11] and combined with oxygen can be used in fuel cells to produce electricity.[14,15] Although its use as a fuel leads to a production up to three times the amount of energy per kg of petrol, [16] it comes with issues concerning storage. In fact, hydrogen is in gas form at standard temperature and pressure, making its use as a fuel for vehicles unpractical because of the high volume of required storage. This problem can be overcome by cryogenic storage at low temperature leading to the advantage of increasing the energy density [13] and refuelling times.[17] Metal hydrides have also been proposed as an alternative for improving the energy density at low pressure and under safe condictions.[13] The cryogenic storage requires decreasing the hydrogen temperature almost below the melting point (-259.2 °C). Unfortunately, cooling down leads to an undesirable energy reduction of the system. Metal hydrides store hydrogen by bonding it in a process called chemisorption that is able to release the gas by increasing the temperature or decreasing the pressure.[16] The process used is exothermic and the heat released by the reaction can ideally be reused to again release the hydrogen when necessary.

Metal hydrides used for energy storage has the advantage of a high gravimetric and volumetric energy density.[16] An example of a widely used metal hydride is aluminium hydride, which has an energy density four times greater than the best performing lithium polymer batteries.[16] However, the energy cannot be stored reversibly making it quite unpractical design for everyday life.

These days steam reforming reaction and coal gasification are responsible for more than 95% of the hydrogen in industry using hydrocarbons from natural gas and water vapour which produce carbon oxide as a product.[11,13,16]

This process consists of a endothermic reaction [18] carried out in a temperature range between 800 − 900 ^{0}C using nickel as catalyst on an alumina support.[17] Unfortunately, a disadvantage of this process is catalyst poisoning by coke and sulphur impurities present in the natural gas, which makes the catalyst less effective over time.[17]

To prevent this catalyst poisoning, the feedstock used is treated preventively by desulfurization, reducing the sulphur level down to 2 ppm. The gas mixture produced contains an amount of carbon monoxide of 5%, which can be further reduced through gas shift reactors. In this context, the production of hydrogen through photoelectrolysis is an environmentally friendly approach, which contrary to the steam reforming method ensures a purity production major of 99.999%. [19,20] However, this is an energy-intensive process and can be carried out only if electricity is cheap to provide or with the use of an efficient low cost catalyst.[21] For those reasons, only 4% of the hydrogen is provided industrially by photoelectrolysis[22] and efforts have been made to increase this percentage. However, this method comes with the advantages to provide a green production with no carbon dioxide emission and with no further purification process.[20]

The device used to perform the water splitting reaction is called an electrolyser (Figure 1.2). Here, the water splitting reaction is performed as the current flows between the two electrodes.[20]
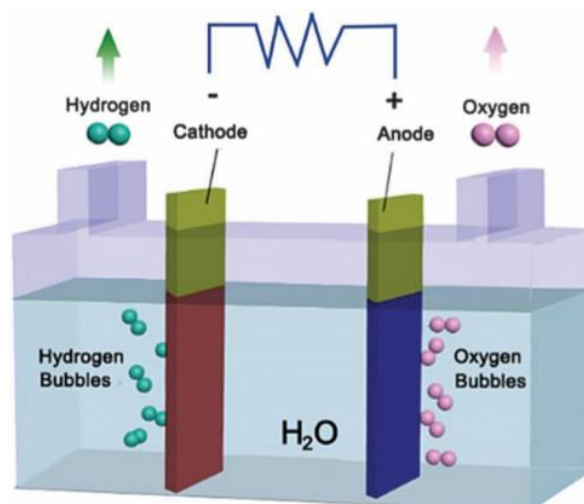
Figure 1-2 Standard electrolyser setup. The picture is reproduced from reference [22]

1.3 Water splitting reaction

The water splitting reaction in acidic conditions (Equation 1.1) can be divided in two semi reactions (1.2) and (1.4), where the proton reduction or hydrogen evolution reaction (HER) is performed at the cathode and the water oxidation reaction or oxygen evolution reaction (OER) at the anode. In addition, the role of the pH on the potential can be taken into account (1.3) and (1.5).

Cathode:

$$2 \text{ H}^+ + 2\text{e}^- \rightarrow \text{H}_2 \qquad \text{with } E^0 = 0 \qquad (1.2)$$

$$E = E^0 + \frac{0.059}{2} log[H^+]^2 = E^0 + 0.059 log[H^+] = 0 - 0.059 pH \qquad (1.3)$$

Anode:

$$\text{H}_2\text{O} \rightarrow 2\text{H}^+ + \frac{1}{2} \text{ O}_2 + 2\text{e}^-, \text{ with } E^0 = 1.23 \qquad (1.4)$$
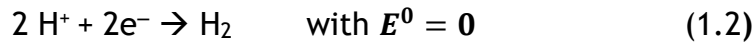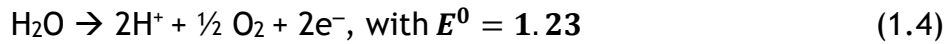
$$E = E^0 + \frac{0.059}{4} log[H^+]^4 = E^0 + 0.059 log[H^+] = 1.23 - 0.059 pH \qquad (1.5)$$

By calculating the Nernstian potential for each semi reaction at the standard conditions of 25 °C and 1 atm, a potential of 1.23 V is necessary to perform the whole reaction. However, the real value applied to the electrolyser is always higher and it is commonly called overpotential (Equation 1.6). This value is directly correlated to different contributions such the cathode and anode material plus other resistances associated with the electrolytic cell design.

$$E_{op} = 1.23V + \eta_{anode} + \eta_{cathode} + \eta_{other} \qquad (1.6)$$

The aim of this work was to find valuable alternative materials for the HER semi-reaction utilising earth-abundant elements and therefore to minimise the $\eta_{cathode}$ contribution in Equation 1.6 with more economical alternatives. This overpotential is highly dependent on the material and is related to the activation

energy of the half reaction 1.2. When the activation energy decreases, the reaction needs less energy to occur leading to a smaller starting overpotential.

The independent study of the cathode half-reactions requires to take into account that the pH contribution, as it is not cancelled in the overall equation. The choice of the potential scale then becomes important, in particular for reactions whose thermodynamics are pH dependent such as the hydrogen evolution reaction. Therefore, sometimes the measurements are written as a function of the Reversible Hydrogen Electrode (RHE), which contrary to the more common Normal Hydrogen Electrode (NHE) takes into account changes in pH. This enables comparison of the position of the redox process studied despite the pH used. The RHE and NHE electrodes are related to each other by the Nernst Equation: E_{RHE} = E_{NHE} + 0.0059 × pH. According to which, at pH =0, E_{RHE} = E_{NHE} while at pH 14 and application of a potential of 1V *vs.* RHE it results in a potential of 1.83 V for NHE.

Figure 1.3 shows how the potential necessary to perform the two half-reactions varies with the Nernst Equation. The values on the y intercepts are referred to as the potential values at the standard conditions for both semi-reactions.
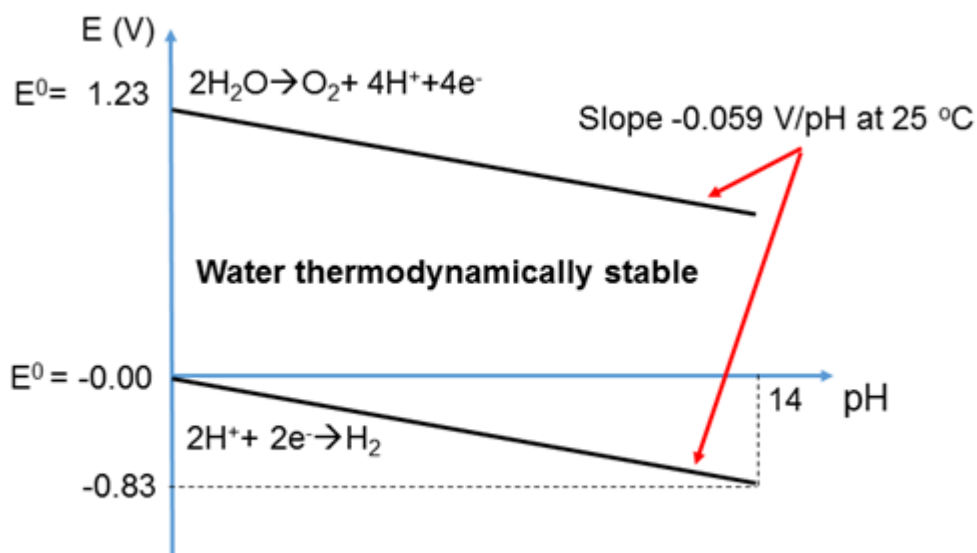
Figure 1-3 Pourbaix diagram for water, mapping the electrochemical stability for different redox states as a function of potential and pH. [23]

The pH also affects the kinetics of the reaction. For a basic reaction the two half-reaction are written as:

$$\text{Cathode: } 2\ H_2O + 2\ e^- \rightarrow H_2 + 2\ OH^- \hspace{2cm} (1.7)$$

$$\text{Anode: } 2\ OH^- \rightarrow H_2O + \tfrac{1}{2}\ O_2 + 2\ e^- \hspace{2cm} (1.8)$$
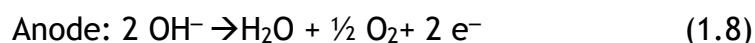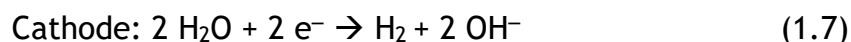
Because of a reaction rate two times slower, mechanistic studies are generally carried out in basic instead of acidic media, where the reaction occurs more rapidly.[24] Those studies are generally carried out in a rotating disk electrode and are important to determine the relationship between the mechanism and the surface structure.

1.4 Mechanism of the HER

The HER is a multistep process taking place on the cathode surface (see Figure 1.4).[25] The first step is known as the Volmer or discharge reaction: it starts with the chemical absorption of the proton H^+ on the catalyst's active site. This absorption is driven by the coupling of the proton with one electrone:

$$H^+ + e^- \rightarrow H^* \hspace{1cm} (1.9)$$
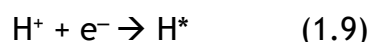
The proton source depends on the pH of the electrolyte and it is H_3O^+ in acid and water in basic solution.

After absorption, two different processes can occur: the Volmer-Tafel and the Volmer-Heyrovsky, which have a different kinetics and depend on the catalyst and on the overpotential, $\eta_{cathode.}$

The Volmer-Tafel mechanism, also known as the recombination mechanism, consists of the production of hydrogen from two protons absorbed in two active sites.

$$H^* + H^* \rightarrow H_2 \hspace{2cm} (1.10)$$

In the Volmer-Heyrovsky mechanism, or electrochemical deposition, the hydrogen production is given by:

$$H^* + H^+ + e^- \rightarrow H_2 \hspace{2cm} (1.11)$$
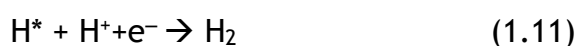
Here the hydrogen is formed due to the coupling between a hydrogen absorbed on the surface and an electron and a proton present in the electrolyte solution.
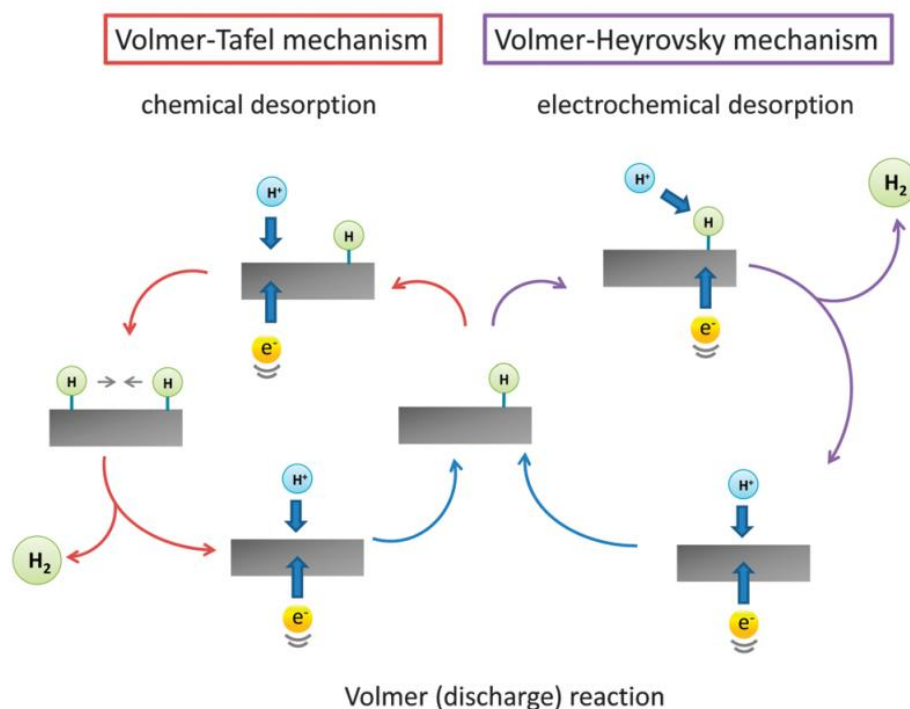
Figure 1-4 Two different hydrogen evolution pathways after the proton H$^+$ has been absorbed on the surface. Picture reproduced from reference [26]

1.5 The kinetics of the HER

As seen in Paragraph 1.3, the HER kinetics is dependent on the potential and is described by the Butler-Volmer Equation.[27,28]

$$j = j_0\left[-e^{-\alpha nF\eta/RT} + e^{(1-\alpha)nF\eta/RT}\right] \qquad (1.12)$$

Where j is the current density (the electrical current per unit area with the unit Acm^{-2}), j_0 is the exchange current density (Acm^{-2}), α is the charge transfer coefficient, F is the faraday constant, R is the gas constant , n is the number of electrons transferred, T is the temperature expressed in K and η is the overpotential in V. The exchange current density, j_0, is a kinetic parameter correlated to the rate of electrons transferred between an analyte in solution and the electrode under reversible conditions (at a potential equal to zero). This parameter is strongly influenced by different catalysts and so it can be used to describe the catalytic activity. For the hydrogen evolution reaction, this value is

estimated, varying between five to six orders of magnitude according to different electrode materials.[29]

When the overpotential is small ($\eta < 0.005V$), the current density and the Butler-Volmer Equation can be re-written as:

$$\eta = \left(\frac{RT}{nFj_0}\right)j \qquad (1.13)$$

Another important value to consider is the Tafel slope, which can be obtained from Equation 1.12 when re-written in the natural logarithmic form:

$$\eta = a + b\log j = \frac{-2.3RT}{\alpha nF}\log j_0 + \frac{+2.3RT}{\alpha nF}\log j \qquad (1.14)$$

The Equation expressed in this way describes a linear relationship between the overpotential, η, and the logarithm of the current density log j. The slope of Equation 1.14 is named Tafel and is equal to:

$$b = \frac{2.3RT}{\alpha nF} \qquad (1.15)$$

The Tafel value is commonly used to discern between the possible HER reaction mechanisms occurring at the cathode. It indicates by definition the necessary overpotential increment to raise the current density by ten-fold. Ideally, a good catalyst should have a low Tafel slope and a high current density. However, those two values are related to each other and so often with a high exchange current density comes a high Tafel slope value and vice versa. For this reason, a good catalyst is simply defined, by having a lower potential at a determined target current density. When defining HER catalysts, the current density used for comparisons is 10 mA cm^{-2}, which is equivalent to a solar to hydrogen efficiency of 12.3%.[22,30]

The HER kinetics are highly influenced by the reaction pathway. Moreover, sometimes more than one phase is catalytic active and therefore the same reaction can occur by different pathways. The Tafel slope can help to estimate

which one of the semi-reactions described above is the rate determining step and then provide insight into the possible reaction way.[31,32,33]

This can be done by calculating the transfer coefficient value α

$$\alpha = \frac{n_f}{\upsilon} + n_\Gamma \beta \qquad (1.16)$$

Where n_f is the number of electron transferred before the RDS (rate determining stem), υ stands for the time of the RDS taking place during the HER process, n_Γ is the number of electrons transferred during the RDS and β is the symmetry factor associated with the activation energy and estimated to be 0.5.

If the absorption of the proton on the surface (Volmer reaction) is the RDS, n_f assumes the value of zero since it is the starting semi-reaction and n_Γ is 1. The υ value can be either 1 or 2 depending on the following semi-reaction, however, this does not lead to any ambiguity since the term which includes this value is null

$$\alpha = \frac{0}{1 \: or \: 2} + 1 * 0.5 = 0.5$$

The calculated α value is 0.5 in this case, which including in Equation 1.15 leads to a Tafel value of 120 mV dec^{-1}.

When the RDS is the Tafel semi-reaction (Equation 1.10), n_f assumes the value of 2 since two Volmer reactions are necessary before the Tafel occurs, υ is 1 and n_Γ is zero since this RDS involves the recombination of the protons already coordinated on the surface and so no electrons are present.

$$\alpha = \frac{2}{1} + 0 * 0.5 = 2$$

In this case α is 2 and the Tafel obtained with is value is 30 mV dec^{-1}.

Finally, in the case the Heyrovsky semi-reaction is the RDS; n_f is 1 because only 1 Volmer reaction is necessary before the Heyrovsky's occurs, n_Γ is 1 because only one electron is involved during the RDS and υ is equal to one.

$$\alpha = \frac{1}{1} + 1 * 0.5 = 1.5$$

The α obtained in this case is then 0.5 and the resulting Tafel slope has a value of 40 mV dec^{-1}.

The use of the Tafel slope enables to discern the Volmer-Tafel and the Volmer-Heyrovsky cases. However, in case the rate limiting step is due to the Volmer Equation, this calculation does not allow to predict which one of the two semi-reactions will the HER reaction perform.

1.6 Turnover frequency

The turnover frequency (TOF) is a parameter used to determine, per unit time, how many reactants are converted to the product. Its value is calculated by estimating the total electrode activity, the number of active sites and then dividing one by the other. The obtained value describes the intrinsic activity of an active site according to the chemical and the physical surface properties.[22] This information is used to compare electrodes.[30] Unfortunately, the TOF is not an easy parameter to define for heterogeneous catalysts since it is challenging to determine the number of active sites and their accessibility. The TOF value is then estimated using the number of active sites on the surface without considering their different accessibility. The results in a TOF value always lower than the real one.

1.7 Faradaic Efficiency

In electrochemistry, the faraday efficiency is described as a ratio between the moles of product detected and the one estimated according to the charge passed through the experiment.

$$\Upsilon_{Faradaic} = \frac{\Delta n_{effective}}{\Delta n_{faradaic}} \qquad (1.17)$$

In Equation 1.17 the number of moles estimated to be produced by the current, $\Delta n_{faradaic}$ are calculated using Faraday's law:

$$\Delta n_{O_2}^{faradaic} = \frac{v_{O_2}}{v_e F} C = \frac{1}{4F} C \quad \text{for OER} \tag{1.18}$$

$$\Delta n_{H_2}^{faradaic} = \frac{v_{H_2}}{v_e F} C = \frac{1}{2F} C \quad \text{for HER} \tag{1.19}$$

Where n is the produced moles, C in Equation 1.18 and 1.19 is the charge during electrolysis, v_e is the electron's stoichiometric number and F is the faraday constant.

By calculating the Faraday efficiency it is possible to asses if the target reaction is the only one carried out during electrolysis or if there are other side reactions. This technique is always coupled with gas analysis to ensure hydrogen or oxygen production as the main reaction. Gas chromatography is the main technique for hydrogen detection, while for the oxygen this technique can be couple or substituted with fluorescence quenching methods or by using O_2 sensitive electrodes like the Clark electrode.

1.8 Stability

Stability is an important parameter that is necessary to take into account in order to make a catalyst commercially appealing. During the performance, excessive bubbling due to an intense hydrogen production or harsh pH condition can damage the material and therefore it is important to measure catalyst stability over time. The majority of studies in the literature test the stability by holding the current density at 10 mA cm^{-2} for a time over more than ten hours.[22] Alternatively, techniques like cyclic voltammetry or linear sweep voltammetry are used for this purpose by repeating the measurement for more than 5000 cycles. [22]

1.9 Comparison of HER catalysts

New catalysts can be found by correlating the reactivity to the hydrogen absorption energy versus the exchange current density for various systems. The exchange current is a function of the forward and reverse rate at equilibrium and therefore a kinetic parameter of the HER process. *Trassati* was the first to suggest this correlation in 1970 using bond enthalpy of metal hydrides to overcome the lack of theoretical and experimental data concerning the hydrogen absorption.[34] In 2005 *Nørskov et al.* [35] improved this model by calculating the hydrogen

absorption free energy, ΔG_{H^*}, on catalytic surfaces and obtaining a volcano plot relating those theoretical data with the exchange current density. The free energy was calculated by density functional theory (DFT) from the hydrogen chemisorption energies. Once the hydrogen chemisorption energy is calculated, the free energy relative to the absorption state is obtained by Equation (1.20).

$$\Delta G_{H^*} = \Delta E_H + \Delta E_{ZPE} - T\Delta S_H \qquad (1.20)$$

where ΔE_H is the hydrogen chemisorption energy, ΔE_{ZPE} is the energy difference in zero-point energy between the absorption and the gas phase and ΔS_H is the vibrational entropy of the absorption state. Those last two Equation's terms are small at standard conditions leading to a simplification of Equation (1.20) to:

$$\Delta G_{H^*} = \Delta E_H + 0.24\ eV \qquad (1.21)$$

The obtained graph is volcano-shaped plot where the maximum is located at the value of $\Delta G_{H^*} = 0$ that separates the two sides of the graph. The Sabatier principle states that for a good catalyst the interaction between the active site and the reactant needs to be neither too strong nor too week to ensure that the reaction occurs efficiently.[36] Platinum density is located close to the peak position of the plot with its Gibbs energy value close to zero and a high exchange current, confirming its excellent performance as hydrogen evolution catalyst.
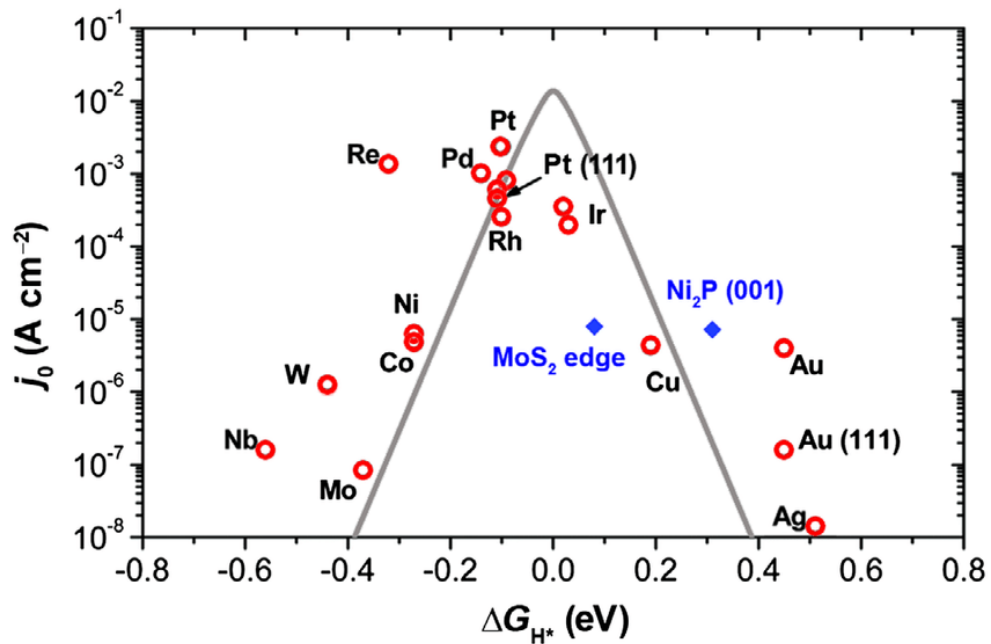
Figure 1-5 Volcano plot showing the free energy charge of absorbed atomic hydrogen as a function of the exchange current density for some of HER catalyst. Picture reproduced from the review [26] in agreement with the kinetic model proposed by *Nørskov and co-workers.* [35]

The metals on the left of the volcano plot ($\Delta G_{H^*} < 0$) are the ones that interact too strongly with the proton on the catalyst surface. On these metals the absorption occurs rapidly while the desorption occurs slowly.[37] This leads to an inhibition of the active sites.[38]

In contrast, the metals on the right of the graph ($\Delta G_{H^*} > 0$) have a weak interaction with the proton, making the interaction with the active sites harder [26]. Once the proton is absorbed on the catalyst surface, the reaction proceeds fast through the desorption process.

The catalysts with $\Delta G_{H^*}= 0$ have an intermediate strength of bonding,[38,39,11] making the competitive reactions of absorption and desorption on the surface well balanced. This is the best condition for a catalyst and scientists aim to create new materials that possess this quality. Hence, the best catalyst is the one which has a free energy of approximately zero and a high exchange current density value ,[40,41] thus sitting at the peak of the volcano shape.

1.10 Strategy to develop a novel Hydrogen Evolution Catalyst

Only 4 % of hydrogen is produced nowadays by electrolysis. The main reason for this is the high production cost associated with the use of platinum and other noble metals (Pt, Rh, Pd, Re and Ir) which are the best performing materials for

this reaction with the highest performances[42] and stability against oxidation and corrosion (see Figure 1.5). However, those metals are very expensive and therefore not suitable for the use in large scale and long time.[15,43]

Ideally, a catalyst suitable for hydrogen evolution reaction should be prepared from cheap and readily available reagents. The material should also be produced in an environmentally friendly way and exhibit stable performance over a long time.[10,22,19]

A good catalyst to scale up industrially is expected to be easy to prepare, without the presence of major impurities and stable in its performances for a time span of 15-20 years.[22] Those materials are also expected to perform under extreme reaction conditions, highlighting the importance to select materials stable and durable over time. As previously describe in Paragraph 1.5, low over potential and high current density are characteristics that are crucial for the selection of a good HER catalyst, together with the cost and the preparation method.

As mentioned before, the bubble effect is a factor which needs to be taken into account since it can affect catalyst stability. While the hydrogen evolution reaction is performed, bubbles of hydrogen are produced at the cathode. Due to the cathode conformation, the gas bubbles are not immediately released and therefore they inhibit the surface by blocking the reaction.[22] This problem can be overcome by using a rotation disk powered by a motor which helps to promote hydrogen release.[30]

The importance of the pH was already highlighted in Paragraph 1.3. Catalysts performing in acidic media are generally preferred as they are compatible with the proton-exchange membrane in the fuel cell and so they ensure an electron transport loss smaller than the one in alkaline.[44] Compared to the cells made in alkaline systems, the ones performing in acid media also have a flexible design, good power efficiency, low overpotential and high current density.[45]

An alternative to the high cost and low availability of noble metals can be found in the development of transition metal and non-metal catalysts, which could enable hydrogen production by water splitting on a large scale. The most used transition metals as hydrogen evolution reaction catalysts are: iron, cobalt, nickel, copper, molybdenum and tugsten.[22] Contrary to noble metals, those catalysts can be deactivated by going through passivation or corrosion in presence of oxygen or water.[19] Those materials have, however, the advantage of being highly available and cheap. Figure 1.6 shows the relative abundance of transition

metals including platinum. As can be seen, platinum is much less abundant compared to other metals, with a percentage of only 3.7×10^{-6} amongst the elements in the earth's crust, while the most abundant element within the transition metals is iron with a percentage of 6.8%. Transition metals in form of sulphides, nitrides and phosphides have already been reported as hydrogen evolution catalysts. In the following sections all those groups will be discussed in more details.
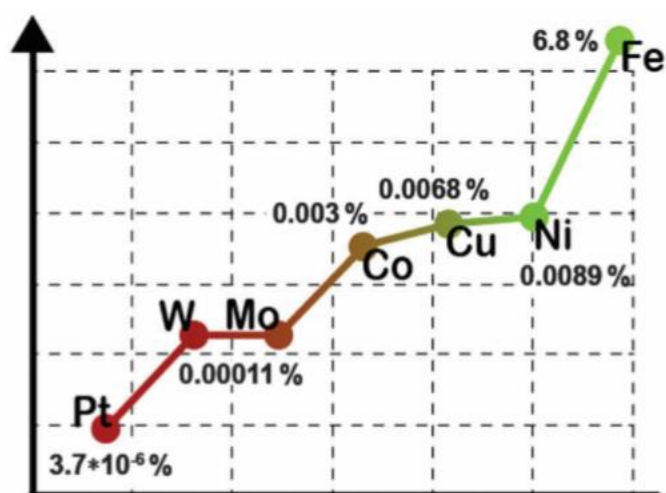
Figure 1-6 Scheme highlighting the relative abundance of the most common transition metals used as hydrogen evolution reaction catalysts in comparison to platinum.[22]

1.11   Transition metal dichalcogenides

Transition metal dichalcogenides (TMDs) are a class of materials known for their graphene like structure, which harbours interesting electrical and optical properties. Contrary to graphene, TMDs are not inert, with a more versatile chemistry making their electronic structure easier to tune and attractive for a large variety of application like electrocatalysts for hydrogen evolution reaction and hydrosulfuration, storage applications (Li-ion battery), supercapacitors and opto-electronics.

1.11.1 TMDs crystal structure and crystal phase.

TMDs have a MX_2 composition where M is a transition metal of group 4-10 and X a chalcogenide (e.g. S, Se and Te).[46] The bond between the metal and the

chalcogenide is covalent, while between the X-M-X layers the interaction (which holds the structure together) is weak and mainly due to Van der Waals forces. [46,47] Because of their structure, TMDs can be easily exfoliated from the bulk form to single layers.

The metal coordination structures present in nature are trigonal prismatic (D_{3h}) or octahedral (O_h), which is sometimes thermodynamically preferred to be distorted and then called trigonal anti prismatic (D_{3d}). Different coordination structures lead to different polymorphs: 2H and 3R for the trigonal prismatic coordination and 1T for the octahedral ones where T stands for tetragonal, H for hexagonal, R for rhombohedral, and the number indicates the number of X-M-X layers in the unit cell.
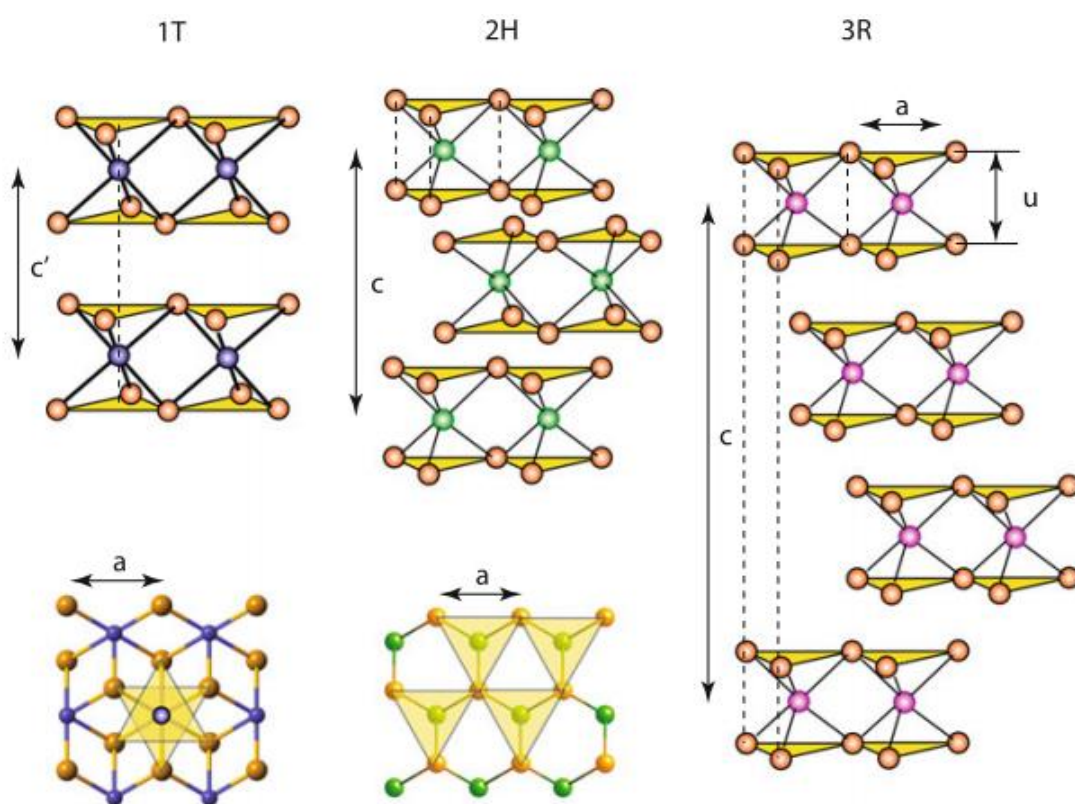
Figure 1-7 Scheme of the TMDs structural polytypes 1T (tetragonal symmetry with one layer per unit cell), 2H (hexagonal symmetry with two layers per unit cell) and 3R (rhombohedral symmetry with three layers per unit cell). Top view is additionally reported for the 1T and 2H polytype.[48]

Polymorphs can have different staking sequences between layers, leading to different polytypes depending on the synthetic method. The natural "phase" 2H of the MoS_2 polytype, for example, have a staking sequence of AbA BaB, where the capital letters stand for the chalcogenides and the lower letters the metal. Despite the metal having a trigonal prismatic coordination, when MoS_2 has a

synthetic origin its phase is 3R with a stacking sequence of AbA CaC BcB. [49] Monolayer TMDs have only two polymorph forms: trigonal prismatic (D_{3h}) and octahedral (D_{3d}) which are referred to 1H and 1T, respectively.

1.11.2 Electronic structure

The TMDs have an electronic structure which varies according to the electron number and the metal coordination. In particular, the electronic properties of the compound are defined by the nonbonding d orbitals lying between the bonding (σ) and antibonding bands (σ^*) of M-X (Figure 1.8). Octahedrally coordinated metals (D_{3d}) can accommodate up to 6 electrons on the d degenerated orbitals d_{z2}, d_{x2-y2} (e_g) and d_{yz}, d_{xz}, d_{xy} (t_{2g}) depending on the TMD's group. For trigonal prismatic coordination (D_{3h}), the d orbitals are divided into groups $d_{z2}(a_1)$, d_{x2-y2}, $d_{xy}(e)$ and d_{xz}, d_{yz} (e') with a difference in energy of circa 1 eV between e and e'.
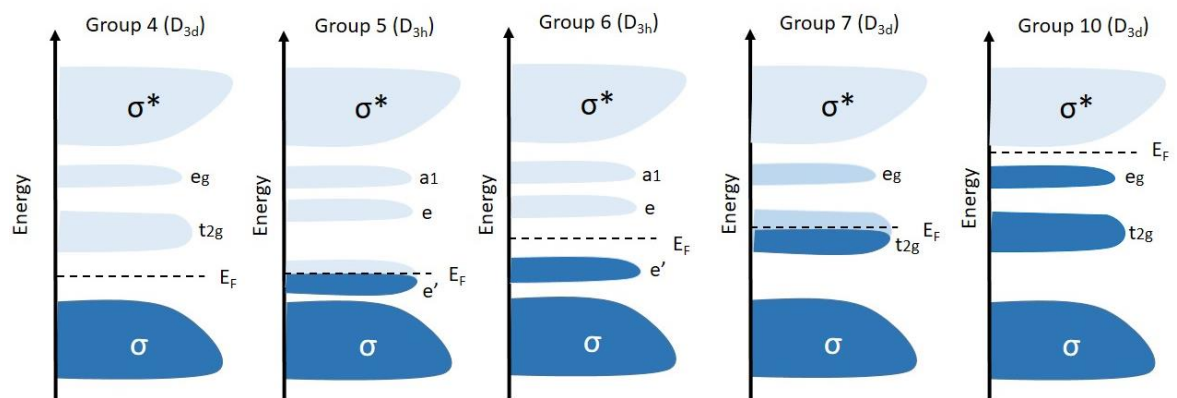
Figure 1-8 Schematic illustration of d orbital arrangement and progressive filling for different TMD groups.

Based on how the d orbitals are occupied by the electrons, TMDs can be semiconductors or with metallic conductivity. Chalcogenides like $1T-ReS_2$ and $2H-NbSe_2$ have the orbitals partially filled and therefore exhibit metallic properties, while materials with fully occupied d orbitals like $1T-HfS_2$ and $2HMoS_2$ act as semiconductors. Chalcogenides have less of an effect than metal on the electronic structure. However, the band gap broadening decreases with an increase in the chalcogenide's atomic number. The phase preferably adopted by TMDs is strongly dependent on the electron count and the most common phases for the different groups are summarized in Table 1.

Table 1-1 Summary of different Chalcogenide's phase and electronic properties. [49]

Group	Metal	Chalcogenides	Electron on the d orbitals	Phase	Properties
4	Ti, Hf, Zr	S, Se, Te	d^0	Octahedral	Semiconducting (E_g= 0.2-2 eV), diamagnetic.
5	V, Nb, Ta	S, Se, Te	d^1	Trigonal prismatic	Superconducting. paramagnetic, antiferromagnetic or diamagnetic.
6	Mo, W	S, Se, Te	d^2	Trigonal prismatic	Semiconducting (sulfides and selenides with an Eg = 1eV). Tellurides are semimetallic.
7	Tc, Re	S, Se, Te	d^3	Distorted octahedral	Small-gap semiconductors, diamagnetic.
10	Pd, Pt	S, Se, Te	d^6	octahedral	Sulfides and selenides are semiconducting (Eg = 0.4eV). Tellurides are metallic and paramagnetic. $PdTe_2$ is superconducting.

Intercalation of alkali metals into the TMD layers can induce a phase change to the structure. For example, the lithium intercalation into MoS_2 structure results in a phase transition from 2H to 1T. [49,50,51,52] The electron transfer between the

alkali s orbital and the metal d band might be the reason behind the 2H phase destabilization in combination with the free energy changes between the two phases.

1.11.3 From bulk to 2D dimensions

TMD monolayers preserve the properties of the material in bulk form with the rises of others due to confinement effect and lack of symmetry elements.[53,54,55] The changes in the TMD electronic band from bulk to monolayer can be predicted using density functional theory (DFT) calculations. For example, MoS_2 valence and conduction bands change from an indirect to a direct band gap when transitioning from bulk to monolayer.[56,57] In the bulk form, the indirect band gap is due to the different location of the valence band maximum and the conduction band minimum at the Γ and K points, respectively, on the hexagonal Brillouin zone. On the contrary, a single monolayer has both the valence band maximum and the conduction band minimum on the K position and therefore exhibits a direct band gap (Figure 1.9). This change is due to the quantum confinement and leads to enhanced monolayer photoluminescence in group 6 TMDs.[57,56,58,59,60] The calculated MoS_2 band gap also changes from 0.88V to 1.71 V [61] and generally becomes about 50% larger for all the other member of the 6 group TMDs.[56,62]

The lack of inversion symmetry in MoS_2 monolayers results in spin splitting of the electronic bands due to the spin-orbit interaction.[62] In this condition, the high symmetry points at the corner of the Brillouin zone K and K', where the valence band maximum and the conduction band minimum are located, have an unequal momentum valley. The strong spin-orbit coupling leads to a valence band split at these valleys, requiring the spin splitting for the different valley to be opposite. The two electrons position can be selectively excited by different circularly polarized light. The light is then remitted back to indicate its preservation during the process. [53,54,55] The ability to achieve and control the valley polarization is an interesting property which can lead the construction of valleytronic devices.
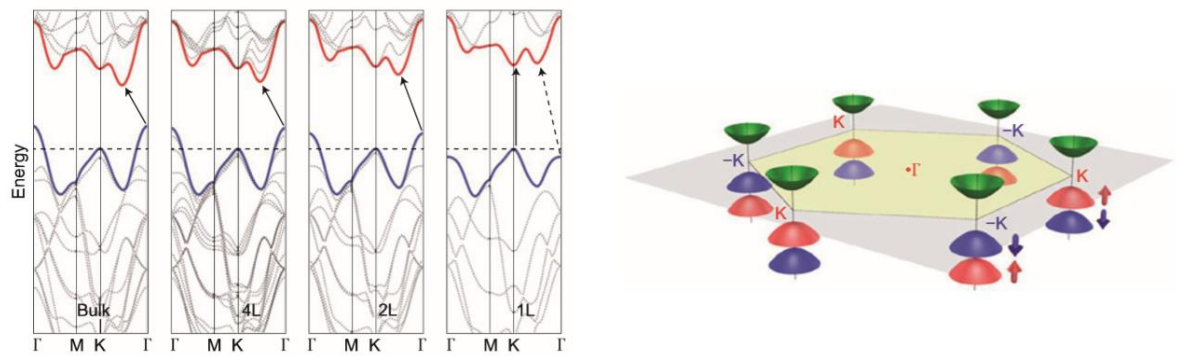
Figure 1-9 Right, The 2H MoS$_2$ monolayer electronic band in the K and K' position of the Brillouin zone highlighting the spin splitting. The spin-orbit-split valence band maxima are represented by the red and blue surfaces according to the different electron spin, while the conduction band minima are in green. Picture are reproduced from reference [56] and [62].

Differences between bulks and monolayers have also been identified on Raman active vibrational modes corresponding to the in plane E^1_{2g} at 382 cm^{-2} and out of plane A_{1g} at 406 cm^{-2}. [63] As the layer thickness decreases, the A_{1g} mode decreases in frequency while the E^1_{2g} mode increases (Figure 1.10).
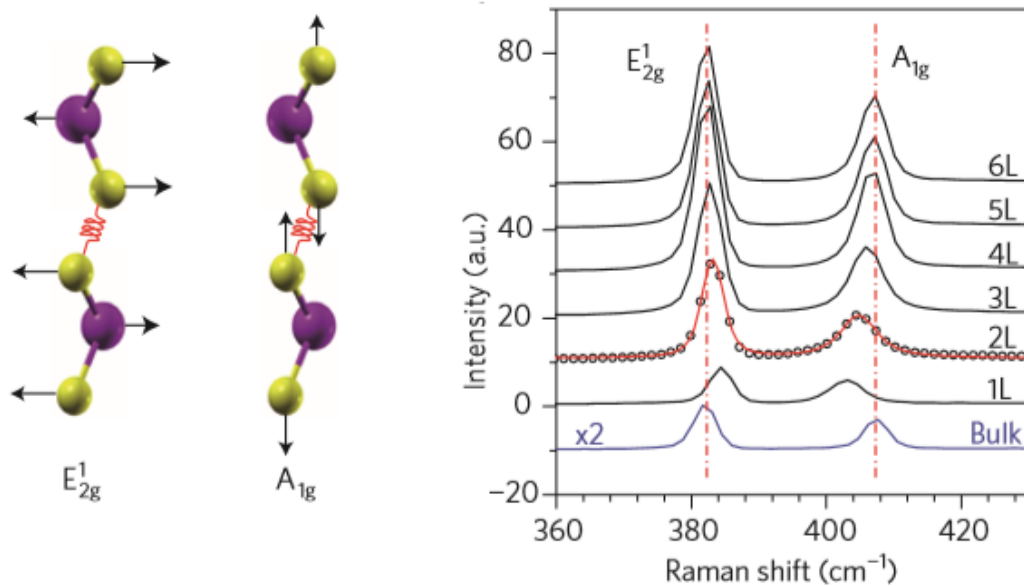
Figure 1-10 Left, in plane E^1_{2g} and out of plane A_{1g} Raman active mode. Right, dependency of mode E^1_{2g} and A_{1g} from the MoS$_2$ material thickness. The pictures are reported from reference [64] and [63] .

1.11.4 Transition metal dichalcogenide applications beyond hydrogen evolution reaction

1.11.4.1   Energy storage applications

The typical structure of TMDs allows the intercalation within the layers of other species, making them possible candidates for energy storage. For this reason, chalcogenides like MoS$_2$ and WS$_2$ in bulk form were investigated as lithium ion

battery material.[65,66] The use as cathodes was however discouraged by their structural instability during the intercalation process together with their low average voltage, energy limits and electrical conductivity.[65] On the contrary, the use of exfoliated nanosheets as anode is a very attractive option since the loosely staked plates can easily accommodate structural changes. The use of composite MoS_2/graphene as anode exhibits a great electrochemical performance with a specific capacity of 1100 mAhg^{-1} at a current of 100 mAg^{-1} and a good cycling stability.[67,68,69,70] Moreover, the columbic efficiency of the graphene oxide based material, the most commonly used anodic material in lithium ion batteries, is much lower than the one obtained for MoS_2. The reason might be the absence of active sites on the basal plane, which avoids the trapping of lithium on the surface common for graphene oxide based materials.

1.11.4.2 TMD transistors

Semiconductor TMDs can be used for transistor applications in digital electronics. The processors currently considered the state of the art are silicon-based metal–oxide–semiconductor field-effect transistors (MOSFETs).[71] Those transistors however, when further scaled down in dimension, cannot overcome heat dissipation problems due to statistical and quantum effects. [71] The FET (field effect transistor) structure consists of a semiconductor interconnecting a source and a drain electrode, which is also separated by the gate electrode on the top by a dielectric layer.[72] The most common semiconductor used is silicone, as it meets all the requirements of a good transistor: high charge carrier mobility, high switching on/off ratio (connected to the material conductance) and high conductivity (defined as the product between charge density and mobility). The charge density can be increased in semiconductors by doping however this also leads to a decrease in mobility due to scattering. [73,74,75]

TMDs with their sizable band gap can support a high switching on/off ratio while maintaining high charge mobility with the additional advantage of the possibility to scale down the material to ultrathin layers. [76,75] Furthermore, their 2D structure offers the important advantage of producing layers with a sub nanometer thickness, which coupled with their band gap range of 1-2eV, results in increased control over the switching and therefore a high on/off ratio.[77] This helps to

decrease the most relevant factors preventing the transistor miniaturization such as the power dissipation and the short-channel effects.

The first implemented MoS_2 thin layer device was a top-gate transistor (Figure 1.11).[76] This device had n-type conduction exhibiting a room-temperature mobility higher than 200 $cm^2\,V^{-1}\,s^{-1}$ with a switching on/off ratio of about 10 [8]. Moreover, the top-gate geometry required a smaller voltage to switch the device, allowing the insertion of more than one device in the same substrate. The mobility of the MoS_2 monolayer was further improved by the use of HfO_2 as a k-dielectric in the device.[78,79,80,81] Despite the use of HfO_2, the mobility for MoS_2 top-gate transistors is still too low to compete with conventional transistors. However, their use can still be interesting for electronics which require low electronic power.[75]
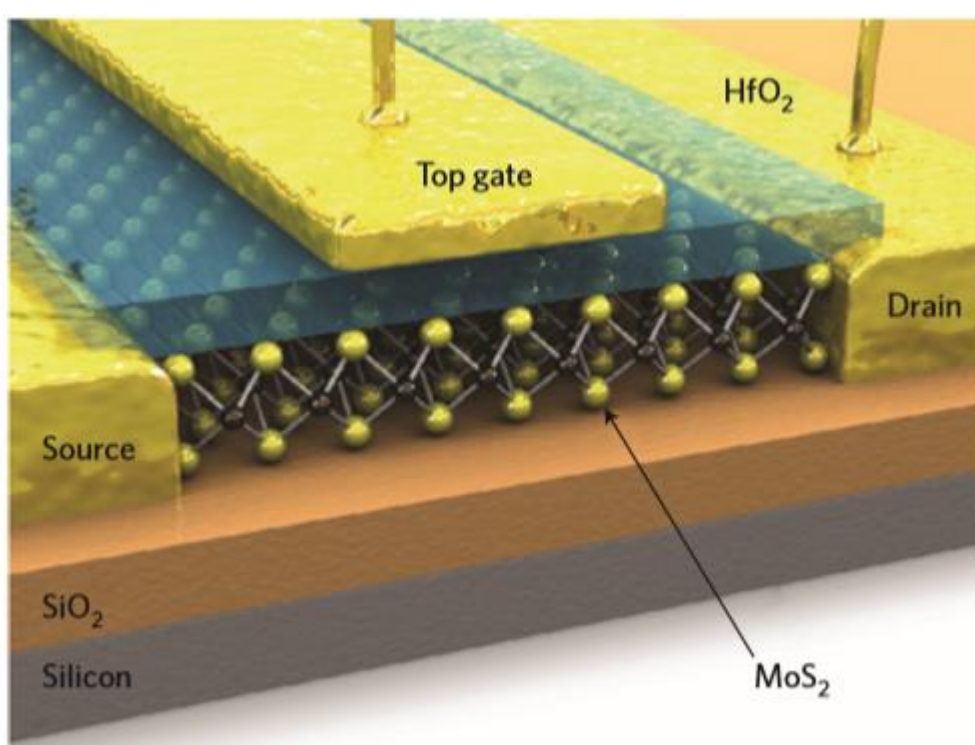
Figure 1-11 Scheme of HfO$_2$-top-gated monolayer MoS$_2$ FET device. The picture is reproduced from reference [76]

1.11.4.3   Optoelectronic devices

Electronic devices, which can control, generate and detect electronic light, are defined as optoelectronics. Common applications of optoelectronic are lasers, LEDs, solar cells, optical switches, photodetectors and displays. For those applications, the electronic band gap structure plays an important role because it influences the ability of the material to absorb and emit light.

TMDs find some of their applications in solar arrays and transparent displays as semiconductors because of their tuneable band gap used as light absorbing or

emitting component. In these applications, the band gap is often tuned by intercalation of metal ions or organic molecules. [82,83]

A thin film of MoS_2 was used within a phototransistor as a photodetector[84] due to its photosensitivity[85], and the resulting device responded to changes of incident light intensities within 50 ms. The bandgap was tuned by preparing MoS_2 layers with different thickness, enabling the photodetection of different wavelengths. [86] Single or double layers of MoS_2 with a band gap of 1.8V and 1.65V, respectively, were used for green light while triple layer MoS_2 and its band gap of 1.35V was used for red light detection.

Electroluminescence and photoluminescence are two interesting material properties. Electroluminescence is the capability to emit photons in response to an electron stimulus and is required to develop LEDs and diode lasers. Examples of electroluminescence in TMD materials were reported for MoS_2 electrically excited by Au nano-contacts [87] and SnS_2 monolayers incorporated into a polymeric matrix.[88] Photoluminescence is the property of some materials to absorb a photon light at certain wavelengths and then reemitting it at a different energy. Materials with direct band gaps can directly absorb or emit photons with an energy bigger than the band gap. On the contrary, indirect band gap materials require the absorption of an additional photon during the process to supply the difference in momentum leading to a less efficient process. MoS_2 monolayers with their direct band gap are good candidates for future flexible optoelectronics requiring active light-emitting layers.[89,73] Even if the photoluminescence of a MoS_2 monolayer is enhanced from its bulk form, its quantum yield is lower than expected for a direct band gap material. For this reason, more studies are required to better understand this photoluminescent emission and quenching before the development of those devices.

1.11.5   Transitional metal phosphides (TMPs)

Transitional metal phosphides can be efficient and resistant catalysts with a wide selection of compounds. Their electron rich surface makes them more reactive than other compounds like carbides, nitrides and sulphides for catalytic applications.[90] In particular, their activity as hydrodesulfurization (HDS) catalysts and therefore their capability of absorbing and desorbing hydrogen has made them good candidates for hydrogen evolution reaction. Beyond water splitting,

phosphides find their use in other applications involving energy conversion and storage as battery and supercapacitors.

.

1.11.5.1   Crystal structure and properties

Phosphides are a very heterogeneous class containing a wide range of structural types with different physical and chemical properties. Generally, phosphide structure is based on trigonal prisms instead of the layer structure typical of TMDs, which allows the formation of more isotropic crystal structures.[22] As a result, phosphides have a higher number of unsaturated surface sites in their structure compared to TMDs and therefore a higher intrinsic activity.[22] The bond type present in this structures is not always defined and it is interpreted as covalent or ionic depending on the case.

Despite their heterogeneity, phosphides are often classified by the metal phosphorous ratio as metal rich (M/P>1), monophosphide (M/P=1) and phosphorous rich (M/P<1). The polyphosphides (M/P>1) are characterized by a P-P bond with a length comparable to the one of black phosphorous (d_{p_p} = 2.23 Å) and varies from 2.15 to 2.30 Å. The physical properties and the structure of polyphosphides are typical of covalent compounds. Their localized valence electrons make them good semiconductors or isolators with only a few exceptions. Moreover, the melting point and the thermal stability are the lowest between other phosphides compounds. Metal-rich phosphides share similar characteristics with refractory hard metal compounds (carbides, nitrides, and borides) like high thermal stability, electrical conductivity and chemical resistance to dilute acids and bases.[91,92,93,94] However, the melting point and the stability is generally lower for the phosphides. The M-M bond length in compounds with MP_x structures decreases with increasing phosphorous molar fraction x. At the same time, the density decreases with increasing phosphorous content; e.g. MoP_4 - 3.9 gcm^{-1} , MoP_2 -5.4 gcm^{-1}, MoP - 7.2 gcm^{-1}, Mo_3P - 9.1 gcm^{-1}, Mo - 10.2 gcm^{-1} [92] Metals in rich phosphides are trigonally or octahedrally coordinated with phosphorous. The most common between those two is the trigonal prismatic coordination, which can extended up to ninefold coordination by additional atoms above the rectangular prism faces. An example of trigonal prismatic coordination is MoP, while Fe_3P, Ni_3P, Ni_2P, Co_2P,and Ru_2P have a tricapped trigonal prismatic coordination.
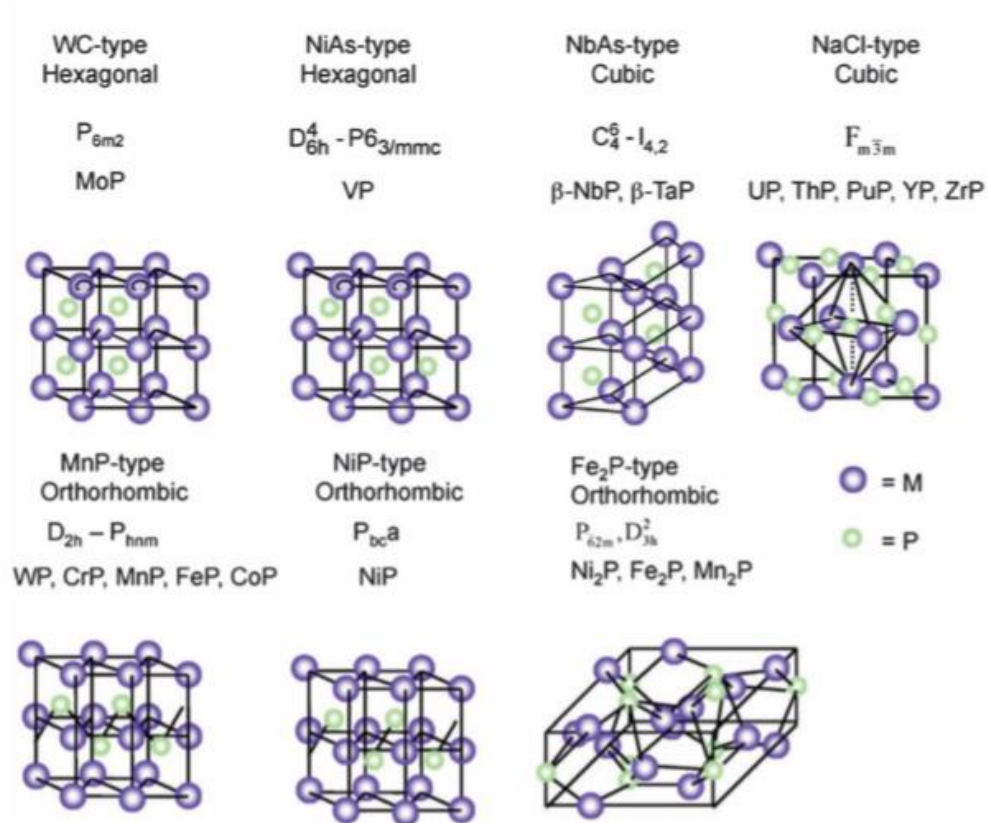
Figure 1-12 Crystal structure of the major transition metal phosphides.[22]

1.11.5.2 Phosphides as HER catalysts

Nickel phosphate was the first material of this class to be studied as hydrogen evolution reaction catalyst after DFT calculations carried out by Liu and Rodriguez identified an excellent activity on the (0001) plane. This phase mimics the mechanism of the NiFe hydrogenase with the advantage of a higher thermostability due to the solid surface.[95]

The (0001) crystal face performs well due to the co-existence of two active sites which take part in the so called "ensemble effect",[95] where the P actively participates in the HER, acting as a proton acceptor site complimenting the hydride acceptor sites on the Ni atoms. Jointly, the two sites therefore perform far better as HER catalysts. The decrease of active nitride sites on the surface due to the presence of phosphorous also seems to moderate the binding strength of the reactant on the surface, making the catalyst acting more like the NiFe hydrogenase rather than a metal surface.[95,96]
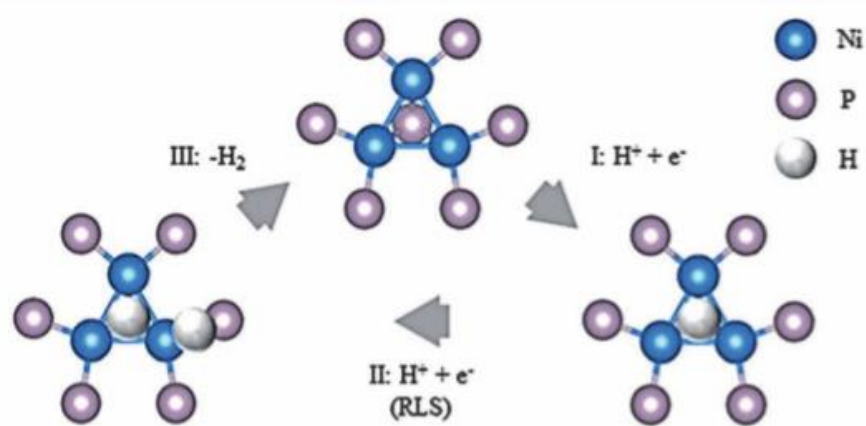
Figure 1-13 Top view of the active site on the (0001) phase showing the "ensemble effect" between the phosphorous and the nickel. The picture is reproduced from reference [95]

Experimentally Lewis *et al.* were the first to undertook the synthesis of Ni_2P as nanoparticles exposing a high density of the Ni_2P (0001) surfaces.[96,95] The particles were tested for hydrogen evolution reaction on a titanium substrate in a solution of 0.5 M H_2SO_4, which lead to an overpotential of 130 mV with a current density of 20 mA cm^{-2} and a Tafel slope of 46 mV dec^{-1}. This excellent HER activity further confirmed the studies by Liu and Rodriguez and increased the interest in phosphides as hydrogen evolution reaction catalysts.

Kucernak *et al.* carried out a study on the effect of phosphorous on nickel phosphides.[45] It turns out that by increasing the phosphorous percentage within the composition, the resistance of the material towards corrosion was increasing along with the catalytic activity.[45] Similarly, a study conducted by Wang's group investigated the effect of different amounts of phosphorous between molybdenum in metal form, Mo_3P and MoP in the hydrogen evolution reaction.[97] As a result, it was found that an increased degree of phosphorylation leads to a change in the catalytic activity of the metal, enhancing its performance. Only MoP had high stability and performance in both basic and acidic media.

The importance of the phosphorous within the structure was also highlighted by DFT calculations, which found a free energy close to zero in the active site with a behaviour similar to the sulphur in MoS_2.[97] Like sulphur in molybdenum sulphates, phosphorous increases the number of edges on the surface, thereby increasing the number of active sites.

1.11.5.3   Water oxidation

The oxygen evolution reaction (OER) is the water splitting semi reaction which requires the highest overpotential to be performed and so its optimization is very important for future applications.[98] One of the many advantages of applying TMDs as water spitting electrocatalysts is their bifunctional use (as HER and OER catalyst) in alkaline and basic media. Since the OER reaction is carried out at high potential in alkaline media, the phosphide catalysis surface often gets oxidised and this influences its catalytic properties. A porous film of Cobalt phosphide/phosphate was the first TMD to be proposed as OER catalyst in basic media. [99] Subsequently, nanoparticles of pure Ni_2P were proposed as OER catalysts, obtaining a current density of 10 $mAcm^{-2}$ from an overpotential of 290 mV in a solution of 1M KOH. [100] This study also highlighted that the catalytic activity was due to the material nature and not to its surface area. After having performed the OER reaction for an hour at 1.5V, the Ni_2P particles changed their composition to a ratio of Ni_2P/NiO_x. This change enhanced the catalytic activity and stability of the material. [101]

Surface oxidise nanorods of CoP were also reported as OER catalyst by Xing et al.[102] The material was synthesised from a hydrothermally obtained Co_3O_4 precursor with the subsequently phosphorization by a low temperature process. The obtained material required an overpotential of 320 mV to obtain a current density of 10 $mAcm^{-2}$ in a solution of 1M KOH. Similar to Ni_2P, the promising performance of the material could be explained by the presence of cobalt oxide on the surface. Other transition metal phosphide electrodes were synthesised as OER electrodes by phosphorization of the metal foils Fe, Co, Ni, Cu and NiFe. [103] The most active among those was NiFeP, achieving a current density of 10 mA cm^{-2} with an overpotential of 277 mV.

The first phosphide tested as bifunctional catalyst was CoP prepared in the form of a 3.3 nm nanosheet [104] The material required an overpotential of 277 and 111 mV for the OER and HER semi reactions to achieve a current density of 10 $mAcm^{-2}$. The performance was also tested in a real water electrolysis device by applying the material as anode and cathode and separating the electrodes by an anion-exchange membrane. The current density obtained by applying an overpotential of 1.8V was 335 mA cm^{-2}. This performance was competitive with the state-of-the-art catalyst Pt/IrO_2 that achieves at the same overpotential a current density

of 399 mVcm^{-2}. Despite this encouraging success, the use of CoP nanosheets still need to overcome some challenges to be considered as competitive bifunctional catalysts. The major challenges associate with the use of CoP in real water electrolysis cells are the cell performance decay generated by the aggregation and rupture of the catalyst at the anode and the anion membrane degradation.

1.11.5.4 Batteries

Nanostructured TMP materials find their use in battery applications as possible replacement of the graphite in the anode. In fact, graphite has its theoretical capacity limited at 372 mAhg^{-1} when completely converted to LiC_6. TMPs are very attractive as anode material because of their high degree of electrode delocalization, which leads to lower oxidation state of the metal and a strong M-P covalent bond connection. The theoretical limited capacity of phosphides is 1200 mAhg^{-1}, with a conversion reaction occurring only after full insertion of the lithium inside the electrode. Unfortunately, this high phosphine capacity tends to decline over multiple cycles because of the volume change during the charge/discharge process and the fact that this conversion is not always reversible. The irreversibility of those reactions is more common for Mn, Fe and Cu while is generally rare for metals such as Ni and Co.[105]

A remarkable work reported GeP$_5$ as anode for storage applications, which used the strategy of carbon confinement on the TMP surface to limit the volume expansion of the material. [106] The material was made using pure Ge powder and amorphous red P by high-energy mechanical milling. With increasing reaction time, a change in morphology from a crystalline to a graphene like structure was observed. This structure showed in its charge/discharge curve a loss in capacity with the number of cycling and a low conductivity. However, the addition of carbon changes the performance, limiting the material aggregation and maintaining a high electrical contact. The resulting composite had a high rate performance with a charge/discharge capacity of 2300 mAhg^{-1} that remained constant for over 40 cycles. The improvement of the performance was due to the formation of P-C bonds between the GeP$_5$ and carbon interface. After those promising results, other carbon composited phosphides were synthesised and also showed very promising applications for lithium ion batteries. [107,108,109,110,111]

Much effort is also put into the development of Na-ion batteries due to the abundance of sodium compared to lithium. TMPs were also applied in those systems as anode material. A reported example was Sn_4P_3 material in a carbon yolk shell structure which confined the particles to avoid loss in performances due to volume expansion.[112] This material gave a capacity of 790 mAhg^{-1} with a stable cycling performance. Material damage due to changes in volume during the charge/discharge process is the main problem faced during lithium ion batteries development. This inconvenience is even more severe for Na-ion batteries because of the higher molar volume of sodium. For this reason, more studies need to be conducted in order to make this material competitive as a type of energy storage.

1.11.5.5   Supercapacitors

Supercapacitors are an attractive type of energy storage form; however their low energy density made their application as primary power source unfavourable compared to lithium ion batteries. Despite this disadvantage, characteristics like their high charge/discharge rate and the long life cycle makes their study and optimization interesting for further development. The most promising way to optimise a supercapacitor is to combine a double-layer capacitor with a pseudocapacitor.

Materials like TMP are of interest for supercapacitor applications because of their metalloid characteristics and superior electrical conductivity.[113,114,115] The first phosphide reported as pseudocapacitor was Ni_2P nanoparticles on rGO.[116] Their capacity was suggested to arise from a pseudo-capacitive capacitance based on a redox process. This redox process was speculated to be due to the $Ni(OH)_2/NiOOH$ couple which is formed and reversed during the charge and discharge process. Moreover, the rGO substrate had the function of dispersing the Ni_2P particles during the synthesis and therefore increase the charge transfer conductivity. This material obtained a specific capacitance of 2266 Fg^{-1} for a current density of 5 mAcm^{-2} with a Columbic charge/discharge efficiency of almost 100% after 2500 cycles. Another phosphide material reported for its pseudocapacitor function was Ni_2P coated uniformly by Ni particles.[117] The amorphous material obtained had a specific capacitance at 2 Ag^{-1} of 1115 Fg^{-1} which declined to 1029 Fg^{-1} after 3000 cycles.

Phosphorization of transition metal oxides and hydroxides as a way to enhance their supercapacitor performance was suggested by Zhou et al. [118] In this study, Ni(OH)2 nanosheets were phosphorizated, creating 3D networked Ni_2P nanosheets. The performance of the resulting material was remarkable, obtaining a specific capacitance of 2141 Fg^{-1} at 50 mVs^{-1} instead of the 747 Fg^{-1} at 50 mVs^{-1} obtained for $Ni(OH)_2$. This improvement was explained by the enhanced conductivity due to the carbon joined with the porous nanosheet structure.

Moreover, this experiment highlighted that phosphorization as an interesting way to enhance the metal oxide performance, further confirming the potential application of TMP in the supercapacitor field.

1.11.6 Ternary transition metal nitrides (TTMN)

Ternary transition metal nitrides are a class of compounds with a rich variety of structural types. In those compounds, the relationship between composition-structure-properties has not yet been fully understood and limited studies are reported. Like binary nitrides, these compounds are used as sensors,[119] supercapacitors,[120,121,122] solar cells[123] and electrocatalysts for ammonia synthesis,[124] hydrogenation and hydrocarbon reaction.[125]

1.11.6.1   Structure

Nitrides have a wide range of structures and stoichiometries consisting of a transition metal T combined with another transition metal M, which is not bound with nitrogen.

The TMN stoichiometry has a crystal structure that can be cubic, hexagonal or perovskite. The cubic structure is observed in transition metals belonging to the first row. Those compounds have the formula of $T_{1-x}M_xN$ and generally do not show any changes in their lattice periodicity after substitution of the nitrogen with carbon. [126] Hexagonal structures are common for compounds like $Ti_{0.7}Co_{0.3}N$, $Ti_{0.7}Ni_{0.3}N$, $Mo_{0.8}Co_{0.8}Ni_{0.9}$ and $Mo_{0.8}Ni_{0.8}N_{0.9}$. In these structures the metals result in a hexagonal arrangement and present a layer sequence of ABACABAC, while the nitrogen is octahedrally coordinated. Ternary nitrides with a perovskite structure are derivates of Mn_4N and have a crystal composition of $Mn_{4-x}Me_xN_{1-x/4}$, where the metal Me can be Cr, Mn, Ni, Cu and Zn. The substitution of Mn with external heteroatoms changes the lattice parameters inside the structure, which increase or decrease depending if Cr and Mn or Ni, Cu and Zn are incorporated,

respectively. Together with the lattice parameters, magnetic properties also change with the substitution of Me within the structure. In fact, the magnetic moment per unit cell strongly depends on the metals inside the structure. The substitution of Mn with other heteroatoms can either increase or decrease the number of electrons leading to a coupling of spin. Metals like nickel, copper and zinc, for example, increase the electron concentration with a spin pairing together with a decrease of the magnetic momentum by the formation of nitrogen vacancies. [127] However, studies in this area did not yet reach a general consensus, and is therefore not possible to delineate a trend and mechanism.

Nitrides with the TMN_2 stoichiometry, like chalcogenides, have a 2D structure and their chemical characteristics are dependent on the nature and size of the cations T and M. Generally, the metals having this stoichiometry are trigonally or octahedrally coordinated and belong to the 2nd or 3rd row of transition metals. The compounds belonging to this class are semiconductors or weekly metallic and behave like paramagnets.
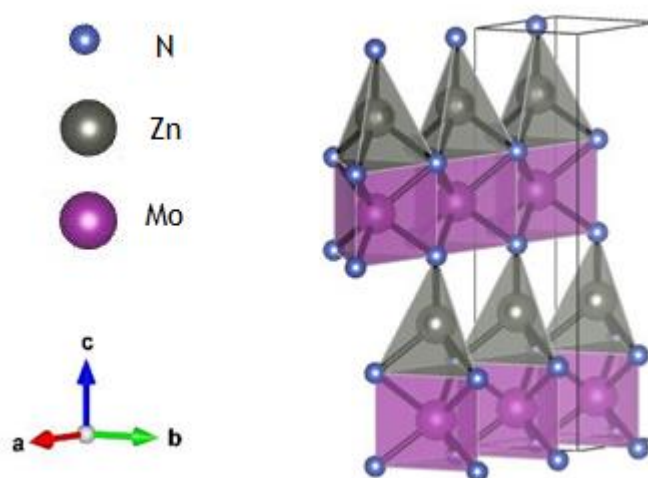
Figure 1-14 Example of the hexagonal structure ZnMoN$_2$ belonging to the structure type TMN$_2$. The picture is reproduced from the reference [128]

Nitrides with the T_2MN stoichiometry contain elements in their highest oxidation state. This type of stoichiometry is also common between some carbides they share the same close packed hexagonal H-phase structure with. In the crystal structure the nitrogen is in an octahedral position and located between two transition metal layers with the elements exhibiting an alternating sequence along the c axis of $M_AT_BNT_AM_BT_ANT_BM_A$. The T metal can belong to groups 4 and 5, while the group of the M metal can vary and therefore affect the compound properties

more. If M belongs to the IIB or IIIB group, the c/a ratio will be high, leading to an almost hexagonal close packing structure with metallic characteristics. On the contrary, when the M is from group 4 or 6, the c/a ratio will be smaller and the metallic nature less pronounced.

The T_3MN stoichiometry crystallizes as anti-perovskite and mixed-anti-perovskite. This structure differs from perovskite by the reversed position of the anions and the cations.[129] Another difference from perovskite, which affects the physical properties, is the presence of two types of anions coordinated with one cation. Using the general formula (ABX), the anion position X is now occupied by a cation (a transition metal), while the positions A and B are now occupied with different types of anions.[130] In Figure 1.14 a perovskite unit cell is shown, with the A, B and X positions indicated at the corner of the cube, at the octahedral site and at the centre of the cubic face, respectively. The unit cell of the anti-perovskite can deviate from the ideal cubic structure to tetragonal or orthorhombic depending on different synthesis conditions used. For example, a study conducted by Sun et al [131] using neutron diffraction analysis observed a phase change in the crystal structure of Mn_3ZnN in the temperature range between 50 K and 295 K. In particular, the cubic structure had only the C1 phase at room temperature and started transitioning to C2 at temperatures below 177 K. The two cubic phases C1 and C2 differ only in their lattice parameters, which are slightly larger for the C2 structure. This difference affects the magnetic order within the structure and therefore changes the crystal properties. Applications for this stoichiometry are found in fuel cells, where Ni_3ZnN is the most important compound reported for this class.[132] This material was also studied as ORR (oxygen reduction reaction) electrocatalyst, exhibiting an onset potential vs. RHE of 0.81 V in alkaline media and good stability. [132]
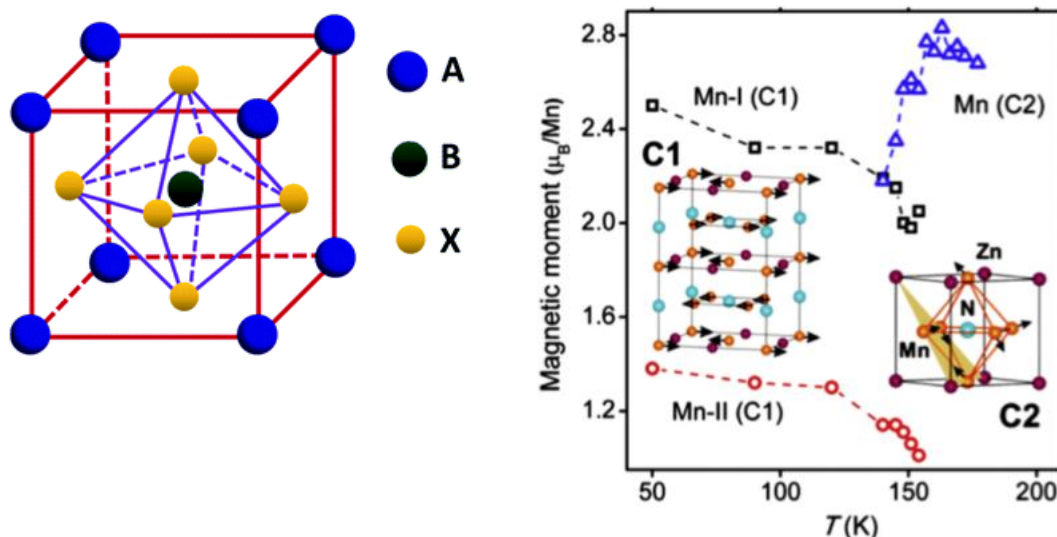
Figure 1-15 Left, anti-perovskite structure. Right, the magnetic moment measured by neutron diffraction at different temperatures. The insert shows the C1 and C2 phase with the magnetic moment at the Mn atom indicated as arrows. The picture is reproduced from reference [131] .

The T_3M_2N structure known as ß-Mn is a cubic system where the metal atoms have a body centre cubic and a cubic face centre arrangement. The stoichiometry of those compounds can be either T_3M_3N or T_3M_2N depending on the different element's stability within the crystal. For example, the Ni_2Mo_3N structure is more common than Ni_3Mo_3N. [133,134] On the contrary, Fe_3Mo_3N has a faster formation than Fe_2Mo_3N, whose structure is not yet fully characterized.[135] When ordered, this structure has interesting potential for superconducting applications.

Nitrides with the η $_2$-carbide type structure are characterized by a T_4M_2N stoichiometry. In this structure, the nitrogen is in the centre of a deformed octahedron whose holes are partially filled by the metal atoms of the lattice. As for ß-Mn, this structure has a different stoichiometry depending on the elements present in the structure and can assume a crystal formula of T_4M_2N or T_3M_3N. The T_3M_3N stoichiometry is also known as η $_6$ and its structure presents a reduction by 50% of the nitrogen on the 16c site. [135,136,137] This class of compounds is very interesting for their long range magnetic order which can be modulated by using different T/M metals and different numbers of electron valence. [135,136,137]

1.11.6.2   Ammonia reaction synthesis

Nitrides has been used as catalyst for ammonia synthesis and decomposition in the last few decades. In particular, ternary transition metal nitrides were shown to

have higher activity than individual nitrides. Gurram et al prepared ternary Mo nitrides using a molybdenum precursor and other ternary transition metals reduced under an ammonia flow.[124] From the obtained compounds, $CoMo_2N$ was the one with the best performance with an increased catalytic activity up to fivefold.

1.11.6.3   Nitrides as catalysts

Dai et al. reported the use of MoTiN as a catalyst for acetylene hydroclorination.[125] The reaction conversion was 89% for a Ti/Mo ratio of 1:3 and selectivity achieved 98.5% for the vinyl chloride monomer (VCM). It was found that the Ti doping was inducing an increase of the absorption capacity of the hydrogen chloride and a reduction of acetylene absorption. Unfortunately, this nitride showed poor stability as a catalyst due to the deactivation induced by the absorption of C_2H_2. However, its activity is comparatively better than Mo_2N and TiN, suggesting the use as a starting point to design other catalysts for the production of vinyl chloride monomers.

The compounds Co_3Mo_3N and Fe_3Mo_3N were synthesised by Noèmie Perreta et al [138] as catalysts for hydrogenation of organic reaction. The Co_3Mo_3N catalyst was determined to be active for hydrodechlorination and used for benzene synthesis. The synthesis of Fe_3Mo_3N by TPR at 773 K resulted in a compound whose hydrogenation rate for the conversion from nitrobenzene to aniline was higher than the corresponding Co_3Mo_3N.

1.11.6.4   Nitrides as sensor

There is great interest to use non-noble metals as electrochemical sensors for molecular detection due to their sensitivity and economic fabrication. In particular, compounds with nano-array architecture are extremely interesting to study because of their large and specific surface area. Fe_2Ni_2N nanosheets on a Ti mesh were used as an electrochemical sensor to quantify glucose.[119] The nitride had a good performance and was able to sense glucose over a linear range of 0.05 μM-1.5 μM with a response time of less than 5 seconds. The sensor had a high sensitivity of 6250 μAmM^{-1} with a long term stability and selectivity.[120]

1.11.6.5 Solar cells

Theoretical and experimental calculations both suggest $CuNbN_2$ as an interesting material for a tandem solar cell.[123] The material has a layer structure belonging to the space group R3m. In the layers NbN_6 is arranged octahedrally and separated by the N-Cu-N bond. The study showed that this material had an absorption between 1.3 and 1.4 eV with the lowest band energy of 0.9 eV.

1.12 Artificial photosynthesis devices

Considerable interest has been raised to find a way that uses sunlight to split water into hydrogen, producing "artificial photosynthesis" devices.

There are two possible set ups which can be implemented in order to commercialize those devices: the coupling of an electrolyser with a standard solar panel or the development of a device able to perform light harvesting and hydrogen production at the same time (Figure 1.13).

While the first approach comes with the advantage of using an already developed apparatus, it has a loss in efficiency due to the additional steps involved.[139]

For this reason, many efforts have been made to develop devices which could directly convert sunlight into hydrogen and use it as a fuel, reducing process steps and thereby gaining efficiency. [140,141,142]

The power of the incoming sun light is very low, achieving a maximum of 0.1 W cm^{-1} and therefore only allowing to collect a current density of maximally 10 mA cm^{-2}.[143] This is insufficient compared to a standard electrolyser of $0.5 - 2$ A cm^{-1}.[144] The production of the same amount of gas per unit time for those electrolysers requires an electrode area around 50-200 times bigger than standard ones, making the use of platinum, the best performing material, inapplicable for larger scales.

Only the use of cheap and largely available compounds can make these systems commercially applicable, and therefore many studies have focussed on finding efficient materials in the compounds belonging to the transition metals.[145]

The pH of the electrolyser is also relevant for hydrogen efficiency. Electrolysers perform best at extreme basic or acid pH where the concentration of charges is the highest. However, most of the semiconductors used as catalysts are not stable at these conditions for long times and efforts have been made to find alternative

electrolysers with good performances at neutral pH. Mild pH will also be beneficial for other parts of the electrolyser such as gaskets, connectors and separator membranes, making the overall electrolyser's life longer and decreasing maintenance cost.[146]

Figure 1.13 shows the two types of solar-to-fuel devices: the wireless configuration with a buried photovoltaic (Figure 1.13a) and the wire configuration using a semiconductor film underneath the electro catalysts for light harvesting (Figure 1.13b).

In 1998, Rocheleau and co-workers made the first wireless photoelectrochemical solar-to-hydrogen device with CoMo and $NiFe_yO_x$ as HER and OER catalyst, respectively.[147] The device was performing stable for over 7 200 hours at pH 14 with a solar-to-hydrogen conversion efficiency of 7.8% for a cell with an area of 1 cm^2. Verlage *et al* improved the performance of wireless solar to hydrogen devices to an efficiency of 8.6 % (per cell of 1 cm^2) by building a GaAs-InGaP tandem-junction for light harvesting. The group used a nickel based OER catalyst and NiMo for the HER half-reaction. Later, a system performing in a borate buffer solution with a pH of 9.2 was reported with triplet-junction silicon as light absorber, cobalt oxy-hydroxide as electrode for the OER and NiMoZn for the HER.[148] The device achieved an efficiency of 2.5% for a cell with an irradiation area of 2 cm^2 using simulated solar light as irradiation source. Since the use of silicon is expensive for large scale production, Jansen et al suggest to use a triplet-junction made with a polymer instead of silicon for light harvesting.[149] The light-to-hydrogen conversion was performed at pH 9 obtaining an efficiency of 4.6% for an area < 0.1 cm^2 and decreasing to 1.3 when the cell area became 1.2 cm^2. The use of organic polymers has also the additional advantages of improving the flexibility and to reduce the production cost.
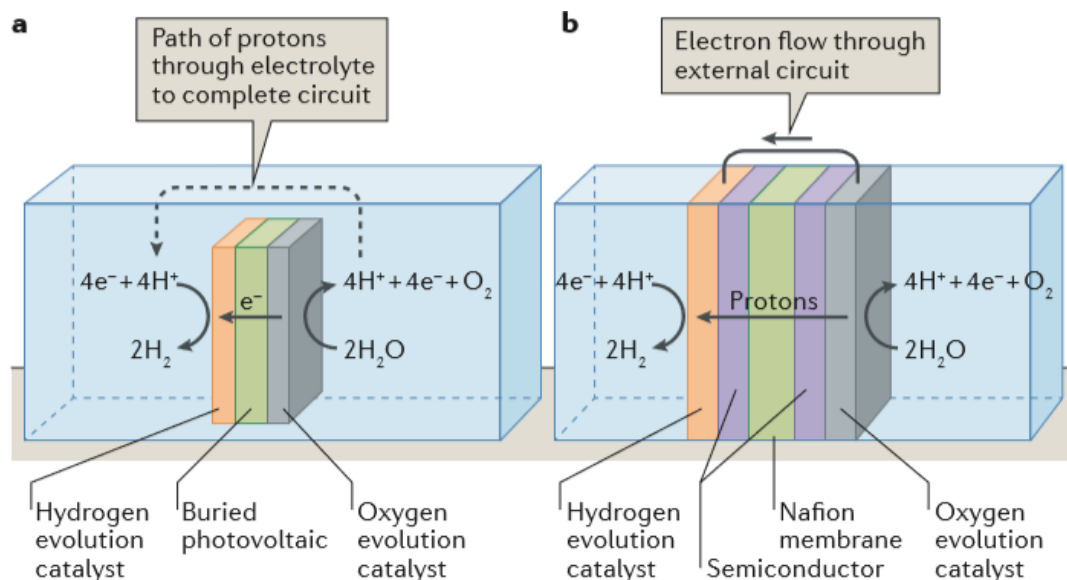
Figure 1-16 Schemes of artificial photosynthesis systems.[150] **a) Wireless configuration where the circuit is closed by the flow of the electrons through the electrolyte. b) Wire configuration with an external circuit. For both setups the light to be absorbed has to pass through the catalyst making thin catalysts desirable.**

1.12.1 Challenges associated with the development of solar-to-hydrogen devices

Despite various new developments in the field, challenges associated with scaling up solar-to-water splitting devices still remain a significant hurdle for their entrance into the market. For example, most of the irradiated areas of systems reported in the literature is 1 cm^2 and therefore it is necessary to find a way to scale them up to arrays of several square meters in order to produce a significant amount of hydrogen. Moreover, more studies need to be done to improve the device performance and increasing the long-term reliability with a robust design that requires low maintainance.[151] Set up components like the membrane, the electro catalysts and the light harvesters were also tried to be substituted with cheaper alternatives in order to keep the cost low. Those requirements challenge the solar-to-hydrogen device construction in both the material as well as engineering development.

The harvesting of hydrogen in a large-scale using extended surface arrays comes with the additional problem of safety, which still needs to be solved. When the current density of the device reaches a value of 10 mA cm^{-2}, the hydrogen and the oxygen produced during the reaction can permeate through the separation membrane and an extensive mix of those gasses is very dangerous.[152]

Even if there are methods which prevent the extensive formation of this gas mixture inside the electrolyser, they often reduce the efficiency of hydrogen production.[153] This adds to the many problems associated with the production of hydrogen in a large scale at atmospheric pressure.

The development of an electron-coupled proton buffer (ECPB) was proposed as a solution, decoupling the HER and the OER reaction and therefore avoiding the presence of both gasses inside the electrochemical cell at the same time.[154,155,156] To avoid this gas mixture the oxygen, which is produced under solar irradiation, is coupled to the reduction and protonation of ECPB, which works as a counter electrode.[157] The ECPB is then deoxidise back electrochemically to generate hydrogen.

The production of "artificial photosynthesis" devices is still facing a lot of challenges and is far from perfect and ready to be released on the market. Much work needs to be done in optimization of the device design as well as in the development of the semiconductors and the electro catalysts before it will be possible to produce a commercial artificial photosynthesis system.

1.13 Conclusion

The necessity to substitute traditional energy sources with renewable energy comes with the need for an investment in energy storage systems. Research on earth-abundant catalysts for photoelectrochemical or electrochemical water splitting helps the hydrogen economy to become suitable for large scale set ups and therefore to be commercialized. Due to widespread availability, these inorganic materials compensate their lower activity as catalysts compared to noble metals with their price. Other than having excellent catalyst performance, an inorganic catalyst also needs to be easily scalable and to exhibit great durability over years in order to be a suitable candidate for industrial purposes. Catalyst classes like sulphides, phosphides and nitrides have shown promising results in this direction. However, many challenges still need to be overcome in order to make solar-to-hydrogen devices available in the market in the close future. Structural problems associated with the necessity of scaling up systems reported in the literature has led to challenges in many different areas. Another relevant issue is the mismatch between the optimal pH conditions in which electrolyser perform best and the milder pH that will prevent the device's damage to maintain the

cost. Despite these many challenges, much progress has been made in the last two decades in order to commercialise solar-to-hydrogen devices leading to the optimistic prediction that those devices will become one day reality.

1.14   Scope of this work

The aim of this work was to investigate new cathode materials for hydrogen evolution reaction able to compete with the already existing but expensive noble metal catalysts. Developing cheap catalysts from earth abundant materials will make hydrogen production by electrolysis commercially favourable, helping to decrease the amount of carbon dioxide release into the atmosphere due to extensive use of fossil fuel. During this work, two compounds belonging to the major inorganic classes and one from a recent study were prepared and electrochemically characterised.

The synthetic strategies were chosen based on the use of cheap reagents and the possibility to scale up. One of the major strategy applied to improve the performance was doping the material with another metal in order to tune the properties by either enhancing the activity of active sites already present or by improving the conductivity. For the case of the Co-doped molybdenum sulphide synthesised in Chapter 3, the material was prepared in distorted form, leading to the advantage of further increasing the number of active sites by the higher presence of defects for this particular morphology. Another strategy to improve the performance was by the selection of the substrate, which improved the electrical conductivity and therefore the overall catalyst's performance. The substrates chosen for this purpose were Fluorine-doped SnO_2 in Chapter 3 because of its transparency suitable for solar-to-hydrogen applications and the more conductive glassy carbon for the electro catalysts studied in Chapter 4 and 5.

All the materials were also characterized electrochemically to test their hydrogen evolution reaction performance in acid and basic media. Besides the importance of obtaining a material with the lowest overpotential possible, other tests were carried out to ensure the stability of the performance over time and the material efficiency in hydrogen production. All those measurements were performed in

order to ensure that the prepared materials were in line with the criteria necessary for commercialization in the future.

1. 19 Bibliography

1. Grätzel, M. Photoelectrochemical cells. *Nature* **414**, 338–344 (2001).
2. Solar Impulse. http://info.solarimpulse.com/timeline/view/7685#.V.
3. MS Turanor PlanetSolar: World's largest solar-powered boat. *The Economic Times* (2014).
4. Carrington, D. Solar plane makes history after completing round-the-world trip. *The guardian* (2016).
5. Fountain, H. Solar Boat Harnessed for Research. *New York Times* (2013).
6. D'Orazio, D. An inside look at the world's largest solar powered boat. *The verge* (2013).
7. Plumer, B. The Netherlands built a bike path entirely out of solar panels. *Vox* (2014).
8. Nocera, Nathan S. Lewis, D. G. Powering the planet: Chemical challenges in solar energy utilization. *Proc. Natl. Acad. Sci. U.S.A* **103**, 15729–15735 (2006).
9. Laursen, A. B., Kegnæs, S., Dahl, S. & Chorkendorff, I. Molybdenum sulfides— efficient and viable materials for electro - and photoelectrocatalytic hydrogen evolution. *Energy Environ. Sci.* **5**, 5577–5591 (2012).
10. Hu, Carlos G. Morales-Guio, X. Amorphous molybdenum sulfides as hydrogen evolution catalysts. *Acc. Chem. Res.* **47**, 2671–2681 (2014).
11. Zeng, M. & Li, Y. Recent advances in heterogeneous electrocatalysts for the hydrogen evolution reaction. *J. Mater. Chem. A* **3**, 14942–14962 (2015).
12. Zohuri, B. *Hybrid Energy Systems.* (2017).
13. Magdalena Momirlana and T. N. Veziroglu. The properties of hydrogen as fuel tomorrow in sustainable energy system for a cleaner planet. *Int. J. Hydrogen Energy* **30**, 795–802 (2005).
14. Tatsuya Shinagawa, A. T. G.-E. K. T. Insight on Tafel slopes from a microkinetic analysis of aqueous electrocatalysis for energy conversion. *Sci. Rep.* **5**, 13801 (2015).
15. Y. Zheng, Y. Jiao, M. J. and S. Z. Q. Advancing the Electrochemistry of the Hydrogen-Evolution Reaction through Combining Experiment and Theory. *Angew. Chemie Int. Ed.* **54**, 52–65 (2014).
16. Graetz, J. New approaches to hydrogen storage. *Chem. Soc. Rev.* **38**, 73–82 (2009).
17. Qimin Ming Todd Healey, L. A. and P. I. Steam reforming of hydrocarbon fuels. *Catal. Today* **77**, 51–64 (2002).
18. C. Koroneos, A. T. Dompros, G. R. and N. M. Life cycle assessment of hydrogen fuel production processes. *Int. J. Hydrogen Energy* **29**, 1443–1450 (2004).
19. F. Safizadeh, E. G. and G. H. Electrocatalysis developments for hydrogen evolution reaction in alkaline solutions – A Review. *Int. J. Hydrogen Energy* **40**, 256–274 (2015).
20. J. Turner, G. Sverdrup, M. K. Mann, P. C. Maness, B. Kroposki, M. Ghirardi, R. J. E. and D. B. Renewable hydrogen production. *Int. J. Energy Res.* **32**, 379–407 (2008).
21. E. Skúlason, V. Tripkovic, M. E. Björketun, S. Gudmundsdóttir, G. Karlberg, J. Rossmeisl, T. Bligaard, H. J. and J. K. N. Modeling the Electrochemical Hydrogen Oxidation and Evolution Reactions on the Basis of Density Functional Theory Calculations. *J. Phys. Chem. C* **144**, 18182–18197 (2010).
22. Zhang, X. Z. and Y. Noble metal-free hydrogen evolution catalysts for water splitting. *Chem. Soc. Rev.* **44**, 5148–5180. (2015).
23. Lefrou, C. ; Fabry, P. ; Poinet, J.-C. *Electrochemistry: The Basics, with examples.* (2012).
24. P. J. Rheinlander, J. Herranz, J. D. and H. A. G. Kinetics of the Hydrogen Oxidation/Evolution Reaction on Polycrystalline Platinum in Alkaline Electrolyte Reaction Order with Respect to Hydrogen Pressure. *J. Electrochem. Soc.* **161**, F1448–F1457 (2014).
25. Egill Skúlason, Gustav S. Karlberg, Jan Rossmeisl, Thomas Bligaard, Jeff Greeley,

H. J. and J. K. N. Density functional theory calculations for the hydrogen evolution reaction in an electrochemical double layer on the Pt(111) electrode. *Phys. Chem. Chem. Phys.* **7**, 3241–3250 (2007).

26. Morales-Guio, C. G., Stern, L.-A. & Hu, X. Nanostructured hydrotreating catalysts for electrochemical hydrogen evolution. *Chem. Soc. Rev. Chem. Soc. Rev* **43**, 6555–6569 (2014).
27. P Atkins, J de Paula, R. F. *Chemical equilibrium*. (2002).
28. Niemantsverdriet., I. C. and J. W. *Concepts of modern catalysis and kinetics*. (2003).
29. Markovic, N. M. & Ross Jr., P. N. Surface science studies of model fuel cell electrocatalysts. *Surf. Sci. Rep.* **45**, 117–229 (2002).
30. J. D. Benck, T. R. Hellstern, J. Kibsgaard, P. C. and T. F. J. Catalyzing the hydrogen evolution reaction (HER) with molybdenum sulfide nanomaterials. *ACS Catal.* **4**, 3957–3971 (2014).
31. A. J. Bard and L. R. Faulkner. *Electrochemical Methods: Fundamentals and Applications*. (2000).
32. Potter, J. O. B. The Mechanism of the Cathodic Hydrogen Evolution Reaction. *J. Electroanal. Soc.* **99**, 169–186 (1952).
33. Eliezer, G. *Physical Electrochemistry*. (2011).
34. Trasatti, S. Work function, electronegativity, and electrochemical behaviour of metals: III. Electrolytic hydrogen evolution in acid solutions. *J. Electroanal. Chem. Interfacial Electrochem.* **39**, 163–184 (1972).
35. J. K. Nørskov, T. Bligaard, A. Logadottir, J. R. Kitchin, J. G. Chen, S. P. and U. S. Trends in the Exchange Current for Hydrogen Evolution. *J. Electrochem. Soc.* **3**, J23–J26 (2005).
36. Sabatier, P. *La Catalyse En Chimie Organique*. (1920).
37. Cook, T. R. *et al*. Solar Energy Supply and Storage for the Legacy and Non legacy Worlds. *Chem. Rev.* **110**, 6474–6502 (2010).
38. Laursen, A. B. *et al*. Electrochemical Hydrogen Evolution: Sabatier ' s Principle and the Volcano Plot. (2012).
39. Schmickler, W. & Trasatti, S. Comment on "Trends in the Exchange Current for Hydrogen Evolution" [J. Electrochem. Soc., 152, J23 (2005)]. *J. Electrochem. Soc.* **153**, L31 (2006).
40. Kourosh E. Zanganeh, A. S. A novel process integration, optimization and design approach for large-scale implementation of oxy-fired coal power plants with CO2 capture. *Int. J. Greenh. Gas Control* **1**, 47–54 (2007).
41. Voiry, D., Yang, J. & Chhowalla, M. Recent Strategies for Improving the Catalytic Activity of 2D TMD Nanosheets Toward the Hydrogen Evolution Reaction. *Adv. Mater.* 6197–6206 (2016) doi:10.1002/adma.201505597.
42. Julien Durst, Christoph Simon, F. H. and H. A. G. Hydrogen Oxidation and Evolution Reaction Kinetics on Carbon Supported Pt, Ir, Rh, and Pd Electrocatalysts in Acidic Media. *J. Electroanal. Soc.* **162**, (2015).
43. E. J. Popczun, C. G. Read, C. W. Roske, N. S. L. and R. E. S. Highly active electrocatalysis of the hydrogen evolution reaction by cobalt phosphide nanoparticles. *Angew. Chemie Int. Ed.* **53**, 5427–5430 (2014).
44. A. I. Carim, F. H. Saadi, M. P. S. and N. S. L. Electrocatalysis of the hydrogen-evolution reaction by electrodeposited amorphous cobalt selenide films. *J. Mater. Chem. A* **2**, 13835–13839 (2014).
45. Sundaram, A. R. J. K. and V. N. N. Nickel phosphide: the effect of phosphorus content on hydrogen evolution activity and corrosion resistance in acidic medium. *2014* **2**, 17435–17445.
46. Chhowalla, M. *et al*. The chemistry of two-dimensional layered transition metal dichalcogenide nanosheets. *Nat. Chem.* **5**, 263-275 (2013).
47. Huang, X., Zeng, Z. & Zhang, H. Metal dichalcogenide nanosheets: preparation, properties and applications. *Chem. Soc. Rev.* **42**, 1934-46 (2013).
48. Alonso-Vante. *Chalcogenide Material for Energy Conversion*. (2018).
49. J.A. Wilson & A.D. Yoffe. The transition metal dichalcogenides discussion and

interpretation of the observed optical, electrical and structural properties. *Adv. Phys.* **18**, 193–335 (1969).

50. Bissessur, R., Kanatzidis, M. G., Schindler, J. L. & Kannewurf, C. R. Encapsulation of polymers into MoS2 and metal to insulator transition in metastable MoS2. *J. Chem. Soc. Chem. Commun.* 1582–1585 (1993).

51. Frindt, R. F. & Yoffe, A. D. Physical properties of layer structures: Optical properties and photoconductivity of thin crystals of molybdenum disulphide. *Proc. R. Soc. Lond. A* **273**, 1963 (1963).

52. Py, M. A. & Haering, R. R. Structural destabilization induced by lithium intercalation in MoS2 and related-compounds. *Can. J. Phys* 76–84 (1983).

53. Ting Cao, Gang Wang, Wenpeng Han, Huiqi Ye, Chuanrui Zhu, Junren Shi, Qian Niu, Pingheng Tan, Enge Wang, B. L. and J. F. Valley-selective circular dichroism of monolayer molybdenum disulphide. *Nat. Commun.* **3**, (2012).

54. Hualing Zeng, Junfeng Dai, Wang Yao, D. X. and X. C. Valley polarization in MoS2 monolayers by optical pumping. *Nat. Nanotechnol.* **7**, 490–493 (2012).

55. Kin Fai Mak, Keliang He, J. S. and T. F. H. Control of valley polarization in monolayer MoS2 by optical helicity. *Nat. Nanotechnol.* **7**, 494-498 (2012).

56. Andrea Splendiani, Liang Sun, Yuanbo Zhang, Tianshu Li, Jonghwan Kim, Chi-Yung Chim, G. G. and F. W. Emerging photoluminescence in monolayer MoS2. *Nano Lett* **10**, 1271–1275 (2010).

57. Kin Fai Mak, Changgu Lee, James Hone, Jie Shan, and T. F. H. Atomically Thin MoS2: A New Direct-Gap Semiconductor. *Phys. Rev. Lett.* **105**, (2010).

58. Goki Eda, Hisato Yamaguchi, Damien Voiry, Takeshi Fujita, M. C. and M. C. Photoluminescence from Chemically Exfoliated MoS2. *Nano Lett* **11**, 5111–5116 (2011).

59. Sefaattin Tongay, Jian Zhou, Can Ataca, Kelvin Lo, Tyler S. Matthews, Jingbo Li, J. C. G. and J. W. Thermally Driven Crossover from Indirect toward Direct Bandgap in 2D Semiconductors: MoSe2 versus MoS2. *Nano Lett* **12**, 5576–5580 (2012).

60. Weijie Zhao, Zohreh Ghorannevis, Leiqiang Chu, Minglin Toh, Christian Kloc, P.-H. T. and G. E. Evolution of Electronic Structure in Atomically Thin Sheets of WS2 and WSe2. *ACS Nano* **7**, 791–797 (2013).

61. H. M. Hill, A. F. Rigosi, K. T. Rim, G. W. F. and T. F. H. Band alignment in MoS2/WS2 transition metal dichalcogenide heterostructures probed by scanning tunneling microscopy and spectroscopy. *Nano Lett* **16**, 4837-4837 (2016).

62. Di Xiao, Gui-Bin Liu, Wanxiang Feng, Xiaodong Xu, and W. Y. Coupled Spin and Valley Physics in Monolayers of MoS2 and Other Group-VI Dichalcogenides. *Phys. Rev. Lett.* **108**, 196802 (2012).

63. Changgu Lee, Hugen Yan, Louis E. Brus, Tony F. Heinz, J. H. and S. R. Anomalous Lattice Vibrations of Single- and Few-Layer MoS2. *ACS Nano* **4**, 2695-2700 (2010).

64. Wirtz, A. M.-S. and L. Phonons in single-layer and few-layer MoS2 and WS2. *Phys. Rev. B* **84**, 155413 (2011).

65. R. R. Haering, J. A. R. S. and K. B. Lithium molybdenum disulphide battery cathode. *US Pat.* 4224390 (1980).

66. R. Bhandavat, L. David and G. Singh, G. Synthesis of surface-functionalized WS2 nanosheets and performance as Li-ion battery anodes. *J. Phys. Chem. Lett.* **3**, 1523–1530 (2012).

67. Chen, K. C. and W. L-Cysteine-assisted synthesis of layered MoS2/graphene composites with excellent electrochemical properties for lithium ion batteries. *ACS Nano* **5**, 4720–4728 (2011).

68. Chen, K. C. and W. In situ synthesis of MoS2/graphene nanosheet composites with extraordinarily high electrochemical performance for lithium ion batteries. *Chem com* **47**, 4252-4254 (2011).

69. Feng, Q. C. Synthesis of molybdenum disulfide (MoS2) for lithium ion battery applications. *Mater. Res. Bull.* **44**, 1811–1815 (2009).

70. S. Ding, D. Zhang, J. S. C. and X. W. Lou. Facile synthesis of hierarchical MoS2 microspheres composed of few-layered nanosheets and their lithium storage

properties. *Nanoscale* **4**, 95–98 (2012).

71. The International Technology Roadmap for Semiconductors. *http://www.itrs.net/Links/2011ITRS/Home2011.htm (Semiconductor Industry Association, 2011).*

72. Ng, S. M. S. and K. K. *Physics of semiconductor devices.* (2007).

73. Schwierz, F. Graphene transistors. *Nat. Nanotechnol.* **5**, 487–496 (2010).

74. Lieber, W. L. and C. M. Nanoelectronics from the bottom up. *Nat. Mater* **6**, 841–850 (2007).

75. Youngki Yoon, K. G. and S. S. How Good Can Monolayer MoS2 Transistors Be? *Nano Lett.* **11**, 3768–3773 (2011).

76. B. Radisavljevic, A. Radenovic, J. Brivio, V. G. and A. K. Single-layer MoS2 transistors. *Nat. Nanotechnol.* **6**, 147–150 (2011).

77. Jean-PierreColinge. Multiple-gate SOI MOSFETs. *Solid. State. Electron.* **48**, 897–905 (2004).

78. Konar, D. J. and A. Enhancement of Carrier Mobility in Semiconductor Nanostructures by Dielectric Engineering. *Phys. Rev. Lett.* **98**, (2007).

79. Aniruddha Konar, Tian Fang, and D. J. Effect of high-κ gate dielectrics on charge transport in graphene-based field effect transistors. *Phys. Rev. B* **82**, (2010).

80. A.K.M. Newaz, Yevgeniy S. Puzyrev, Bin Wang, S. T. P. and K. I. B. Probing charge scattering mechanisms in suspended graphene by varying its dielectric environment. *Nat. Commun.* **3**, 734 (2012).

81. Fang Chen, Jilin Xia, D. K. F. and N. T. Dielectric Screening Enhanced Performance in Graphene FET. *Nano Lett* **9**, 2571–2574 (2009).

82. Yoffe, R. H. F. and A. D. Electronic properties of intercalation complexes of the transition metal dichalcogenides. *Adv. Phys.* **36**, 1–94 (1987).

83. E. Benavente, M. A. S. Ana, F. M. and G. G. Intercalation chemistry of molybdenum disulfide. *Coord. Chem. Rev.* **224**, 87–109 (2002).

84. Zongyou Yin, Hai Li, Hong Li, Lin Jiang, Yumeng Shi, Yinghui Sun, Gang Lu, Qing Zhang, X. C. and H. Z. Single-Layer MoS2 Phototransistors. *ACS Nano* **6**, 74–80 (2012).

85. Zhihao Yu, Zhun-Yong Ong, Yiming Pan, Yang Cui, Run Xin, Yi Shi, Baigeng Wang, Yun Wu, Tangsheng Chen, Yong-Wei Zhang, G. Z. and X. W. Realization of Room-Temperature Phonon-Limited Carrier Transport in Monolayer MoS2 by Dielectric and Carrier Screening. *Adv. Mater* **28**, 547–552 (2016).

86. Bhim Chamlagain, Qing Li, Nirmal Jeevi Ghimire, Hsun-Jen Chuang, Meeghage Madusanka Perera, Honggen Tu, Yong Xu, Minghu Pan, Di Xaio, Jiaqiang Yan, D. M. and Z. Z. Mobility Improvement and Temperature Dependence in MoSe2 Field-Effect Transistors on Parylene-C Substrate. *ACS Nano* **8**, 5079–5088 (2014).

87. Lin Yanqing Wu, Keith A. Jenkins, Alberto Valdes-Garcia, Damon B. Farmer, Yu Zhu Ageeth, A. Bol Christos, Dimitrakopoulos Wenjuan, Zhu Fengnian Xia, P. A. andYu-M. State-of-the-Art Graphene High-Frequency Electronics. *Nano Lett* **12**, 3062–3067 (2012).

88. J. T. Ye, Y. J. Zhang, R. Akashi, M. S. Bahramy, R. A. and Y. I. Superconducting Dome in a Gate-Tuned Band Insulator. *Science (80-.).* **338**, 1193–1196 (2012).

89. Babak Fallahazad, Hema C. P. Movva, Kyounghwan Kim, Stefano Larentis, Takashi Taniguchi, Kenji Watanabe, S. K. B. and E. T. Shubnikov-de Haas oscillations of high mobility holes in monolayer and bilayer WSe2: Landau level degeneracy, effective mass, and negative compressibility. *Phys. Rev. Lett.* **116**, (2016).

90. S. T. Oyama, P. Clark, X. Wang, T. Shido, Y. Iwasawa, S. Hayashi, J. M. Ramallo-López, F. G. R. Structural Characterization of Tungsten Phosphide (WP) Hydrotreating Catalysts by X-ray Absorption Spectroscopy and Nuclear Magnetic Resonance Spectroscopy. *J. Phys. Chem. B* **106**, 1913–1920 (2002).

91. Lundström, B. A. and T. *Borides, Suicides and Phosphides A Critical Review of Their Preparation, Properties and Crystal Chemistry.*

92. Corbridge, D. E. C. *Phosphorus 2000 - Chemistry, Biochemistry & Technology.* (1965).

93. Motojima, Tetsuo Wakamatsu, Kohzo Sugiyama, S. Corrosion stability of vapour-

deposited transition metal phosphides at high temperature. *Less-Common Met.* **82**, 379–383 (1981).

94. B. Gillot, K.El Amri, P. Pouderoux, J. P. B. and A. R. Corrosion resistance in oxygen of electrolytic nickel and cobalt phosphorus coatings. *J. Alloys Compd.* **189**, 151–155 (1992).

95. Liu, P., Rodriguez, A. & York, N. Catalysts for Hydrogen Evolution from the [NiFe] Hydrogenase to the Ni 2 P (001) Surface : The Importance of Ensemble Effect. 14871–14878 (2005) doi:10.1021/ja0540019.

96. Popczun, E. J. *et al.* Nanostructured Nickel Phosphide as an Electrocatalyst for the Hydrogen Evolution Reaction. (2013).

97. Peng Xiao, Mahasin Alam Sk, Larissa Thia, Xiaoming Ge, Rern Jern Lim, Jing-Yuan Wang, K. H. L. and X. W. Molybdenum phosphide as an efficient electrocatalyst for the hydrogen evolution reaction. *Energy enviromental Sci.* **7**, 2624–2629 (2014).

98. Michaela S. Burke, Lisa J. Enman, Adam S. Batchellor, Shihui Zou, S. W. B. Oxygen Evolution Reaction Electrocatalysis on Transition Metal Oxides and (Oxy)hydroxides: Activity Trends and Design Principles. *Chem. Mater.* **27**, 7549–7558 (2015).

99. Yang Yang, Huilong Fei, G. R. and J. M. T. Porous Cobalt-Based Thin Film as a Bifunctional Catalyst for Hydrogen Generation and Oxygen Generation. *Adv. Mater.* **27**, 3175–3180 (2015).

100. Lucas-Alexandre Stern, Ligang Feng, F. S. and X. H. Ni2P as a Janus catalyst for water splitting: the oxygen evolution activity of Ni2P nanoparticles. *Energy Environ. Sci.* 2347–2351 (2015).

101. Ali Han, Huanlin Chen, Zijun Sun, J. X. and P. Du. High catalytic activity for water oxidation based on nanostructured nickel phosphide precursors. *Chem. Commun.* **27**, 11626–11629 (2015).

102. Jinfa Chang, Yao Xiao, Meiling Xiao, Junjie Ge, C. L. and W. X. Surface Oxidized Cobalt-Phosphide Nanorods As an Advanced Oxygen Evolution Catalyst in Alkaline Solution. *ACS Catal.* **5**, 6874–6878 (2015).

103. Carlos G. Read, Juan F. Callejas, C. F. H. and R. E. S. General Strategy for the Synthesis of Transition Metal Phosphide Films for Electrocatalytic Hydrogen and Oxygen Evolution. *ACS Appl. Mater. Interfaces* **8**, 12798–12803 (2016).

104. Jinfa Chang, Liang Liang, Chenyang Li, Minglei Wang, Junjie Ge, C. L. and W. X. Ultrathin cobalt phosphide nanosheets as efficient bifunctional catalysts for a water electrolysis cell and the origin for cell performance degradation. *green Chem.* **18**, 2287–2295 (2016).

105. Jun Jiang, Chunde Wang, W. L. and Q. Y. One-pot synthesis of carbon-coated Ni5P4 nanoparticles and CoP nanorods for high-rate and high-stability lithium-ion batteries. *J. Mater. Chem. A* **3**, 23345–23351 (2015).

106. Yujie Liu, Xuezhang Xiao, Xiulin Fan, Meng Li, Yiwen Zhang, W. Z. and L. C. GeP5/C composite as anode material for high power sodium-ion batteries with exceptional capacity. *J. Alloys Compd.* **744**, 15–22 (2018).

107. Xia Wang, Pingping Sun, Jinwen Qin, Jianqiang Wang, Y. X. and M. C. A three-dimensional porous MoP@C hybrid as a high-capacity, long-cycle life anode material for lithium-ion batteries. *Nanoscale* **8**, 10330–10338 (2016).

108. Wang, Y. Z. Z. F. and L. Unique Fe2P Nanoparticles Enveloped in Sandwichlike Graphited Carbon Sheets as Excellent Hydrogen Evolution Reaction Catalyst and Lithium-Ion Battery Anode. *ACS Appl. Mater. Interfaces* **7**, 26684–26690 (2015).

109. Wang, Y. B. D. H. Z. L. L. H. X. P. D. Y. Tunable and Specific Formation of C@NiCoP Peapods with Enhanced HER Activity and Lithium Storage Performance. *Chem. Eur. J.* **22**, 1021– 1029 (2016).

110. Feipeng Zhao, Na Han, Wenjing Huang, Jiaojiao Li, Hualin Ye, F. C. and Y. L. Nanostructured CuP2/C composites as high-performance anode materials for sodium ion batteries. *J. Mater. Chem. A* **295**, 21754–21759 (2015).

111. Dr. Wang, Huijuan Zhang, Yangyang Feng, Yan Zhang, Ling Fang, Wenxiang Li, P. Q. L. P. K. W. and P. Y. Peapod-Like Composite with Nickel Phosphide

Nanoparticles Encapsulated in Carbon Fibers as Enhanced Anode for Li-Ion Batteries. *ChemSusChem* **7**, 2000–2006 (2014).

112. Jun Liu, Peter Kopold, Chao Wu, Peter A. van Aken, J. M. and Y. Y. Uniform yolk–shell Sn4P3@C nanospheres as high-capacity and cycle-stable anode materials for sodium-ion batteries. *Energy Environ. Sci.* **8**, 3531–3538 (2015).

113. Panel Dan Wang, Ling-Bin Kong, Mao-Cheng Liu, Wei-Bin Zhang, Yong-Chun, L. L. K. Amorphous Ni–P materials for high performance pseudocapacitors. *J. Power Sources* **274**, 1107–1113 (2015).

114. Chih-Feng Yen, M.-K. L. Electrical characteristics of TiO2/Al2O3/InP capacitor after removal of native oxides by atomic layer deposited Al2O3 self-cleaning and (NH4)2S treatments. *Thin Solid Films* **595**, 12–16 (2015).

115. Cheng, Chun-Hu; Hsu, Hsiao-Hsuan; Chou, K.-I. TiO2-Based Indium Phosphide Metal-Oxide-Semiconductor Capacitor with High Capacitance Density. *J. Nanosci. Nanotechnol.* **15**, 2810–2813 (2015).

116. Cuihua An, Yijing Wang, Yaping Wang, Guang Liu, Li Li, Fangyuan Qiu, Yanan Xu, L. J. and H. Y. Facile synthesis and superior supercapacitor performances of Ni2P/rGO nanoparticles. *RSC Adv.* **3**, 4628–4633 (2013).

117. Yi Lu, Ji-kang Liu, Xia-yuan Liu, Sen Huang, Ting-qiang Wang, Xiu-li Wang, Chang-dong Gu, J. T. and S. X. M. Facile synthesis of Ni-coated Ni2P for supercapacitor applications. *CrystEngComm* **35**, 7071–7079 (2013).

118. Chen, K. Z. W. Z. L. Y. J. L. S. C. W. M. Z. T. L. L. S. Ultrahigh-Performance Pseudocapacitor Electrodes Based on Transition Metal Phosphide Nanosheets Array via Phosphorization: A General and Effective Approach. *Adv. fuctional Mater.* **25**, 7530–7538 (2015).

119. Chao You, Rui Dai, Xiaoqin Cao, Yuyao Ji, Fengli Qu, Zhiang Liu, Gu Du, Abdullah M Asiri, X. X. and X. S. Fe2Ni2N nanosheet array: an efficient non-noble-metal electrocatalyst for non-enzymatic glucose sensing. *Nanotechnology* **28**, (2017).

120. Jing Qi, P. W. Z. and P. R. C. Porous Materials as Highly Efficient Electrocatalysts for the Oxygen Evolution Reaction. *ChemCatChem* **10**, 1206–1220 (2018).

121. Bo Zhang, Z. P. & , Ke Yu, Guangwen Feng, Jun Xiao, Shoukun Wu, Jinghong Li, Chun Chen, Yingsheng Lin, G. H. & Z. W. Titanium vanadium nitride supported Pt nanoparticles as high-performance catalysts for methanol oxidation reaction. *J. Solid State Electrochem.* **21**, 3065–3070 (2017).

122. A.Achoura, R.Lucio-Portob, M. Chakera, A.Armanc, A.Ahmadpourianc, M. A. Soussoud, M. Boujtitae, L. Le Brizoualf, M. A. D. and T. B. Titanium vanadium nitride electrode for micro-supercapacitors. *Electrochem. commun.* **77**, 40–43 (2017).

123. Andriy Zakutayev, Amy J. Allen, Xiuwen Zhang, Julien Vidal, Zhiming Cui, Stephan Lany, Minghui Yang, F. J. D. and D. S. G. Experimental Synthesis and Properties of Metastable CuNbN2 and Theoretical Extension to Other Ternary Copper Nitrides. *Chem. Mater* **26**, 4970–4977 (2014).

124. Gurram, V. R. B. & , Siva Sankar Enumula, Raji Reddy Chada, Kumara Swamy Koppadi, D. R. B. & S. R. R. K. Synthesis and Industrial Catalytic Applications of Binary and Ternary Molybdenum Nitrides: A Review. *Catal. Surv. from Asia* 166–180 (2018).

125. Hui Dai , Mingyuan Zhu, Haiyang Zhang, Feng Yu, C. W. and B. D. Activated Carbon Supported Mo-Ti-N Binary Transition Metal Nitride as Catalyst for Acetylene Hydrochlorination. *Catalysts* (2017).

126. Itoh F, Tsuchida T, T. H. Hall Effect of the Solid Solution of TiCxN1-x and TixV1-xC. *J. Phys. Soc. Jpn* **19**, 136–137 (1964).

127. Kuriyama M, Hosoya S, S. Electron number ofthe nitrogen atom inMn 4N. *Phys Rev* **130**, (1963).

128. Elisabetta Arca, Stephan Lany, John D. Perkins, Christopher Bartel, John Mangum, Wenhao Sun, Aaron Holder, Gerbrand Ceder, Brian Gorman, Glenn Teeter, W. T. and A. Z. Redox-Mediated Stabilization in Zinc Molybdenum Nitrides. *J. Am. Chem. Soc.* **140**, 4293–4301 (2018).

129. SV., K. Minerals with antiperovskite structure: a review. *Z Krist.* **223**, 109–113

(2008).

130. Disalvo, M. Y. C. D. A. V. F. J. Synthesis, structure, and properties of anti-perovskite nitrides Ca3MN, M=P, As, Sb, Bi, Ge, Sn, and Pb. *J. Solid State Chem.* **96**, 415–425 (1992).

131. Ying Sun, Cong Wang, Qingzhen Huang, Yanfeng Guo, Lihua Chu, Masao Arai, K. Y. Neutron Diffraction Study of Unusual Phase Separation in the Antiperovskite Nitride Mn3ZnN. *Inorg. Chem.* **51**, 7232–7236 (2012).

132. Bo He, Yao Yuan, Jiacheng Wang, Erum Pervaiz, X. D., Shao, Z. & Yan, and M. Hierarchical Ni3ZnN Hollow Microspheres as Stable Non-Noble Metal Electrocatalysts for Oxygen Reduction Reactions. *Electrocatalysis* **9**, 452–458 (2018).

133. K. S. Weila, P. N. K. and J. G. Revisiting a Rare Intermetallic Ternary Nitride, Ni2Mo3N: Crystal Structure and Property. *J. Solid State Chem.* **146**, 22–35 (1999).

134. K., J. New interstitial alloy hardmetals. *Met Powder Rep* **42**, 478–480 (1987).

135. Timothy J Prior, P. Db. Facile synthesis of interstitial metal nitrides with the filled β-manganese structure. *J. Solid State Chem.* **172**, 138–147 (2003).

136. Prior TJ, B. P. Superparamagnetism and metal-site ordering in quaternary nitrides with the η-carbide structure. *J Mater Chem* **14**, 3001–3007 (2004).

137. Battle, T. J. P. E. O. J. C. D. Ferromagnetic Nitrides with the Filled β-Mn Structure: Fe2-xMxMo3N (M = Ni, Pd, Pt). *Chem. Mater* **17**, 1867–73 (2005).

138. Diana C. Phillips, Stephanie J. Sawhill, R. S. and M. E. B. Synthesis , Characterization , and Hydrodesulfurization Properties of Silica-Supported Molybdenum Phosphide Catalysts. *J. Catal.* **273**, 266–273 (2002).

139. Styring, S. Artificial photosynthesis for solar fuels. *Faraday Discuss* **155**, 357–376 (2012).

140. Le Formal, F., Bourée, W. S., Prévot, M. S. and Sivula, K. Challenges towards economic fuel generation from renewable electricity: the need for efficient electro-catalysis. *Chimia (Aarau).* **69**, 789–798 (2015).

141. Joya, K. S., Joya, Y. F., Ocakoglu, K. and van de Krol, R. Water-splitting catalysis and solar fuel devices: artificial leaves on the move. *Angew. Chem. Int. Ed* **52**, 10426–10437 (2013).

142. Tachibana, Y., Vayssieres, L. and Durrant, J. R. Artificial photosynthesis for solar water-splitting. *Nat. Photonics* **6**, 511–518 (2012).

143. McCrory, C. C. L. et al. Benchmarking hydrogen evolving reaction and oxygen evolving reaction electrocatalysts for solar water splitting devices. *J. Am. Chem. Soc.* **137**, 4347–435 (2015).

144. Carmo, M., Fritz, D. L., Mergel, J. and Stolten, D. A. A comprehensive review on PEM water electrolysis. *Int. J. Hydrog. Energy* **38**, 4901–4934 (2013).

145. Faber, M. S. and Jin, S. Earth-abundant inorganic electrocatalysts and their nanostructures for energy conversion applications. *Energy Environ. Sci* **7**, 3519–3542 (2014).

146. Nocera, D. G. The artificial leaf. *Acc. Chem. Res.* **45**, 767–776 (2012).

147. Rocheleau, R. E., Miller, E. L. and Misra, A. High-efficiency photoelectrochemical hydrogen production using multijunction amorphous silicon photoelectrodes. *Energy Fuels* **12**, 3–8 (1998).

148. Steven Y. Reece, Jonathan A. Hamel, Kimberly Sung, Thomas D. Jarvi, A. J. E. & Nocera, J. J. H. P. and D. G. Wireless solar water splitting using silicon-based semiconductors and earth-abundant catalysts. *Science (80-.).* **334**, 645–648 (2011).

149. Serkan Esiner, Robin E. M. Willems, Alice Furlan, Weiwei Li, M. M. W. and R. A. J. J. Photoelectrochemical water splitting in an organic artificial leaf. *J. Mater. Chem. A* **3**, 23936–23945 (2015).

150. Isolda Roger, M. A. S. and M. D. S. Earth-abundant catalysts for electrochemical and photoelectrochemical water splitting. *Nat. Rev.* **1**, (2017).

151. Roger Sathre, Corinne D. Scown, William R. Morrow, III, John C. Stevens, Ian D. Sharp, Joel W. Ager, III, Karl Walczak, F. A. H. and J. B. G. Life-cycle net energy assessment of large-scale hydrogen production via photoelectrochemical water

splitting. *Energy Environ. Sci.* **7**, 3264–3278 (2014).

152. Barbir, F. PEM electrolysis for production of hydrogen from renewable energy sources. *Sol. Energy* **78**, 661–669 (2005).

153. Berger, A., Segalman, R. A. and Newman, J. Material requirements for membrane separators in a watersplitting photoelectrochemical cell. *Energy Environ. Sci.* **7**, 1468–1476 (2014).

154. Symes, M. D. and Cronin, L. Decoupling hydrogen and oxygen evolution during water splitting using a protoncoupled-electron buffer. *Nat. Chem.* **5**, 403–409 (2013).

155. Rausch, B., Symes, M. D. and Cronin, L. A. Bio-inspired, small molecule electron-coupled-proton buffer for decoupling the half-reactions of electrolytic water splitting. *J. Am. Chem. Soc.* **135**, 13656–13659 (2013).

156. Rausch, B., Symes, M. D., Chisholm, G. and Cronin, L. Decoupled catalytic hydrogen evolution from a molecular metal oxide redox mediator in water splitting. *Science (80-.).* **345**, 1326–1330 (2014).

157. Bloor, L. G. *et al.* Solar-driven water oxidation and decoupled hydrogen production mediated by an electron-coupled-proton buffer. *J. Am. Chem. Soc.* **138**, 6707–6710 (2016).

2 Experimental

The aim of this chapter is to give a brief background about the methods used for preparation and characterization of the materials described in Chapters 3 to 5.

The structure and phases of the catalysts was determined by X-RD analysis, followed by a refinement procedure for some of the sample analysed. All samples were furthermore characterized by scanning electron microscopy (SEM) and EDX measurements to determine their morphology and sample composition.

For the synthesis of Co doped MoS_2 on a FTO surface (Chapter 3), additional structural studies were performed with Raman spectroscopy, X-Ray Photoelectron Spectroscopy (XPS), UV-Vis and Atomic force microscope (AFM). In particular, Raman spectroscopy was used to identify active mode characteristics of the MoS_2 structure and XPS was used to determine the oxidation state of each element. Film thickness was measured by AFM, and their transparency by detecting the transmittance in UV-Vis measurements.

Finally, all the catalysts prepared were characterized for their electrochemical performance. In section 2.3, the electrochemical techniques performed during this work will be described, highlighting advantages and disadvantages of each to justify their specific use.

2.1 Preparative methods:

2.1.1 Hydrothermal synthesis (HT)

Hydrothermal synthesis is an important branch of inorganic chemistry, based on the synthesis in aqueous or organic solvent using a sealed container at high temperature (100-1000 °C) and pressure (1-100 MPa).[1]

In a more classical solid state synthetic approach, the reaction mainly occurs at the interface between the raw materials and therefore its efficiency primarily relies on diffusion. To overcome the problem of concentrating the reagents at the reacting sites, these syntheses are generally performed at high temperature. During hydrothermal synthesis, the reaction occurs in solution at high temperature and pressure conditions. These different conditions in which those two methods are performed leads to the possibility of obtaining different structures and products from the same starting reagents. The advantage of hydrothermal

synthesis is to enable the preparation of compounds or materials which would not be possible to synthesise otherwise or to prepare the same product at more mild conditions. Many functionalized materials or compounds with particular morphology, such as nanostructures, fine powders or sol-gels, are synthesized by using this technique, making it a very flexible and powerful tool.

The strength of HT synthesis relies on its reaction medium, which is under supercritical conditions during the reaction.[2] Water is the most common solvent used, because of its availability, price and safety. Under high temperature and pressure, the density surface tension and viscosity decreases, while vapour pressure and ion production increases. When the reaction system is heated above the water's boiling point, the ion rate production will increase enormously. At this pressure and temperature condition, the water is completely dissociated into H_3O^+ and OH^- and acts as a molten salt with a low viscosity. Hence, in HT the ion mobility is much higher than under normal conditions. Therefore water may act as a solvent or reagent accelerating the reaction and changing the chemical and physical properties of the reagents.

The HT reaction is carried out in a hydrothermal autoclave composed of two parts: the high-quality stainless steel jacket and a Teflon liner (Figure 2.1). This Teflon autoclave enables reactions at a maximum temperature of 240 °C. An important criterion for reproducible HT synthesis is to keep the amount of solution used constant, as the pressure inside the sealed cylinder depends on the volume inside the reaction chamber. In a standard reaction, the vessel is generally filled between 50% and 80%, generating a pressure change from 0.02 to 0.3 GPa.[2]
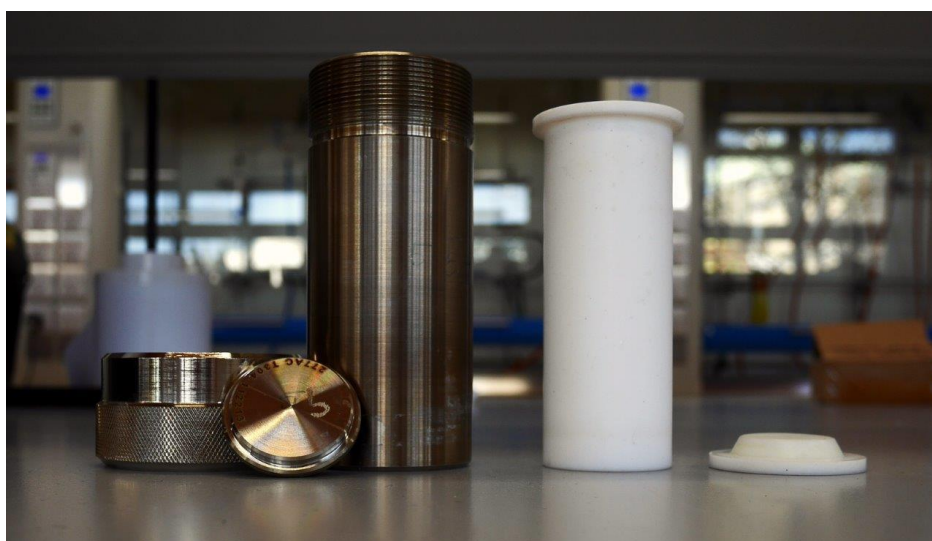
Figure 2-1 Autoclave used for hydrothermal synthesis.

2.1.2 Time programmed reduction (TPR)

Time programmed reduction is a technique used in heterogeneous catalysis to determine the optimal time and temperature condition for a specific reaction.[3] The reagent, here an oxide mixture (see Chapter 4), is placed in a catalyst reactor and inserted into a furnace tube (Figure 2.2). During the reaction, the material is exposed to a gas flux, and while the temperature increases according to the selected program it is monitored with a thermal conductivity detector. The parameters controlled in order to optimise the reaction are the time, the speed rate, the type of gas used, the gas flow speed and the temperature. Single parameters were changed to identify optimal conditions for the final product. As the tube furnace used for the reaction heats by following a gradient that increases from the outside to the inside of the chamber, the sample was always located in the centre of the furnace at the same position.

Figure 2-2 Tube furnace used for TPR

2.2 Structural determination and characterization techniques:

2.2.1 Power X-Ray diffraction

2.2.1.1 Background

Crystalline solids are characterized by the internal order of the atoms inside the structure. The smallest repeated unit showing the full symmetry of the structure is defined as unit cell.[4] This is described by the three angles a, β, γ and the three distances a, b, c. (Figure 2.3).
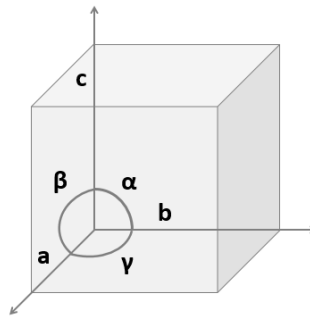
Figure 2-3 Representation of a general unit cell with the three vectors and the three angles used to define the lattice indicated.
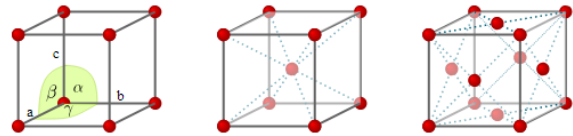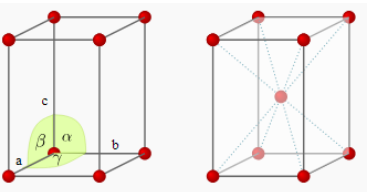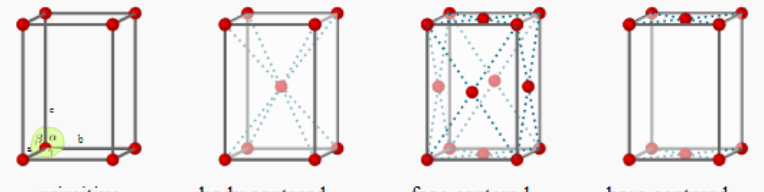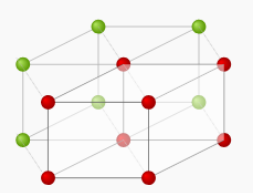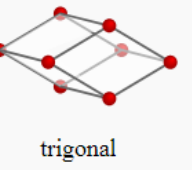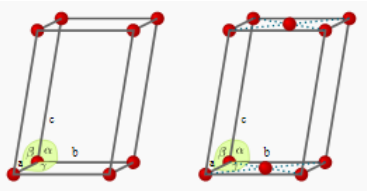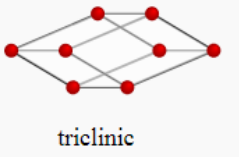
In a three dimensional system, the unit cells are divided in seven crystal systems defined by the fundamental symmetry operations. Each of this system is described by a unique volume formula and by the presence or the absence of a particular symmetry inside the structure. (See Table 2.1)

Table 2. 1 Summary of the volume and the symmetry elements for each unit cell.[5]

Unit Cell	Volume	Essential symmetry
Cubic	$V = a^3$	Four C_3 axes in a tetrahedral arrangement
Tetragonal	$V = a^2 c$	One C_4 axis
Orthorhombic	$V = abc$	Three perpendicular C_2 Axes
Hexagonal	$V = \dfrac{\sqrt{3}a^2 c}{2} = 0.866 a^2 c$	One C_6 axis
Monoclinic	$V = abc \sin \beta$	One C_2 axis
Triclinic	$V = abc(1 - \cos^2 \alpha - \cos^2 \beta - \cos^2 \gamma + 2 \cos \alpha \cos \beta \cos \gamma)^{1/2}$	None
Trigonal	$V = a^2 c \sin(60^o)$	One C_3 axis

According to where the atoms or ions are located inside the crystal (lattice points), four different lattices can be defined: primitive (P), body centred (I), Face centred (F) and side-centred (A, B or C) (see Table 2.2). From the combination of the seven crystal systems and the four lattice points, it is possible to obtain the 14 Bravais lattices which can describe all the possible systems. Combining the 32 point group with the 14 Bravais lattice, 230 three dimensional space groups can be defined, describing all the possible crystal structures adopted.[6] Further information about the space groups can be found in the International Tables for Crystallography.[7]

Table 2. 2 with the crystal system and the possible lattice for each of them.

Crystal system	Bravais lattices			
Cubic $a = b = c$ $\alpha = \beta = \gamma = 90°$	 primitive	 body centered	 face centered	
Tetragonal $a = b \neq c$ $\alpha = \beta = \gamma = 90°$	 primitive	 body centered		
Orthorhombic $a \neq b \neq c$ $\alpha = \beta = 90°,$ $\gamma = 120°$	 primitive	 body centered	 face centered	 base centered
Hexagonal $a = b \neq c$ $\alpha = \beta = 90°,$ $\gamma = 120°$				
Trigonal $a = b = c$ $\alpha = \beta = \gamma \neq 90°$	 trigonal			
Monoclinic $a \neq b \neq c$ $\alpha = \gamma = 90°,$ $\beta \neq 90°$	 primitive	 base centered		
Triclinic $a \neq b \neq c$ $\alpha \neq \beta \neq \gamma \neq 90°$	 triclinic			

X-ray diffraction (XRD) is the most common technique used for solid state structure analysis. The electromagnetic radiation is obtained by bombarding a metal with a beam of accelerating high-energy electrons provided by a tungsten filament. Once the electrons plunge into the metal, they decelerate, generating a radiation in the order of 10^{-10}m. This radiation is called Bremsstrahlung and it is a continuous range of emitted radiation with few high intensity sharp peaks due to the collision between the incoming electrons and electrons of the inner shell of the atoms. This collision causes the expulsion of some of the 1s (K shell) electrons. The empty vacancy is then filled by outer orbital (2p or 3p) electrons transitioning to the inner orbital, which leads to the emission of an X-ray photon called K radiation. In copper, the most commonly used source the X-ray radiation Kα is associated with the $2p \rightarrow 1s$ transition with a wavelength of 1.5418 Å.

X-ray radiation has a wavelength of 1 Å, which is very comparable to the inter-atomic distances inside a crystal (~0.8 – 3 Å), allowing the diffraction to occur when the x-ray beam strikes the solid.[8] Hence, this technique can be used to determine the crystal structure and the presence of phase mixture inside the sample. Moreover, the refinement of the X-ray pattern can be used to obtain information about the dimension of the unit cell.

Bragg was the first to detect the potential of this technique in defining a model to explain the XRD diffraction patterns (Figure 2.4). In his approach, a crystal was viewed as a build-up of lattice with planes formed by neatly distributed atoms, with a space between the planes defined as $d_{(hkl)}$. Considering two parallel rays being reflected by two lattice layers, the first ray strikes the lattice at point A1. A second ray needs to travel an additional distance of B before being reflected at the second layer at point A2, and an additional distance of C after being reflected. The path difference between those two layers can then be expressed as:

$$B + C = 2d \sin \theta \qquad (2.1)$$

When the pathwave B+C is not an integer number of the wavelength, the radiations interfere in a destructive way between each other. However, when the B+C value is an integer number of the wavelength, the radiations have a

constructive interaction and a signal is detected. Therefore, these constructive radiations are described by the Bragg's law with the formula (2.2), in which n stands for the path-length differences of the in-phase wavelengths.[9]

$$\lambda n = 2d \sin \theta \qquad (2.2)$$

An advantage of the Bragg's law is the possibility to calculate the d value by knowing the reflection angle θ.
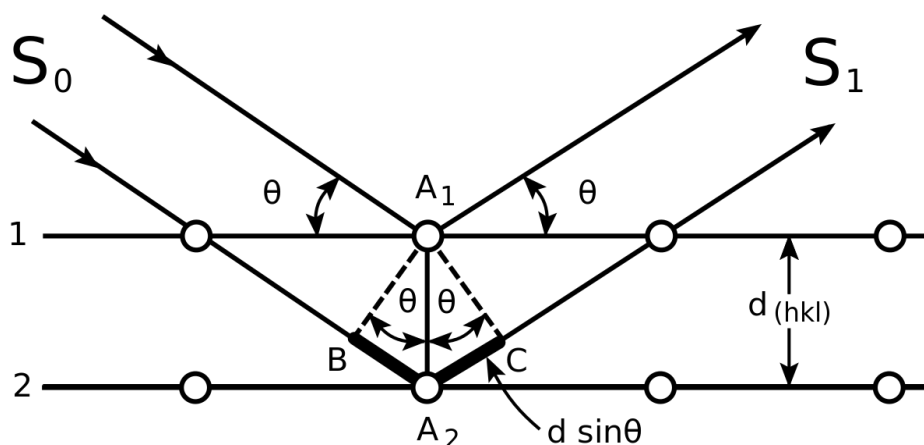
Figure 2-4 Conventional derivation of Bragg's law. S_0 and S_1 are the incoming and diffracted x-ray radiation, respectively, scattered from the crystal surface with an angle of θ. The lattices are indicates as planes in black, while their distance is indicated by d_{hkl}.

Knowing the d-spacing between the layers in the lattice allows one to obtain the Miller indices. These indices (h, k, l) are reciprocal to the intersectional distances and are defined by the orientation of crystal planes and how those intersect the axes of the unit cell. The d_{hkl} value can be defined for each crystal system by following the equations listed in Table 2.3.

Table 2. 3 Equations for calculating the d-spacing in different crystal systems.

Crystal system	d_{hkl} as a function of the Miller indices and lattice parameters
Cubic	$$\frac{1}{d_{hkl}{}^2} = \frac{h^2 + k^2 + l^2}{a^2}$$
Tetragonal	$$\frac{1}{d_{hkl}{}^2} = \frac{h^2 + k^2 + l^2}{a^2} + \frac{l^2}{c^2}$$
Orthorhombic	$$\frac{1}{d_{hkl}{}^2} = \frac{h^2}{a^2} + \frac{k^2}{b^2} + \frac{l^2}{c^2}$$
Hexagonal	$$\frac{1}{d_{hkl}{}^2} = \frac{4}{3}\left(\frac{h^2 + hk + k^2}{a^2}\right) + \frac{l^2}{c^2}$$
Monoclinic	$$\frac{1}{d_{hkl}{}^2} = \frac{1}{\sin^2 \beta}\left(\frac{h^2}{a^2} + \frac{k^2 + \sin^2 \beta}{b^2} + \frac{l^2}{c^2} - \frac{2hl\cos\beta}{ac}\right)$$
Triclinic	$$\begin{aligned}\frac{1}{d_{hkl}{}^2} = \frac{1}{V^2}[&h^2b^2c^2\sin^2\alpha + k^2a^2c^2\sin^2\beta + l^2a^2b^2\sin^2\gamma \\ &+ 2hkabc^2(\cos\alpha\cos\beta - \cos\gamma) \\ &+ 2kla^2bc(\cos\beta\cos\gamma - \cos\alpha) \\ &+ 2hlab^2c(\cos\alpha\cos\gamma - \cos\beta)]\end{aligned}$$

2.2.1.2 Instrument and sample preparation

The X-ray diffractometer is composed of four main components; the X-ray source, the slits, the sample stage and the detector (Figure 2.5). The slit regulates the amount of radiation emitted from the source, which can be adjusted to the sample configuration. The scattering of the sample is generated by oscillation of the atom electrodes due to the incoming electromagnetic wave and it is collected with a detector. To identify the sample, the collected pattern is compared to XRD patterns present in a database.

Before a measurement, the sample was ground in a mortar and processed into a homogenous powder to allow the distribution of small crystals in a random orientation and therefore to detect all possible interplanar distances.[10] To increase the random orientation of the crystal, some diffractometer use a rotating stage called "spinner".

All the data were collected using a Panalytical XPert-pro diffractometer. The instrument was equipped with programmable divergent slits (PDS) and an ultrafast solid state pixel detector (PIXcel3D). The measurements were performed on a Bragg-Bretano stage using a Cu x-ray tube with the power capability of 2kW as radiation source. A monochromator was used to select the Kα radiation at 1.544187Å. A monochromatic wavelength was used to guarantee a well defined application of the Bragg's law. Experimentally, the beam was collimated through the use of a 10 mm mask, 0.2 rad soller slit. Moreover, the Kß radiation was filtered by a nickel beta-filter of 0.02 nm. The detector used to collect the data was a real time multiple strip detector (RTMS) allowing to obtain ultra fast detection. The data were collected on a diffraction spectrum where the intensity of the peaks were plotted against the diffraction angle range.
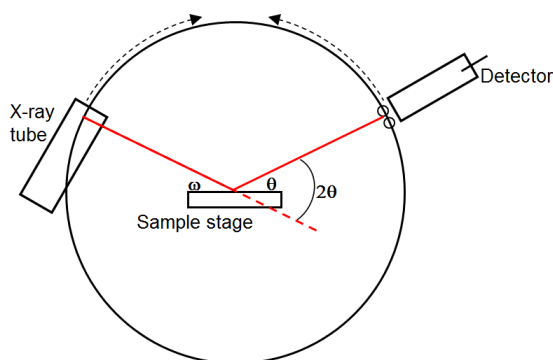
Figure 2-5 Schematic representation of the typical Bragg-Brentano geometry where ω is the incident angle between the x-ray source and the sample. The angle 2ɵ is the diffraction angle between the incident beam and the detector.
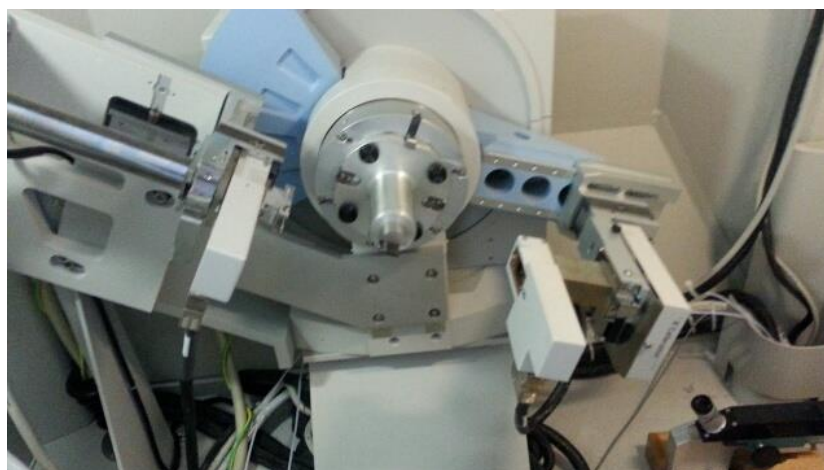
Figure 2-6 The Panalytical XPert-pro diffractometer used to measure in the Bragg-Bretano reflection geometry.

2.2.2 Data analysis:

2.2.2.1 Rietveld refinement

Power diffraction data obtained by crystalline structures can be characterized with the use of the Rietveld refinement technique. In this method a Gaussian shape is assigned to each peak present in the pattern to describe the overall profile obtained from the overlap. The data analysis starts with the use of a trial structure on which the atoms' position can be modified. The process of refinement is carried out until the best fit is obtained and the calculated and observed data become almost identical. Since the procedure require structural information, it cannot be used for structure determination but rather as a refinement technique. The data collected in this work were refined with the GSAS software package[11] using ESEGUI as interface.[12]

The Rietveld method uses structural information to produce a y_{calc} value and compare it to the y_i obtained from the X-ray pattern. The calculated X-ray profile is obtained using the least square approach by weighting the difference between the observed (y_i) and the calculated values (y_{calc}) of the diffraction patterns (see equation 2.3).

$$S_y = \sum_i w_i [y_i - y_{calc}]^2 \qquad (2.3)$$

The calculated intensities are functions of the structural factor F_k, which is obtained from the crystal model by summing all the contributions calculated from the Bragg K_{hkl} reflection. The y_{calc} equation can be expanded as:

$$y_{calc} = s \sum_K L_K |F_K|^2 \Phi(2\theta i - 2\theta k) P_k A + y_{bi} \qquad (2.4)$$

where s is the scale factor depending on the amount of irradiated sample, L_k is a function containing the Lorentz polarization, Φ is a value related to the profile peak shape, P_k is the preferred orientation function, y_{bi} is the background intensity for the point i and A is the absorption correction factor.

The structural factor contains various structural and experimental information about the peak shape and the background. It can be written as:

$$F_k = \sum_{j=1}^{N} N_j f_j \, exp\left[2\pi\left(hx_j + ky_j + lz_j\right)\right] exp\left[-M_j\right] \qquad (2.5)$$

where the position of a j atom is expressed by the coordinates x_j, y_j, and z_j, the indices h, k, l indicates the Braggs reflections, the value N_j expresses the atom multiplicity for a particular occupation and the value f_j refers to the number of electrons when $\sin\theta/\lambda = 0$. M_j is the scattering length and it is expressed by equation 2.6:

$$M_j = 8\pi^2 \overline{u_s^2} \sin^2\theta \,/\lambda^2 \qquad (2.6)$$

Where $\overline{u_s^2}$ is the root-mean-square thermal displacement of the jth atom parallel to the diffraction vector.

The background intensity y_{bi} in equation 2.4 is described as a polynomial function in 2θ where N_b is the polynomial degree and a_n is the coefficient.

$$y_{bi} = \sum_{n=0}^{Nb} a_n (2\theta_i)^n \qquad (2.7)$$

The peak shape, related to the Φ value in equation 2.4, is instrument dependent and can be described by a combination of Lorentzian and Gaussian functions using the Pseudo-Voigt (pV) function:

$$pV = \eta L + (1 - \eta)G \qquad (2.8)$$

Where the Lorentzian and Gaussian functions, equations 2.10 and 2.11 below, are expressed by the symbols L and G. The Gaussian value generally represent better the experimental values, while the Lorentzian value describes possible broadening of diffraction peaks due to a different crystals size. The value η is the mixing

factor and is described as a linear function of 2θ where N_a and N_b are parameters which can be optimised.

$$\eta = N_a + N_b(2\theta) \tag{2.9}$$

$$G = \frac{(2\ln2)^{\frac{1}{2}}}{H_k\sqrt{\pi}} \exp\left(-4\ln2(2\theta_i - 2\theta_k)^2/H_k^2\right) \tag{2.10}$$

$$L = \frac{2}{\pi H_k} / \left[1 + 4\frac{(2\theta_i - 2\theta_k)}{H_k^2}\right] \tag{2.11}$$

The Lorentzian and Gaussian contribution are expressed with the observable and calculated position, θi and θk, for the Kth reflection. The Full-Width at Half Maximum (H_k) is expressed as a function of the scattering angle and modelled by varying the U, V and W values, which are instrument and sample dependent.

$$H_k^2 = U\tan^2\theta + V\tan\theta + W \tag{2.12}$$

The preferred orientation function, P_k, attempts to correct variation in intensity due to a preferred orientation of certain crystals by the optimization of the parameters G_1 and G_2. The angle a_k is the angle difference between presumed cylindrical symmetry and the preferred orientation axis direction.

$$P_k = \left[G_2 + (1 - G_2)exp\left(-G_l a_k^2\right)\right] \tag{2.13}$$

To evaluate if there is a good fit with the experimental data, R or residual factor indices are often used. The R- weighted profile, R_{wp}, is the most meaningful value, since its numerator is described by the least square function minimised on the refinement process (equation 2.14). The other R indices are R-expected Re (equation 2.15), R-profile Rp (equation 2.16), R-intensity Ri (equation 2.17) and R Bragg (equation 2.18)

$$R_{wp} = \left\{\frac{\sum_i w_i[y_i - y_{calc}]}{\sum_i w_i(y_i)^2}\right\}^{1/2} \tag{2.14}$$

$$R_e = \left\{\frac{(N-P+C)}{\sum w_i(y_i)^2}\right\}^{1/2} \tag{2.15}$$

$$R_p = \frac{\sum|y_i - y_{calc}|}{\sum I_{ki}} \tag{2.16}$$

$$R_i = \frac{\sum|I_{Ki}^2 - I_{K\,calc}^2|}{\sum I_{Ki}^2} \tag{2.17}$$

$$R_B = \frac{\sum I_{Ki} - I_{K\,calc}}{\sum I_{Ki}} (2.18)$$

Where N, P and C on equation 2.15 are the number of observations and I_{ki} and I_{calc} on equation 2.16 to 2.18 are the observed and calculated Bragg intensities of the reflection K.

Ideally, R_{wp} and R_e should be a comparable in value and their ratio (equation 2.19) should be in a range between $1 \leq \chi^2 \leq 1.5$ for the fit to be considered satisfactory. If the χ^2 has a lower value, the background signal is still relevant in the measurement.

$$\chi^2 = \left[\frac{R_{wp}}{R_e}\right]^2 \qquad\qquad (2.19)$$

2.2.2.2 Le Bail Refinement method

Le Bail is an iterative method which extends the Rietveld approach on systems where there is not an initial structural model. This method assumes that when the structural factors of a system are unknown, the easiest approximation that can be done is to assume that all the initial integrated intensities are equal to one.[13] The overlap of an N peak can be expressed mathematically as:

$$A_m^{(r+1)}(obs) = \sum_i \frac{A_m^{(r)}(obs)xq_m(i)}{\left(\sum_{n=1}^N A_n^{(r)}(cal)xq_n(i)\right)}(obs(i) - back(i)) \qquad (2.20)$$

Where A is the integrated intensity, q_m is the product between $c_m(i)$ and $H_k(i)$, where the c_m value contains the Lorentz polarization and $(obs(i) - back(i))$ is the observed peak contribution for an i point.

The values of the denominator A_n are all equal to one for the first iteration (r=1) and represents the initial calculated intensities. The $A_m^1(obs)$ value calculated in this way will then be used as the denominator of the algorithm as new calculated intensities. By Recursion of this algorithm, there is a rapid conversion between the estimated and the calculated peak areas, independent of the initial assumption. This is because the algorithm lost memory of the starting values after five interactions. The final intensity value can then be used to obtain structural

information about the unit cell, since it is expressed as a function of the structural factor F_k. Despite the huge advantage coming from the adoption of this method, it does not perform well for the resolution of weak peaks where the background can be overestimated. In this case, the Le Bail estimates are chaotic and oscillatory with the repetition of the interaction making this method not applicable.

2.2.3 Raman spectroscopy

Raman spectroscopy is a technique that studies the changes of the molecular state through the radiation scattered by the sample. Using this technique, it is possible to get some information about molecular vibrations and rotations. When a monochromatic radiation probes a sample with an energy value not corresponding to any electronic transition, the system is forced to move from a ground state to a "virtual" excited level[14] (Figure 2.7). This transition leads to an unstable situation, which quickly reverts back with the emission of a photon with the same energy as the ones probing the system. This interaction, which is named Rayleigh component, corresponds to the elastic scattering and is the major part of the radiation interaction.

A minor part of the incident photons, about 1 to 10^7, interact inelastic and therefore they transfer or absorb some energy leaving the system to a different vibrational level. The Stoke component of the spectrum is when the emitted radiation has a lower energy than the initial one. On the contrary, the Anti-Stoke component is due to an emission in which the light emitted is of a higher energy than the initial light. The Anti-Stoke radiation is less probable because it requires the starting molecular system in a vibrational level different then the level equal to one. Both Stokes and Anti-Stoke processes are defined as Raman Effect and are the ones investigated with this technique.

The shift in frequency observed in a Raman experiment corresponds to the energy level of the vibrational and rotational mode of the molecule. However, not all the modes are Raman active, but only the ones which the lattice deformation imply a change in polarizability.
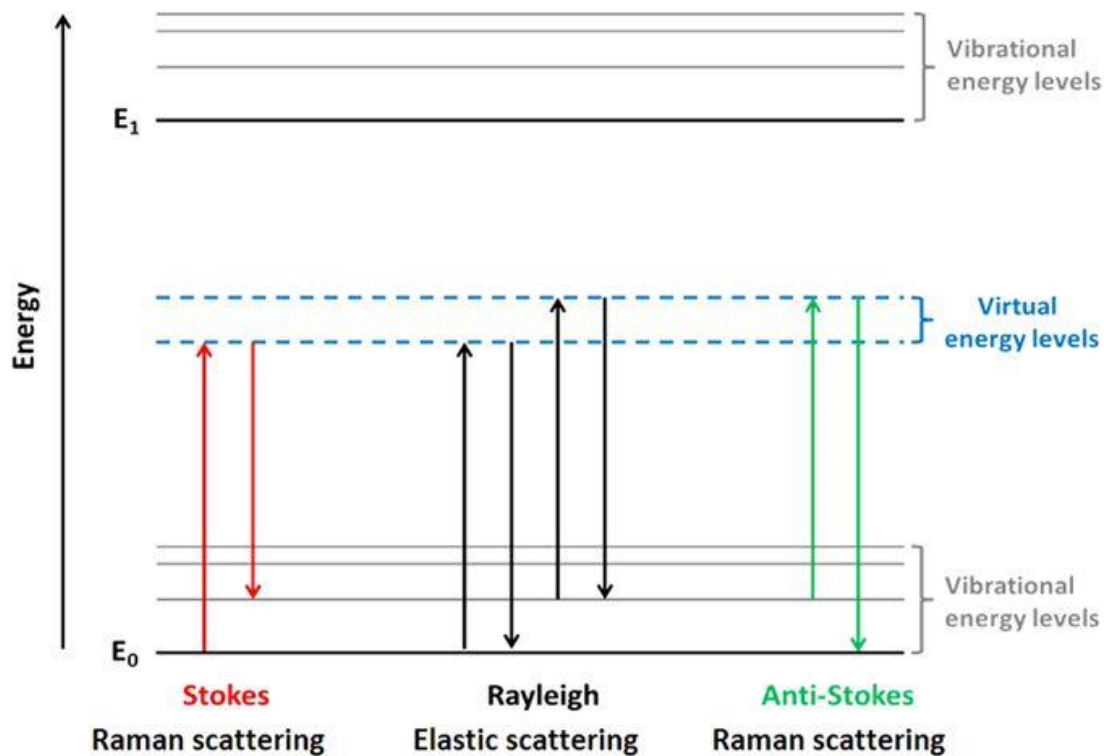
Figure 2-7 Energy level diagrams with the transitions involved in Raman and Rayleigh scattering.[15] The Raman scattering is inelastic when the electron on the ground state is forced on a virtual excited state and re-emitted as a scattering photon with lower (Stokes) or higher (Anti-Stokes) energy. On the contrary, Rayleigh transition is elastic with the incident photon having the same energy as the emitted.

A typical Raman spectrometer is composed of a laser beam using monochromatic light as a source of radiation to increase the intensity of the scattered light. Monochromatic light is used in order to be able to better observe small changes of light emission in the scattered light. Moreover, the use of this light allows a system stimulation on an energy value close to the one where absorption occurs. Raman spectra were collected on a Horiba-Jobin-Yvon LabRam HR confocal microscope. The apparatus uses a 532 nm laser light with a 50 X objective lens and a Synapse CCD detector. The measurements were carried out in an acquisition range of 100-1000 cm^{-1} with a laser intensity decreased to the 10%.
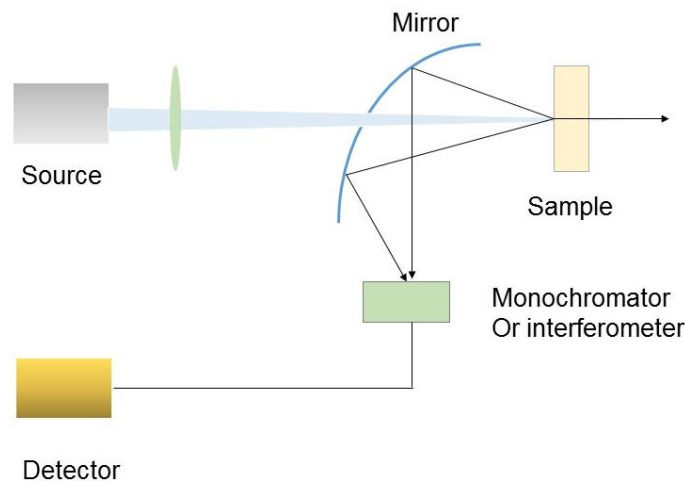
Figure 2-8 Common setup of a Raman spectrometer.[16] The laser beam passes through a lens and a small hole on a mirror before it hits the sample. The scattering light is then directed by the mirror to be collected and analysed on a monocromator or an interferometer at 90 degrees from the incident beam.

2.2.4 Scanning Electron Microscopy (SEM) and Energy-Dispersive X-ray spectroscopy (EDX) analysis

Scanning electron microscopy (SEM) is an experimental technique used to study the composition and the structure of a solid surface. This technique uses high-energy electrons to interact with the sample and reveals information such as external morphology, chemical composition and crystalline structure by generating a 2-dimensional high-resolution image.

The electron beam is generated by heating a tungsten filament, which is then focussed through magnetic fields into a single beam to probe the sample under high vacuum conditions. The vacuum is necessary to avoid air particles to interact with the generated electrons. Since the resolution is inversely proportional to the wavelength, the use of highly accelerated electrons (and therefore with a small wavelength) leads to a resolution down to 3.5 nm.

The accelerated electrons obtained carry a significant amount of kinetic energy, which is dissipated in various signals due to electron-sample interactions. An energy transfer from the primary electrodes to the atoms of the sample characterizes these interactions and generates an emission of secondary electrodes (SE), x-rays and backscattered (BSE) electrons[17],which are used for image production. The SE originate from the atoms of the sample by an inelastic interaction with the electron beam and are responsible for the more detailed surface information showing the morphology and the topography of the sample,

whereas the BSE are generated from elastic interactions and come from deeper regions of the sample. The image information obtained with this source has lower resolution but with the brightness expressed as a function of the atomic number. A detector collects the electrodes generated by the interaction with the beam and converts them into a signal which is sent to the screen.

The EDX measurements are often performed together with SEM and used to characterise the chemical composition of the material. As mentioned previously, the use of an electron beam generates the emission of X-rays, which can be used to identify the different elements present in the sample. The X-rays are formed after ionization of the inner cell electron, which is ejected and the subsequently generated hole is filled with an electron from the outer shell. By this transition, the energy difference is emitted as an X-ray, and since this energy difference is related to the inner core electron energy levels it is specific for a particular atom.
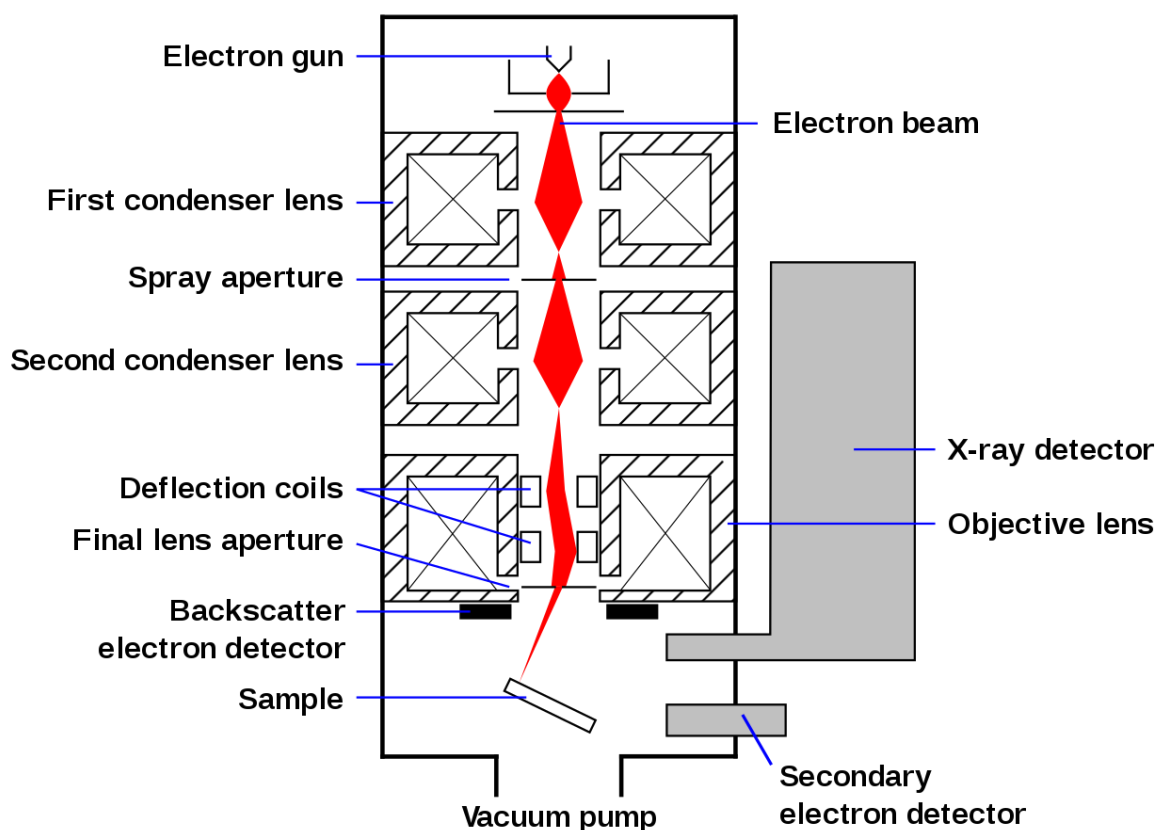
Figure 2-9 Schematic SEM setup.

In this work, a Philips XL 30 ESEM instrument with an accelerating voltage of 25 kV was used to investigate the sample's morphology. EDX measurements were coupled with SEM and performed using an Oxford Instrument X-act spectrometer.

The INCA EDX analysis software using Cu as a standard calibrated the instrument. Some samples were coated with gold in order to facilitate the imagine acquisition, preventing the sample to charge and to avoid overexposure of the image.

2.2.5 X-Ray Photoelectron Spectroscopy (XPS)

X-ray photoelectron spectroscopy is an ionization technique used to gather information about the surface composition and the nature of the chemical bonds using the photoelectric effect. By irradiating a sample with an X-ray beam, the kinetic energy and the number of electrons ejected from the material is quantified. This method has the advantage of providing sensitive measurements without destroying the material. Moreover, XPS provides quantitative information about the chemical bonding and composition of the molecule. On the downside a high vacuum is needed to ensure that the photoelectron does not collide with gas molecules and loses its energy before it reaches the detector.

When an incoming X-ray (with an energy of 200-4000 eV) hits the sample surface with sufficient energy, the radiation will be absorbed by the atom and an inner shell electron will be ejected. This phenomenon is known as photoelectric effect. Because the energy of the X-ray photon is known, the electron expelled by the atom has a kinetic energy which can be calculated to be equal to the energy of the incident X-ray minus the binding energy and the work function of the element:

$$E_k = h\nu - E_b - \varphi \qquad (2.21)$$

The work function is defined as the minimum energy needed to remove an electron from the solid to a point in the vacuum outside the solid surface. By detecting and measuring the energy of each expelled electron, which is unique for each element, it is possible to determine the sample composition. After the photoelectric process, the atom is left in an excited ion form. One of the ways for the atom to relax is by having an upper shell electron fill the vacancy created by the X-ray beam. During this process to preserve the energy, an Auger electron is emitted.
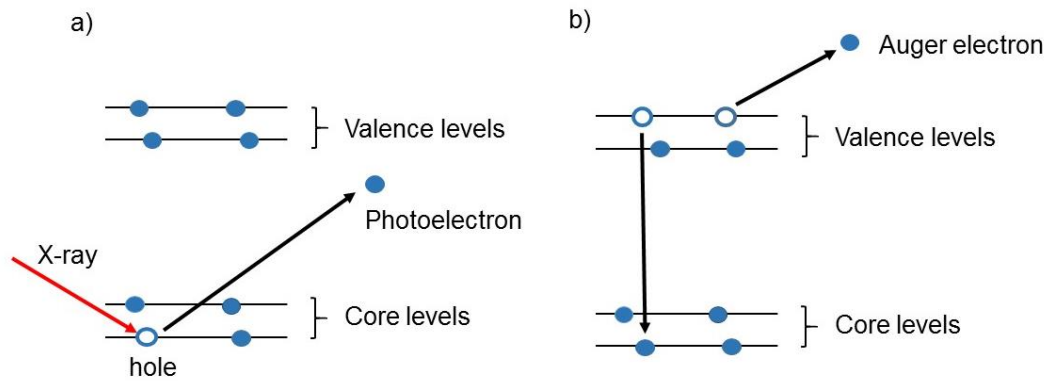
Figure 2-10 Schematic portray the photoelectric effect. a) The x-ray source ejects the electron on the core level of the atom and leaves a vacancy hole behind. b) An electron from the valence level fills the hole vacancy, causing the ejection of an Auger electron to preserve the energy.

Experimentally, a sample under vacuum is targeted with monochromatic X-ray light and the photo-emitted electrons are ejected. The most common X-ray monocromatic sources are Al Kα X-rays and Mg Kα X-rays with a photon energy of 1486.7 eV and 1253 eV, respectively. The emitted electrons are deflected to the detector by a path made with electromagnetic lenses. Those electrons arrive at the detector which counts the electrons and measure their kinetic energy.

The E_k is then represented on a spectrum as a function of ejected electrons over an energy range. The energy and intensity peaks displayed can be used to identify the surface elements presents on the sample based on the binding energy characteristics of each atom. The peak area can also be used to estimate the concentration of a certain element, since it is an indication of how many electrons are on a specific energy level.

The photoemission is dependent on the X-ray source used, which means that the Kinetic energy shifts when the same sample is analysed by using a different X-ray source and therefore photoelectric line move in position when the same sample is analysed by using a different X-ray source. On the contrary, Auger electrons have a kinetic emission only dependent on the electronic state, allowing them to be recorded at the same position independent of the X-ray source.[18] The XPS measurements are commonly reported as a function of the binding energy instead of the kinetic energy. However, in this case the Auger peak changes its location with the X-ray source and therefore is very important to specify the instrument that is used.
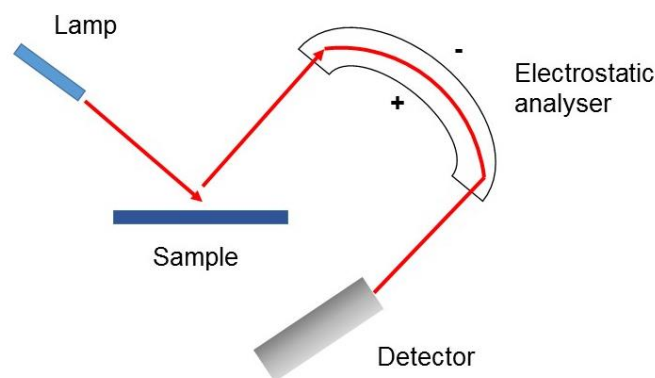
Figure 2-11 Simple scheme of a photon electron spectrometer showing the ionising radiation (an X-ray source), an electrostatic analyser and an electron detector. The deflection of the electron path depends on the electron speed.[5]

According to which kind of radiation source is used both Ultraviolet Photoelectron microscopy (UPS) and X-ray photoelectron spectroscopy (XPS) use the photoelectric effect. UPS uses probing photons with an energy of 10-45eV to investigate the electron ejected from the valence shells and the details about the bonding characteristics. On the contrary XPS uses an X-ray source (200-4000 eV) to probe the system on the core energy levels.

2.2.6 Ultraviolet-visible (UV-VIS) spectroscopy

UV-Vis spectroscopy is an absorption spectroscopy occurring in the region between ultraviolet and visible light. This spectroscopy technique is used to determine in which wavelength in the range between 200 and 800 nm a molecule is absorbing, with the transitions detected being relative to the electronic levels.

A light source is directed through a monochromator to select a single wavelength. The selected radiation is then divided in two by a beam splitter and hits with equal intensity the sample as well as a reference. The light passing thought the sample will be partially absorbed and the detector will collect the transmitted light (Figure 2.12). The light collected is converted into an electric signal by the detector. The transmittance obtained from the machine is then expressed as a ratio between the sample and the reference signal and reported as a percentage by the following the equation:

$$T\% = \frac{I_s}{I_b}X100 \qquad\qquad (2.22)$$

Usually the UV-Vis data are reported as a function of the absorbance:

$$A = -log\frac{I_s}{I_b} = \varepsilon l C \qquad\qquad (2.23)$$

The Lambert-Beer equation uses the absorbance A as proportional to the concentration C expressed in molarity, the absorbance path wave expressed in cm and the molar absorptivity coefficient, ε. This value describes the probability of the molecule to absorb at a particular wave of light and is given as $\frac{L}{mol\ cm}$.

The maximum absorbance wavelength of a sample is generally used in equation 2.23 to calculate the molecular concentration inside the sample. The molar absorptivity coefficient to calculate the concentration is obtained by generating a calibration curve in the linear range where the absorbance is in relation to different sample concentrations, with the obtained slope being εl.
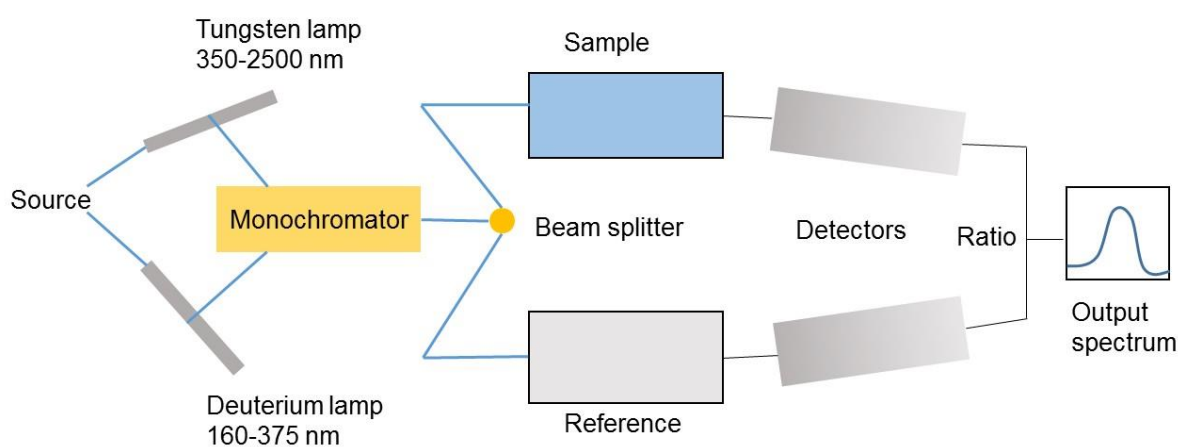
Figure 2-12 Example of a typical UV-Vis spectrophotometer layout.[19]

2.2.7 Atomic force microscope (AFM)

AFM is a technique which provides a 3D profile on a nanoscale definition. The image is obtained by measuring the forces between a sharp probe of around 10 nm and the surface at 0.2 nm sample separation. The probe with a supporting cantilever gently touches the surface, while the interaction between the probe and the surface is collected. The entity of the collected forces are dependent on

the spring constant relative to the stiffness of the cantilever (generally around 0.1-1 N/m) and the distance between the probe and the surface. Hooke's law describes the force collected as

F=-kx (2.24)

Where k is the spring constant and x is the surface distance. The force collected is typically in the range between 10^{-6} and 10^{-9} N.

The AFM has a z-scanner which moves the cantilever up and down the surface, and a xy-scanner that moves the sample back and forward underneath the tip probe (Figure 2.13). A position detector registers the movement of the cantilever by tracking the laser movement reflected from the top. Any bending of the cantilever will affect the laser reflection and the detector records those changes during the measurement. The topographic imagine is generated by using a feedback loop to control the height of the tip above the surface.
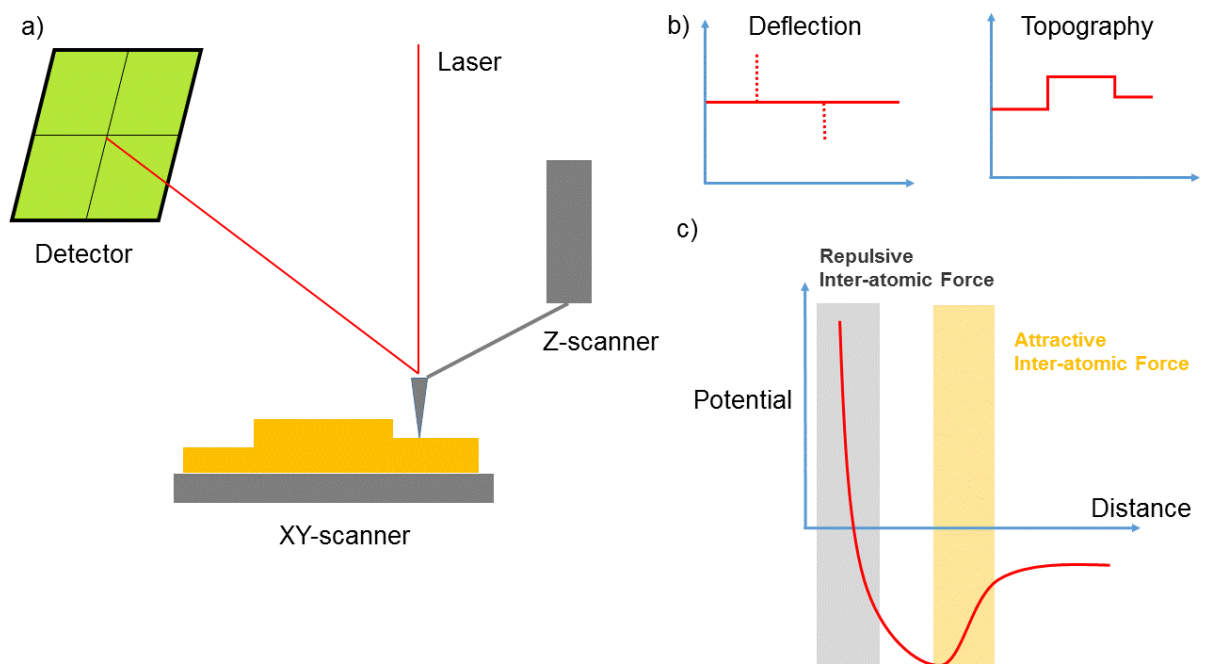
Figure 2-13 a) Schematic of the AFT experimental setup. b) Schematic showing the deflection cantilever over time and how it is related to the topography image. c) Graph describing the potential as a function of the distance. The kind of force between the tip and the surface occurring at specific distances are indicated.

Typically, a probe is made from silicate nitride or silicone. The cantilever can have different lengths, materials and shapes affecting the spring constant and the

resonance frequency. The types of forces measured are the repulsive Van der Waals VdW forces, and when the tip moves away also the surface attractive VdW forces. AFT has three modes to collect the image: contact, intermittent contact (or tapping mode) and non-contact.[20]

The contact mode is in the repulsive VdW regime and is generally used for resistant surfaces because the probe can damage or deform these materials. Because of the repulsive forces, the cantilever bends as it passes over the sample features. The image of the sample is obtained by maintaining the cantilever deflection constant using the DC feedback amplified. The forces applied to maintain the distance between the tip and the sample constant is then used to produce the image.

The tapping mode produces an image similar to the contact mode. In contrast to the contact mode, the cantilever oscillates in a resonance frequency with an amplitude of 20-100 nm. During scanning the probe lightly taps the surface. The oscillation of the tap allows to probe the sample at a constant timespan. The advantage of this technique is the possibility to collect high quality images without damaging the sample. However, the collection of images in liquid is often challenging in this mode and therefore the contact mode is preferred.

Finally, the non-contact mode is a type of scan, which consists of a measurements where the probe never touches the surface. It is performed in the attractive VdW regime by making the probe oscillate above the sample without touching it. Every sample has some water absorbed on the surface due to air humidity. A precise high speed feedback loop is used to monitored the changes in oscillation due to the attractive VdW forces and to keep the tip from crashing into the surface. This technique has the advantage to not damage the material during the scanning. However, the images collected in this mode are often of low resolution and their resolution can be affected by contaminations of the surface. For this last reason, other modes are generally preferred unless there is the possibility to operate in an ultra-vacuum chamber.

The AFM technique has some limitation due to the type of sample probed. For example, the resolution is limited by the size or the tip angle when the probing sample has a very rough surface or a very steep slope. As a consequence, if the probe tip is not sharp enough, the recorded image does not truly reflect the sample morphology but rather only the interaction between the tip and the

sample. Another limitation occurs when dealing with too rough samples that affect the piezo movement limit.

2.2.8 Gas chromatography (GC)

Gas chromatography is a technique used in analytical chemistry to separate and identify a mixture of compounds. In GC the mobile phase is in gas form, while the stationary phase is liquid or solid. The gas solution to be analysed is extract by a calibrated syringe from the headspace of a tight electrochemical cell and then inserted into an injection port. The used column can either be packed, where all the gas extracted from the syringe is plugged directly into the column or capillary, where the gas enters into the column in small amount per time, while the rest is kept in a chamber. Some GC machines are capable of switching between those two types of injection modes. During the measurements the gas acts as a carrier and transports the analytes through the column, where they arrive at the detection unit at different rates based on their respective retention coefficient. The detectors used to identify the gases can vary; the one used in this work measures the changes in thermal conductivity of the gasses coming out of the column. The values obtained were compared to the ones of a reference Ar gas flow. Once the different gasses are detected, a signal is sent to the computer and the value of each analyte is reported as a function of the arrival time. The different arrival time is used to identify the type of gas present, while the peak area correlates to the percentage of that particular gas inside the electrochemical cell headspace. This percentage is calculated by the use of a calibration line that is made for each analysed gas by using commercial gas cylinders containing a specific percentage of the target gas in argon.

The gas percentages obtained from the measurements are converted into moles by based on the volume of the headspace. The values are then compared to the theoretical moles calculated, assuming that all the charge passing though the cell is used to produce hydrogen.
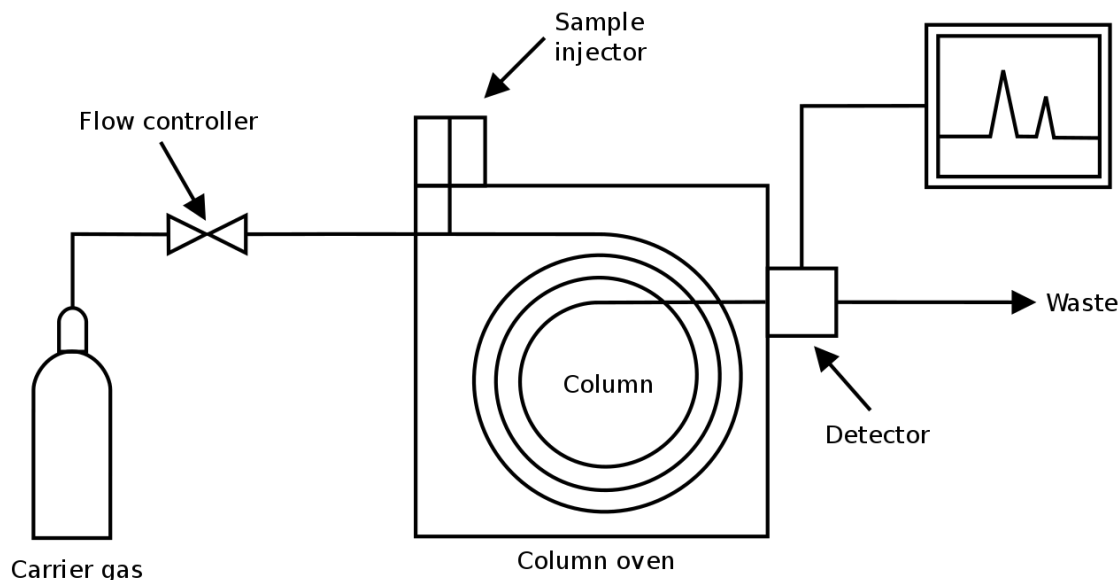
Figure 2-14 Gas chromatography setup scheme.

2.3 Electrochemical methods:

2.3.1 Experimental setup

Voltammetry studies the kinetic of a process by looking at electrode current changes as a function of the voltage applied. The experiment is carried out in an electrolysis cell, which can consist of two or three electrodes. The two electrode set up is formed by a working electrode (WE), where the reaction occurs, and by a counter electrode (CE) which closes the circuit.[21] The counter electrode does not have any influence on the reaction occurring at the WE and therefore is generally made with inert material such as Pt or with less expensive carbon cloth. [22] The two electrodes setup is used to analyse the whole electrochemical cell performance because it measures the difference of potential between the working and the counter electrode.

The WE half-reaction can be studied independently by introducing a reference electrode (Ref) within the set up. The potentiostat in this configuration ensures that the current flow between the WE and the CE, leaving the reference electrode stable and therefore allows the WE potential to be expressed relative to it. For this reason, the reference's potential needs to be stable over time and temperature with a fixed and well-defined electrochemical activity.

Most of the electrochemical measurements are reported using a standard hydrogen electrode (NHE) as a reference (half-reaction $2H^+ + 2\,e^- \leftrightarrow H_2$). The NHE potential is defined as zero by convention. Even if most of the data are reported using this reference, the use in the laboratory is not common due to difficulties in maintaining unit activity for H_2 (g) in the half-cell. Most of the reactions occurring in aqueous solution are carried out using as reference electrodes the saturated calomel electrode (SCE) or the silver-silver chloride electrode (Ag/AgCl).

The reason to use a particular reference electrode is based on availability and the pH present inside the electrochemical cell. The reference electrode used during this work was a (Ag/AgCl) electrode in a NaCl 3 M solution. It is composed of a silver wire immersed in a NaCl solution whose concentration slightly influences the half-cell potential. In this work the reference electrode has a potential of 209 mV, which was used to correct all the potential measurements and refer the measurement to the NHE electrode.

Most of the experiments in this work were conducted on a single cell three-electrode setup as shown in Figure 2.15. The two electrode setup was only used for the galvanostatic measurements coupled with the GC.
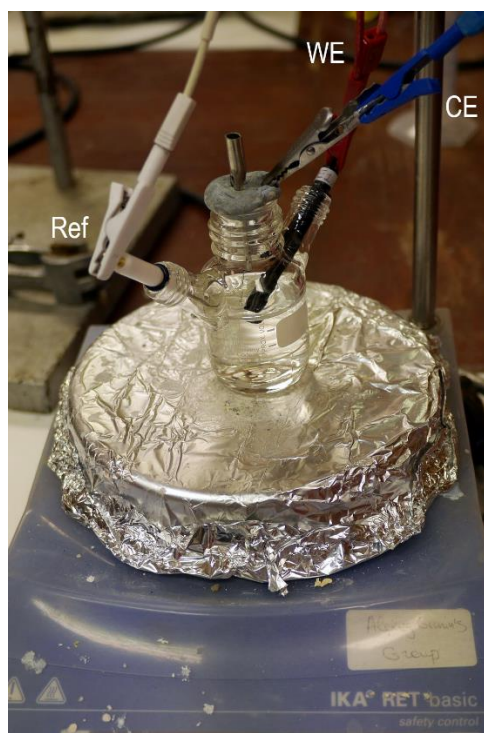
Figure 2-15 Standard single cell three-electrode setup. The white wire is used for the Ag/AgCl 3M reference electrode, the blue wire is linked to a Pt wire used as the counter electrode (CE) and the red wire is linked to a glassy carbon acting as a working electrode (WE).

2.3.2 Linear sweep voltametry (LSV)

This method is the most commonly used way to electrochemically test a system due to speed and simplicity. During the measurement the starting potential, E1, varies as a function of time to a final value E2, and in the meantime the resulting current is collected.[23]
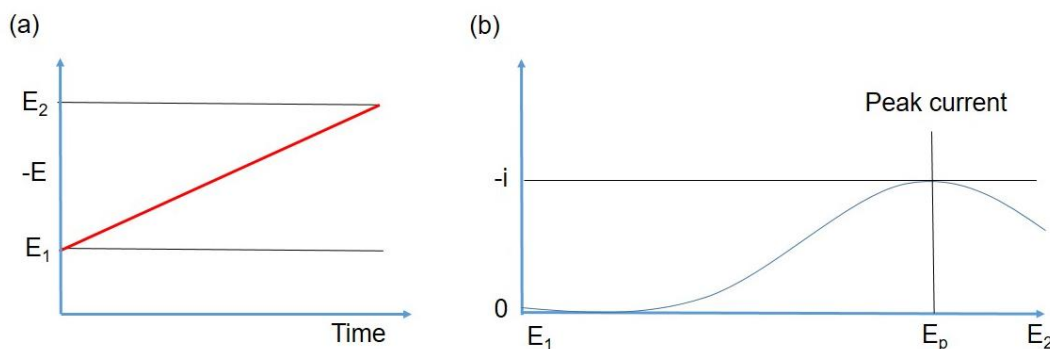
Figure 2-16 Potential sweep (a) and the resulting current (b) for an irreversible reaction.

The collected linear sweep voltamogram (Figure 2.16 b) shows the current/voltage behaviour during the measurement, which can be better understood by assuming the electrode kinetics in the oxidation reaction between A and B (equation 2.25) irreversible.

$$A_{(aq)} + e^- \underset{K_{ox}}{\overset{K_{red}}{\rightleftharpoons}} B_{(aq)} \tag{2.25}$$
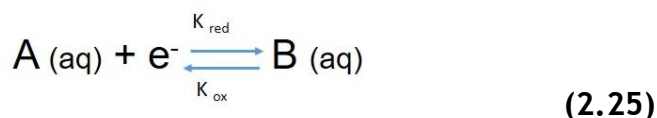
At the beginning of the measurement, the potential applied to the system is low and therefore the detected current is due to the migration of the ions in the solution. Once the applied potential achieves a more reducing value, the A species starts to be reduced to B at the electrode surface and more current starts to be detected. As the potential keeps increasing in its module, the current detected at the electrode increases exponentially with time, indicating an increase of the reduction rate K_{red} in equation (2.25). On the voltammogram, the current increases as more negative potential is reacted until a maximum, after which it starts to decrease. The final decrease of the current is due to the consumption of A on the electrode surface. The maximum peak on the voltammogram represents the point where the increase of the reduction constant is compensated by the

decrease of the A species on the electrode surface. After that, the current flow reflects how fast A can diffuse back to the electrode surface.

When the reaction in equation 2.25 becomes reversible, the sweep voltammogram shows a higher current and a lower potential. This is because once the equilibrium is achieved, the total kinetic is described by both the processes. The species A and B on the electrode surface are in equilibrium in a ratio described by the Nernst equation.
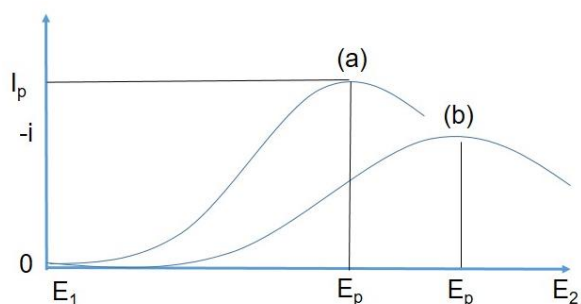
Figure 2-17 Example of reversible (a) and irreversible (b) linear sweep voltammograms

LSV measurements were used during this work to evaluate the activity of a material for the Hydrogen Evolution Reaction (HER), as well as to calculate the Tafel slope if performed on a slow scan rate (approximately 2 mV s^{-1}).

2.3.3 Cyclic Voltammetry (CV)

Cyclic voltammetry is an extension of linear sweep voltammetry, based on reversing the direction of the applied potential once it reaches the most negative value E2.[24] The reduction part of the voltammogram follows the same dynamic already described for LSV. When the E2 potential sweeps back, the species B formed during the reduction starts to be oxidised back to species A, generating a current with the opposite sign. This current becomes bigger as the potential becomes more positive. The peak intensity and location on the reverse scan gives an indication about the reversibility of the A/B couple (equation 2.25).
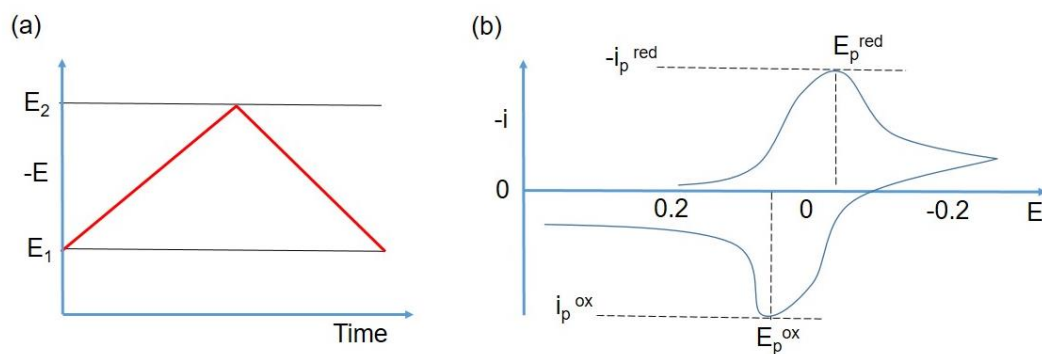
Figure 2-18 Potential variation during a cyclic voltammetry experiment (a) and the cyclic voltammogram obtained for a reversible reaction (b).

In Figure 2.18 b typical reversible cyclic voltammogram is displayed. In the graph, the reductive and oxidative peaks have the same intensity and are separated by a peak distance of 59 mV (at 25 °C), which is independent of the scan rate. If the number of electrons transferred during the process are more than one, the peak separation can be calculated by the equation 2.26.

$$\left| E_p^{ox} - E_p^{red} \right| = 2.218 \frac{RT}{nF} \qquad (2.26)$$

When reaction 2.25 is irreversible, B is not reconverted back to A and therefore the voltammogram does not show the return peak present for a reversible reaction (Figure 2.19 a and b). The "reversible" and "irreversible" electron reactions are the two limiting cases, and a real system can also be semi-reversible (Figure 2.19 c). In this case, the difference in concentration between the A and B species depends on the kinetic oxidation or reduction rate and on the mass transport rate. A non-ideal system can be recognised from a reversible system because the peak distance between the reduction and the oxidation peak is not fixed but rather depends on the scan rate. In particular, the irreversible peak will only be seen by using a fast scan rate. The B species requires a higher oxidising potential to be reconverted back to A. If this process occurs too slowly, the B molecules formed have time to decompose and therefore they cannot be reconverted.
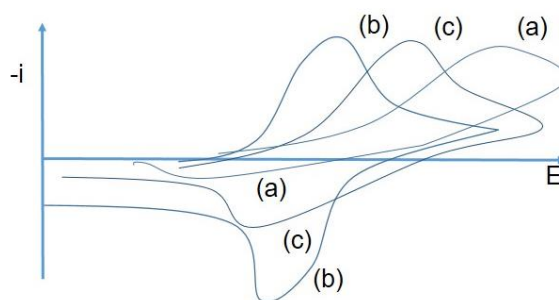
Figure 2-19 Cyclic voltammetry example of (a) irreversible, (b) reversible and (c) semi-reversible.

As for the LSV technique, CV scans were used to evaluate the catalyst performances in the hydrogen evolution reaction. Contrary to LVS, CV can scan the material consecutively for a selected number of cycles, allowing to investigate if the measurements are reproducible or if the material undergoes some chemical rearrangements. Moreover, the repetitive cycling of the material for a high number of times (e.g. 1000 cycles) can be used as a stability test for the catalyst. However, this method is considered less reliable than others and testing electrocatalysts by chronoamperometry or galvanostatic techniques is generally preferred.

2.3.4 Bulk electrolysis or Chronoamperometry.

Bulk electrolysis is an electrochemical technique where a constant potential is applied on the WE over time and the resulting current is monitored. As potential a value is chosen with which complete conversion of the reaction A to B at the electrode is observed.[25] At the beginning on the measurement, an immediate drop of the current is observed due to the rapid consumption of the A species in proximity of the electrode, after which the species to be reduced has to diffuse to the electrode (Figure 2.20 b). The current decreases as the concentration gradient drops and therefore decrease the amount of the fresh reagent approaching the surface.
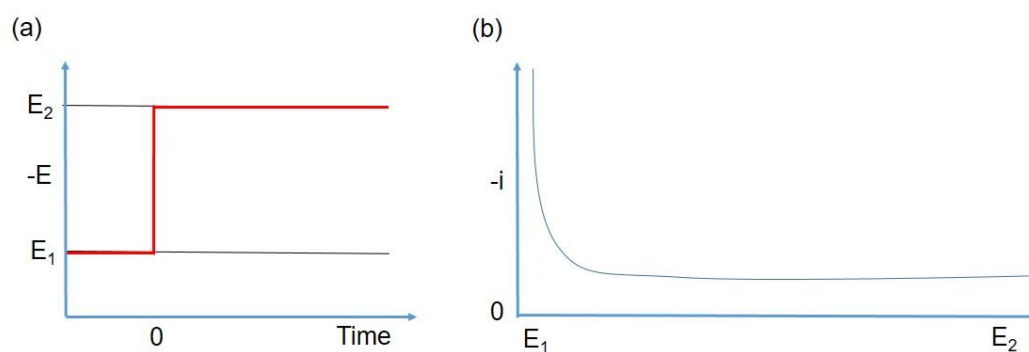
Figure 2-20 Variation of the potential at the beginning of the measurement (a) and the current response in a Chronoamperometry experiment (b).

The Current response as a function of time is describe by the Cottrell equation:

$$|i| = \frac{nFAD^{\frac{1}{2}}[A_{bulk}]}{\pi^{\frac{1}{2}}t^{\frac{1}{2}}} \qquad (2.27)$$

Where I is the current expressed in A, F is the faraday constant, A is the electrode area and $[A_{bulk}]$ is the initial concentration expressed in mol/cm^3. This equation can be used to calculate the diffusion coefficient.

Chronoamperometry has a wide range of uses such as electrodeposition, stability testing of an electrode catalyst or as an alternative way to collect the Tafel slope (as in Chapter 3). The stability of a catalyst is generally tested by applying a potential for a long period of time in a particular medium and monitoring the changes of the produced current. The Tafel slope measurement is performed using multi-potential steps, which consist of applying a constant potential for 5 minutes and then repeat the measurement with the potential increased by 30 mV over a range of potentials.

2.3.5 Galvanostatic measurement

This type of measurement is performed by applying a constant current on the WE and monitor how the potential necessary to maintain this current changes during the measurement (see Figure 2.21 a and b).
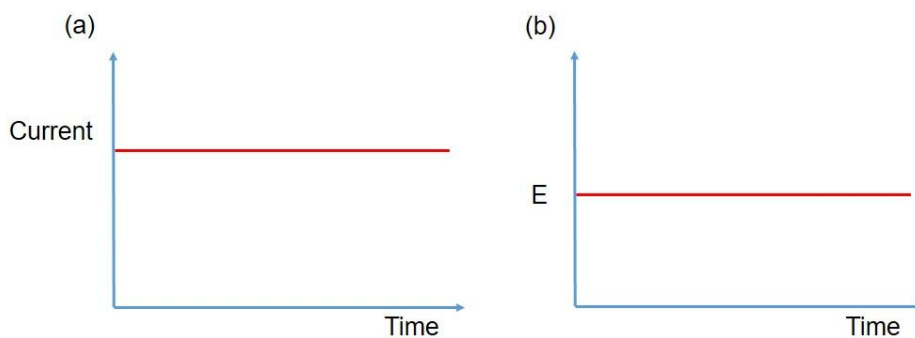
Figure 2-21 (a) Current value maintained constant during the Galvanostatic measurement and the resulting potential (b).

Experimentally, this offers a complementary technique to bulk electrolysis. Stability tests of the catalyst were generally performed using a current of 0.71 mA, which enabled a current density of 10 mA cm^{-2} on a glassy carbon electrode. The same measurement performed on a closed cell was used to generate hydrogen, which was detected by coupling this technique to gas chromatography.

2.3.6 Electronic impedance spectroscopy (EIS)

EIS is a non-invasive technique to investigate the electrochemical properties of a system. The potentiostat probes the system by shifting the potential away from the equilibrium and thus generating an electrochemical reaction. EIS can be performed in the time domain (DC) or in the frequency domain (AC). In the DC mode, the applied potential is sometimes too large and can therefore irreversibly change the system. The current detected as outcome is the sum of all the currents from the different processes in the reaction. In the AC mode, a wave with a small fixed potential amplitude is applied over a frequency range. The frequency dependencies on different processes allows to separate the contributions to the response.[26]

The electrochemical resistance is the capability of a system to oppose an electrical perturbation and can be expressed by Ohm's law:

$$R = \frac{E}{I} \qquad\qquad (2.28)$$

In equation x R is the resistance (Ω), E is the voltage (V) and I the current (A). While in a DC experiment the ratio between the voltage and the current is expressed by the resistance, in an AC experiment this value is substituted by the more general term of impedance. The term impedance covers any reason why the current is not flowing in the cell, which can be resistance, capacitance or diffusion.

$$Z = \frac{E}{I} \hspace{3cm} (2.29)$$

During a typical EIS experiment in AC mode a stimulus is applied as a voltage, and an AC current is measured as a system response (see Equation 2.30 and 2.31 and Figure 2.22).

$$E = dE \sin(\omega t) \hspace{3cm} (2.30)$$
$$I = dI \sin(\omega t + \varphi) \hspace{2.5cm} (2.31)$$
Where $\omega = 2\pi f$ $\hspace{3cm}$ (2.32)

In the equations above, E and I represent the instantaneous values of the voltage and the current, while dI and dE are their maximum amplitude. Both E and I values are described as a function of the radial frequency ω (rad). It is defined in equation 2.32, where f is the frequency (Hz) and the φ value represents the phase delay between the applied voltage and the detected current.
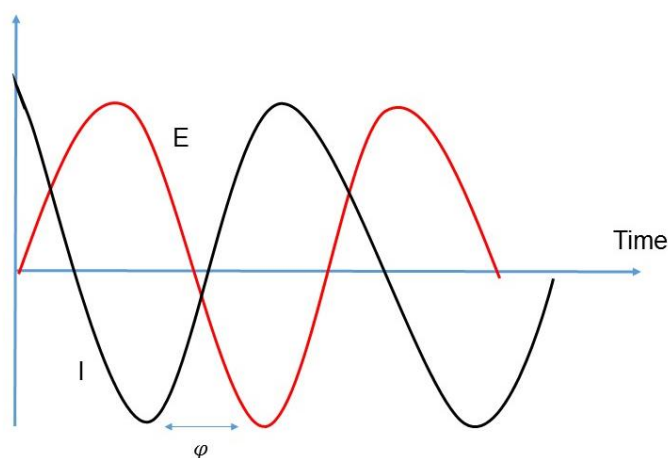
Figure 2-22 Alternative current (AC) measurement showing a potential sinusoidal wave E and the current generated from the system as a response to the potential I. The two waves oscillate with a phase delay of φ.

The ratio between these two waves expressed by equation x and x is defined as impedance.

$$Z = \frac{E_t}{I_t} = \frac{E_o \sin(\omega t)}{I_o \sin(\omega t+\varphi)} = Z_0 \frac{\sin(\omega t)}{\sin(\omega t+\varphi)} \qquad (2.33)$$

It is possible to rewrite the potential and the current with the Euler relationship:

$$exp(j\varphi) = \cos\varphi + \mathbf{j}\sin\varphi \qquad (2.34)$$

Where φ is a real number and j is the imaginary unit. The potential and the current can be described as complex functions:

$$E_t = E_o exp(j\omega t) \qquad (2.35)$$
$$I_t = I_0 exp(j\omega t + \varphi) \qquad (2.36)$$

The impedance can then be rewritten as a complex number:

$$Z(\omega) = \frac{V_t}{I_t} = Z_0 exp(j\varphi) = Z_0(\cos\varphi + j\sin\varphi) \qquad (2.37)$$
$$Z = |Z|\cos(\varphi) + j|Z|\sin(\varphi) \qquad (2.38)$$
$$Z = Real(Z) + Imaginary\,(Z) \qquad (2.39)$$

Impedance data are conveniently described as a plot where the imaginary and the real part are plotted on the y and x axes, respectively. This graphic representation is called Nyquist plot and will be described in more detail in paragraph 2.3.7. Alternatively, the impedance can be displayed by the Bode graph, where the logarithm of the impedance and the phase on the y axis are reported as a function of the logarithm of the frequency in the x axis.

The criteria which need to be satisfied in order to consider EIS measurements reliable are linearity, stability and causality. A system is in a linear range when after application of a potential it responds with a current proportional to the applied potential. Therefore the impedance level measured and calculated does not change (equation 2.29). This condition generally occurs when the perturbation is very small. Another important criterion is the time span in which the measurement occurs. Long frequency measurements take a longer time to be collected (e.g., a point at 1 mHz takes approximately 20 minutes). Therefore, if

the system is not stable during the course of the measurement, the low frequency data would not be valid. Finally, the system response has to be caused by the perturbing signal (criterion of causality).

2.3.7 Equivalent circuit for the interpretation of electrochemical cells

The data obtained from the measurement are fitted with an equivalent circuit, which describes the physical processes taking place. The association between the electrochemical processes and circuits is not surprising since they both obey the fundamental laws connecting charge and potential. However, this analogy has some limitations because only simple circuits can be used to describe a system unambiguously, and some physical considerations are required for systems that are more complex.[27]

The electrical components have a defined relationship between the applied frequency and the impedance. The simplest circuit element is the resistor, and its impedance is described by the resistor's value (equation 2.40). It generally represents the solution's resistance or the charge transfer resistance into the electrochemical cell. Since this circuit element is not frequency dependent, its value is independent of the frequency range applied.

$$Z = R \qquad (2.40)$$

On the contrary, a capacitor's impedance is frequency dependent and its value is inversely proportional to the applied frequency (equation 2.41). In this case, the phase difference between current and voltage is $\pi/2$, whereas there is no phase difference in the resistance case.

$$Z = -\frac{j}{\omega C} \qquad (2.41)$$

The capacitance model describes physical processes such as the electrochemical double-layer, which is a region where electrolyte ions can accumulate with a major entity in respect to the bulk. The capability of an interface to store charges makes the surface act as a capacitor. Sometimes the capacitor is substituted by a constant phase element (CPE), which is defined as an imperfect capacitor. This

is generally used to define rough surfaces. The CPE uses two degrees of freedom to fit the data and therefore will give a better fit of the data compared to the normal capacitor.

The electrical elements described above have a different representation on a Nyquist plot.[28] The resistor does not have a phase dependency and therefore its impedance does not have any imaginary contribution. Its impedance is then represented by a single point on the x-axes (Figure 2.23 a). The capacitor is phase dependent and its contribution will be displayed on the y-axes. Since this contribution is frequency dependent (see equation 2.41), its value will vary during the measurement and it will be represented as a vertical line at the x origin (Figure 2.23 b).

The impedance behaviour becomes more complex when the resistor and the capacitor are placed in parallel. In this arrangement, the current can flow in both circuit components. However, the capacitor's impedance dependency on the frequency makes the current preferentially flow through the capacitor at higher frequencies, and to the resistor at lower frequencies. The resulting Nyquist plot is a semicircle where the x interception at low frequency represents the value of R (Figure 2.23 c). This circuit is generally used to describe a standard electrochemical three electrodes model (as defined in paragraph 2.3.1), where it is assumed that no electrolysis is occurring. In this circuit the resistance mimics the one of the solution, while the double layer capacitance at the working electrode represents the capacitor's element.
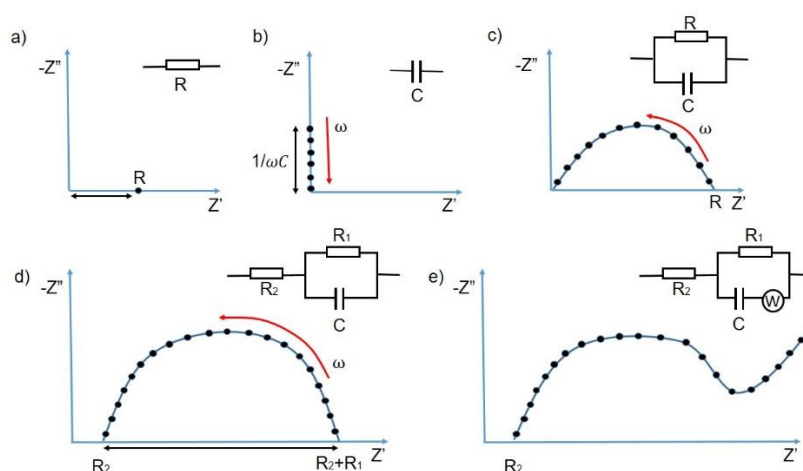
Figure 2-23 Nyquist plot showing the impedance dependency with the single circuit element resistor (a) and capacitor (b). Impedance plot representing the impedance response of a resistor and a capacitor in parallel (c) and the same circuit linked in series with another resistance R_2 (d). Nyquist plot representing the impedance response for a parallel RC circuit in series with a resistor with the Warburg term in parallel with RC describing the diffusion contribution (e).

The third and most common Randles circuit consists of a resistor R_2 in parallel with the R_1 and C components. In this system, the current has to pass through R_2 and then splits into the other two components. The obtained Nyquist plot is a semicircle starting at R_2 with the width of R_1. This circuit is generally used to describe a three-electrode system in the presence of electrolysis, where R_1 represent the charge transfer resistance (Figure 2.23 d).

Some three-cell systems need to take into account a diffusive parameter, which is described by the Warburg impedance term. This is inserted in parallel with the capacitor and the charge transfer resistance. The solution resistance mainly dominates the impedance at high frequency. At those frequencies the charge transfer does not occur and the current mainly flows through the capacitor. As the frequency starts to decrease, the charge transfer starts to occur, showing a semicircle on the Nyquist plot (Figure 2.23 e). Finally, at low frequencies the impedance starts to rise largely because of the diffusion described by the Warburg term.

2.4 Bibliography

1. R. Xu and X.Yan. *Modern Inorganic Synthetic Chemistry*. (2017).
2. A. Rabenau The Role of Hydrothermal Synthesis in Preparative Chemistry. *Angew. Chem. Int. Ed. Engl.* **24,** (1985).
3. J.A. Moulijn, S. P.W.N.M. van Leeuwen and R.A. van Santen *Catalysis: An integrated Approach to Homogeneous , Heterogeneus and Industrial Calatysis*. (1993).
4. R. A. West. *Basic Solid State Chemistry*. (1999).
5. P. Atkins and J. de Paula. *Physical Chemistry*. (2014).
6. H. P Myers *Introductory solid state physics*. (1997).
7. T. Hahn *International Tables for Crystallography: Volume A Space group symmetry*. (2006).
8. L. Moore *Solid state chemistry, an introduction*. (2005).
9. C. Hammond *The basics of crystallography and diffraction*. (1997).
10. D. A. Skoog, J. Holler and T. A. Nieman *Principles of Instrumental Analysis*. (2017).
11. A. C. Dreele and R. B. Von. General Structure Analysis System (GSAS). *Los Alamos Natl. Lab. Rep.* 86–748 (1994).
12. B. H. Toby EXPGUI, a graphical user interface for GSAS. *J. Appl. Crystallogr* **34,** 210–213 (2001).
13. K. Shankland, L.B. McCusker and Ch. Baerlocher in *Structure Determination from Powder Diffraction Data* 140–143 (2002).
14. A. C. F. Basko Raman spectroscopy as a versatile tool for studying the properties of graphene. *Nat. Nanotechnol.* **8,** 235–246 (2013).
15. K. J. I. Ember, M. A. Hoeve, S. L. McAughtrie, M. S. Bergholt, B. J. Dwyer, M. M. Stevens, K. Faulds, S. J. Forbes and C. J. Campbell Raman spectroscopy and regenerative medicine: a review. *Regen. Med.* **12,** (2017).
16. P. Atkins and J. de Paula. *Physical Chemistry*. (2014).
17. L. E. Smart and E. A. Moore. *Solid state chemistry, an introduction, Chapter 2*. (2005).
18. http://www.casaxps.com/help_manual/XPSInformation/IntroductiontoXPS.htm.
19. M. Weller, T. Overton, J. Rourke and F. Armstrong *Inorganic Chemistry*. (2010).
20. https://www.doitpoms.ac.uk/tlplib/afm/printall.php.
21. A. C. Fisher. in *Electrode Dynamics* 26–27 (1996).
22. https://chem.libretexts.org/Bookshelves/Analytical_Chemistry/Supplemental_Modules_(Analytical_Chemistry)/Analytical_Sciences_Digital_Library/JASDL/Courseware/Analytical_Electrochemistry%3A_The_Basic_Concepts/05_Experimental_Hardware/B._Reference_and_Auxil.
23. Fisher, A. C. in *Electrode Dynamics* 28-29 (1996).
24. Fisher, A. C. in *Electrode Dynamics* 31–33 (1996).
25. Fisher, A. C. in *Electrode Dynamics* 32–33 (1996).
26. Ametek scientific instrument. Available at: https://www.ameteksi.com/library/application-notes/solartron-analytical.
27. E. Macdonald and J. R. Barsoukov *Impedance Spectroscopy: Theory, Experiment, and Applications*. (2005).
28. A. C. Fisher in *Electrode Dynamics* 64–66 (1996).

3 Transition metal sulphides as non-precious catalysts for HER

Synopsis

The goal of this project was to synthesise molybdenum sulphide on a transparent electrode, which could help to integrate future sulphide-based materials into solar-to-fuel devices. Direct hydrothermal synthesis on a transparent conductive substrate was considered impractical in the past because of the harsh environment caused by the hydrothermal synthesis. Therefore, this explored the possibility of using benign conditions of one-pot reactions to synthesize metal-chalcogenides directly on transparent metal-oxide-electrodes. The aim was to deposit translucent films that could be prepared by simply reducing the starting concentrations. The films obtained could achieve an overpotential of 260 mV at a current density of 10 mA cm^{-2} with a Tafel slope of 64 mV dec^{-1} in acidic media, which is comparable to the results previously reported on sulphides in the literature.

3.1 Introduction

3.1.1 Transition metal sulphides as non-precious catalysts for HER

Metal sulphides are a subclass of the metal chalcogenides group.

The thermodynamically stable MoS_2 polymorph forms are 2H and 3R, which are semiconducting with an indirect band gap of 1.7 eV, while the conducting 1T form can only be obtained by lithium intercalation.[15,16,17,18,19]

This class of metal chalcogenides paved the way for the production of catalyst bio-inspired by enzymes such as nitrogenase or hydrogenase.[20, 21,22,23,24,25]
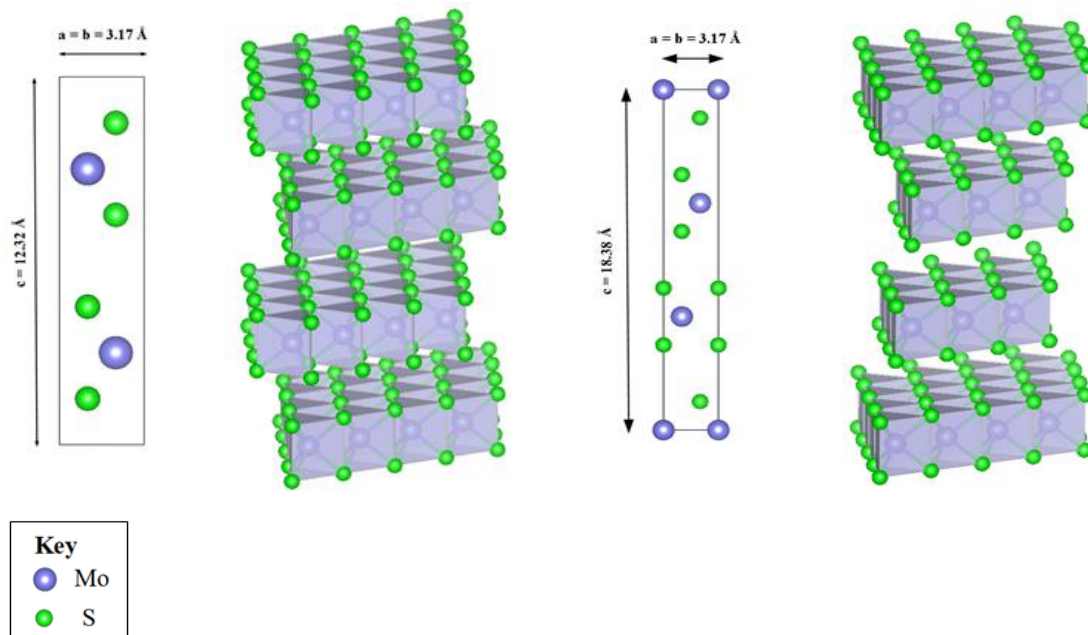
Figure 3-1 Left, 2H-MoS₂ unit cell crystal structure and layer stacking. Right, 3R-MoS₂ unit cell crystal structure and layer stacking. [26]

In 2005 Hinnemann et al [27] did *density functional theory calculations* (DFT) which proved that, despite MoS₂ in crystalline bulk form not being reactive,[28] the (10-10) Mo edges have an activity similar to nitrogenase.[27] These results were proven experimentally by synthesizing and testing the activity of MoS₂ nanoparticles on graphite.

Jaramillo et al synthesized MoS₂ on a clean Au(111) substrate by physical vapour deposition and thereby managed to generate different sizes of MoS₂ nanoparticles with a high amount of Mo edges exposed.[29] This confirmed the HER was proportional to the length of the exposed edges and not the coverage of MoS₂ nanoparticles, further confirming the Hinnemann calculations.

3.1.2 Challenges associated with sulphides as HER catalysts

The catalytic activity of MoS₂ can be increased by active site engineering or electronic conductivity engineering. Active site engineering can include steps such as increasing the number of exposed active sites or enhancing the reactivity of active sites, while improving the electrical contact to active sites can be achieved by utilizing a conductive substrate.

Some research has been focused on improving the HER activity by doping the material with other metals to increase the formation of defects on the basal plane

and therefore the number of active sites.[40] Xie et al showed that the basal plane could crack by the presence of other elements, enlarging the number of active sites across it.[41,42] The doping can also modify the catalytic performance by altering the charge distribution inside the compound and so to tune the activity. Metals like Co and Cu have been successfully incorporated into the MoS_2 lattice.[30,31] A theoretical study conducted by Chorkendorff et al performing DFT calculation on Co doped MoS_2 suggested that the free energy associated with the S-edges dropped from 0.18 to 0.10 eV, achieving a comparable value to the 0.08 eV of the Mo-edges.[43]

The use of Co and Cu as dopant has resulted in a significantly improved HER activity on a wide range pHs. In particular, Co doping achieved the best performances at neutral pH, achieving an overpotential of 250 mV with a Tafel slope of 85 mV dec^{-1}.[30] Inspired by the improvement of the MoS_2 performances by Co doping, Sun et al tested Co-S film as HER electro-catalyst. The material was prepared by electrodeposition of $CoCl_2$ and a thiourea solution on a conductive fluorine tin oxide (FTO) surface followed by the further annealing of the material at 300 ^{o}C under an Ar atmosphere. The material was tested in a potassium phosphate buffer obtaining an overpotential of 150 mV at 10 mA cm^{-2} with a Tafel slope of 93 mV dec^{-1}.

The Cu_2MoS_4 crystalline material was synthesised at 135 ^{o}C under nitrogen atmosphere, adapting a procedure previously described by Pruss *et al*.[44] The material was active in neutral and basic media achieving the best performance at acidic pH with an overpotential of 135 mV and a Tafel slope of 95 mV dec^{-1}. No Tafel slopes calculated matched with any of the principle steps for the hydrogen evolution reaction[45] but they were comparable with other MoS_2 doped materials present in the literature.[46]

The choice of a substrate in the design of a catalyst is an important parameter to enhance the catalytic activity. The use of a conductive substrate has the additional advantage of binding the catalyst on the surface without the need to use expensive building agents such as Nafion. For this reason, many solvothermal syntheses have been reported mainly using graphene paper, carbon cloth or carbon fibre as support. [47,48,49]

In 2013 Laursen et al [33] published the electrodeposition of a MoS_x catalyst on a highly porous network of carbon fibres, increasing the electrochemically active

surface area and therefore enhancing the catalyst's activity. The fibre structure also enabled a better release of the hydrogen during its reduction, resulting in a longer-lasting material. This electrodeposit exhibits an overpotential of 150 mV at the current density of 10 mA cm^{-2}. The synthesis was also performed on a FTO surface obtaining an overpotential of 210 mV for 5 mA cm^{-2}. Graphene and reduced graphene oxide (rGO) were also used to create a composite with 5-20 nm nanoplatelet of MoS_2 exhibiting photocatalytic and electrocatalytic activities. The nanoplatelet structure of MoS_2 was generated with a large percentage of edge sites and therefore with a high number of active sites to increase the MoS_2/rGO interface, leading to a major charge transfer promotion. The obtained particulate was tested on a FTO substrate obtaining an overpotential of 250 mV for 10 mA cm^{-2} in a 1M NaOH basic solution.

The use of porous substrates has the advantage of combining the support function of enhancing the surface area with the possibility of benefitting from a conductive framework. Jaramillo et al engineered MoS_2 by using mesoporous silica as a growing surface for the films by electrodepositing Mo onto silica with further sulphidization.[35] The high surface curvature and large surface area enhanced the exposure of the edges, leading to an overpotential of 230 mV with a Tafel slope of 50 mV dec^{-1}.

Another strategy to increase the defects in the structure is to synthesise a compound in its amorphous form. This has the advantage of preparing a highly efficient compound under mild temperatures. Hu et al decided to undertake this route by electrodepositing amorphous MoS_x films on different conductive substrates (e.g. glassy carbon, ITO and FTO). [37] The resulting electrocatalysts were performing in a wide range of pH with an overpotential value of 200 mV for a solution of 1M H_2SO_4 and a Tafel slope of 40 mV dec^{-1}, reflecting the Heyrovsky mechanism. The same group analysed the mechanism of the reaction by XPS analysis and identified MoS_{2+x} as the active phases of all the films.[36] However, the condition in which the electrodeposition was carried out was not suitable for many substrates. Therefore Vrubel et al investigated deposition methods applicable to a wider range of substrates.[38] The prepared amorphous MoS_3 particles were deposited on a glassy carbon or a FTO electrode by drop-casting using a MoS_3 solution containing multiwalled carbon nanotubes (MWCNT) to increase the electron transfer. The best performing substrate was glassy carbon with a catalyst

loading of 32 μg cm^{-2} obtaining an overpotential of 220 mV in acidic media. The Tafel slope value increased with the catalyst loading from 41 to 63 mV because of the lower efficiency in electron and proton transfer, while the value obtained for lower loading agrees with the ones previously detected for MoS_x films[37], indicating a HER occurring with a Heyrovsky mechanism.

An alternative way to improve HER performance is to design a molecule that mimics the MoS_2 edge. DTF calculation found a Gibbs free energy near to zero on the terminal bridge di sulphide ligand, suggesting that molecules on high exposure of those such as dimers would result in a significant increase of catalytic activity.[39] $[Mo_2S_{12}]^{2-}$ was designed and prepared in the form of $(NH_4)_2[Mo_2(S_2)_6]2H_2O$ following different modified Muller methods.[50] The material was finally deposited on a FTO substrate by drop casting and tested in a 0.5M H_2SO_4 solution obtaining an overpotential of 160 mV with a Tafel slope of 39 mV dec^{-1}.

3.2 Experimental methods

3.2.1 Hydrothermal synthesis of $Co_2Mo_9S_{26}$

Reagents: $(NH_4)_6(Mo_7O_{24})\cdot4H_2O$ (Sigma Aldrich, 99%); $SC(NH_2)_2$ (Alfa Aesar, 99 %); $CoSO_4\cdot7H_2O$ (Sigma Aldrich, 99%); F-doped SnO_2 deposited on soda-lime glass (Hartford Glass Co,.7Ω per sheet)

The synthesis of products with a nominal $Co_2Mo_9S_{26}$ composition was performed by using *hydrothermal synthesis,* which is an environmentally friendly technique that allows the experimenter to perform reactions in water at a higher temperature than its boiling point (100 ^{o}C). The dissolved reagents were mixed in a stoichiometric ratio of 1:6:15 and poured into a 20 mL Teflon-liner bomb. The substrate was then placed at 45° to the base of the reaction chamber (Figure 3.2). The bomb was finally sealed and heated in an oven to the desired temperature.

Figure 3-2 The Teflon liner with a substrate (right) and the liner with the stock solution

The synthesis of the material was carried out by monitoring different parameters and then choosing the range, which gave the best HER performance. The reagents selected were polyoxometalate (POM) with the formula; $(NH_4)_3(CoMo_6O_{24}H_6)\cdot7H_2O$ as the first option and the two salts $(NH_4)_6Mo_7O_{24}4H_2O$ and $CoSO_4\cdot7H_2O$ as the second option. Both the synthetic strategies had $SC(NH_2)_2$ as the sulphur source. After this preliminary selection, the reagent's concentration in the deposition solution was decreased. This led to thinner films with higher light transmission.

300 nm-thick films of $Co_2Mo_9S_{26}$ were prepared by making 15 ml of a stock solution by mixing 28 mL of 0.05 M $(NH_4)_6Mo_7O_{24}$ $4H_2O$, 70mL of 0.05 M of $SC(NH_2)_2$ and 4.66mL of 50 mM $CoSO_4\cdot7H_2O$ in distilled water. The concentrations of the reacting elements were 2.3 mM Co, 13.6 mM Mo and 34.1 mM S, in order to obtain a Co :Mo :S ratio of 1:6:15. The Teflon liner with the stock solution was then sealed inside a stainless steel reaction vessel and heated at a rate of 1° / min to 180°C in a convection oven. After 72 hours reaction time, the vessel was cooled at a rate of 10°/min to ambient temperature. After the reaction, the vessel exhibited a black translucent film covering the substrates' conductive side in a colourless solution with a pH of around 8. The obtained film was washed with distilled water and then dried in a desiccator over silica gels (freshly regenerated at 100°C) overnight.

The attempt to anneal the material at 300°C in Ar did not lead to any improvement in the electrochemical performance making the addition of this further step unnecessary.

The *150nm-thick films* were made by following the strategy described above but changing the reagent concentrations to 4.66 mL of $CoSO_4*7H_2O$ 0.02M, 28 mL of $(NH_4)_6Mo_7O_{24}*4H_2O$ 0.03M and 7-mL of $SC(NH_2)_2$ 0.02M. The ratio between the target elements was left at 1:6:15.

The substrates tested for the synthesis were iodium tin oxide (ITO) and fluorine doped tin oxide (FTO) due to their intrinsic transparency, which would be advantageous in possible solar-to-fuel device applications. The substrates were cleaned by sonication in a KOH/iso-propanol solution for 10 minutes followed by rinsing with a 1M solution of HCl and water.

Once the substrate and the precursors were selected, a temperature study was carried out by heating the bomb at a rate of 1°C min^{-1} up to a temperature of 180°C or 230°C. The temperature was kept for 72 hours before cooling down to room temperature at a rate of 10 °C min^{-1}. After the reaction, the substrate was washed with water to remove loosely-held material. The grey-black film obtained was deposited on the substrate only on the conductive side for both substrates.

3.2.2 Electrochemical characterization:

All the electrochemical measurements were carried out by CH instrument potentiostats. The experiment was performed in a single electrolysis cell within a 25ml beaker filled with 15ml of 0.5M H_2SO_4 solution. The analysed sample, acting as a working electrode and cathode, respectively, was immersed in 0.5 M H_2SO_4 solution with the $Co_2Mo_9S_{26}$ film facing the Ag/AgCl (NaCl, 3 M) reference electrode. The sample was immersed in the solution for 1 cm^2 of its surface in order to keep the active area constant during the measurements. A piece of carbon mesh (purchased by Alfa Aesar, 2.5 ×1 cm^2) was used as an auxiliary electrode (which acted as an anode). All the electrodes were fixed at a constant distance using Parafilm. All the potentials were reported according to the NHE reference scale through the converting equation E (NHE) = E(Ag/AgCl) + 0.209 V. Moreover, the potentials applied were corrected manually for ohmic resistance.[51]

The HER activity was measured through *linear sweep voltammetry* (LSV) on a three-electrode configuration with a scan rate of 2 mV s^{-1}. The bulk electrolysis

was carried out with the same experimental setup at a constant current of 0.71 mA.

The Tafel slopes measurement were obtained by using LSV (as described above) or by *multi-potential steps* programmes where stated. For the slopes collected by *multi-potential steps voltammetry* technique, the range of potentials tested for the measurements was between –0.2 to –0.83 V and each potential was held for 5 minute in order to be stable before being recorded. During the measurement the solution was kept homogeneous by stirring at a constant rate of 250 rpm (rotations per minute). Finally, all the potentials recorded were corrected for the resistive losses.

Figure 3-3 The experimental setup with the working electrode (WE), the reference electrode (RE) and the auxiliary electrode (AE) labelled.

3.2.3 Gas chromatography

Gas chromatography was carried out with the use of an airtight cell on an Agilent Technologies 7890A GC system. During the bulk electrolysis, 50 μL of the gas on the headspace was collected periodically and injected in regular intervals into the GC column. The GC column was a 30-metre long 0.320 mm wide-bore HP-molesieve column (Agilent) kept at a temperature of 27°C and Ar as carrier gas. The machine was calibrated for H_2 by using a standard hydrogen mixed with argon at different percentages purchased from CK Gas product limited (UK).

3.2.4 Raman spectroscopy

Raman spectroscopy was performed with a Horiba Jobin-Yvon LabRam Raman HR800. The sample on an FTO substrate was placed on a glass slide and loaded horizontally into the sample space. The focus on the surface of the sample was performed using controls with the help of a microscope with 10× and 50× magnification. Before the measurement the instrument was calibrated using Si as a standard.

The sample was initially focussed using an optical microscope to identify the area of interest. The laser was then turned on and the spectra were recorded using the standard parameters as shown in Table 3.2

Table 3. 1 Typical instrument parameters for collecting Raman spectra. The analysis of the Raman spectra was carried out by comparing the vibrational modes of Co2Mo9S26 with the ones found for MoS_2.

Laser	Filter	Hole	Grating	Objectives	Acquisition Range
532 nm	10%	200µm	600nm	10× / 50×	$100 - 1000$ cm^{-1}

3.2.5 Powder X-ray diffraction (PXRD)

The powder X-ray diffraction measurements were obtained using Panalytical XPert-pro diffractometer ($Cu_{K\alpha}$ radiation corresponding to λ= 1.54178 Å wavelength). A typical XRD experiment was performed at room temperature in a Bragg-Bretano reflection geometry with a 0.033^0 / step in a 2ϴ range from 10 to 60^0 for 20 minutes. Using the *so-called bracket holder* the substrate was inserted directly into the sample stage with the film facing the detector as shown in Figure 2.6. The diffraction patterns obtained were analysed in reference to the ICSD database by comparing the reference peaks of the pure phases with those observed from the sample.

3.2.6 Scanning Electron Microscopy (SEM)

A Philips XL30 ESEM with an attached Oxford Instruments x-act EDX detector was used for scanning electron microscopy in conjunction with Energy-dispersive X-ray

(EDX) spectroscopy. The samples were mounted onto the carbon covered SEM holders. Before the measurements the surfaces of the selected samples were covered with a thin layer of gold using metal sputtering to improve the conductivity of the sample and thus to avoid charging of the surface and achieve an improved image quality. SEM pictures as well as EDX analysis was performed with a beam current of 20 kV. The SEM images were collected using magnifications of: 20×, 100×, 800× and 4000×. The EDX spectroscopy was then carried out on selected areas in order to obtain the elemental composition of the samples. Before performing the measurements, the apparatus was calibrated by the use of a Cu foil as a standard.

For the EDX spectra typically 2-minute scans were performed at two or three different points on each sample. However, due to the strong overlap of Mo and S peaks, the results of the EDX analysis were only semi-qualitative. The elemental mapping was also performed over a wide area within each sample in order to detect the distribution of Co atoms on the surface.

3.2.7 Atomic absorption spectroscopy (AAS)

Atomic absorption spectroscopy was carried out by using a Perkin Elmer Analyst 400 instrument. The powder scratched from the substrate was weighed and added to 5 mL of aqua regia and boiled at 120 °C for 30 minutes. After cooling, the solution was transferred to a 25 mL volume flask and diluted with water to bring the concentration to the AAS linear range. A blank sample was prepared by the same procedure with 5 mL of aqua regia. The standards were prepared with a concentration range of 0-5 mg L^{-1} for cobalt and 0-50 mg L^{-1} for molybdenum. The flame used to measure molybdenum was oxide/acetylene at 313.3 nm and acetylene at 240.7 nm for cobalt.

3.2.8 UV/Vis

The transmittance measurements were carried out using a Shimadzu UV-2101PC scanning spectrophotometer. The measurement was performed by comparing the transmittance obtained from the bare FTO substrate used as a reference and the

ones obtained from films with different thickness. The measurement was detected in the range between 350-850 nm.

3.2.9 X-ray photoelectron analysis (XPS)

X-ray photoelectron spectra were collected by the National EPSRC XPS Users' service at the University of Newcastle on a K-alpha instrument (Thermo Scientific, East Grinstead, UK), with a 1486.6 eV monochromatic AlKa source and probing the sample with a spot size of 400 X 800 microns. The emission angle was zero and the sample was probed with 200eV energy for a survey and 40 eV for high resolution. The spectra were analysed by using the free-software CasaXPS and referenced to the adventitious C 1S peak (285.0 eV).

3.2.10 Atomic Force Microscopy (AFM)

A Bruker Dimension Icon AFM was used to generate the 3D nanostructured images. The films deposited on the FTO substrate were scanned over an area of 20 μm × 6.7 μm. The step edge measured was generated by performing an electrolysis of the film in acid media until the complete exfoliation of the catalyst substrate. The relative height was then measured in three areas and the data reported as an average with an uncertainty of ±50nm. For the 300 nm film, the measurement taken with a step of 4μm gave a height value of 270 nm with an average roughness of 26 nm, which proved to be very close to the FTO ones (20 nm Ra [52]). To minimise the error, the tip was substituted after each AFM measurement.

3.3 Results and discussion

3.3.1 Hydrothermal synthesis parameters

The FTO substrate was chosen based on its conductivity and transparency. Initial tests were carried out at different temperatures and reaction times on blank substrate with the conductivity checked with a voltmeter after the reaction. FTO showed low conductivity after being hydrothermally heated without the reagents within the temperature range between 160 – 220 °C. The reason of the conductivity loss without the film protection was not pursued but we assumed it might be due to the leeching of F from SnO_2. An attempt to prepare MoS_2 from

ammonium heptamolydbate and thiourea did not produce films sufficiently stable for an electrolysis test. However, after mechanically removing the film the underlying substrate showed conductivity similar to pristine substrate. The formation of the sulphide coating thus plays an important role for stability of FTO layer. Attempts to dope Co into the system led to more stable films. Consequently, it was concluded that a successful film formation was dependent on the presence of both cobalt and molybdenum sources inside the reaction chamber.

After the preliminary study, FTO was selected as substrate and the $CoSO_4 \cdot 7H_2O$ used as a relevant metal precursor for doping process due to improved stability of films containing Co during the HER performances. The optimal temperature was selected at 180 °C with the reaction time set to 72 hours before cooling down at a rate of 10 °C min^{-1} to the room temperature. These reaction conditions were adopted from the previous work carried out in Ganin's group by a project student who worked on preparation of powder samples (no substrate) of sulphides.

Atomic absorption spectroscopy (AAS) revealed a relative weight percentage of Mo and Co of 47.4 wt. % and 6.5 wt. %, respectively, indicating a Co: Mo ratio of 1:4. This percentages were lower than the ones in the deposition solution. Assuming from the CHN analysis an insignificant amount of carbon, hydrogen and nitrogen, it was possible to assign the formula of $Co_2Mo_9S_{26}$ to the material. Two types of coatings were made with 300 nm and 150 nm thickness (as determined by AFM spectroscopy). The 150 nm film showed relatively good optical characteristics as evident from the Figure 3.4.

Figure 3-4 The 150 nm-thick film of $Co_2Mo_9S_{26}$ on a FTO substrate.

3.3.2 Raman Spectroscopy

Since the Co–doped structure is similar to that of MoS_2, we can analyse our film by probing the vibrational Raman active modes that lie on similar wavelengths as the one calculated for MoS_2. In particular, the out-of-plane and in-plane modes A_{1g} and E^1_{2g} (Figure 3.5) are located at 407 cm^{-1} and 374 cm^{-1}, respectively.
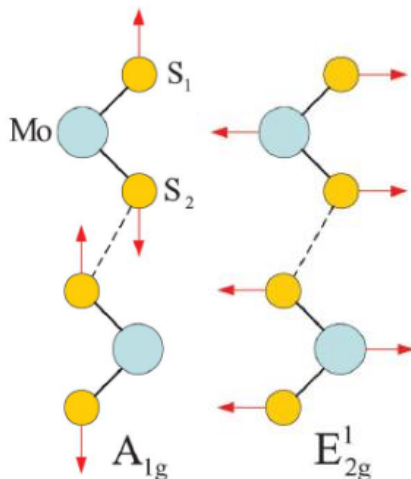
Figure 3-5 Raman-active vibrational modes in MoS_2.[53]

To analyse objectively our sample, we decided to set standard parameters for all our measurements (see Table 3.2). As can be seen from Figure 3.6, the two dominant peaks of the Raman spectra are at E^1_{2g}= 374 cm^{-1} and A_{1g}= 403 cm^{-1}, corresponding to the vibrational modes relative to MoS_2 in bulk form previously reported in the literature.[54,55] The presence of only these two peaks on the spectra shows the monophasic nature of our compound and therefore the absence of other impurities such as CoS_x and MoO_x. The shift observed between the two peaks is equal to Δk=29 cm^{-1} and agrees with that reported in the literature for the multi-layered products.[56]
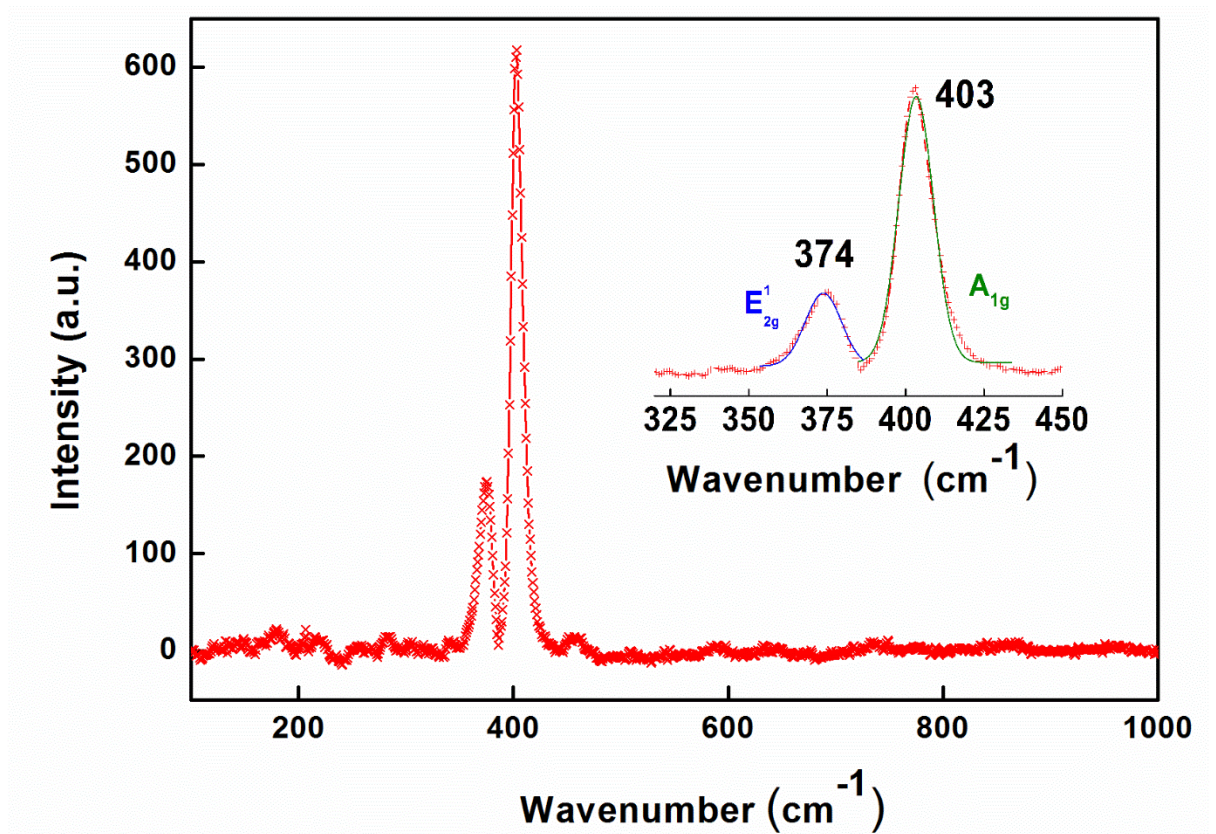
Figure 3-6 Raman spectra of a 300nm - thick film deposited on the FTO surface showing the peaks associated to the Co$_2$Mo$_9$S$_{29}$ phase. In the insert, a magnified region showing the peak associated with the Raman active modes in plane E_{2g}^1 and out of plane A_{1g} fitted with a Gaussian function is depicted.

3.3.3 X-ray photoelectron spectroscopy

The XPS measurements highlight a homogenous presence of Mo, Co and S on the entire FTO surface. The material was probed on the molybdenum 3d region to identify the Mo valence state (Figure 3.7). On the spectrum the presence of two main peaks related to Mo (IV) was found, corresponding to 87% of the total molybdenum. Moreover, other minor peaks associated with molybdenum in the oxidation state of Mo(V) and Mo(VI) were identified with a percentage of circa 6.5, each associated to MoO$_2$OH and MoO$_3$, respectively.[36,57]
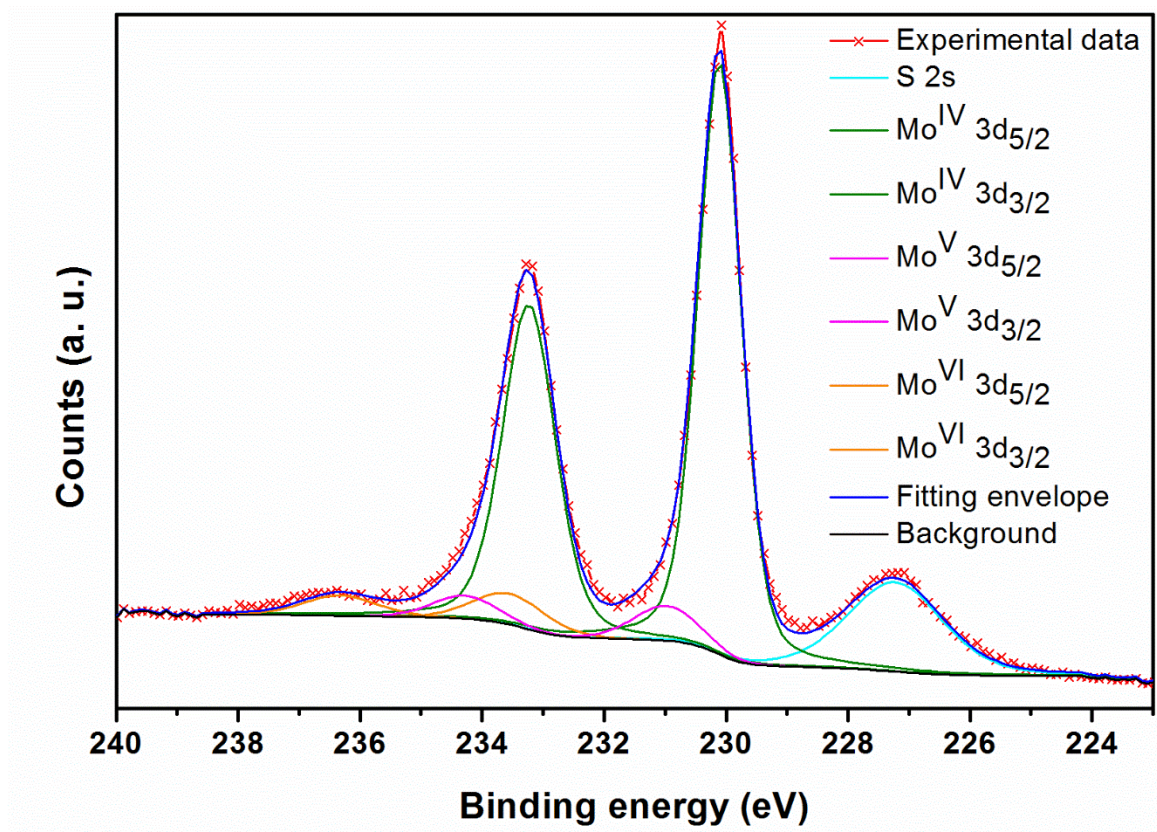
Figure 3-7 XPS spectrum of the 3d Mo and 2S region for a 600 nm-thick film. The data were fitted by a Gaussian-Lorentzian profile function and are associated with molybdenum in different oxidation state: Mo(IV) at 87%, Mo(V) at 6.5% and Mo(VI) at 6.5%.

The presence of cobalt was detected in the 2p region of the high-resolution spectrum (Figure 3.8). The spectrum shows the presence of two doublets with a mixed valence of cobalt: Co(II) at 57% and Co(III) at 43%. This might be due to the presence of the cobalt in an oxide form. The peaks associated to S on the $2p_{3/2}$ region (see Figure 3.9) were fitted in a single doublet associated with a binding energy of 162.2 and 163.4 eV according to the oxidation state of sulphur S^{2-}.
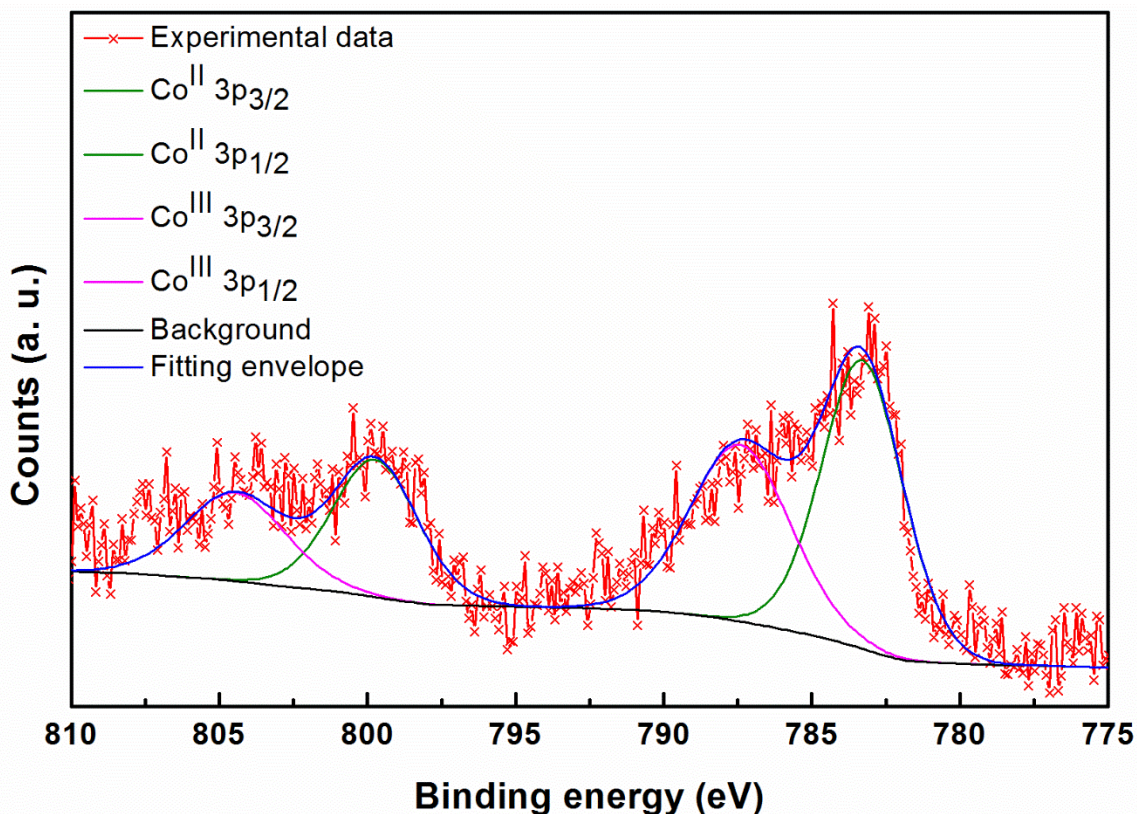
Figure 3-8 XPS spectrum on the 3p region of Co for a 600 nm-thick film. The peaks were fitted with a combination of Gaussian-Lorentzian profile showing the presence of cobalt in different oxidation states: Co(II) at 57% and Co(III) at 43%.
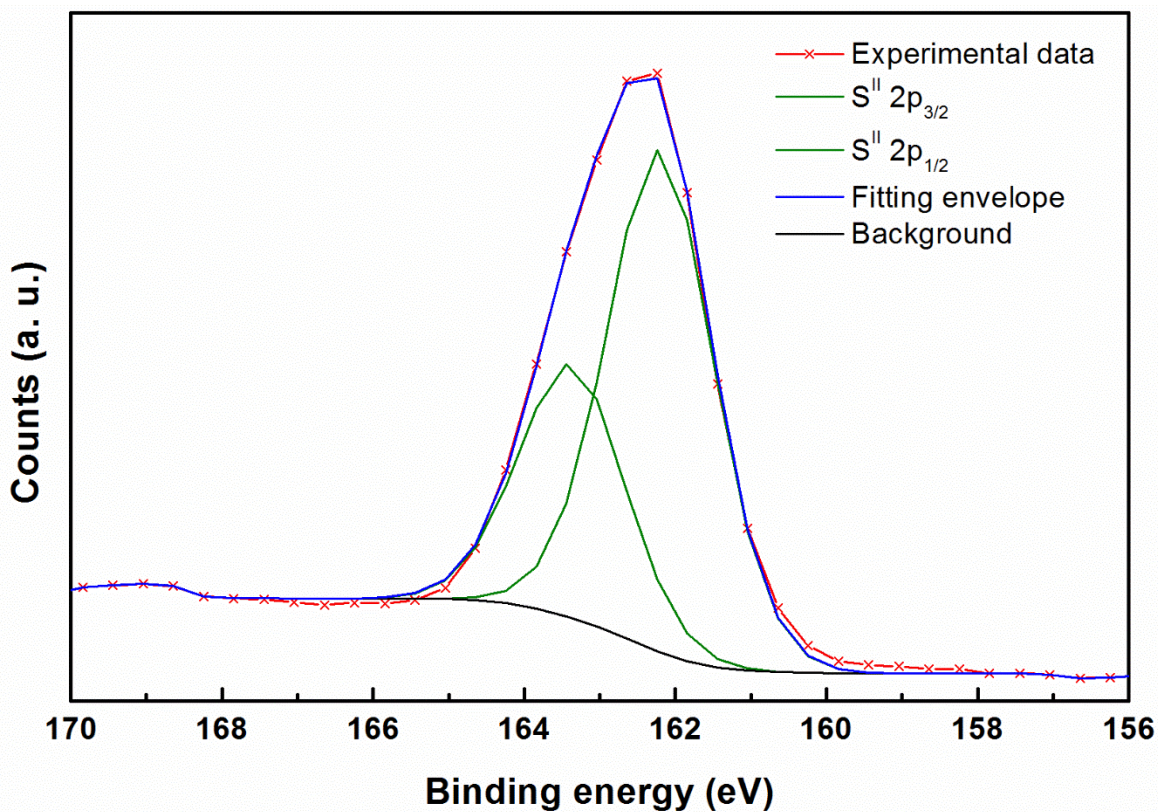
Figure 3-9 XPS spectrum for a 300 nm-thick film in the S 2p region. The peaks are fitted with a single doublet by a Gaussian-Lorentzian profile in agreement with the S^{2-} oxidation state.

3.3.4 Atomic Force Microscopy (AFM)

The different thickness of the films obtained by scaling the reagents concentration, were characterized by AFM measurements. By comparing those with the transmittance measurements of the UV-VIS paragraphs 3.3.5 below, the thickest substrates showed to be on the order of 300±50 nm while the ones showing translucent properties was on the order of 150±50 nm.
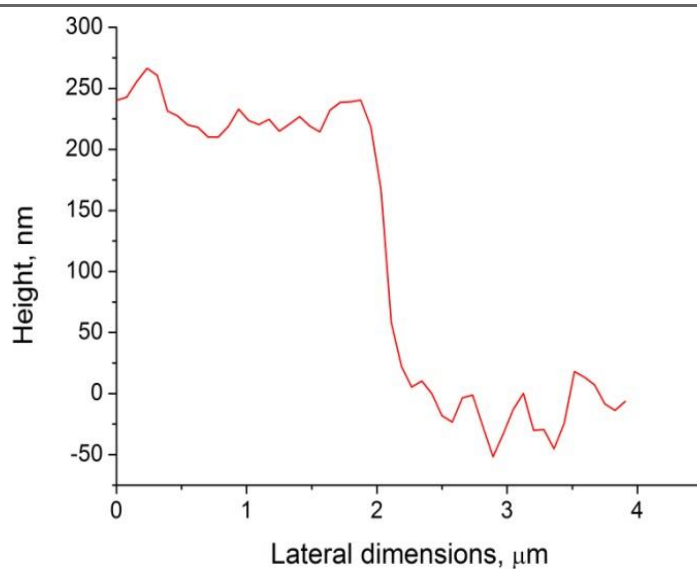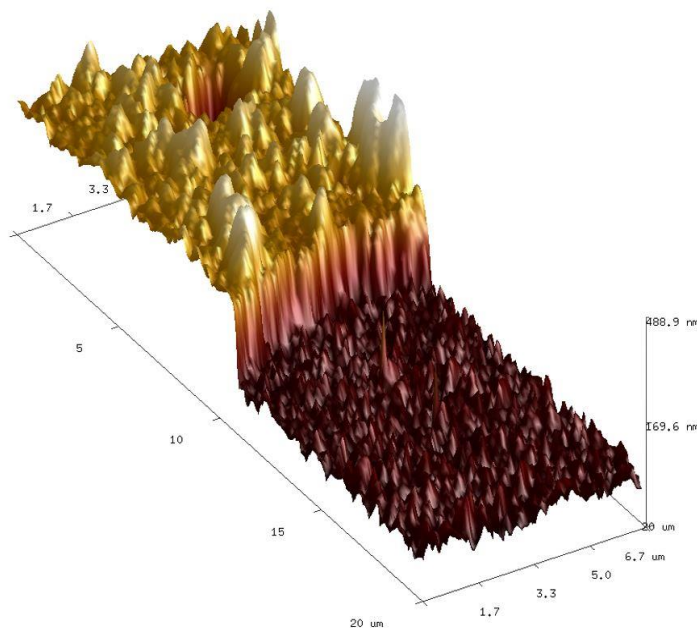
Figure 3-10 Top 3D topographical profile of 300 nm thick film. Bottom line scan highlighting the height difference measured indicating the film thickness.

3.3.5 UV spectra

The UV-VIS spectra of samples were recorded in order to compare the light transmission of films with a thickness of 150 nm or 300 nm on FTO and a bare FTO substrate. The 150 nm thin films are translucent, making them useful as catalysts in solar-hydrogen devices because of their capability to transmit light through the electro catalyst onto the light-harvesting material underneath.
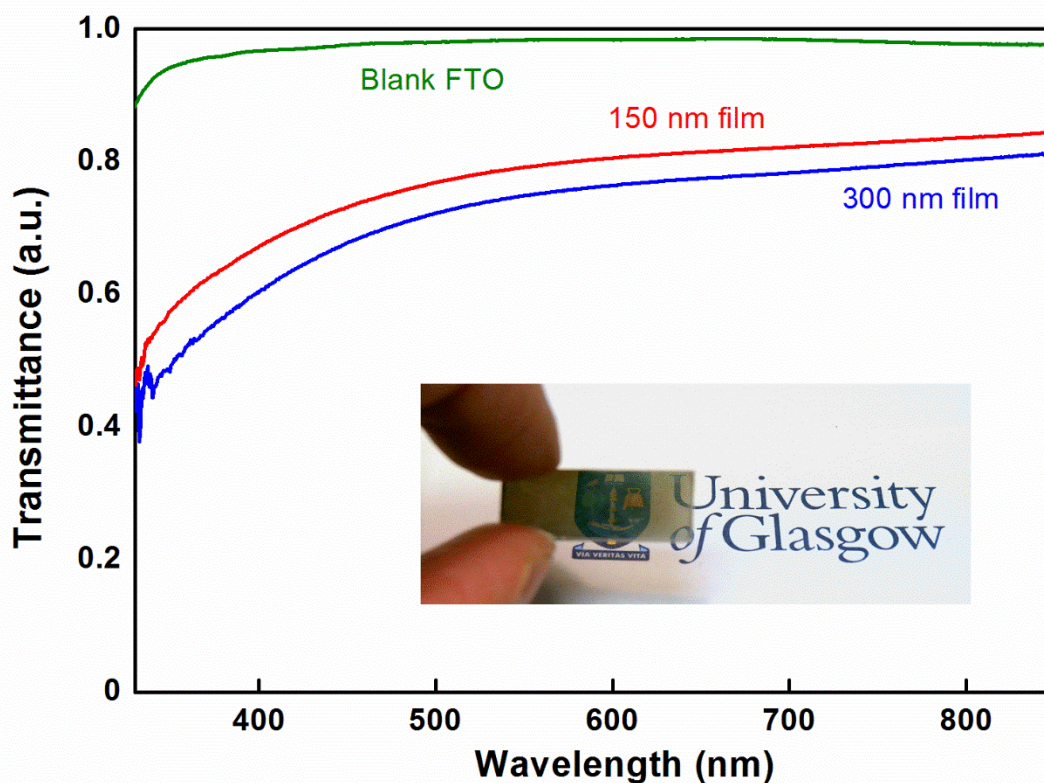
Figure 3-11 Comparison between the UV-vis transmission spectra with 300 nm-thick Co$_2$Mo$_9$S$_{26}$ on FTO, 150 nm-thick Co$_2$Mo$_9$S$_{26}$ on FTO and the uncovered FTO. In the insert a picture of the sample after synthesis is shown.

3.3.6 XRD

The diffraction pattern of the material shows the polycrystalline nature of the film (see Figure 3.12).
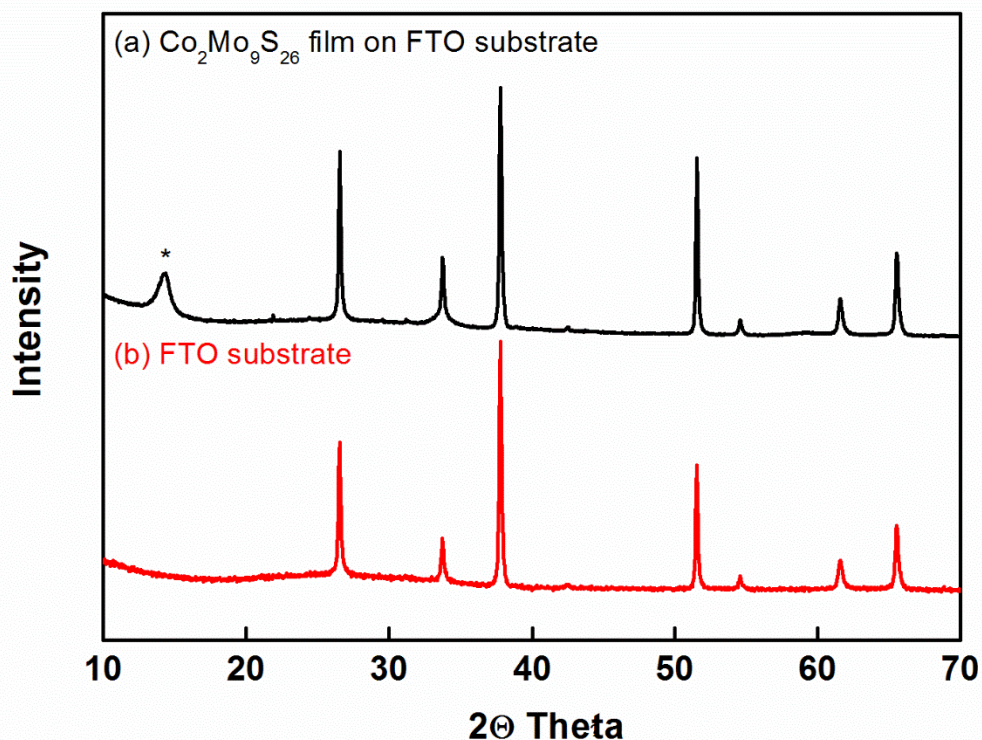
Figure 3-12 (a) XRD pattern of Co$_2$Mo$_9$S$_{26}$ film on FTO substrate; the peak highlighted with a star is associated to the MoS$_2$ structure type in the hexagonal form. (b) XRD diffraction pattern of the FTO bare substrate.

By comparing the XRD structures of Co$_2$Mo$_9$S$_{26}$ on the FTO surface (Figure 3.12 a) and the bare FTO (Figure 3.12 b), we can see that the majority of the sharp peaks on the diffraction profile (a) are related to the FTO surface underneath the film. This means that the covered material protects the FTO surface from degradation during the hydrothermal synthesis. The only peak related to the product is the broad reflection peak (0002) located at the low diffraction angle of c = 12.36 Å. It corresponds with the peak expected for the MoS$_2$ phase with a hexagonal structure. The absence of cobalt sulphide reflections suggests that Cobalt and Molybdenum are incorporated onto the film structure and so they do not contribute to the XRD spectra by adding an additional phase.

3.3.7   Scanning Electron Microscopy (SEM)

The morphology of the material was assessed by using a scanning electron microscopy telescope. The films resulted in a homogenous distribution of Co, Mo and S as determined by the elementary mapping. The structure of the film is composed of "sea-urchin-type" blocks, which are likely to represent some

misalignment between the chalcogenide layers. This misalignment between the layers along the c-axis of the hexagonal structure might cause the broadening of the peak corresponding to the MoS_2 hexagonal structure phase on the PXRD pattern. From a catalytic point of view, the lack of order in the structure is beneficial because the misfit between the layers generates an increased number of catalytic sites. [58,59,11,60, 61,62,]
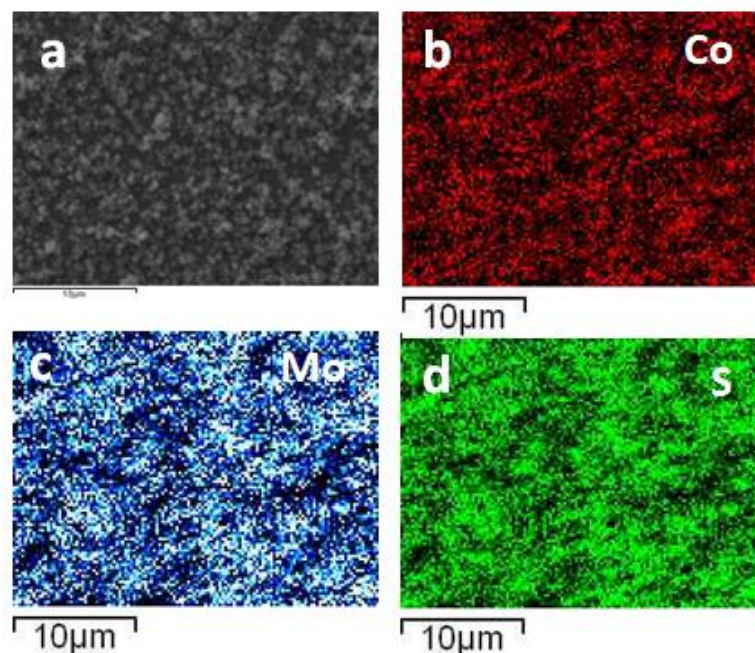
Figure 3-13 (a) SEM image of the sample showing the morphology at magnification 4000× (b, c and d) Elemental mapping of Co, Mo and S in the $Co_2Mo_9S_{26}$ product indicating the distribution of the elements homogeneous for all samples.

EDX elemental analysis yielded a ratio between Co and Mo of 1:5, which is close to the stoichiometry of the target material $Co_2Mo_9S_{26}$. However, it should be noted that the EDX analysis only has an indicative value in this case because of an overlap between the Mo and S peaks.
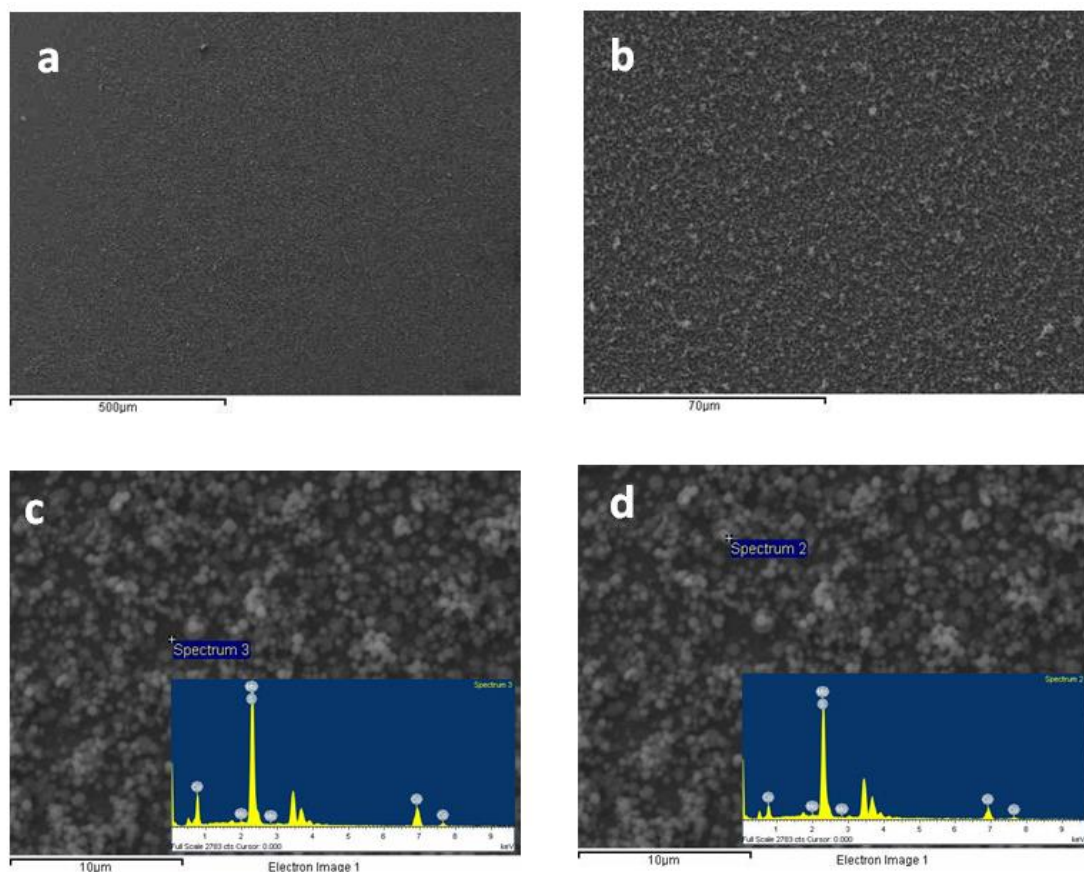
Figure 3-14 a) and b) images of two samples at magnification of 100× and 800×, respectively. c) and d) are images of a sample at a magnification of 4000× with the probe point indicated. The corresponding EDX spectra with Co, S and Mo peaks marked are shown as inserts. The unlabelled peaks between 3-4keV originate from Sn.

3.3.8 The electrochemical hydrogen evolution reaction (HER)

The 300 nm Co-doped molybdenum sulphide material was tested as a cathode for the hydrogen evolution reaction in 0.5 M H_2SO_4. The cyclic voltammetry scan was collected by linear sweep voltammetry technique with a scan speed of 2 mV sec^{-1}.

Figure 3.15 shows the electrochemical performance of bare FTO substrate compared to the ones obtained for the FTO covered with the 300 nm film thick catalyst. The overpotential obtained for the catalyst was 262 ± 8mV for a current density of 10 mA cm^{-2}.
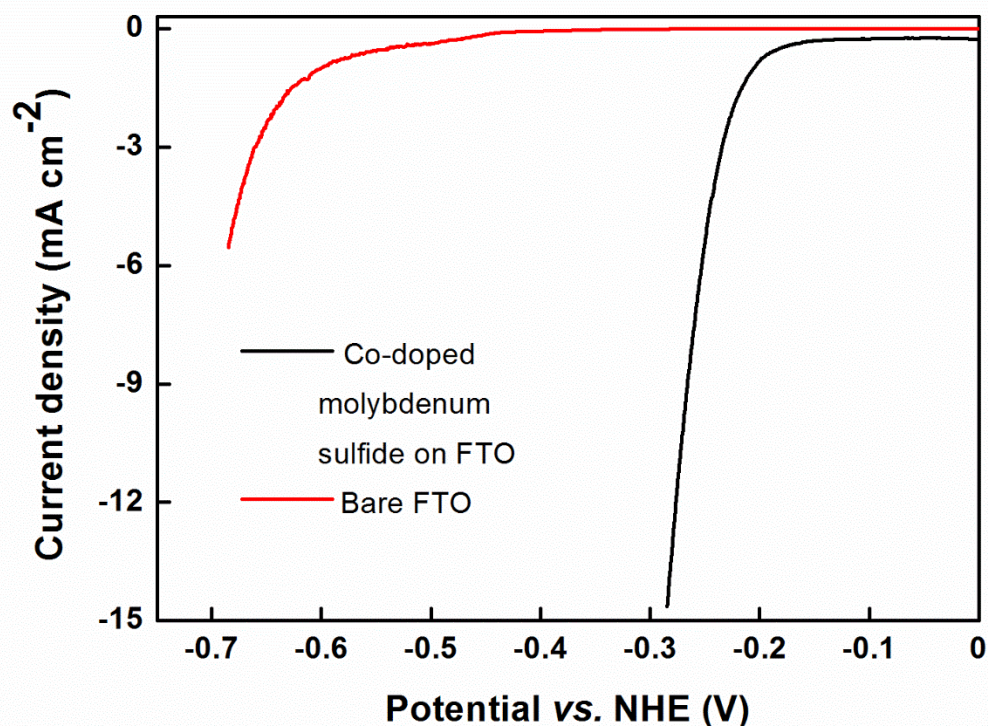
Figure 3-15 Comparison between the current densities of Bare FTO substrate and the ones obtained for 300 nm Co-doped molybdenum sulphide film on FTO. The data were collected in a 0.5 M H_2SO_4 solution by linear sweep voltammetry with a scan speed of 2 mV sec^{-1}.

To further characterize the material, the Tafel slope was determined by measuring the current density after 5 minutes of electrolysis in a potential range from -0.2 to -0.83 V with an addition of 0.03V after each measurement. The value obtained with this measurement was 66 mV dec^{-1}. However, it was not possible to obtain a constant current density for potentials higher than 250 mV due to delamination of the material, which required an alternative way to collect this data (see Figure 3.16). For this reason, the Tafel slope was measured by using linear sweep voltammetry, which by measuring the current density for shorter times was avoiding the delamination issue. The value obtained by LSV was 64 mV dec^{-1}, indicating a good agreement between the two measurements (see Figure 3.17).
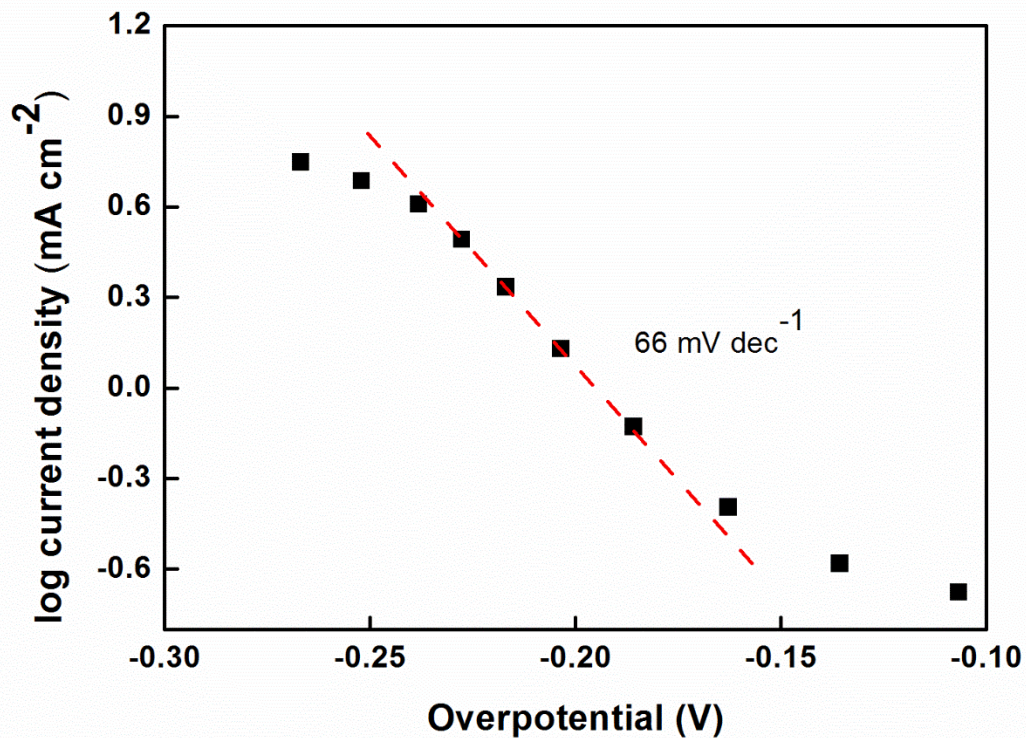
Figure 3-16 The Diagram shows the Tafel slope obtained by the multipotential steps technique for a 300 nm thick film of Co$_2$Mo$_9$S$_{26}$. The black square indicates the different current densities collected after 5 minutes of bulk electrolysis.
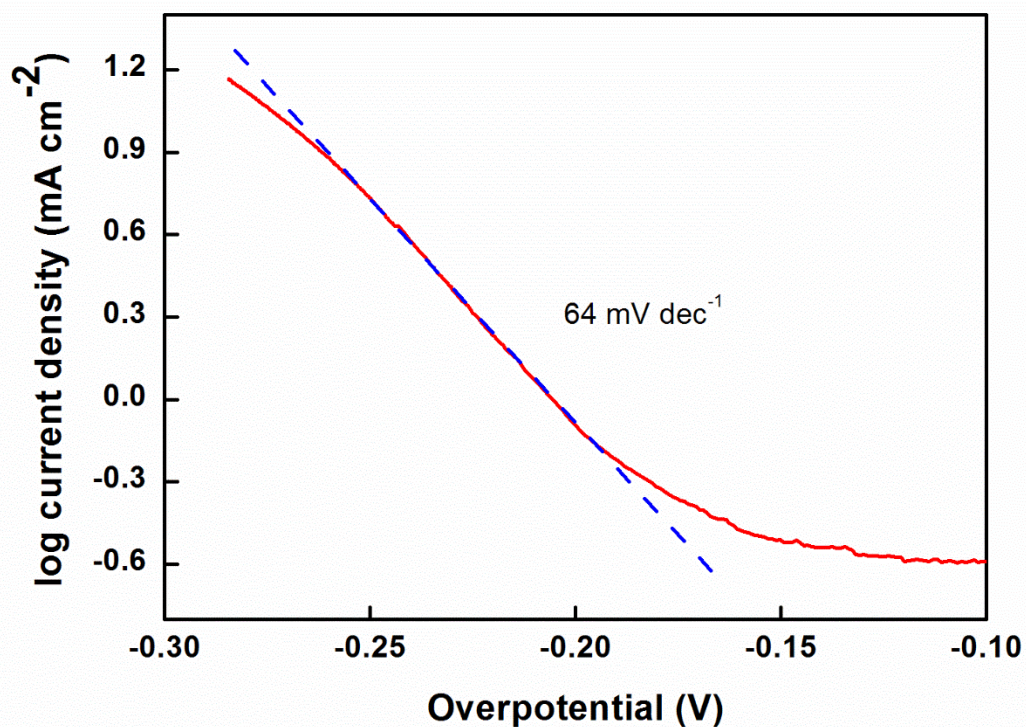
Figure 3-17 The graph shows the Tafel slope collected by linear sweep voltammetry for a 300 nm thick film of Co$_2$Mo$_9$S$_{26}$. Both measurement were collected in a solution of 0.5M H$_2$SO$_4$ with Ag/AgCl as a reference electrode and with carbon cloth as a counter electrodes.

The thinner 150 nm films exhibited a poorer performance, requiring an overpotential of 300 mV to achieve a current density of 10 mA cm^{-2} with a Tafel slope of 85 mV dec^{-1} (Figure. 3.18). The decrease in activity might be explained by the sample morphology, which is permeable to the solvent. The sample with the major catalyst load allowed an increased access of active sites and was therefore more active.
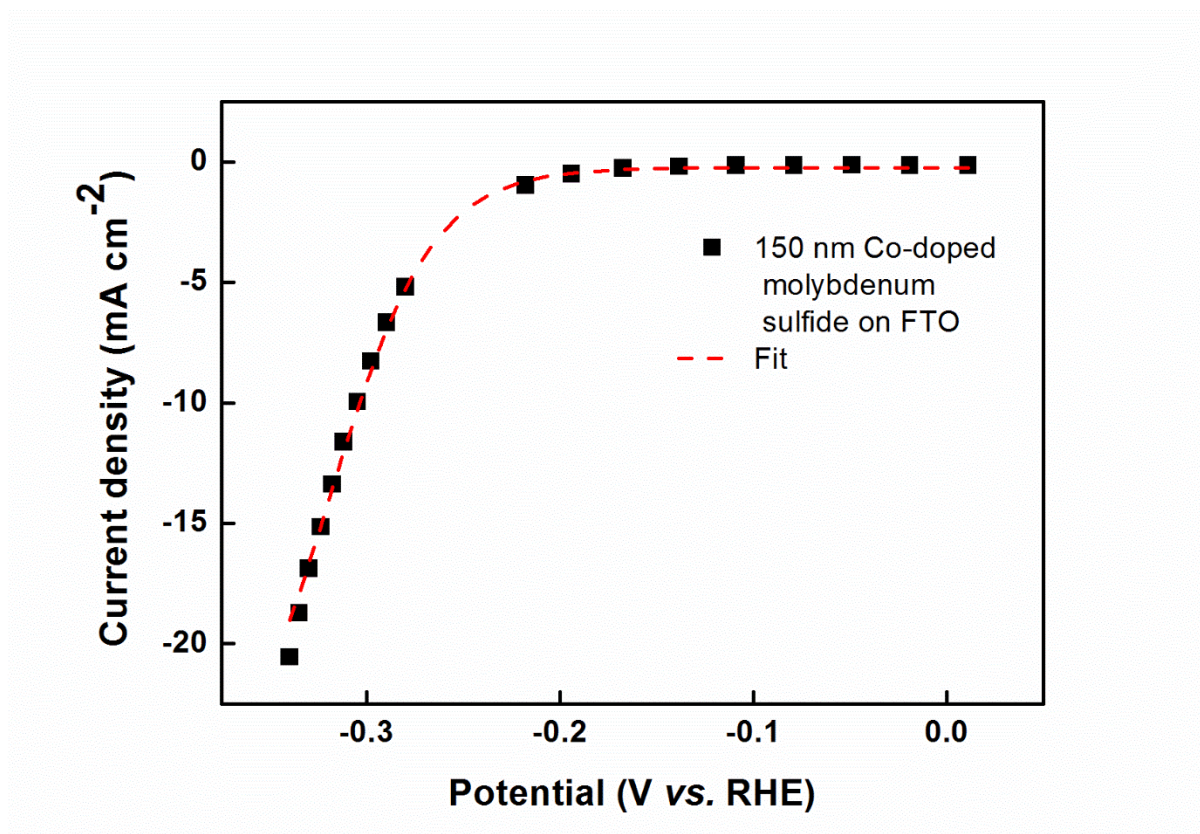
Figure 3-18 Current density of the 150 nm-thick film of Co$_2$Mo$_9$S$_{26}$, the black square indicate the current density for each potential collected after 5 minutes of polarization. The values are collected in an acidic solution of 0.5M H$_2$SO$_2$ using Ar/AgCl as reference electrode and carbon cloth as a counter electrode. A fitted curve is shown in red.
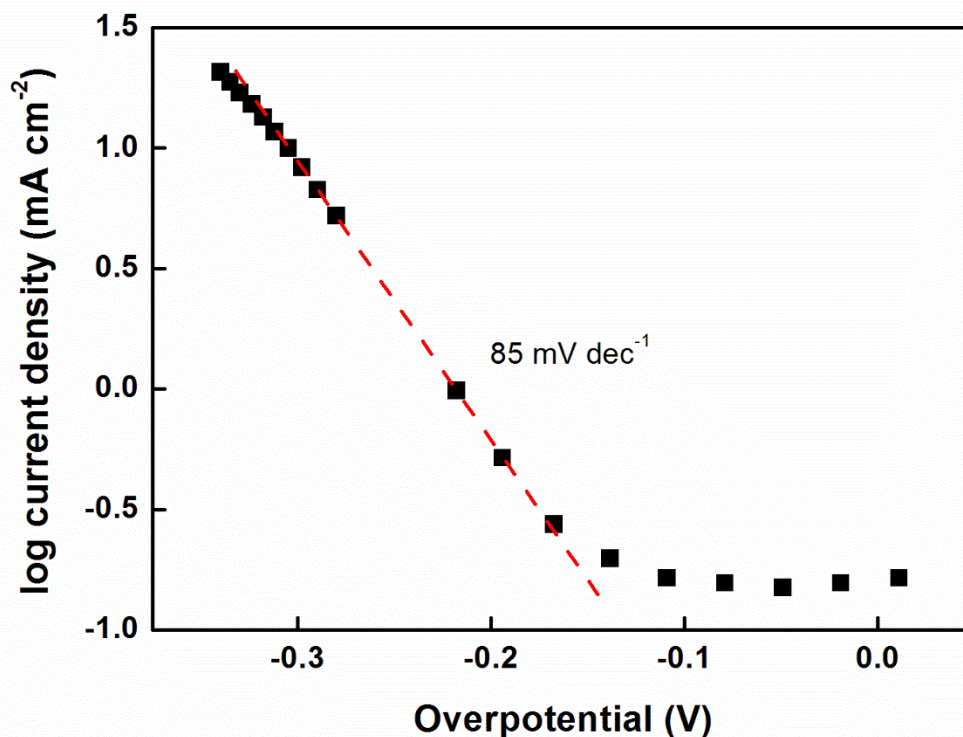
Figure 3-19 Tafel slope obtained for 150 nm-thick film of $Co_2Mo_9S_{26}$ by the multipotential step technique in a 0.5M H_2SO_4 solution. Each potential collected after 5 minutes of electrolysis corresponding to a different potential is indicated by a black square. The data were collected by using Ag/AgCl as a reference and carbon cloth as a counter electrode.

3.3.9 Study of the electrochemical performances at different pH.

The 150 nm films were also tested in a neutral and basic pH range by using a 0.5 M sodium phosphate buffer and 1M NaOH, respectively. Films tested at neutral pH show poorer performances than in acidic media with an overpotential of approximately 210 mV at a current density of 1 mA cm^{-2} compared to approximately 460 mV at 10 mA cm^{-2} (Figure 3.20). These results are similar to the ones obtained for $Co-MoS_3$ on glassy carbon substrates by Hu and co-workers.[63] However, it must be noted that no current density higher than 1 mA cm^{-2} has been reported, while the Tafel slope in the range from -0.5 to -5 mA cm^{-2} resulted to be 220 mV dec^{-1} (Figure 3.21). The films have poor stability at a basic pH, thus not allowing the collection of the data.
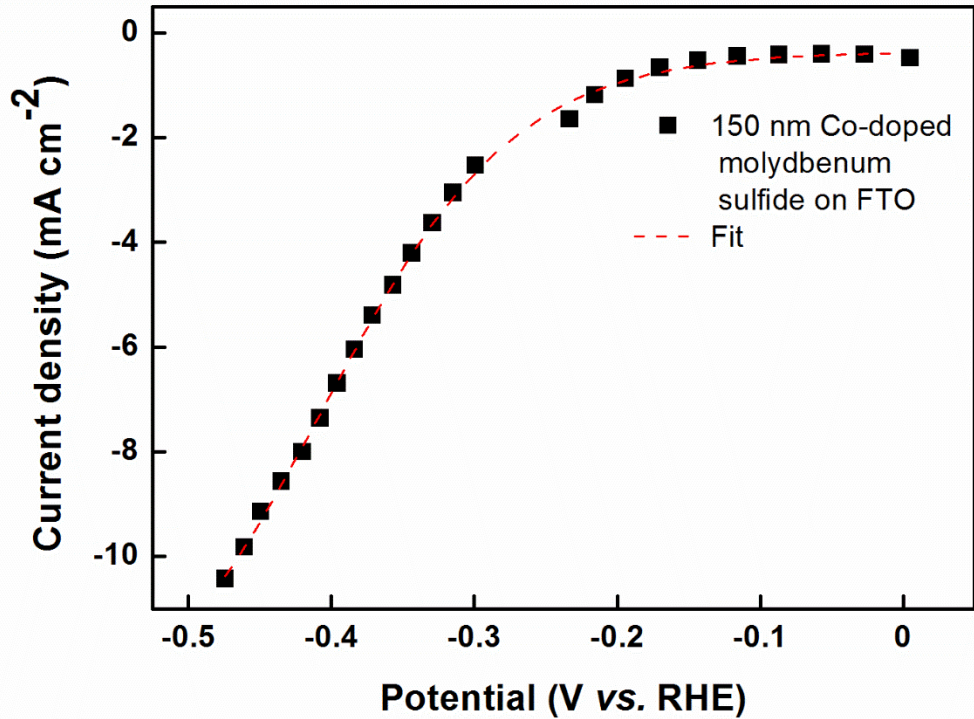
Figure 3-20 The black square shows the steady state current density after 5 minutes at different potentials on a neutral pH for a 150 nm-thick Co$_2$Mo$_9$S$_{26}$ film. The measurements were made by using Ag/AgCl as a reference electrode and carbon cloth as a counter electrode.
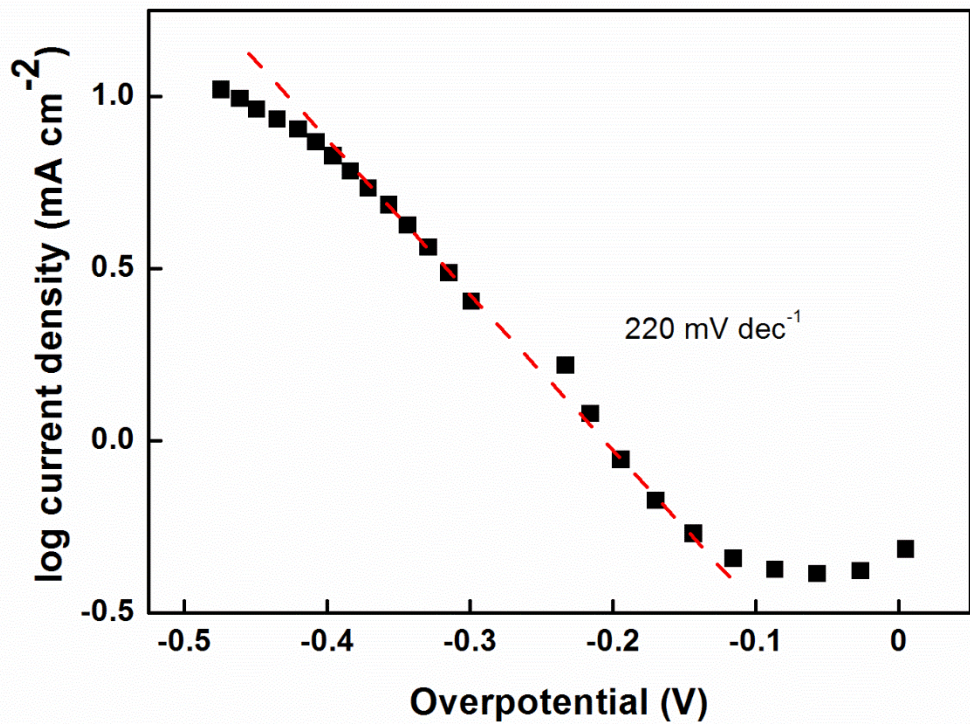
Figure 3-21 Tafel slope calculated in a sodium phosphate buffer for a 150 nm-thick film of Co$_2$Mo$_9$S$_{29}$ on a FTO substrate. The measurement was collected by using a multi potential steps technique with Ag/AgCl as a reference and carbon cloth as a counter electrode.

Table 3.1 summarises the Tafel slopes and the overpotentials at a current density of 10 mA cm^{-2} of the materials synthesised in this thesis compared to similar others previously reported in the literature. At neutral pH, the new material yields lower performances than the Co/Mo sulphide prepared on FTO by electrodeposition by Tran at al.[30] However, the performance of the new material achieves similar values at pH 0. This confirms that hydrothermal conditions are a viable route to the molybdenum Co-doped sulphide derivative on conductive surface as FTO.

Table 3. 2 HER metal chalcogenide properties of molybdenum sulphide derivatives (Tafel slope and the overpotential at the current density of 10 mA cm^{-2}).

Reference	Catalytic material	pH	η at 10 mA cm^{-2} (mV)	Tafel slope mV per decade	Catalyst deposition method
Tran et al. (2013)[30]	CoMoS$_x$	7	250	85	electrodeposition
Tran et al. (2012)[31]	Cu$_2$MoS$_4$	0	135	95	Precipitation of simple salt
Sun et al. (2013) [32]	Cobalt sulphides	7	150	93	electrodeposition
Laursen et al [33]	MoS$_2$ on activated carbon	0	150	-	electrodeposition
Laursen et al [33]	MoS$_2$ on FTO	0	210 (5 mAcm-2)	-	electrodeposition
Meng et al. [34]	MoS$_2$ on rGO	13	250	_	Solvothermal, then dip-coat
Jaramillo et al.(2012)[35]	MoS$_2$	0	230	50	electrodeposition

Vrubel and Hu(2002) [36]	Amorphous MoS$_3$	0	170	-	electrodeposition
Merki et al. (2011)[37]	Amorphous MoS$_2$	0	200 (14 mA cm^{-2})	40	electrodeposition
Vrubel et al.(2012)[38]	MoS$_2$ and MoS$_3$	0	220	41-63	Drop casting
Huang et al (2015).[39]	Mo$_2$S$_{12}$	0	160	39	Various, none Hydrothermal
This Work	Co$_2$Mo$_9$S$_{26}$ on FTO	0	262	64	Hydrothermal synthesis

3.3.10 Stability and gas analysis

Gas chromatography analysis was performed on the 300 nm-thick Co$_2$Mo$_9$S$_{26}$ film to ensure that hydrogen was the dominant reduction product. The experiment was carried out on the headspace of sealed cells by applying an electrolysis for an extended period of time at an overpotential of -0.25 V (Figure 3.23). This analysis indicates that hydrogen is the main reduction product with a yield of 89 ± 6% (Figure 3.22). During electrolysis, the film fell off partially because of bubbles forming during the measurement. Increased film thickness could improve the endurance of the film and therefore lead to longer electrochemical performances.
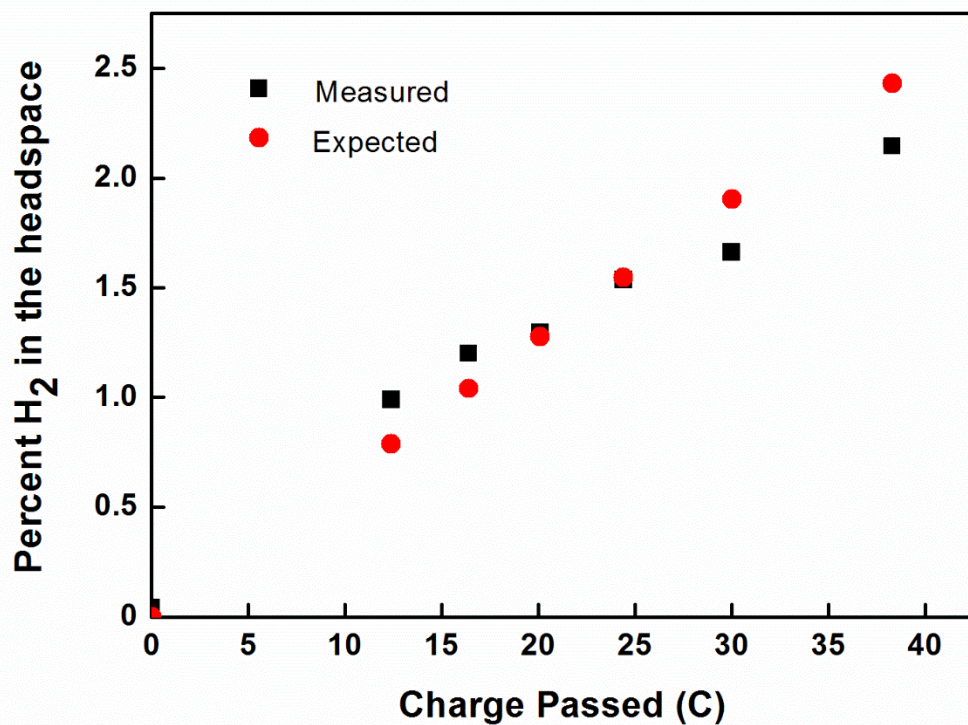
Figure 3-22 Gas chromatography analysis from the headspace of a close cell obtained by electrolysis in acidic media of a 0.5M H_2SO_4 solution. The expected values are indicated by red points, while the measurements obtained by gas chromatography are indicated by black squares.
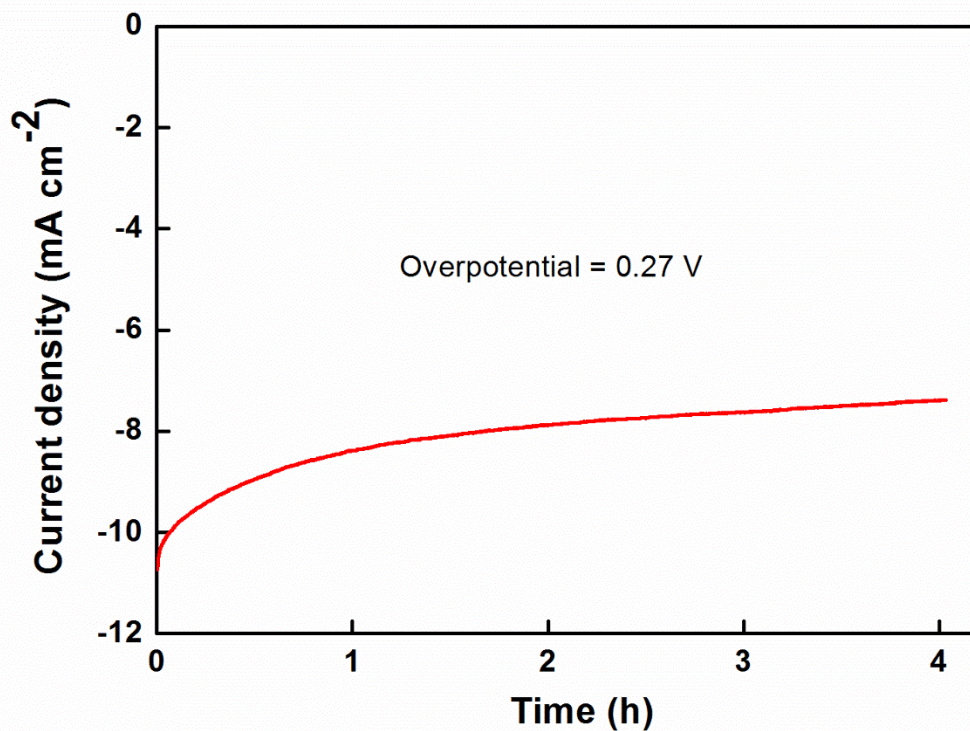
Figure 3-23 Bulk electrolysis of the 300 nm $Co_2Mo_9S_{26}$ thick film on a FTO support at the applied overpotential of -0.27V. The measurement was done by using carbon felt as a counter

117

electrode, Ag/AgCl as a reference electrode and an area of 1.4 cm^2 of working electrode previously washed with distilled water.

Figure 3-24 A 300 nm Co$_2$Mo$_9$S$_{26}$ film before and after the electrochemical measurement. The sample after testing looks "thinner" compared to the one before the measurement.

3.4 Conclusions

In this study, a mixed-metal chalcogenide Co$_2$Mo$_9$S$_{26}$ was produced by hydrothermal synthesis, which performs very effectively for proton reduction under acidic conditions. The thickness of the film was adjusted by varying the precursors' concentrations inside the hydrothermal vessel. The material was morphologically characterised by XRD, EDX and Raman spectroscopy. From the analysis, the sample resulted in a homogeneous distribution of Co throughout the predominantly MoS$_2$ lattice. To conclude, the material obtained has a good HER performance in acidic conditions, obtaining a current density of 10 mA cm^{-2} at 260 mV with a Tafel slope of 64 mV per decade for the 300nm-thick film. Thinner films show a substantial translucency, which makes them good candidates for solar-to-hydrogen applications.

3.5 Bibliography

1. M. A. Bissett, S. D. Worrall, I. A. Kinloch. and J. Dryfe Comparison of Two-Dimensional Transition Metal Dichalcogenides for Electrochemical Supercapacitors. *Electrochim. Acta* **201,** 30–37 (2016).

2. M. Pumera, Z. Sofer and A. Ambrosi Layered transition metal dichalcogenides for electrochemical energy generation and storage. *J. Mater. Chem. A* 8981–8987 (2014). doi:10.1039/c4ta00652f

3. R. Poulomi and K. Suneel Nanostructured anode materials for lithium ion batteries. *J. Mater. Chem. A* **3,** 2454-2484 (2015).

4. T. Heine. Transition Metal Chalcogenides: Ultrathin Inorganic Materials with Tunable Electronic Properties. *Am. Chem. Soc.* **48,** 65-72 (2015).

5. W. Zhao, R. M. Ribeiro and G. Eda Electronic Structure and Optical Signatures of Semiconducting Transition Metal Dichalcogenide Nanosheets. **48,** 91–99 (2015).

6. X. Xu, W. Yao, Di Xiao and T. F. Heinz Spin and pseudospins in layered transition metal dichalcogenides. *Nat. Phys.* **10,** 343-350

7. Lhuillier, E. *et al.* Two-Dimensional Colloidal Metal Chalcogenides Semiconductors : Synthesis , Spectroscopy , and Applications Published as part of the Accounts of Chemical Research special issue ' 2D Nanomaterials beyond Graphene ' . (2015). doi:10.1021/ar500326c

8. T. J. Marks and M. C. Hersam Semiconductors grown large and thin. *Nature* **520,** 631–632 (2015).

9. F. H. L. Koppens, T. Mueller, Ph. Avouris, A. C. Ferrari, M. S. Vitiello and M. Polini Photodetectors based on graphene, other two-dimensional materials and hybrid systems. *Nat. Nanotechnol. Vol.* **9,** 780-793 (2014).

10. M. Buscema. *et al.* Photocurrent generation with two-dimensional Van der Waals semiconductors. *Chem soc. rev.* **44,** 3691–3718 (2015).

11. A. B. Laursen, S. Kegnæs, S. Dahl and I. Chorkendorff Molybdenum sulfides—efficient and viable materials for electro - and photoelectrocatalytic hydrogen evolution. *Energy Environ. Sci.* **5,** 5577–5591 (2012).

12. Y. Yan, B. Xia, Z. Xu and X. Wang Recent Development of Molybdenum Sul fi des as Advanced Electrocatalysts for Hydrogen Evolution Reaction. (2014). doi:10.1021/cs500070x

13. M. Chhowalla *et al.* The chemistry of two-dimensional layered transition metal dichalcogenide nanosheets. *Nat. Chem.* **5,** 263-275 (2013).

14. X. Huang, Z. Zeng and H. Zhang Metal dichalcogenide nanosheets: preparation, properties and applications. *Chem. Soc. Rev.* **42,** 1934-46 (2013).

15. J.A. Wilson and A.D. Yoffe. The transition metal dichalcogenides discussion and interpretation of the observed optical, electrical and structural properties. *Adv. Phys.* **18,** 193–335 (1969).

16. R. Bissessur, M. G. Kanatzidis, J. L. Schindler and C. R. Kannewurf Encapsulation of polymers into MoS2 and metal to insulator transition in metastable MoS2. *J. Chem. Soc. Chem. Commun.* 1582–1585 (1993).

17. R. F. Frindt and A. D. Yoffe Physical properties of layer structures: Optical properties and photoconductivity of thin crystals of molybdenum disulphide. *Proc. R. Soc. Lond. A* **273,** 1963 (1963).

18. M. A. Py and R. R. Haering Structural destabilization induced by lithium intercalation in MoS_2 and related-compounds. *Can. J. Phys* 76-84 (1983).

19. K. Zhang, H. J. Kim, J-T Lee, C. Gee-Woo, X. Shi; K. Wanjung, M. Ma,K-J Kong, J-M Choi, M-S Song and J. H. Park Unconventional Pore and Defect Generation in Molybdenum Disulfide for Application in High-Rate Lithium-Ion Batteries and the Hydrogen Evolution Reaction. *ChemSusChem* 2489-2485 (2014).

20. I.J. McPherson and K. Vincent Electrocatalysis by Hydrogenases: Lessons for Building Bio-Inspired Devices. *J. Braz. Chem. Soc.* **25,** 1–15 (2014).

21. R. R. Eady Structure–Function Relationships of Alternative Nitrogenases. *Chem. Rev.* **96,** 3013–3030 (1996).

22. W. T. Eckenhoff, W. R. McNamara, P. Du and R. Eisenberg Cobalt complexes as artificial hydrogenases for the reductive side of water splitting. *Biochim. Biophys. Acta - Bioenerg.* **1827,** 958–973 (2013).

23. S. Kaur-Ghumaan and M. Stein [NiFe] hydrogenases: how close do structural and 0functional mimics approach the active site? *Dalt. Trans.* **43,** 9392 (2014).

24. P. J. Hallenbeck and J. R. Benemann Biological hydrogen production; Fundamentals and limiting processes. *Int. J. Hydrogen Energy* **27,** 1185–1193 (2002).

25. B. K.Burgess and D. J. Lowe Mechanism of Molybdenum Nitrogenase. *Chem. Rev.* **96,** 2983–3012 (1996).

26. V. Petkov, S. J. L. Billinge, P. Larson, S. D. Mahanti, T. Vogt, K. K. Rangan and M. G. Kanatzidis Structure of nanocrystalline materials using atomic pair distribution function analysis: Study of LiMoS2. *Phys. Rev. B* **65,** 092105/1-092105/4 (2002).

27. Hinnemann, B. *et al*. Biomimetic Hydrogen Evolution: {MoS}_2 Nanoparticles as Catalyst for Hydrogen Evolution. *J. Am. Chem. Soc.* **127,** 5308–5309 (2005).

28. W.Jaegermann and H.Tributsch. Interfacial properties of semiconducting transition metal chalcogenides. *Prog. Surf. Sci.* **29,** 1988 (1988).

29. T. F. Jaramillo, K. P. Jørgensen, J. Bonde, J. H. Nielsen, S. Horch and I. Chorkendorff Identification of Active Edge Sites for Electrochemical H2 Evolution from MoS2 Nanocatalysts. *Science (80-.).* **317,** 100–102 (2007).

30. P.D. Tran Novel cobalt/nickel-tungsten-sulfide catalysts for electrocatalytic hydrogen generation from water. *Energy Environ. Sci.* **6,** 2452 (2013).

31. D. P. Tran *et al*. Copper molybdenum sulfide: a new efficient electrocatalyst for hydrogen production from water. *Energy Environ. Sci.* **5,** 8912 (2012).

32. Y. Sun *et al*. Electrodeposited cobalt-sulfide catalyst for electrochemical and photoelectrochemical hydrogen generation from water. *J. Am. Chem. Soc.* **135,** 17699–17702 (2013).

33. A. B. Laursen, P.C.K. Vesborg and I. A. Chorkendorff high-porosity carbon molybdenum sulphide composite with enhanced electrochemical hydrogen evolution and stability. *Chem. Commun.* **49,** 4965-7 (2013).

34. F. Meng, J. Li, S. K. Cushing, M. Zhi, M. and N. Wu Solar Hydrogen Generation by Nanoscale p – n Junction of p - type Molybdenum Disul fi de/ n - type Nitrogen-Doped Reduced Graphene Oxide. *J. Am. Chem. Soc.* **135,** 10286–10289 (2013).

35. J. Kibsgaard, Z. Chen, B. N. Reinecke and T.F. Jaramillo Engineering the surface structure of MoS2 to preferentially expose active edge sites for electrocatalysis. *Nat. Mater.* **11,** 963–969 (2012).

36. H. Vrubel and X. Hu. Growth and activation of an amorphous molybdenum sulfide hydrogen evolving catalyst. *ACS Catal.* **3,** 2002-2011 (2013).

37. D. Merki, S. Fierro, H. Vrubel and X. Hu. Amorphous molybdenum sulfide films as catalysts for electrochemical hydrogen production in water. *Chem. Sci.* **2,** 1262 (2011).

38. H. Vrubel, D. Merki and X. Hu Hydrogen evolution catalyzed by MoS3 and MoS2 particles. *Energy Environ. Sci.* **5,** 6136 (2012).

39. Z. Huang *et al*. Dimeric [Mo2S12]2- Cluster: A Molecular Analogue of MoS2 Edges for Superior Hydrogen-Evolution Electrocatalysis. *Angew. Chemie - Int. Ed.* **54,** 15181–15185 (2015).

40. L. Yang, W. Zhou, J. Lu, D. Hou, Y. Ke, G. Li et al. Hierarchical spheres constructed by defect-rich MoS2/carbon nanosheets for efficient electrocatalytic hydrogen evolution. *Nano Energy* 490–498 (2016).

41. J. Xie, J. Zhang, S. Li, F. Grote, X. Zhang, H. Zhang et al. Controllable disorder engineering in oxygen-incorporated MoS2 ultrathin nanosheets for efficient hydrogen evolution. *J Am Chem Soc.* 17881–17888 (2013).

42. J. Xie, H. Zhang, S. Li, R. Wang, X. Sun, M. Zhou et al. Defect-rich MoS ultrathin nanosheets with additional active edge sites for enhanced electrocatalytic hydrogen evolution. *Adv. Mater.* 5807–5813 (2013).

43. J. Bonde, P. G. Moses, T. F. Jaramillo and J.K.N. Chorkendorff, J. K. N. Hydrogen evolution on nano-particulate transition metal sulfides†. *Faraday Discuss.* **140,** 219–231 (2008).

44. E. A. Pruss, B. Snyder, A. M. Stacy A New Layered Ternary Sulfide: Formation of Cu2WS4 by Reaction of WSurn:x-wiley:05700833:media:ANIE199302561:tex2gif-stack-1 and Cu+ Ions. *Angew. Chemie - Int. Ed.* **32,** (1993).

45. YangTeng, A. Wang, X. Li, J. Xie, Y. Wang and Y. kang Hu Preparation of high-performance MoP hydrodesulfurization catalysts via a sulfidation–reduction procedure. *J. Catal.* **266,** 365–379 (2009).

46. D. Merki , H. Vrubel , L. Rovelli, S. Fierro and X. Hu Fe, Co, and Ni ions promote the catalytic activity of amorphous molybdenum sulfide films for hydrogen evolution. *Chem. Sci.* **3,** 2515–2525 (2012).

47. C-B Ma *et al*. MoS2 nanoflower-decorated reduced graphene oxide paper for high-performance hydrogen evolution reaction. *Nanoscale* **6,** 5624 (2014).

48. Y. Yan *et al*. Vertically oriented MoS2 and WS2 nanosheets directly grown on carbon cloth as efficient and stable 3-dimensional hydrogen-evolving cathodes. *J. Mater. Chem. A* **3,** 131–135 (2015).

49. H. Wang, Z. Lu, D. Kong, J. Sun, T. M. Hymel, and Y. Cui Electrochemical Tuning of MoS2 Nanoparticles on Three-Dimensional Substrate for Efficient Hydrogen Evolution. *ACS Nano* **5,** 4940–4947 (2014).

50. D. Philip and J. F. Stoddart Self-Assembly in Natural and Unnatural Systems. *Angew. Chem. Int. Ed. Engl* **35,** 1154-1196 (1996).

51. P. He, P and L. R. Faulkner Intelligent , Automatic Compensation of Solution Resistance. 517–523 (1986). doi:10.1021/ac00294a004

52. R. K. Leach Good Practice Guide No. 37: The Measurement of Surface Texture using Stylus Instruments. National Physical Laboratory Publications (UK). (2016). Available at: http://publications.npl.co.uk/npl_web/pdf/mgpg37.pdf .

53. Y. Cheng, Z. Zhu and U. Schwingenschlögl. Role of interlayer coupling in ultra thin MoS2. *RSC Adv.* **2,** 7798 (2012).

54. E. Payen, S. Kasztelan, S. Houssenbay, R. Szymanski and J. Grimblot Genesis and Characterization by Laser Raman Spectroscopy and High-Resolution Electron Microscopy of Supported MoS2 Crystallites J â€^{TM} Tl y /. *J. Chem. Phys.* 6501–6506 (1989). doi:10.1021/j100354a043

55. E. Anastassakis and C. H. Perry Light scattering and ir measurements in XS2 pryite-type compounds. *J. Chem. Phys.* **64,** 3604–3609 (1976).

56. H. Li , Q. Zhang , C. Chong Ray Yap, B. Kang Tay, T. H. T. Edwin, Aurelien Olivier, and D. Baillargeat From Bulk to Monolayer MoS_2 : Evolution of Raman Scattering. *Mater. views* **22,** 1385–1390 (2012).

57. J, Kibsgaard,Z Chen , B.N. Reinecke and T. Jaramillo Engineering the surface structure of MoS2 to preferentially expose active edge sites for electrocatalysis. *Nat matter* 963–969 (2012).

58. M. Zeng and Y. Li Recent advances in heterogeneous electrocatalysts for the hydrogen evolution reaction. *J. Mater. Chem. A* **3,** 14942-14962 (2015).

59. M. S. Faber and S. Jin Earth-abundant inorganic electrocatalysts and their nanostructures for energy conversion applications. *Energy Environ. Sci.* **7,** 3519–3542 (2014).

60. J. D. Benck, T.R. Hellstern, J. Kibsgaard, P. Chakthranont and T. F. Jaramillo Catalyzing the hydrogen evolution reaction (HER) with molybdenum sulfide nanomaterials. *ACS Catal.* **4,** 3957–3971 (2014).

61. D. Voiry, J. Yang and M. Chhowalla Recent Strategies for Improving the Catalytic Activity of 2D TMD Nanosheets Toward the Hydrogen Evolution Reaction. *Adv. Mater.* 6197–6206 (2016). doi:10.1002/adma.201505597

62. Q. Lu, Y. Yu, Q. Ma, B. Chen and H. Zhang 2D Transition-Metal-Dichalcogenide-Nanosheet-Based Composites for Photocatalytic and Electrocatalytic Hydrogen Evolution Reactions. *Adv. Mater.* **28,** 1917-1933 (2016).

63. D. Merki, H. Vrubel, L. Rovelli, S. Fierro and X. Hu Fe, Co, and Ni ions promote the catalytic activity of amorphous molybdenum sulfide films for hydrogen evolution. *Chem. Sci.* **3,** 2515 (2012).

4   The role of Mo content on the activity of $Mo_xNi_{2-x}P$ towards the hydrogen evolution reaction from water

Synopsis

In this project, the Ni_2P bulk structure was fine-tuned by modulating the metal composition (i.e. Mo and Ni) with the use of the synthetic solid solution method followed by a time programmed reduction (TPR) in a 5% H_2 / 95% Ar gas mixture. The HER activity was then investigated in acid and basic media and compared with the value obtained for MoP in bulk form. The study shows that the selective substitution of the molybdenum into the (0002) crystal face enhances electrochemical performances in acid media, resulting in performances competitive with the bulk MoP. Moreover, the method applied to produce $Ni_{(2-x)}Mo_xP$ compounds is easy to scale up and therefore possible to exploit for industrial purposes.

4.1   Introduction

4.1.1   Crystal structure of Ni_2P

The physical properties of Ni_2P, including high mechanical strength, electrical conductivity and chemical stability, make this compound a well-studied material for HER[1] and hydrogen desulfurization (HDS) processes.[2] It is therefore important to discuss the crystal structure of this compound, which is composed of a network of edge-sharing Ni-centred tetrahedral and square pyramidal units coordinated by phosphorous (Figure 4.1a). Ni_2P adopts the Fe_2P crystal structure-type ($P\bar{6}2m$ space group with the lattice parameters of a = 5.862 Å and c = 3.382 Å. [3]

Inside the unit cell there are two types of Ni-sites, which are commonly denoted as Ni1 and Ni2 depending on the coordination environment by P. The Ni1 atom is tetrahedrally coordinated by P, while the Ni2 atom displays a square pyramidal coordination. Ni1 has some distortion from the ideal tetrahedral arrangement as the two types of coordinated phosphorous have slightly different bond lengths (Figure 4.1b). Similarly, Ni2 polyhedra have an arrangement slightly different from the perfect square pyramidal geometry. In particular, the bond length between

the nickel and the phosphorous apex of the pyramid is shorter than the ones on the pyramidal base (Figure 4.1c).
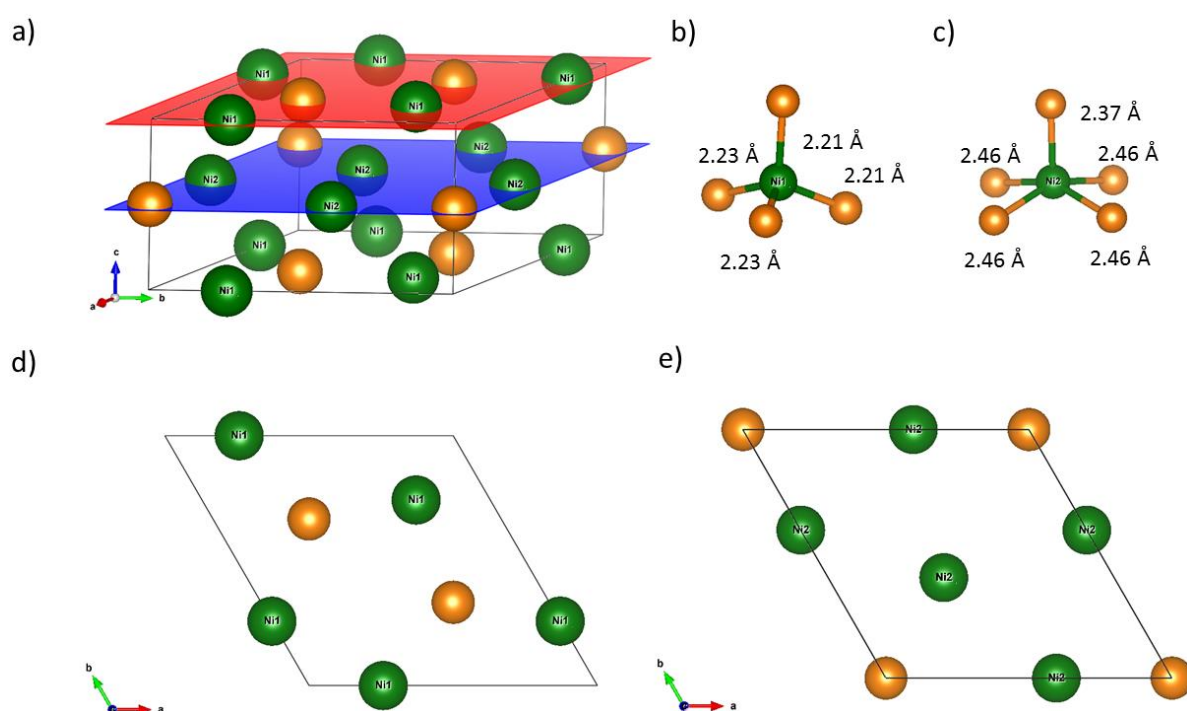
Figure 4-1 The unit cell of Ni$_2$P with Ni1 and Ni2 in tetrahedral and square planar coordination. The unit cell is shown by a solid line box. P atoms outside the unit cell are omitted for clarity. The red and blue planes represent (0001) and (0002)-planes respectively (a). Polyhedral coordination around Ni1 (b) and Ni2 (c) along with selected bond lengths based on data from [Ref. 3].The cross section at the distance 0.5 and 1 of the *c*-parameter are shown in (d) and (e), respectively.

Figures 4.1 d/e show two cross sections through the unit cell of the *c*-axis which coincide with (0001) and (0002) planes. Within the unit cell boundaries the (0001)-plane has a stoichiometry of Ni$_{1.5}$P. Similarly, the (0002) cross section displays a Ni$_3$P stoichiometry. Therefore, the overall unit cell formula is Ni$_6$P$_3$, *e.g.* in line with the Ni$_2$P formula.

In the (0002) plane the central P of the Ni$_3$P subunit is slightly above the plane (Figure 4.2).[4] This subunit is located below but in a rotated orientation to the Ni-trimer hollow of plane (0001) known to be the active site of the HER reaction (see paragraph 1.11.5.2). Modifications in the composition of the Ni$_3$P subunit can potentially affect the Ni-trimer activity by changing its distance with the phosphorous below belonging to the (0002) plane.
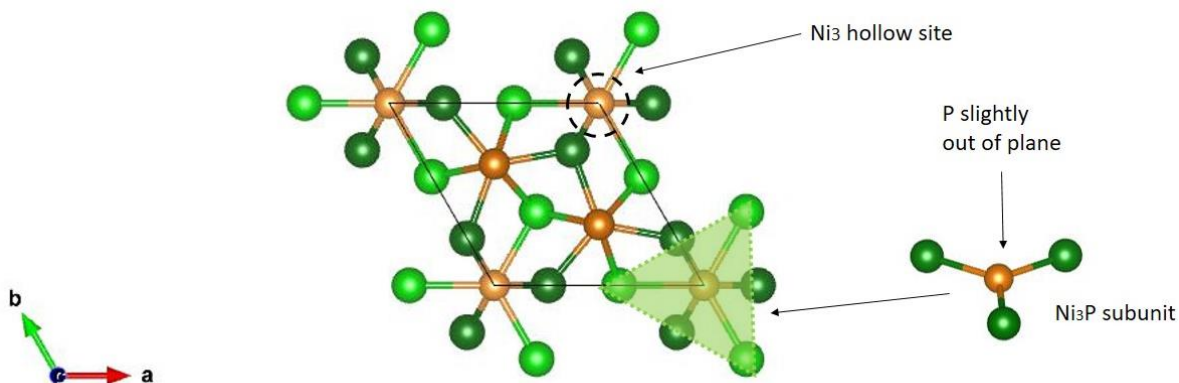
Figure 4-2 Ni$_2$P unit cell highlighting the Ni trimer hollow (HER active site) together with the Ni$_3$P subunit belonging to the (0002) plane. Ni1 and P belonging to the (0001) plane and in the top of the unit cell are in dark green and orange, respectively, while Ni2 and P on the (0002) plane are labelled in a lighter colour.

4.1.2 The nature of the electrocatalytic site in Ni$_2$P

The Ni$_2$P structure is stabilised by the presence of an additional P covering the Ni-trimer hollow on the (0001) plane (Figure 4.3 c) as highlighted by Low-energy electron diffraction experiments (LEED)[5] together with scanning tunnelling microscope (STM) studies on Ni$_2$P single crystals [6].

As mentioned above, this hollow is known to be the HER active site for Ni$_2$P according to DFT calculations.[7] Yet, the (0001) plane is P-covered in circa 80% of the cases,[5] questioning the DFT calculations of most of the studies reported in the literature and carried out without the capping phosphorus (Figures 4.3 b/d).
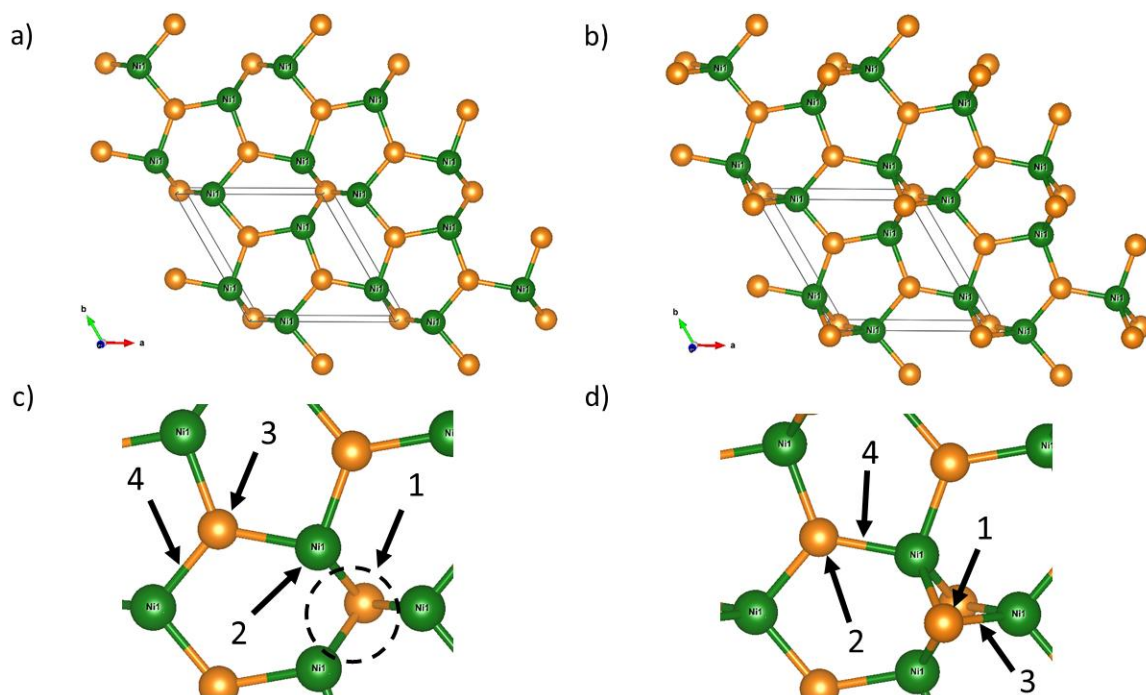
Figure 4-3 (a) View of the Ni$_2$P (0001) surface over a 2x2 supercell of the (0001) surface to highlight the network of tetrahedra without the terminating phosphorus atoms. **(b)** View of the 2x2 supercell with capping P consistent with Ni$_3$P$_2$ stoichiometry. **(c)** and **(d)** The possible adsorption sites of the (0001) cross sections are highlighted. The adsorption energies of hydrogen depending on the nature of the site are summarized in Table 4.1.

Table 4.1 compares the absorption energies between the energy sites with and without the P layer on the (0001) plane. From this table it is evident that there is a substantial difference in the energy of the sites if there are phosphorus atoms above the layers. When DFT calculations take into account extra phosphorus, it is the Ni-P bridging site which is the site lowest in energy (site 3 in (Figure 4.3d).[6] In this respect, the adsorption of hydrogen on the bridging site presents an interesting opportunity to explore the role of the crystal structure (Ni-P bond length) on the process of HER. Replacing Ni atoms with another element (e.g. transition metal) may have a positive effect on the electronic properties and as a result the catalytic properties of newly formed systems in general. For example, Mo-atoms favour a square pyramidal arrangement that can potentially be used to tune the properties of Ni$_2$P and make it more HER active.

Table 4. 1 Hydrogen absorption energies sites on (0001) surface obtained by DFT calculations.[8]

Surface	Site of hydrogen	E_{ads} (eV)
Ni_3P	**1** Ni threefold trimer	-0.65
	2 Ni at top	-0.01
	3 P at top	0.09
	4 Ni-P bond	-0.05
Ni_3P-P	**1** P at top	-0.22as
	2 P second at top	0.15
	3 Ni-P top bound	-0.04
	4 Ni-P bridge site	0.23

4.1.3 Substitution of Ni for a transition metal within Ni_2P structures

It is possible to synthesize a range of compositions (solid solutions) with the Fe_2P structure-type and a general formula $(M_{1-x}Ni_x)_2P$, where M is a transition metal.[9,10,11,12,13] Depending on the ionic radius of M, various amounts of substitutions are possible. However, only the $(Fe_{1-x}Ni_x)_2P$ system shows a complete solid solution across the entire range of $0<x<1$, *e.g.* the hexagonal structure is retained for both Ni_2P and Fe_2P end members.[14,15,16] There are solid solutions consisting of $(Co_{1-x}Ni_x)_2P$; $(V_{1-x}Ni_x)_2P$ and $(Mn_{1-x}Ni_x)_2P$ systems where the hexagonal phase is found across a relatively large range of $0<x<0.85$; $0<x<0.75$ and $0<x<0.8$, respectively (Type 1).[17,15,16,18,19,20] In the Type 2 system, which includes Mo, Cr, Pd, Rh, W, the hexagonal structure is preserved within the narrow compositional range of $0<x<0.5$.[21,22] Remarkably, in the Type 2 compounds the substituting transition metal M preferentially replaces only Ni2 in pyramidal sites, *e.g.* the stoichiometry of the (0001)-slab is preserved independent of the value of x and contains only Ni atoms. At the extreme value of $x = 0.5$, the chemical formula corresponds to a 1:1:1 stoichiometry *e.g.* MNiP. For example, MoNiP displays a crystal structure where the metal atoms within the (0002) plane are Mo, while Ni takes the sites on the (0001) plane as shown in Figure 4.3. This is in contrast with Type 1 compounds, where the M sites are evenly distributed between Ni1 and Ni2 sites independent of the stoichiometry.[11] Therefore, Type 2 compounds like MoNiP can provide an efficient route for controlling the electronic structure without obscuring the effect of doping into the (0001)-layer.
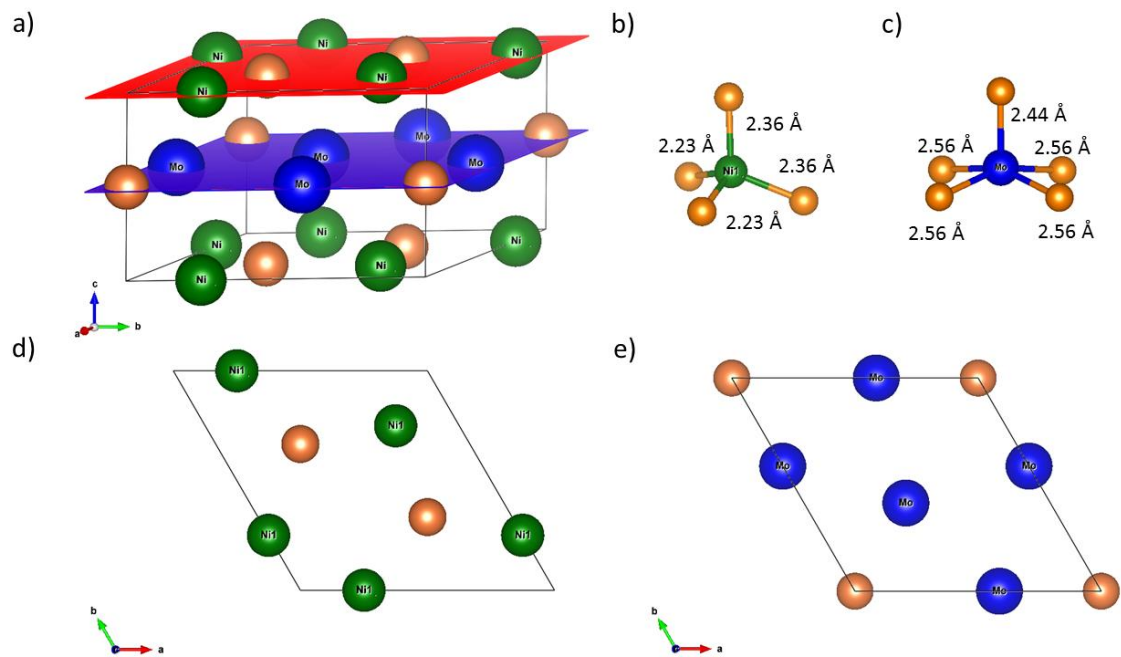
Figure 4-4 The unit cell of MoNiP with Ni and Mo in tetrahedral and square planar coordination. The unit cell is shown by a solid line box. Phosphorus atoms outside the unit cell are omitted for clarity. The red and blue planes represent (0001) and (0002)-planes, respectively (a). Coordination polyhedral around Ni1 (b) and Ni2 (c) along with selected bond lengths based on data from [Ref. [17]]. The cross section at the distance 0.5 and 1 of the *c*-parameter are shown in (d) and (e), respectively.

4.1.4 Electrocatalytic properties of $(M_{1-x}Ni_x)_2P$ compounds

Acidic solutions

Table 4.2 summarizes the $(M_{1-x}Ni_x)_2P$ electrocatalysts studied in acidic solution. The research is dominated by studies of the $(Co_{1-x}Ni_x)_2P$ system and there is a huge variety of the overpotential values reported even for the materials with the same composition. An interesting trend emerges, however, showing that replacing Ni for Co leads to an improved performance, *e.g.* all Co-doped composites outperforming Ni_2P with the performance peaking for NiCoP.[23] The associated change in unit cell parameters confirms that solid solutions are generally formed. As discussed above, since Co and Ni are equally distributed irrespective of the crystallographic site, it is unclear what might be the origin for improved catalytic performance. While the DFT calculations were carried out, one general assumption was that the (0001) surface was terminated by metal atoms in contrast to clear evidence from STM that this is the case in the real system. Furthermore, the identical Tafel slopes may further indicate that the change in catalytic performance is probably driven by the change in surface area.

Table 4. 2 The electrochemical properties of $(M_{1-x}Ni_x)_2P$ compounds in acidic solutions

Reported material description	η at 10 mA cm^{-2} in 0.5M H$_2$SO$_4$	Tafel slope, mV dec^{-1}	Ref.
Ni$_{2-x}$Co$_x$P on reduced graphene oxide	Ni$_2$P 130 mV	51	[23]
	Ni$_{1.8}$Co$_{0.2}$P 119 mV	51	
	Ni$_{1.4}$Co$_{0.6}$P 98 mV	51	
	Ni$_{1.2}$Co$_{0.8}$P 80 mV	51	
	NiCoP 59 mV	51	
Ni$_{2-x}$Co$_x$P nanoparticles	Ni$_2$P 136 mV	76	[24]
	Ni$_{1.8}$Co$_{0.2}$P 130 mV	70	
	Ni$_{1.4}$Co$_{0.6}$P 115 mV	58	
	NiCoP 98 mV	51	
NiCoP free-standing powder	316 mV	122	[25]
NiCoP on carbon quantum dots	216 mV	80	[25]
NiCoP on Ru nanoparticles	49 mV	49	[26]
NiCoP on a Ni foam	80 mV	37	[27]
NiFeP	101 mV	43	[28]

Similar results were reported for crystalline Ni$_{2-x}$Co$_x$P nanoparticles.[24] However, in this work there seems to be a gradual decrease in Tafel slopes from 76 mV dec^{-1} to 51 mV dec^{-1} indicating changes in reaction kinetics and thus implying that the Co doping may lead to Heyrovsky reaction (2) being the rate determining step.

$$M + H^+ + e^- \rightarrow MH_{ads} \quad \text{Volmer reaction is fast} \quad (1)$$
$$MH_{ads} + \text{H}^+ + \text{e}^- \rightarrow M + H_2 \quad \text{Heyrovsky reaction is slow} \quad (2)$$

This suggests that replacing Ni with Co makes protons to be adsorbed more strongly to the surface of the catalyst.

At this point it should be pointed out that it is rather challenging to assess to what extent the electrocatalytic properties of $(M_{1-x}Ni_x)_2P$ originate from the material itself as the literature reports are dominated by composite and nanoparticulated materials.[29,30] As a result there is a significant difference in surface areas and it is very difficult to discriminate between the actual change due to doping or change in morphology. However, a recent work on free-standing NiCoP provides an

interesting story in this respect.[25] The overpotential (reaching 316 mV at 10 mA cm^{-2}) reported for this free-standing material is significantly higher than for nanostructured materials discussed above. In addition the Tafel slope of 122 mV dec^{-1} suggests the Volmer reaction is the rate determining step.

$$M + H^+ + e^- \rightarrow MH_{ads} \qquad \text{Volmer reaction is slow} \quad (3)$$
$$2MH_{ads} \rightarrow 2M + H_2 \qquad \text{Tafel reaction is fast} \quad (4)$$

Unfortunately, no comparison with different amount of Co was made; although authors showed that adding carbon nanodots led to an improved overpotential and reduction in the Tafel slope. This tentatively suggests that the role of the carbon is to facilitate improved adsorption of protons on the surface of the catalyst.

$(Fe_{1-x}Ni_x)_2P$ system have been studied as alternative to Co compounds due to relatively high abundance of iron and low costs.[30] However, it seems to be challenging to prepare phase pure compounds without significant amount of contamination from potentially (more) electrocatalytic Ni_5P_4 phase making it difficult to tell whether the performance originates from the replacing nickel for iron or the impurities.

As discussed above Co and Fe are not optimal (from the perspective of understanding the role doping has on electrocatalytic properties) ions for replacing Ni within Ni_2P structure as they tend to take the position randomly within the 0001 and 0002 layers. Therefore, the origin of a superior catalytic performance within Co-Ni-P is still unclear or at least does not provide new advance strategies for future development of electrocatalysts. In this respect, replacing Ni for Mo can offer a much better strategy (at least from the fundamental point of view) since Mo does not take positions in the 0001 layer, which contains solely Ni atoms.

Alkaline solutions

One attraction of $(Co_{1-x}Ni_x)_2P$ composites (and possible reason for comprehensive research efforts) is that they display impressive performance in alkaline media as well (Table 4.3). They can therefore, work as bimodal catalysts. For example, attempts to prepare $(Mo_{1-x}Ni_x)_2P$ composite on Ni foil yielded poorly characterised multi-phase sample which, however, showed an exceptional performance in alkaline solution.[31] The improvement over Ni_2P may be driven by increased

conductivity as was evident from the comparison of results of the impedance measurements for Ni_2P and $Ni_{2(1-x)}Mo_{2x}P$ products. From this perspective, Ni-Mo-P system is very promising as bimodal catalyst especially if the phase pure materials can be isolated and tested.

Table 4. 3 The electrochemical properties of $(M_{1-x}Ni_x)_2P$ compounds in alkaline solutions

Reported material description	η at 10 mA cm⁻² In 1M KOH	Tafel slope mV dec⁻¹	Ref.
NiMoP carbon nanotube	135 mV	45	[29]
NiCoP nanoflower	83 mV	47	[30]
NiCoP on Ru nano particle	52 mV	50	[26]
NiCoP nanocrystals	270 mV	124	[23]
Nanostructured NiCoP on a Ni foam	105 mV	79	[27]
$Ni_{2(1-x)}Mo_{2x}P$ nanowire on Ni foam	72 mV	46	[31]

4.2 Experimental preparation and characterization of $(Mo_xNi_{1-x})_2P$ solid solutions

Reagents: $(NH_4)_6(Mo_7O_{24})\cdot4H_2O$ (Koch-Light Laboratories Ltd, ≥99.985%); nickel(II) nitrate hexahydrate $(Ni(NO_3)_2\cdot6H_2O)$ (Alfa Aesar, ≥99.9%, stored under Ar), di-ammonium hydrogen phosphate $((NH_4)_2HPO_4)$ (Sigma-Aldrich, ≥99.0%) and citric acid (C_6H_8O) (Fisher Scientific 99.9%).

The synthesis of solid solutions of phosphides was carried out with an oxidic precursor followed by a time program reduction step using a gas tube furnace under a 0.2 sL/min gas flux of 5% H_2 / 95% Ar with a heating rate of 15 °C/min. Different Mo:Ni:P ratios and reduction temperatures were investigated in order to obtain a pure and crystalline phase composition. Finally, some compounds were prepared with the addition of citric acid to stabilize the mixture.[32] All the relevant samples and precursors were repeated twice to ensure the reproducibility of the study.

The synthesis of the oxidic precursor was followed without modification using the synthetic protocol reported elsewhere.[33,34] The reagents were dissolved separately, at the desired stoichiometry, in deionised water before being mixed together. The resulting solution with the presence of a suspension was then left

to dry overnight on a hot plate at 120°C and stirring at 220 rpm. The obtained green-yellow precipitate, was finally left in an oven for further 24 hours at 120°C.

To optimize the reduction of the precursor, different temperatures and times were tested. *Ca.* 1 g of precursor was placed into a 6.7 cm long quartz sample tube with a diameter of 1.4 cm and a wall thickness of 1 mm that was open on both ends. The openings on both ends was then sealed using silica wool. Finally, the sample was placed into the horizontal quartz reactor tube located in the middle of the tube furnace. Once the best temperature was determined, samples were annealed further one or two times to improve crystallinity the phase purity.

4.2.1 Electrode preparation and electrochemical measurements.

4.2.1.1 Electrode preparation

Materials: CHI glassy carbon disk working electrode (CH instrument Inc.), DMF (dimethylformaldeide)(Honeywell ≥99%) and Nafion (Sigma-Aldrich, 5 wt.%)

The ink was prepared by mixing 1 mL of DMF, 50 μL of Nafion and 8 mg of the testing catalyst. The resulting mixture was then sonicated for 1 h to facilitate the dispersion of the catalyst. After sonication, a pipette was used to deposit 30 μL of the mixture onto the surface of the GC electrode (0.071 cm^2) to reach the catalyst loading of 3.4 mg cm^{-2}. Finally, the electrode was left to dry at room temperature overnight.

After each electrochemical characterization, the GC electrode was cleaned by polishing the surface with a microcloth polishing pad moistened with distilled water and coated with 0.05 micron alumina polishing powder. The electrode was cleaned by holding it vertically and firmly while making figure of eight on the pad. The electrode was finally cleaned electrochemically by using a three electrodes configuration and by running the CV scans between 0.6 and -0.8 V for 20 cycles at a scan rate of 100 mV s^{-1} to remove any remaining catalyst.

4.2.1.2 Electrochemical measurements

The electrochemical characterization was carried out using a Biologic SP 150 in a three electrodes configuration at room temperature, using a glassy carbon GC as

a working electrode (WE), Pt as a counter electrode (CE) and Ag/AgCl (3M) as a reference (Ref). The potentials were reported with the NHE scale using the conversion equation E (NHE) = E(Ag/AgCl) + 0.209 and the Ohmic resistances were compensated.

The HER activity and Tafel slope were measured by using the *linear sweep voltammetry* technique (LSV) with a scan rate of 2 mV s^{-1} and a 0.5 M H$_2$SO$_4$ solution as electrolyte. The catalytic performances in basic media were carried out with the *cyclic voltammetry* (CV) technique in a 1M KOH solution at a scan rate of 100 mV s^{-1}.

The electrochemically active surface area (ECSA) of the catalyst was carried out in a 0.5 M H$_2$SO$_4$ by recording the CV scans at different scan rates from 0.155 V to 0.250 V vs. NHE and by taking the potential obtained for -0.209 V at each cycle.

The stability of the material was probed by *chronopotentiometry* (CP) in an unstirred solution by applying a constant reductive current to the working electrode of -0.71 mA over time.

The *Electrochemical impedance spectroscopy* (EIS) measurements were conducted using a potentiostat with an EIS function, using a three-electrode cell (on the standard setup) in order to analyse the cathode as an individual electrode. The potentiostat was programmed to determine the impedance in a frequency range from 200 kHz to 1 MHz where the kinetics related to the charge transfer dynamics are detected. All the data were collected in potentiostatic mode at -500 mV with an amplitude of 10 mV.

The potential was chosen in a range where the HER reaction was occurring in order to probe its catalytic kinetics.[35]

The Nyquist plots obtained were modelled by using a simplified Randles circuit model widely reported in literature.[36,37,38,39,40] This circuit consists of a resistor (Rs) in series with a parallel arrangement of a resistor (Rct) and a constant phase element (CPE). The resistance Rs can be obtained from the intercept of the Nyquist plot with the real axes and corresponds to the resistance between the electrode-electrolyte interface. It depends on the space between the working electrode and the reference as well as on the related conductivity of the material and therefore varies between measurements and samples. The value associated with the resistor R$_{ct}$ is named charger transfer resistance and is related to the HER kinetics. A small

R_{ct} value is associated to a faster kinetic and therefore to a more efficient HER reaction.

4.2.2 Morphological characterization

4.2.2.1 Powder x-ray diffraction measurements

The X-ray measurements were collected using a Bragg-Bretano geometry by a Panalytical XPert-pro diffractometer ($Cu_{K\alpha}$ radiation corresponding to λ= 1.54178 Å wavelength). Each pattern was collected for 25 minutes in a range between 10 to 65 $^{o.}$.

4.2.2.2 Scanning Electron Microscopy (SEM) and Energy-Dispersive X-ray spectroscopy (EDX) analysis

The instrument used to collect electron microscopy pictures was a Philips XL30 ESEM with an attached Oxford Instruments x-act EDX detector. Before performing the measurement, the apparatus was calibrated using a Cu foil standard. As in Chapter 3, all the images were obtained using magnifications of 20×, 100×, 800× and 4000×. EDX spectroscopy was used to detect the composition of the phosphides by probing the sample in three points for each area and then average the value for each element. Finally, mapping analysis was performed only for compound $Mo_{0.6}Ni_{1.3}P$ to ensure a homogeneity of the composition in the overall sample.

4.3 Result and discussion:

4.3.1 Synthesis of $(Mo_xNi_{1-x})_2P$ solid solutions

4.3.1.1 Synthesis of oxide precursors

The $(Mo_xNi_{1-x})_2P$ series were synthesised by using a solid solution approach already reported in literature.[12] The protocol was chosen because of the simplicity of the experimental procedure and molecular ratios scalability. Moreover, the reagents used for the research were cheap and easy to find.

The precursors obtained exhibited a range of colours becoming more intensely green with increasing nickel percentage (Table 4.4). After the precursor was

ground with pestle and mortar, the powder obtained was studied by PXRD to determine the phase composition (Figure 4.4.). However the amorphous patterns were obtained with the presence of $(NH_4)(H_2PO_4)$ and NH_4NO_3 as crystalline impurities.
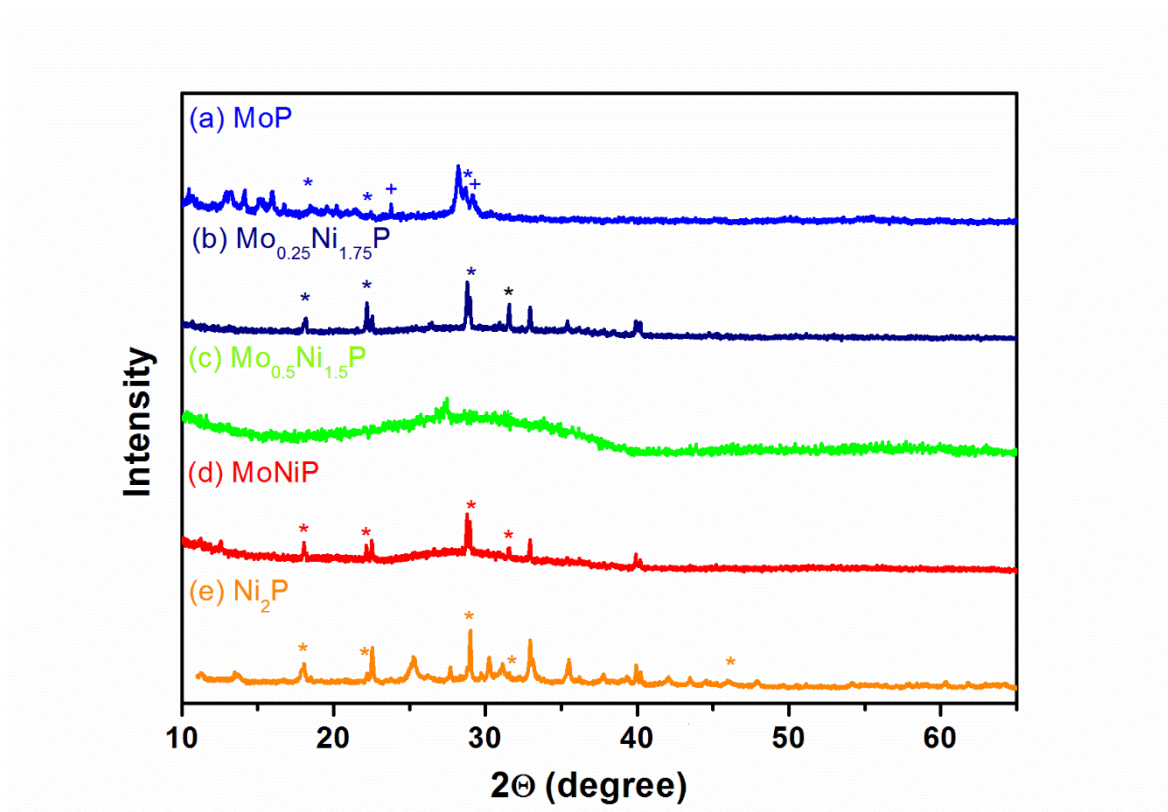
Figure 4-5 XRD patterns of the phosphides precursors. Stars indicates NH_4NO_3 while plusses $NH_4H_2PO_4$.

Table 4. 4 Summary of Precursors for MoP, Ni_2P and the $(Mo_xNi_{1-x})_2P$ transition metal phosphides series obtained by solid solution synthesis.

Targeted composition	Precursor colour	Crystalline phases
MoP	White	$(NH_4)(H_2PO_4)$ / NH_4NO_3
$Mo_{0.25}Ni_{1.75}P$	Yellow-green	NH_4NO_3
$Mo_{0.5}Ni_{1.5}P$	Light green	-
MoNiP	Green	$(NH_4)(H_2PO_4)$, NH_4NO_3
Ni_2P	Green	NH_4NO_3

4.3.1.2 Optimisation of the reaction parameters

4.3.1.2.1 Investigation of the role of temperature on phase composition of MoNiP product

The solid solution synthesis was carried out according with the reaction procedure reported elsewhere in literature.[33,12] However, in the original study the reduction was carry out in pure H_2 atmosphere. Since the pure hydrogen was not available in our laboratory we therefore decided to investigate the role of temperature on the phase composition using commercially available Ar/H_2 95 vol.% / 5 vol.%.

Each reduction was performed on a fresh oxide precursor using a heating ramp rate of 15 °C /min and a dwell time of 11 hours. The first reduction temperature tested was 750 ° C and has led to a product which showed a strong presence of MoP, MoO_2 and MoP_2O_7 in the X-ray diffraction pattern (Figure 4.5). The MoNiP phase was obtained at 850 °C with the minor presence of MoP and Mo_3P as impurities.

After the reduction at 850°C, the samples showed a change of colour from green to black with a weight loss of 61.46 wt. % (Table 4.5). This variation was due to the reduction of the phosphate-type groups (P_yO_x) by hydrogen which made the phosphorous available for the phosphide formation.[33]
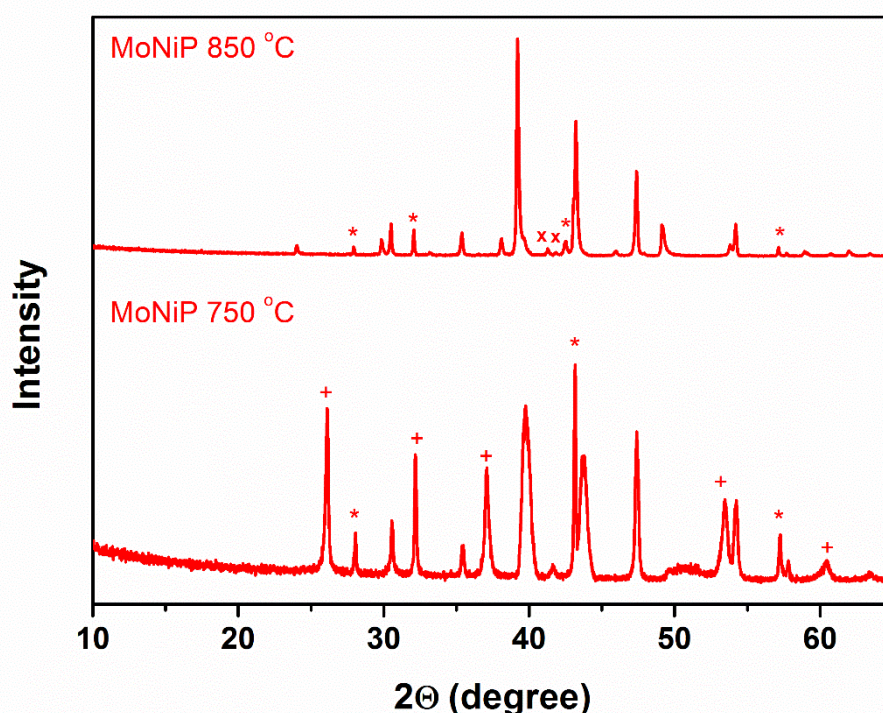
Figure 4-6 X-ray pattern of MoNiP depending on the reaction temperature. Plusses MoO$_2$, stars MoP and crosses Mo$_3$P, respectively.

Table 4. 5 Percentage of weight loss after the MoNiP precursor's annealing at different temperature

MoNiP Temperature °C	% of weight loss
750	2.37
850	61.46

4.3.1.2.2 Investigation of the role of annealing time on phase composition of MoNiP product

Once the optimal temperature of 850 °C was selected, a time reduction study was carried out by annealing samples for 11, 22 and 33 hours. This was done in order to identify if longer reduction times have any role on the phase assembly. The time dependence studies were conducted for MoNiP only and the products obtained investigated by PXRD.

The resulting XRD patterns did not show any substantial impact on phase composition (Figure 4.7). However, the PXRD refinements showed the unit cell becoming slightly bigger and closer to the unit cell value reported in literature after increasing the reduction time (Table 4.6). The MoNiP volumes for 11 hours reduction has a value of 109.558 Å^3, which is still close to the ones reported in the literature of 110.19 Å^3. [Ref 17] Unfortunately, a negative correlation (*vide infra*) between the crystallinity and electrochemical performance of the material was observed when the MoNiP samples with different reduction times were tested for the hydrogen evolution reaction. A higher overpotential at 10 mA cm^{-2} was observed for the materials, which underwent longer reaction times. This could be explained by the fact that more crystalline (and longer annealed products) showed lower dispersability in the solvent and it was harder to turn them into inks. For this reason, it was decided to use 11 hours as a time parameter for all the compounds prepared in this work.
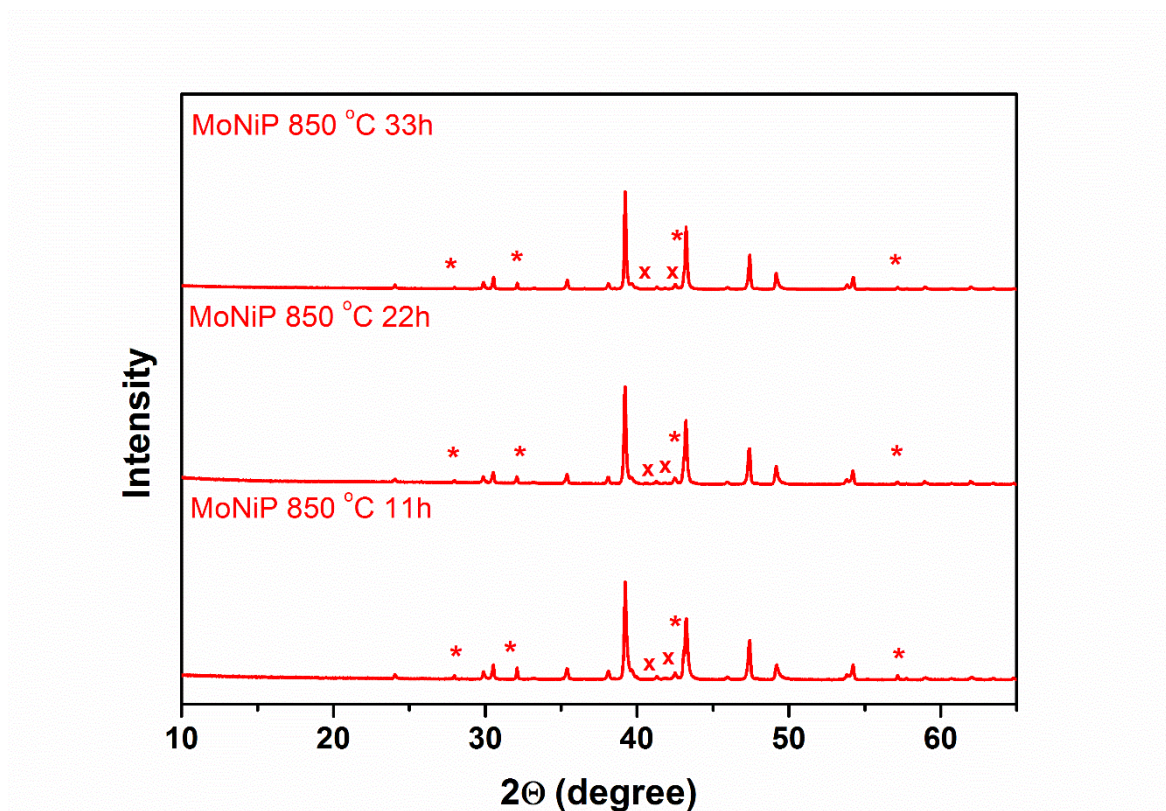
Figure 4-7 PXRD patterns of MoNiP depending on reaction times. Stars correspond to MoP and crosses to Mo_3P respectively.

Table 4. 6 The unit cell parameters obtained for MoNiP products depending on reaction times

Time, hours	a, Å	c, Å	V, Å^3
11	5.8533(1)	3.6923(1)	109.558(5)
22	5.8548(9)	3.6989(1)	109.810(3)
33	5.8582(3)	3.7022(2)	110.036(1)

4.3.2 Synthesis and characterisation of $(Mo_xNi_{1-x})_2P$ series

Once the optimal temperature and reduction conditions of 850 °C and 11 hours were established, four compounds belonging to the $(Mo_xNi_{1-x})P$ series were synthesised and compared. The common impurity of MoP was also made for comparison since known to be electrochemically active for HER.[41,42] A comparison between the PXRD patterns on the $(Mo_{1-x}Ni_x)_2P$ series is shown in Figure 4.7. The PXRD patterns displayed in Figure 4.7 show that with the exception of binary Ni_2P and MoP compounds none of the ternary phases were made as pure phase compounds. For all the samples belonging to the $(Mo_xNi_{1-x})P$ series a presence of impurities were found. However, with exception of MoP these were not

electroactive and thus, would not have a substantial effect on the electrochemical performance.
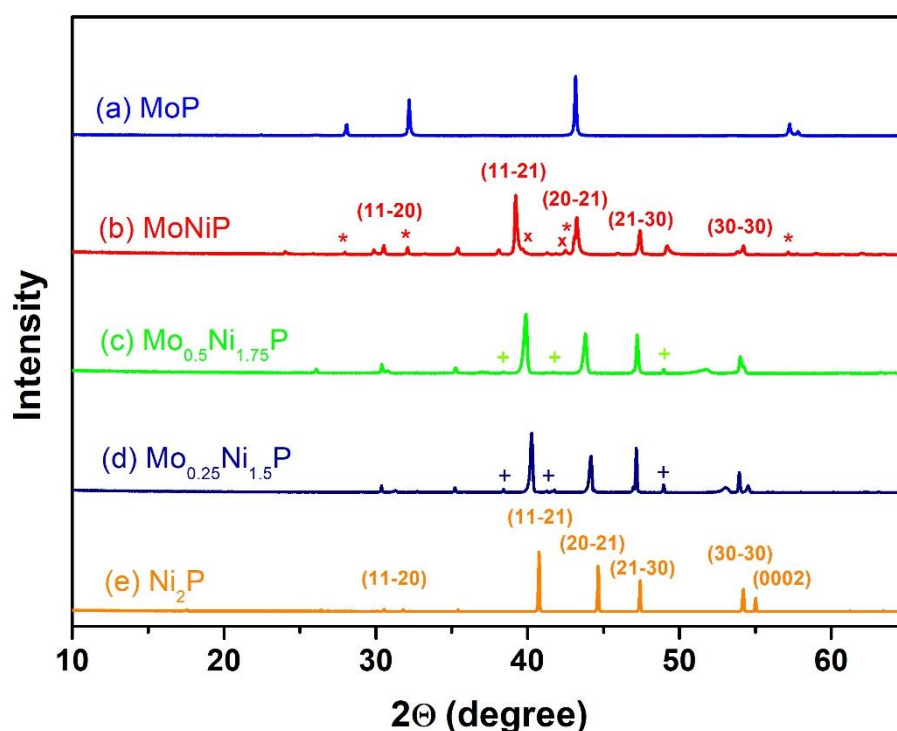
Figure 4-8 PXRD patterns of (a) MoP, (b) MoNiP, (c) $Mo_{0.5}Ni_{1.75}P$, (d) $Mo_{0.25}Ni_{1.5}P$ and (e) Ni_2P after being reduced T 850 °C for 11 hours. Stars denote MoP, plusses $Ni_{12}P_5$ and crosses Mo_3P. The numbers correspond to the associated Miller indices for the selected reflections of $(Mo_{1-x}Ni_x)_2P$.

On overall, the phosphide patterns agree with those previously reported in the literature.[12] For the stoichiometric Ni/Mo=1 ratio, MoNiP was synthesized showing the unit cell parameters of a=5.8598(2) Å and c=3.6992(2) Å, which were slightly smaller than the ones reported with cell values: a=5.861 Å and c=3.704 Å.[Ref [17]] The samples of the series obtained for Ni/Mo > 1 have a very similar XRD pattern, which exhibits a right shift of the (11-21), (20-21) and (21-30) peaks with the increase of the Ni content (Fig. 4.7); while there is a linear increase of the cell volume with the Mo composition (Table. 4.7). According to the Vegard's law, this linear trend indicates a homogenous substitution of nickel by molybdenum with increasing the Ni/Mo ratio. It should be noted that the products with Ni/Mo < 1 showed change in structure from Ni_2P to a mixture of various phases with MoP acting as a dominant phase and are not shown.

Table 4. 7 The unit cell parameters of $(Mo_{1-x}Ni_x)_2P$ products

Sample	a, Å	c, Å	V, Å³
Ni_2P	5.86448(5)	3.38820(5)	100.906(3)
$Mo_{0.25}Ni_{1.75}P$	5.88292(5)	3.45190(7)	103.461(2)
$Mo_{0.5}Ni_{1.5}P$	5.8744(2)	3.5401(3)	105.522(5)
MoNiP	5.8533(1)	3.6923 (1)	109.558(5)
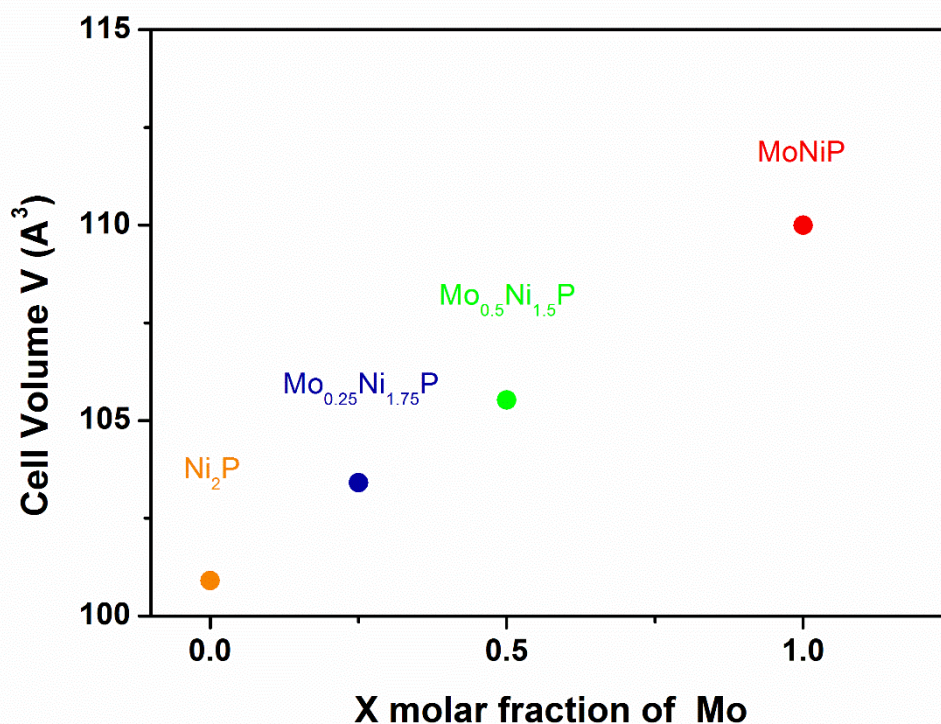
Figure 4-9 The dependence of the unit cell volumes with x in $(Mo_xNi_{1-x})_2P$.

4.3.3 Electrochemical investigation of $(Mo_xNi_{1-x})_2P$

4.3.3.1 Electrochemical performance of $(Mo_{1-x}Ni_x)_2P$ in acidic solution

The materials belonging to the $(Mo_{1-x}Ni_x)_2P$ series were tested for the hydrogen evolution reaction. There was an enhancement of the HER activity as more nickel was replaced by molybdenum within the structure (Figure 4.9). For all the compounds tested, MoNiP showed the best performance.

Overall, it appeared that the substitution of the molybdenum on Ni2 site had a positive effect on the catalytic performance in bulk form. It was evident that the overpotential of 229 mV obtained for MoNiP appeared to be very comparable to the overpotential of MoP (242 mV) at the current density of 10 mA cm⁻², which was prepared using the same conditions and used as a control sample. However,

since MoNiP showed a similar current density as MoP, it was unlikely that its improved performance was due to minor MoP impurities.
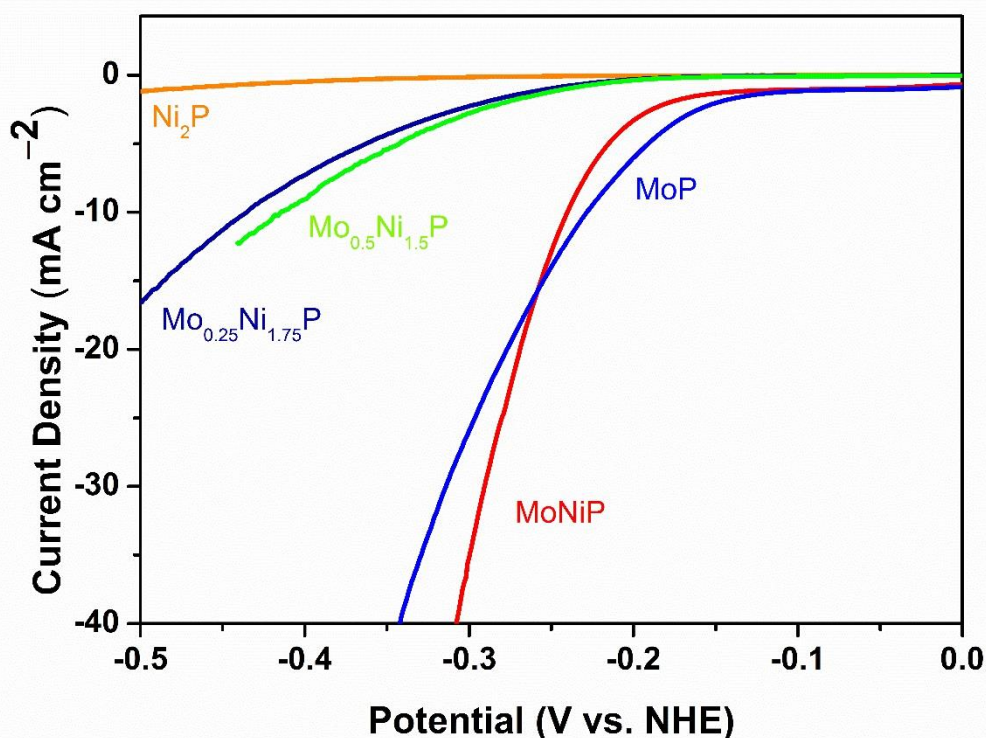
Figure 4-10 Cyclic voltammograms of MoP, MoNiP, $Mo_{0.25}Ni_{1.75}P$, $Mo_{0.5}Ni_{1.75}P$ and Ni_2P at 0.5M H_2SO_4.

Table 4.8 summarizes the performance of the materials. It is noticeable that Ni_2P was a remarkably inefficient electrocatalyst when compared with the nanostructured form reported earlier.[1]

Table 4. 8 Overpotential of the $Mo_xNi_{(2-x)}P$ series at 0.5 M H_2SO_4.

Sample	η at 10 mA cm^{-2}
MoP	229 mV
MoNiP	242 mV
$Mo_{0.5}Ni_{1.5}P$	401 mV
$Mo_{0.25}Ni_{1.75}P$	436 mV
Ni_2P	Not obtained

There are several explanations for this phenomenon. Firstly, it was extremely difficult to disperse Ni_2P into inks. As a result, the material tended to fall off the electrode during the measurements. Secondly, the free-standing and highly

crystalline product may have the most active sites blocked for the HER. Finally, it is still open to debate[43] whether it is Ni_2P or other phases that are more active for HER. However, the underlying trend is very similar to the one discussed above in Co-Ni-P system. The replacement of Ni with Mo clearly leads to improvement of the electrocatalytic performance. This highlights the potential of MoNiP as a good electrocatalyst. Even in free-standing form and without additional nanostructuring / composites with carbon it shows a very good performance outperforming free-standing CoNiP compound.[25]

4.3.3.2 Electrochemical performance of $(Mo_{1-x}Ni_x)_2P$ in basic solution

The materials were also tested for their catalytic performances in a 1M KOH base solution. To test the material, the potential was converted using the Nernst equation and the resulting values were reported according to the RHE electrode. In contrast to the acid media experiments, the control MoP sample had a substantially better performance showing the overpotential of 174 mV at the current density of 10 mA cm^{-2}, while MoNiP showed the value of 223 mV (Figure 4.10 and Table 4.9).
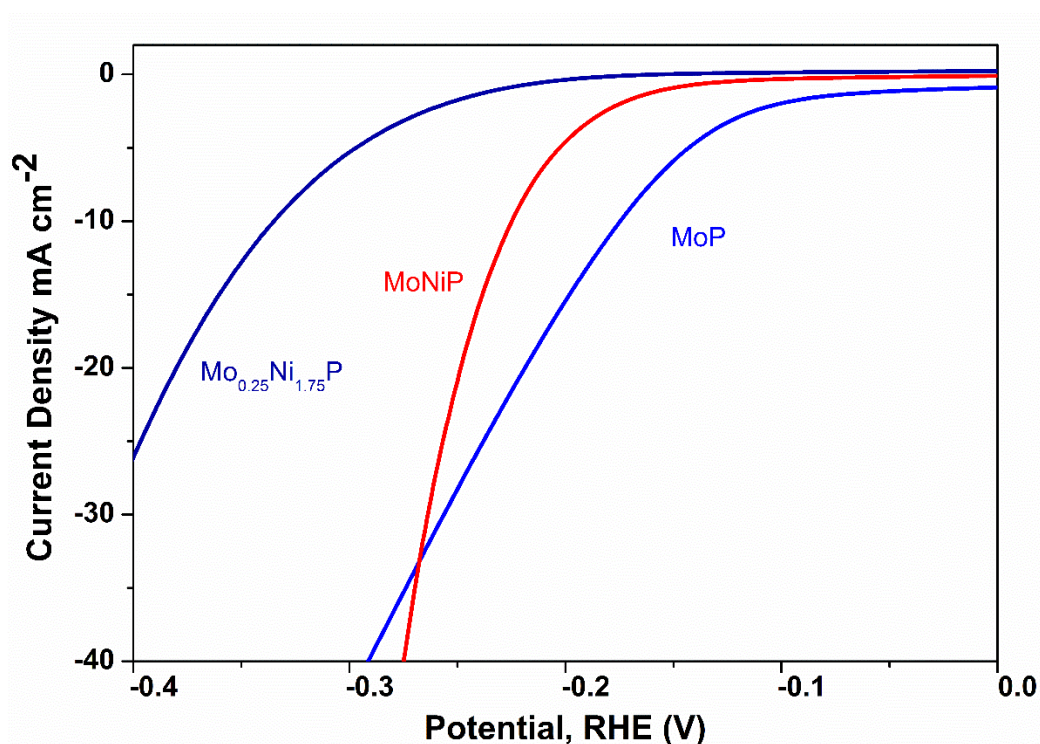
Figure 4-11 Cyclic voltammogram of MoP, MoNiP and $Mo_{0.25}Ni_{1.75}P$ synthesized tested for HER in basic media at 1 M KOH.

Table 4. 9 Overpotentials at 10 mA cm^{-2} for the bulk form phosphides tested in basic media.

Sample	η at 10 mA cm^{-2}
MoP	174 mV
MoNiP	223 mV
Mo$_{0.25}$Ni$_{1.75}$P	336 mV

It appears that with the reduced amount of Mo within the structure there was a clear trend for a worse HER performance in alkaline media. This was evident from the η obtained for Mo$_{0.25}$Ni$_{1.75}$P which was relatively high suggesting that at least in case of alkaline solution the catalytic process might happen on the Mo sites. Therefore, there might be completely different HER mechanisms, which occur on the catalyst surface at acidic and basic condition. However, this time MoP significantly outperformed MoNiP and it was unclear whether the catalytic performance in alkaline media is solely due to impurities of MoP or intrinsic. Therefore, we decided to investigate an alternative reaction route to see if the phase purity can be improved. The use of citric acid as a stabilizer was used in the synthesis of phase pure phases in Mo-Ni-P system before.[44,45,41] Moreover, addition of citric acid led to an increase of the catalyst surface area which may help to improve dispersibility after the addition of the stabilizer. The high dispersibility may play an important role on the activity of the material making it more strongly attached to the surface of the testing electrode.

4.3.4 Synthesis of (Mo$_x$Ni$_{1-x}$)$_2$P solid solutions with citric acid

4.3.4.1 Synthesis of oxide precursors

Citric acid was added to the starting solution as the early literature reports suggested that it may lead to single phase samples.[44,45,41] Furthermore, the carbon residues can act as a structural promoter and helps avoid the formation of side products.[32] The synthesis of the phosphides MoP and Ni$_2$P with the use of citric acid was carried out by following the temperature-programmed reduction protocol identical to the one identified for the MoNiP above, $e.g.$ 850 °C and 11 hours.

The citric acid was dissolved in the 13 : 10 molar ratio with the phosphide source and mixed with the metal precursors. The solution dried overnight showed the presence of a sticky precipitate which colour vary between brown to green

depending on the composition. After drying in the oven, the precipitate doubled in its volume showing porous texture. All the powders obtained showed PXRD patterns with very broad background suggesting amorphous products (Table 4.10). The one exception was the precursor for MoNiP, which showed NH_4NO_3 as a crystalline impurity.
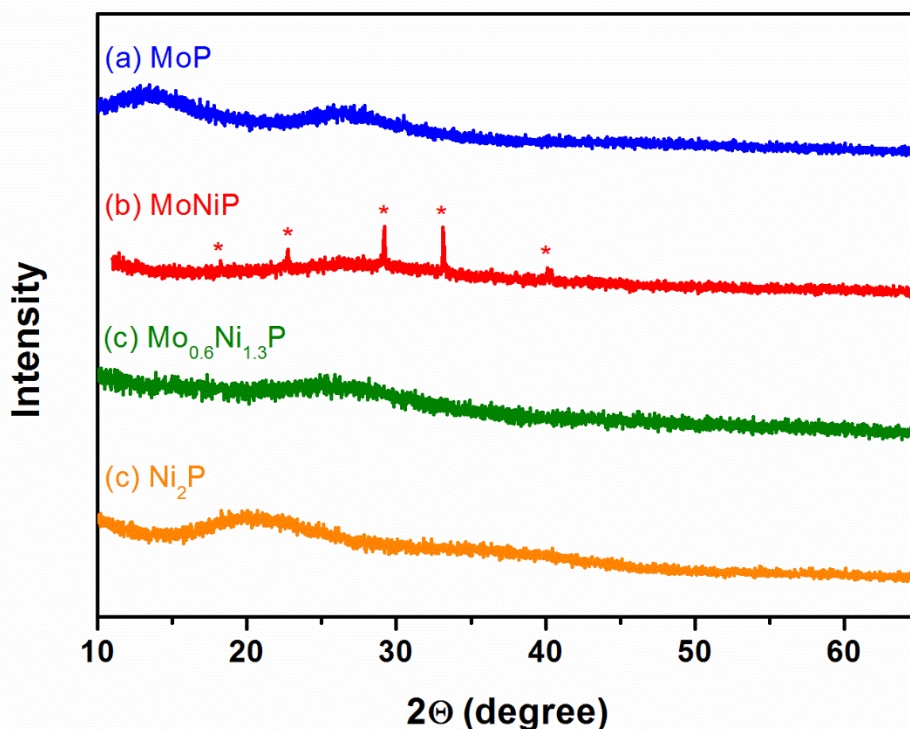
Figure 4-12 XRD patterns of the oxide precursors made with the presence of the citric acid as a stabilizer. Stars denotes NH_4NO_3.

Table 4. 10 Appearance of oxide precursors for synthesis of MoP, Ni_2P and the $Mo_{0.6}Ni_{1.3}P$.

Targeted composition	Precursor colour	Crystalline phases
MoP	Brown	Amorphous
$Mo_{0.6}Ni_{1.3}P$	Yellow-green	Amorphous
MoNiP	Yellow-green	Amorphous with NH_4NO_3
Ni_2P	Green	Amorphous

4.3.4.2 Synthesis and characterisation of $(Mo_xNi_{1-x})_2P$ series with the presence of citric acid

The products obtained after reducing the relevant precursor at 850 °C for 11 hours in 5% H_2 / Ar are shown in Figure 4.12. All products can be identified as phase pure from their XRD patterns suggesting that citric acid plays a key role in isolating a

pure phosphide. The PXRD data were refined by Rietveld refinement against the Fe_2P crystal structure-type model (see annex paragraph 7.3 for the results) further confirming excellent purity of the samples. The obtained unit cell parameters are summarized in the Table 4.11 and compare favourably with those reported in literature for MoNiP and Ni_2P.
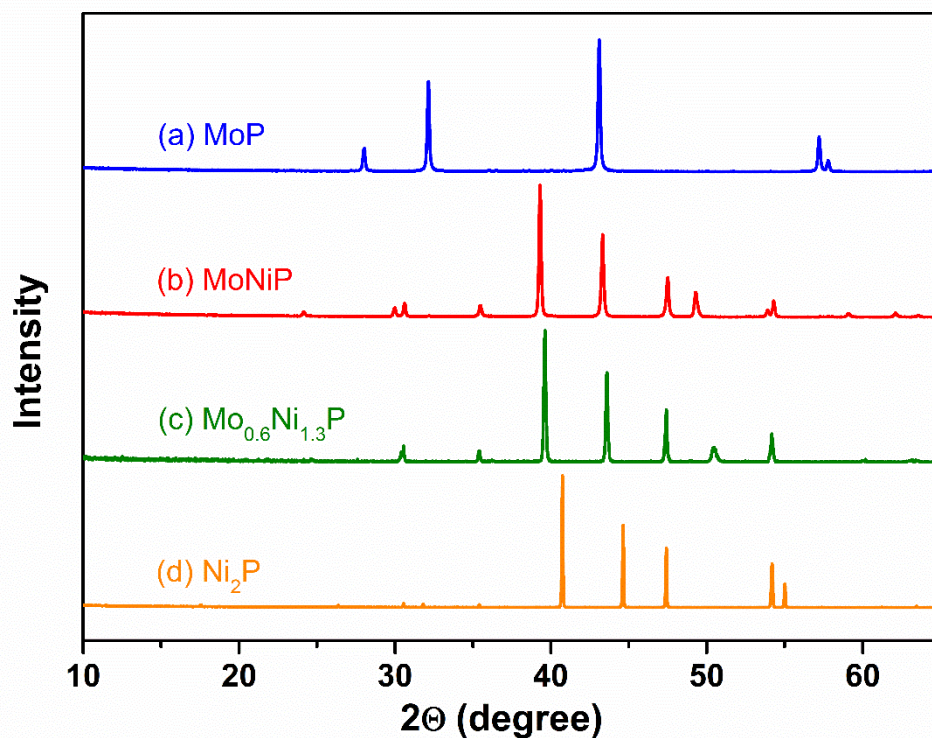
Figure 4-13 PXRD patterns of MoP, MoNiP, $Mo_{0.6}Ni_{1.3}P$ and Ni_2P synthesized with the addition of citric acid.

Table 4. 11 The unit cell parameters of Ni_2P, $Mo_{0.6}Ni_{1.3}P$ and MoNiP.

Sample	a, Å	c, Å	V, Å³
Ni_2P	5.86490(3)	3.38922(3)	100.961(1)
$Mo_{0.6}Ni_{1.3}P$	5.8572(1)	3.6132(1)	107.355(4)
MoNiP	5.85937(7)	3.70152 (8)	110.056(4)
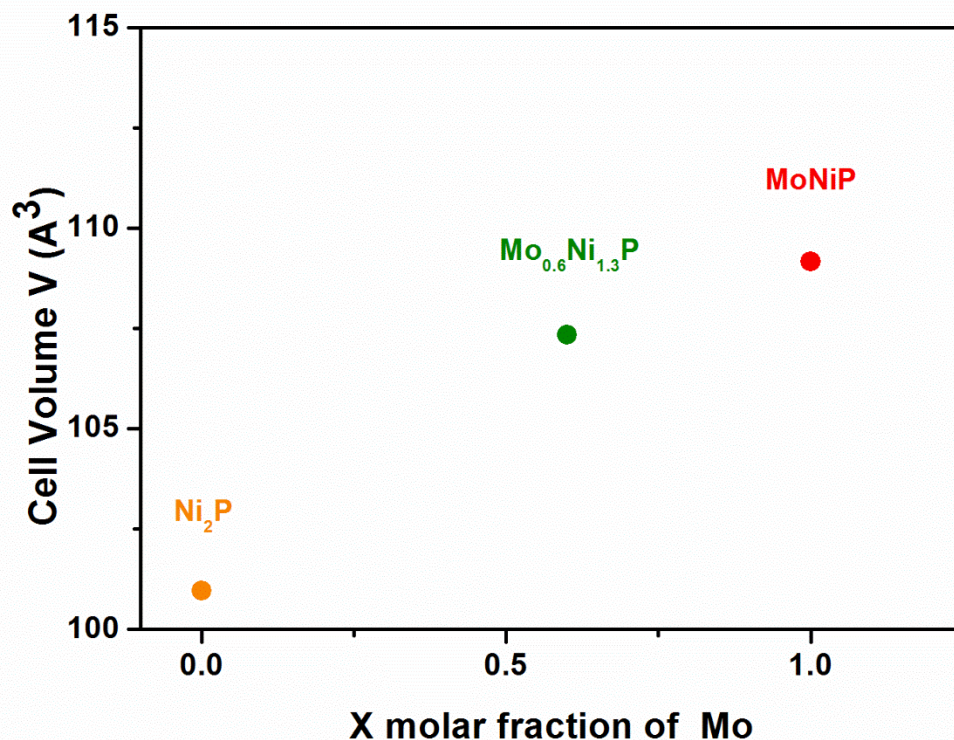
Figure 4-14 The unit cell volume versus the molar fraction of molybdenum in $(Mo_xNi_{1-x})_2P$ series.

The unit cell volume of 110.056(4) $Å^3$ for MoNiP phase with addition of citric acid was slightly larger than the one observed without addition of the structural promoter 110.002(6) $Å^3$ and compared more favourably with the literature data for MoNiP (110.19 $Å^3$) prepared directly from the elements.[17,12] This may indicate that it was much closer to stoichiometric composition and also eliminates the possibility of potential incorporation of carbon within the crystal structure.

4.3.5 Electrochemical Characterization

4.3.5.1 Hydrogen evolution reaction activity of $Mo_xNi_{(2-x)}P$ series with citric acid in basic media

The MoP sample showed a marginal increase in overpotential (compared to the one without citric acid discussed above) from 174 mV to 187 mV at 10 mA cm^{-2} (Figure 4.14 and Table 4.12). However, the overpotential of MoNiP decreased from 223 mV (without citric acid) to 199 mV (with citric acid) at 10 mA cm^{-2}.

Remarkably, there was no clear trend of electrochemical performance in the $Mo_xNi_{(2-x)}P$ series. In fact, other than Ni_2P, the measurements lie within the

experimental error and therefore performed similarly despite their composition. For this reason, $Mo_{0.6}Ni_{1.3}P$ could be a good competitor for MoP because of the lower cost of nickel compared to molybdenum.
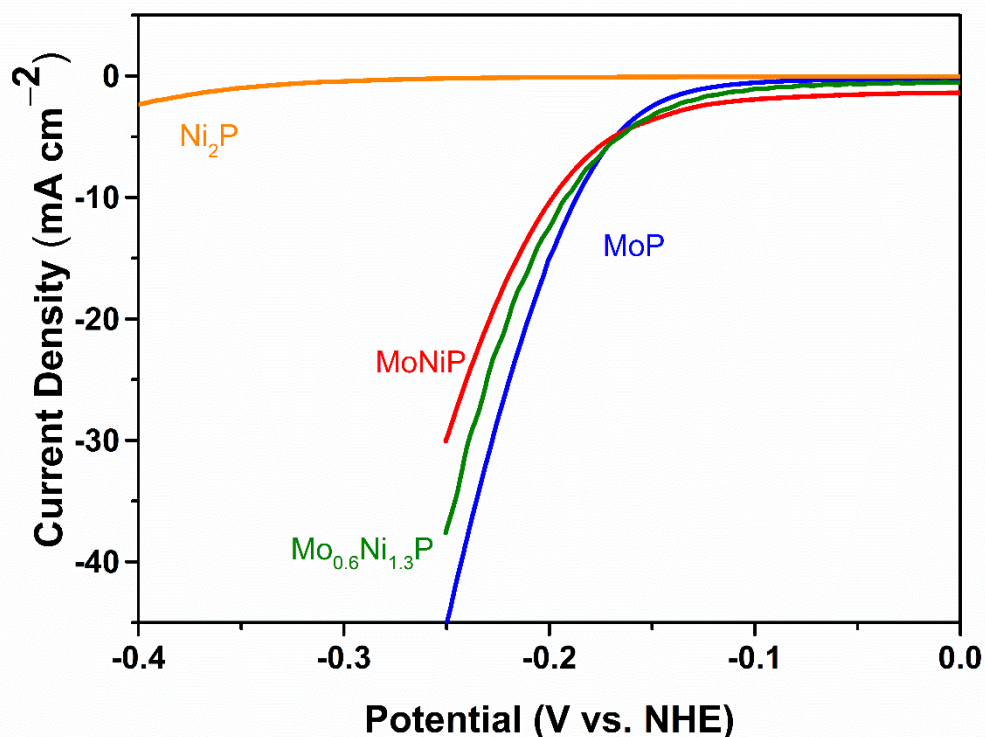
Figure 4-15 Cyclic voltammogram of MoP, MoNiP, $Mo_{0.6}Ni_{1.3}P$ and Ni_2P synthesized in presence of citric acid and tested for HER in basic media at 1 M KOH.

Table 4. 12 Overpotentials at 10 mA cm^{-2} for the bulk form phosphides synthesized with citric acid in basic media.

Sample	η at 10 mA cm^{-2} with citric acid	Tafel slope mV dec^{-1}
MoP	187 mV	74
MoNiP	199 mV	96
$Mo_{0.6}Ni_{1.3}P$	192 mV	88
Ni_2P	509 mV	150

Figure 4.15 shows the Tafel slopes for the tested catalysts. As can be seen on the CV scan, except for Ni_2P the Tafel slope values were very similar between MoP and members of the $Mo_xNi_{(2-x)}P$ series, possibly indicating a similar HER mechanism.
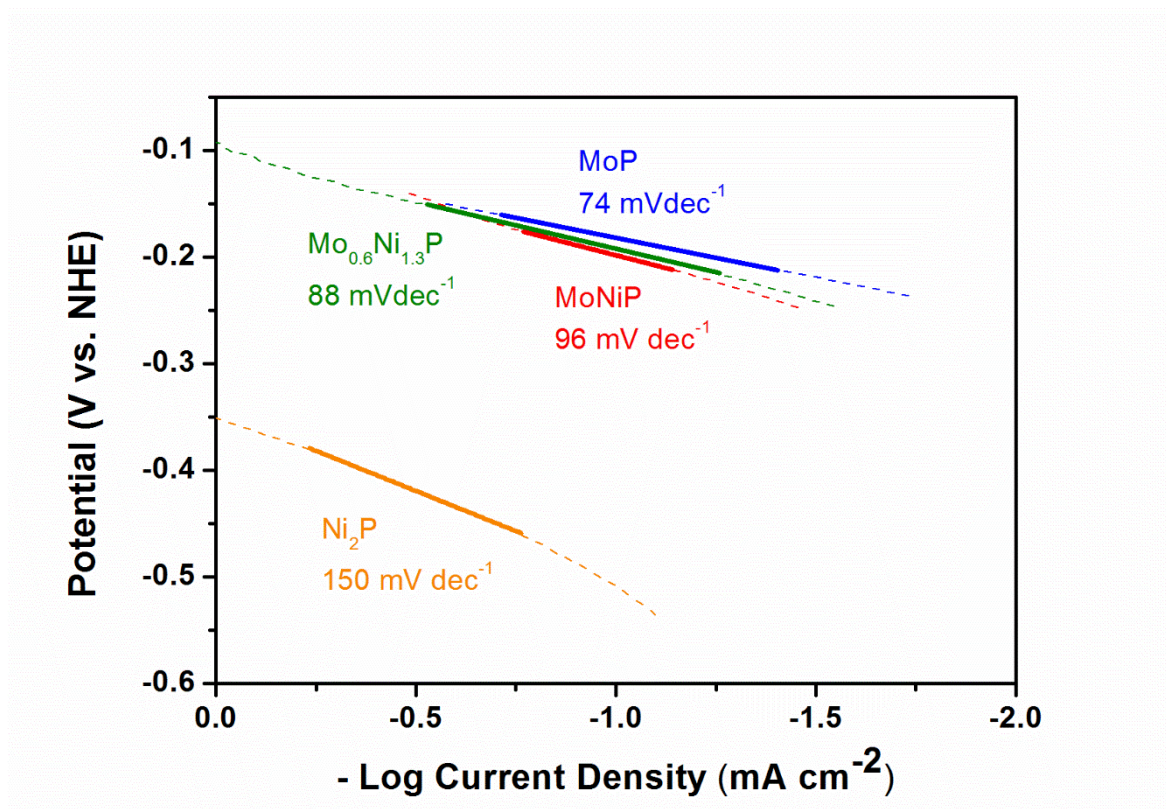
Figure 4-16 Tafel slopes for phosphides synthesized by the addition of citric acid from CV measurements at 1M KOH.

4.3.5.2 Hydrogen evolution reaction activity of $Mo_xNi_{(2-x)}P$ series with citric acid in acidic media

The results of electrochemical characterisations in acidic media are shown in Figure 4.16. The products followed a general trend similar to one observed for samples without addition of citric acid, *e.g.* replacement of Ni for Mo leads to improved performance within $Mo_xNi_{(2-x)}P$ series. However, there was a substantial reduction in the activity of MoP. The citric acid addition made MoP underperform with an overpotential of 314 mV compared with the 224 mV observed for the sample without citric acid. On the other hand, the MoNiP overpotential did not seem to be affected by the addition of citric acid, exhibiting a value of 241 mV.
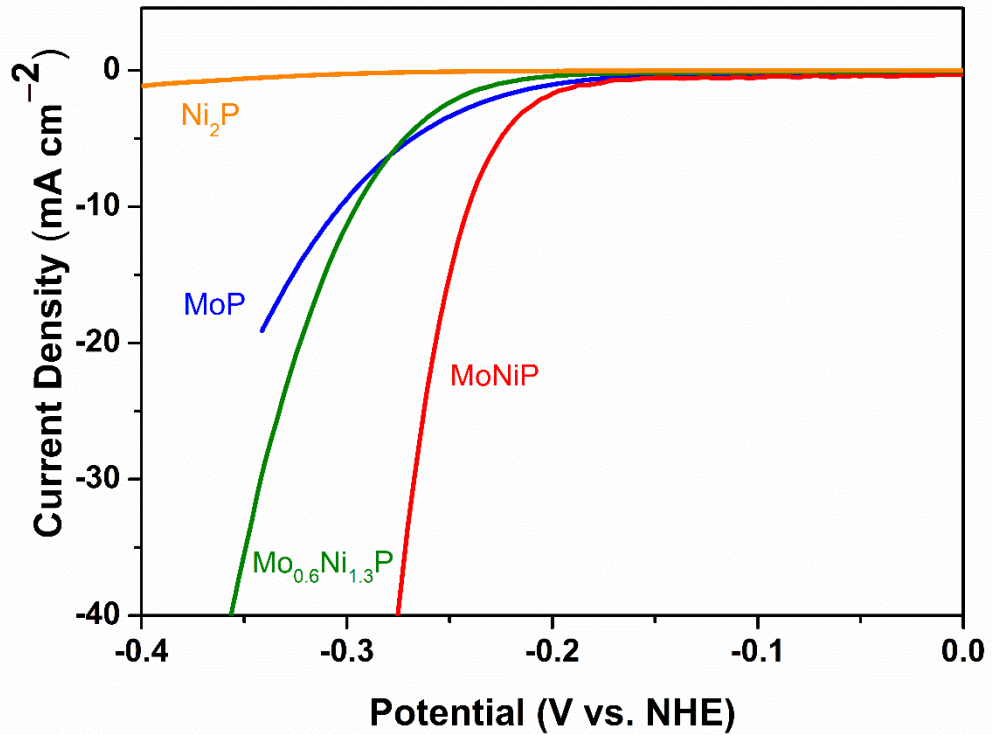
Figure 4-17 Cyclic voltammograms of MoP, MoNiP, $Mo_{0.6}Ni_{1.3}P$ and Ni_2P made with citric acid in 0.5 M H_2SO_4.

Figure 4.17 shows the Tafel slopes of the resulting compounds. MoNiP with the Tafel slope of 53 mV dec^{-1} was very close to the one reported for CoNiP nanoparticles.[25] This indicates that the Heyrovsky reaction may be the rate determining step.

$$M + H^+ + e^- \rightarrow MH_{ads} \qquad \text{Volmer reactionj is fast} \qquad (1)$$
$$MH_{ads} + H^+ + e^- \rightarrow M + H_2 \qquad \text{Heyrovsky reaction is slow} \qquad (2)$$

In this case, the reaction permitted hydrogen gas formation through a recombination of adsorbed hydrogen atoms and protons on the surface of the catalyst. This may indicate that the surface coverage is relatively high. The Tafel slopes for $Mo_{0.6}Ni_{1.3}P$ and MoP with the values of 66 and 86 mV dec^{-1} were intermediate in value and therefore it was difficult to define the rate determining step.
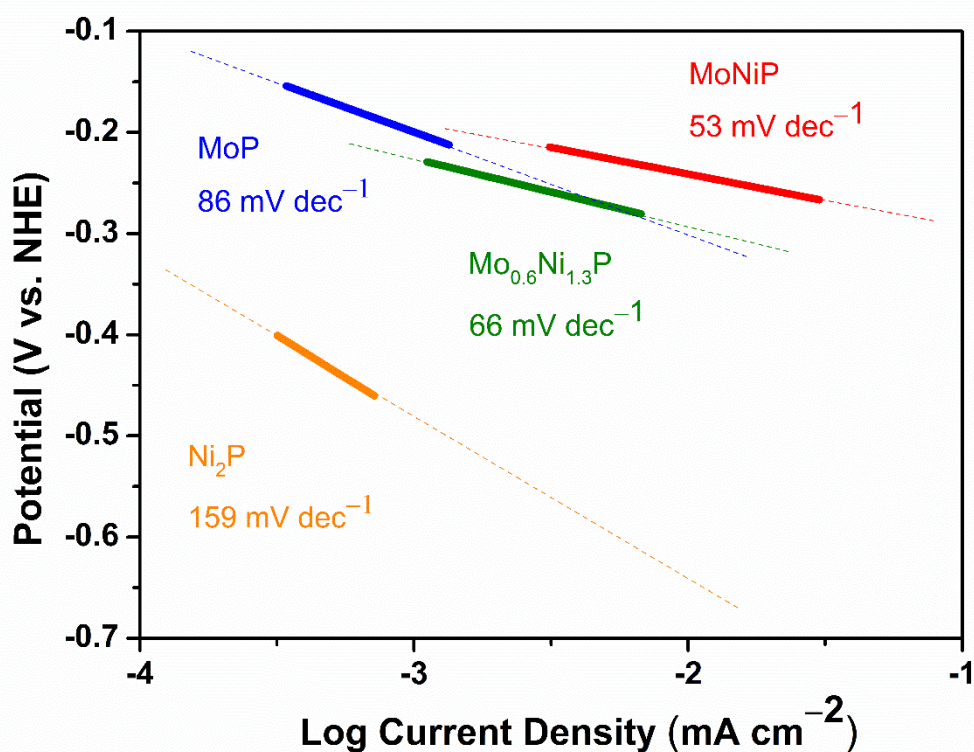
Figure 4-18 Tafel slopes for phosphides synthesized by the addition of citric acid from LSV measurements with a scan rate of 2 mV s^{-1} at 0.5 M H_2SO_4.

Table 4. 13 Electrochemical performance of the phosphides in acid media prepared with the addition of citric acid.

Sample	η at 10 mA cm^{-2}	Tafel slope mV dec^{-1}
MoP	314 mV	86
MoNiP	241 mV	53
Mo$_{0.6}$Ni$_{1.3}$P	296 mV	66
Ni$_2$P	Not obtained	159

4.3.5.3 Stability of phosphides synthesized with citric acid in acidic media

The stability of all the phosphides was probed by a galvanostatic scan in aqueous solution of 0.5 M H_2SO_4. A constant current intensity of 0.71 mA, which corresponds to the value for the reference current density 10 mA cm^{-2}, was applied over time to probe the constancy of the performances (Figure 4.18).

Overall, all the samples showed a good stability during the measurement. Samples MoNiP and MoP had a constant overpotential with slight decreases over 48 hours from 240 to 250 mV and from 336 to 346 mV, respectively. On the contrary, the

performance of $Mo_{0.6}Ni_{1.3}P$ improved from 450 to 415 mV over time, although not reaching the performances of the other compounds.
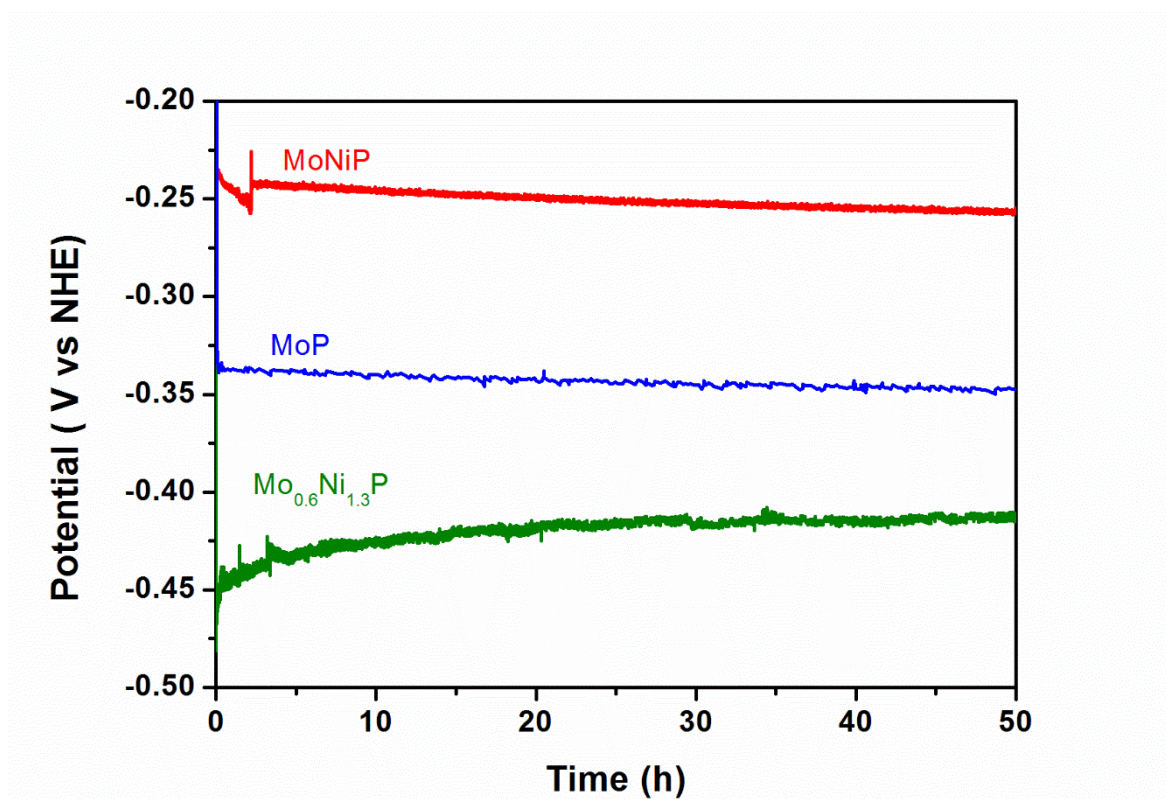
Figure 4-19 The galvanostatic curves of MoNiP, MoP and $Mo_{0.6}Ni_{1.3}P$ at 10 mA/cm^2 in 0.5 M H_2SO_4.

4.3.5.4 Electrochemical impedance spectroscopy (EIS)

All the EIS data are reported on Nyquist plots with the relative fitting obtained by the EC Biologic, which applies the Levenberg-Marquard minimization based on a complex nonlinear least-square procedure.[46] Sample Ni_2P was not catalytically active at the selected potential and therefore it was decided to exclude it from the EIS measurements.

From the fitting of the data obtained for the described materials, the charger transfer resistances conform to the HER activity values detected from the CV scan.

Sample MoNiP was electrochemically more active in acid media and resulted in lower charge transfer resistance with a value of 8.59 Ω. On the other hand, MoP sample had a higher charge transfer resistance of 71.11 Ω, which might be the reason for a high overpotential. The $Mo_{0.6}Ni_{1.3}P$ product showed the charge transfer resistance of 23.1 Ω which indicates that the improvement of overpotential with x could be driven by change in resistance.
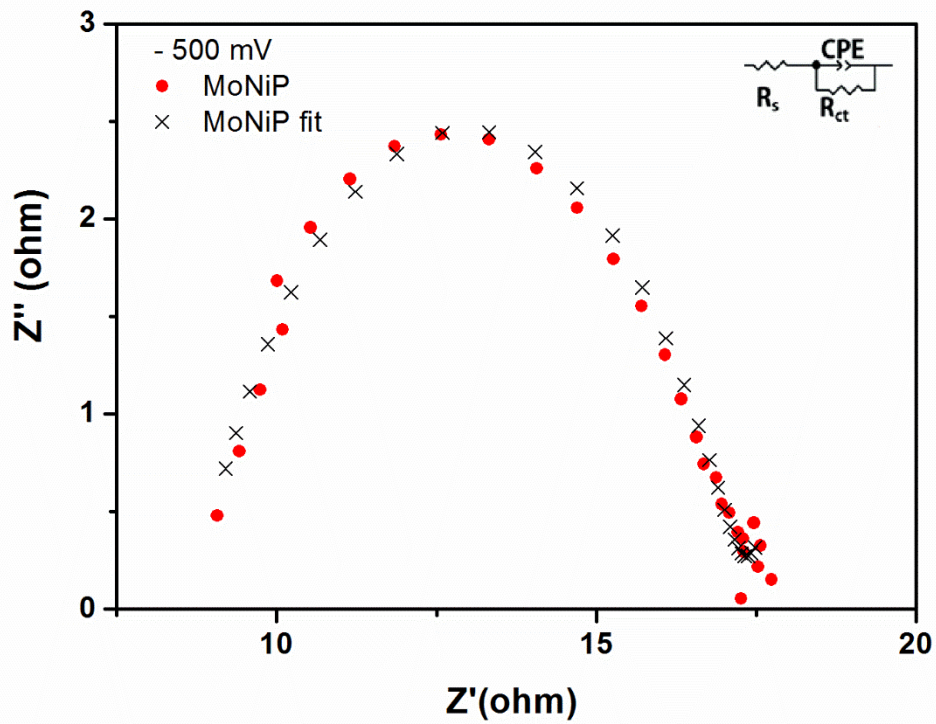
Figure 4-20 Nyquist plots of MoNiP sample for the HER in 0.5M. Crosses represent the fitted data by the 1 CPE model, experimental data as red circles.
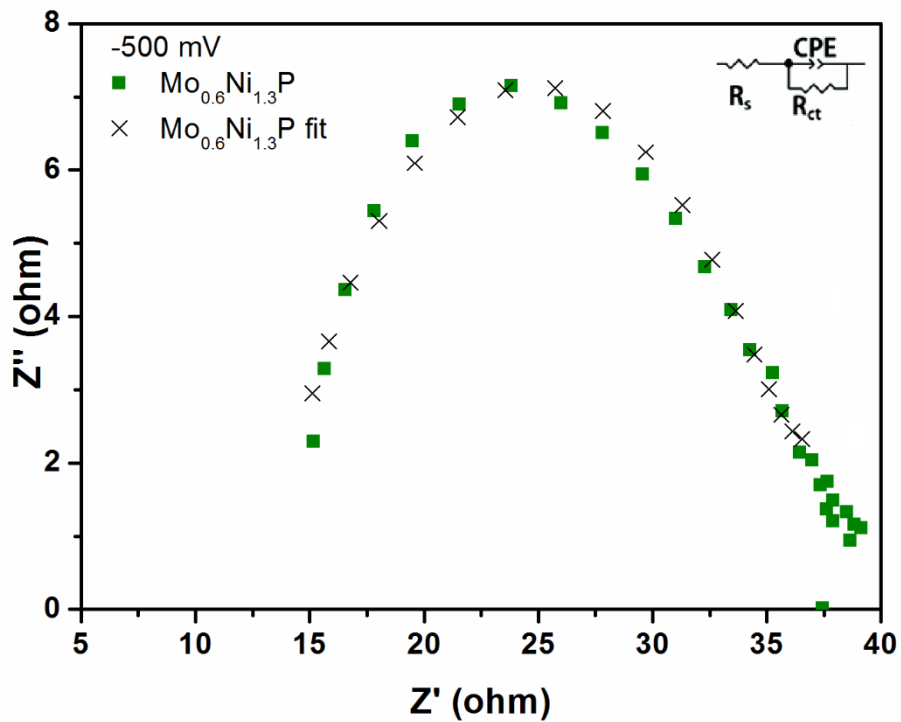
Figure 4-21 Nyquist diagram of sample $Mo_{0.6}Ni_{1.3}P$ for the HER in 0.5M H_2SO_4 solution. Crosses represent the fitted data by the 1 CPE model, experimental data as green square.
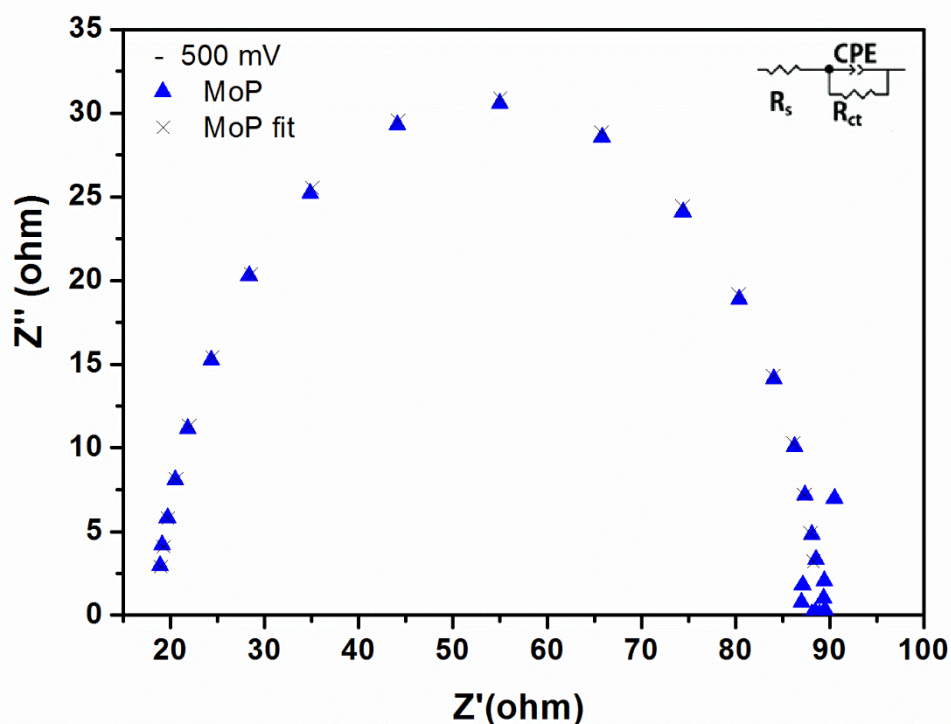
Figure 4-22 Nyquist diagram of sample MoP for the HER in 0.5M H_2SO_4 solution. Crosses represent the fitted data by the 1 CPE model, experimental data as blue trianlge.

Table 4. 14 Electronic impedance data fitted using the Randles circuit model consisting of a resistor (R_s) in series with a parallel arrangement of a resistor (R_{ct}) and a constant phase element (CPE).

Sample	MoNiP	$Mo_{0.6}Ni_{1.3}P$	MoP
R_s solution resistance (Ω)	8.68±0.57	13.04±2.052	18.43±0.598
R_{ct} charge transfer resistance (Ω)	8.59±1.78	23.1±1.44	71.11±1.68
x^2 chi-square	0.928	2.085	1.028

4.3.5.5 The electrochemical surface area (ECSA)

The higher activity of MoNiP might be attributed to the larger amount of exposed active sites. Hence, the electrochemical surface area (ECSA) for all the samples with citric acid were estimated from the double-layer capacitance (C_{dl}) of the catalysts using cyclic voltammetry (Figure 4.22). The C_{dl} is proportional to the ECSA and therefore can be used as a good estimation of the electrochemical surface area.[47,48] From the measurement, MoNiP resulted the sample with the substantially higher ECSA meaning a major anion exchange ability between the electrolyte and the catalytic active sites. This might be due to a possible porous

nature of the material as was evident from SEM studies discussed below, which would enhance the anion accessibility and therefore the increase of active sites.
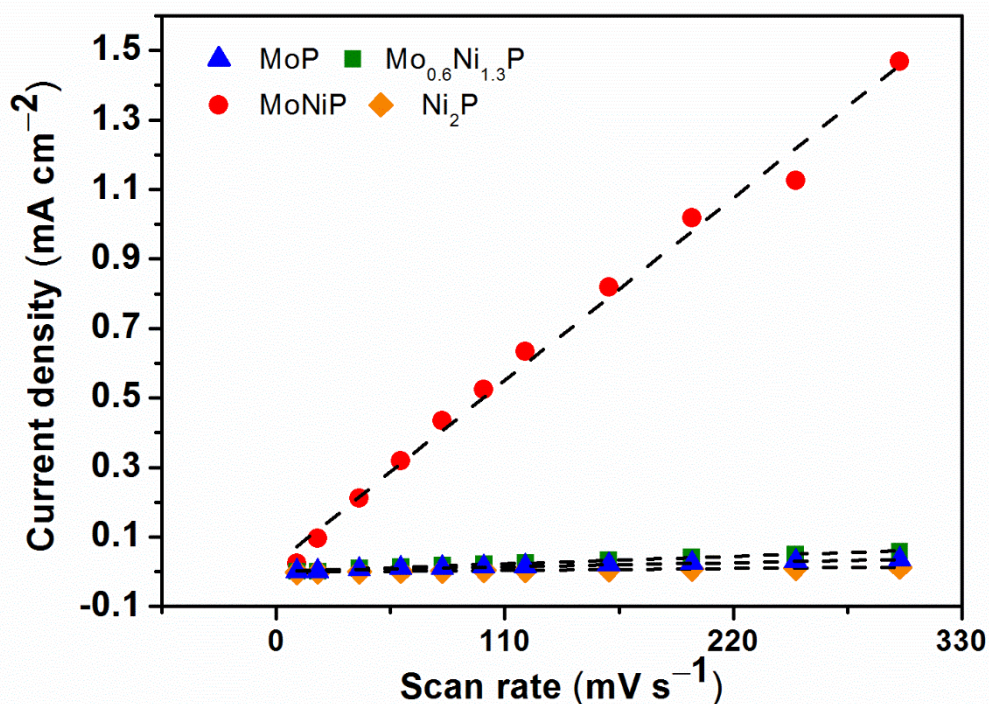
Figure 4-23 Current density as a function of the scan rate in 0.5 M H$_2$SO$_4$. The different scan rates vary from 10 to 300 mV s^{-1}.

4.3.6 Morphology characterization

The morphology of the compounds was investigated by electron microscopy. All the compounds were characterized by EDX spectroscopy and the elemental mapping analysis was carried out for the Mo$_{0.6}$Ni$_{1.3}$P to ensure a homogenous dispersion of the elements.

The sample morphology suggests porous morphology for MoNiP and Mo$_{0.6}$Ni$_{1.3}$P compounds examined (Figure 4.23). It is unclear what the origin for the pores but one can speculate this may stem from the decomposition of citric acid. The diameter of the pores seems to be smaller for MoNiP, which may explain the increased ECSA. MoP and Ni$_2$P sample on the other hand does not seem to show the porous feature.
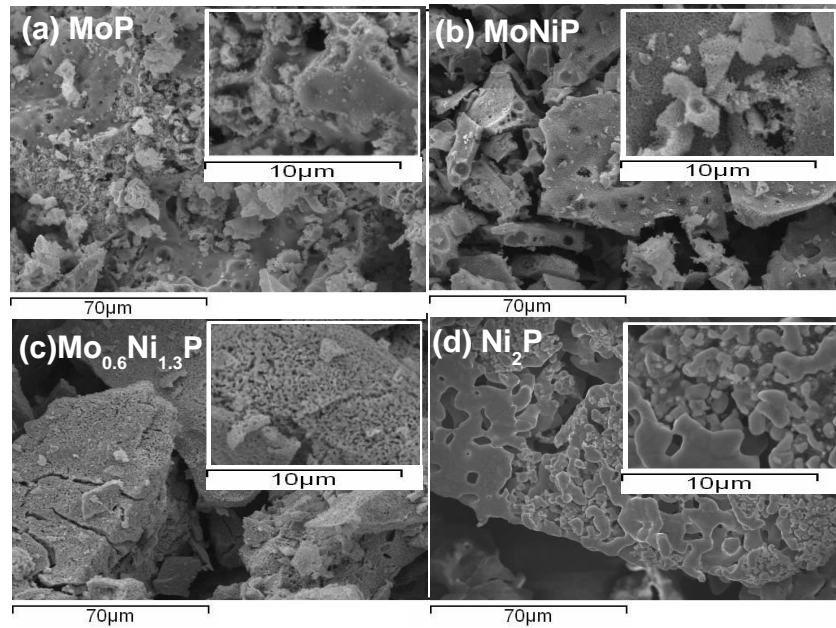
Figure 4-24 SEM images at magnifications of 800x and 4000x for (a) MoP, (b) MoNiP, (c) $Mo_{0.6}Ni_{1.3}P$ and (d) Ni_2P

The results of the elemental analysis by EDX summarized in Tables 4.15 - 4.18 show that samples composition in good agreement with the expected theoretically within the error of the measurements. However, there is a slight deficiency in phosphorus for $Mo_{0.6}Ni_{1.3}P$. Since the elemental analysis from EDX measurements was typically based on averaging the analysis from 3 spots it was decided that the elemental maps should be additionally recorded for this sample in order to identify possible phase inhomogeneity and provide a more representative sample composition.

Table 4. 15 Elemental analysis (at. %) by EDX for MoP

Composition	Experimental At. %	Theoretical at. %
Mo	49.15±1.18	50
P	50.85±1.50	50

Table 4. 16 Elemental analysis (at. %) by EDX for MoNiP

Composition	Experimental At. %	Theoretical at. %
Mo	33.99±1.46	33.33
Ni	31.05±1.91	33.33
P	34.47±1.43	33.33

Table 4. 17 Elemental analysis (at. %) by EDX for $Mo_{0.6}Ni_{1.3}P$

Composition	Experimental At. %	Theoretical at. %
Mo	23.31±2.31	22.22
Ni	43.78±3.55	44.44
P	29.71±5.43	33.33

Table 4. 18 Elemental analysis (at. %) by EDX for Ni_2P

Composition	Experimental At. %	Theoretical at. %
Ni	66.08±1.79	66.66
P	33.95±1.77	33.33

EDX elemental mapping of $Mo_{0.6}Ni_{1.3}P$ is shown in Figure 4.24 and indicates that the Mo, Ni and P are equally distribiuted on the surface. Moreover, the EDX values obtained from the mapping (Table 4.19) rather than spot checks are much closer to the ideal $Mo_{0.6}Ni_{1.3}P$ composition.
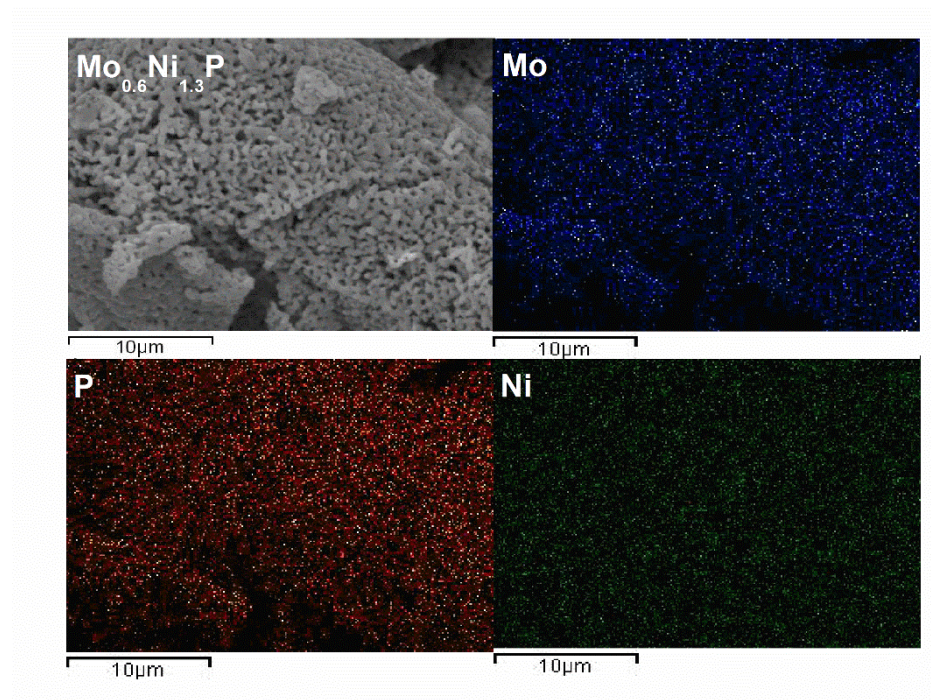
Figure 4-25 Elemental mapping of $Mo_{0.6}Ni_{1.3}P$ by EDX at magnifications of 4000x.

Table 4. 19 Averaged elemental analysis (at. %) from the $Mo_{0.6}Ni_{1.3}P$ mapping.

Composition	Experimental At. %	Theoretical at. %
Mo	21.6	22.22
Ni	45.85	44.44
P	32.54	33.33

4.4 Conclusions

In conclusion, it is possible to obtain solid solutions within Mo-Ni-P system from metal chlorides and phosphates route using 5 vol. % H_2 / 95 vol. % Ar gas mix. The optimal synthetic temperature and reaction time for the product with a good catalytic performance was found to be 850°C and 11 hours respectively. Longer reaction times has led to more crystalline products which, however, showed poor electrocatalytic properties. In line with the literature, it was found that the hexagonal structure within solid solutions $Mo_xNi_{(2-x)}P$ exists to the maximum value of x = 1.

The addition of citric acid as a stabilizer was required in order to obtain pure phase samples. The product without citric acid tended to contain MoP as an impurity, which might have obscured the results of electrocatalytic performance. However, when the pure phase samples were tested a clear trend of improved electrocatalytic performance as the solid solutions became Mo-rich was found in acidic media. The performance was peaking for MoNiP (x=1) with an overpotential of 241 mV at 10 mA cm^{-2}

The Tafel slope of 53 mV dec^{-1} suggests that recombination of adsorbed hydrogen atoms at the surface of the MoNiP may be the limiting stage for the reaction. The surface area might be the underlying reason for good catalytic performance as evidenced by ECSA and SEM measurements. Furthermore, the charge transfer resistivity decreases with the increasing x within $Mo_xNi_{(2-x)}P$ that may additionally contribute to a better performance of the MoNiP.

Remarkably, Ni_2P tended to be the worst performing material whether the citric acid was added or not. Although, the primarily cause for such behaviour may be associated with the difficulty to disperse the catalyst into ink it is evident that Ni_2P is not a particularly good electrocatalyst (at least in free-standing form). In this context, the effect of Mo replacing Ni within hexagonal structure of Ni_2P is

rather striking. This is especially true since the replacement occurs preferentially on 0002 (not 0001) layer. However, since the electrocatalytic performance of Ni_2P was attributed to sites on the 0001 planes this work opened up an interesting opportunity for understanding the actual catalytic surface in phosphide systems. From this prospective follow up computational studies would be extremely beneficial.

Finally, all the materials prepared showed stable performances over 48 hours, making them competent catalyst for future application. In addition, the hydrogen evolution reaction experiments in basic media revealed that there was no clear trend within $Mo_xNi_{(2-x)}P$ series, as was the case for acidic media. However, $Mo_{0.6}Ni_{1.3}P$ showed a very low overpotential of 192 mV at 10 mA cm^{-2} in 1 M KOH. Given the fact that Ni is a cheaper (and more earth-abundant) metal than Mo, $Mo_{0.6}Ni_{1.3}P$ presents a good prototype for future electrocatalysis.

4.5 Bibliography

1. Popczun, E. J. *et al*. Nanostructured Nickel Phosphide as an Electrocatlyst for the Hydrogen Evolution Reaction. (2013).

2. Ted Oyama, Travis Gott, H. Z. and Y. K. L. Transition metal phosphide hydroprocessing catalysts: A review. *Catal. Today* **143**, 94–107 (2009).

3. Stig Rundqvist, Margareta Yhland, Richard Dahlbom, J. Sjövall, O. T. and H. F. X-Ray Investigations of Mn3P, Mn2P, and Ni2P. *Actra Chem. Scand* **116**, 992–998 (1962).

4. Robert B. Wexlerm, J. M. P. M. and A. M. R. Stable Phosphorus-Enriched (0001) Surfaces of Nickel Phosphides. *Chem. Mater*. **28**, 5365–5372 (2016).

5. Alvin B. Hernandez, Hiroko Ariga, Satoru Takakusagi, Kumiko Kinoshita, Shushi Suzuki, Shigeki Otani, S. Ted Oyama, K. A. Dynamical LEED analysis of Ni2P (0 0 0 1)-1 × 1: Evidence for P-covered surface structure. *Chem. Phys. Lett*. **513**, (2011).

6. Md. Golam Moula, Shushi Suzuki, Wang-Jae Chun, Shigeki Otani, Shigeo Ted Oyama, and K. A. The First Atomic-scale Observation of a Ni2P(0001) Single Crystal Surface. *Chem. Lett*. **35**, 90–91 (2006).

7. Liu, P., Rodriguez, A. & York, N. Catalysts for Hydrogen Evolution from the [NiFe] Hydrogenase to the Ni 2 P (001) Surface : The Importance of Ensemble Effect. 14871–14878 (2005). doi:10.1021/ja0540019

8. Hiroko Ariga, Mayumi Kawashima, Satoru Takakusagi, and K. A. Density Function Theoretical Investigation on the Ni3PP Structure and the Hydrogen Adsorption Property of the Ni2P(0001) Surface. *Chem. Lett*. **42**, 1481–1483 (2013).

9. Goodenough, J. B. Interpretation of structure and magnetism in transition-metal pnictides M2X and (M1–xM'x)2X. *J. Solid State Chem*. **7**, 428–447 (1973).

10. Hulliger, F. *Structure and Bonding*. (1968).

11. Senateur, J.P.; Rouault, A.; l'Heritier, P.; Krumbuegel-Nyland, A.; Fruchart, R.; Fruchart, D.; Convert, P.; Roudaut, E. La selectivite des substitutions dans les phases MM'P etude de l'ordre par diffraction neutronique dans Ni Co P. *Mater. Res. Bull*. **8**, 229–238 (1973).

12. Ding Ma, Tiancun Xiao, Songhai Xie, Wuzong Zhou, S. L. G.-C. and M. L. H. G. Synthesis and Structure of Bimetallic Nickel Molybdenum Phosphide Solid. *Chem. Mater*. **16**, 2697–2699 (2004).

13. Ibrahim I. Abu, K. J. S. Hydrodenitrogenation of carbazole over a series of bulk Ni x MoP catalysts. *Catal. Today* **125**, 248–255 (2007).

14. Fruchart R., Roger, A. and S. J. P. Crystallographic and Magnetic Properties of Solid Solutions of the Phosphides M2P, M =Cr, Mn, Fe, Co, and Ni. *J. Appl. Phys*.

40, 1250–1257 (1969).

15. Nylund, A.; Roger, A.; Senateur, J.P.; Fruchart, R. *Strukturelle Übergänge zwischen Phosphiden, Arseniden und Arsenophosphiden der ZusammensetzungM2P,M2As undM2(P1—xAsx). Monatshefte fuer Chemie* **102**, (1971).

16. J. P. Sénateur, A. Rouault, P. L'Héritier, Mme A. Krumbügel-Nylund, R. Fruchart, D. Fruchart, P. C. and E. R. La selectivite des substitutions dans les phases MM'P etude de l'ordre par diffraction neutronique dans NiCoP. *Mater. Res. Bull.* **8**, 229–238 (1973).

17. Roland, P. A. R. *et al*. Structure Cristalline de NiMoP. *Acta Crystallogr. Sect. B* **3**, 2820–2823 (1977).

18. A Roger, JP Senateur, R. F. Les proprietes cristallographiques et magnetiques des solutions solides entre les phosphures Ni2 P - Co2 P - Fe2 P - Mn2 P et Cr2 P. *Ann. Chim* **4**, 79–91 (1969).

19. Orishchin, S.V.; Kuz'ma, Yu.B. (Kuzma, Yu.B.); Shchebel', L.Yu. (Shchebel, L. Y. . The Mn-Ni-P system. *Inorg. Mater.* **22**, (1986).

20. Chaudouet, P.; Roy-Montreuil, J.; Senateur, J.P.; Boursier, D.; Rouault, A.; Fruchart, R. New compounds M M' As and M M' P involving a 3d and a 4d element. *Solid Compd. Transit. Elem. VII Int. Conf. Grenoble* (1982).

21. Guerin, R.; Sergent, M. Nouveaux arseniures et phosphiures ternaires de molybdene ou de tungstene et d'elements 3d, de formule: M2-x Mex X (M = element 3d; Me= Mo, W; X = As, P). *Mater. Res. Bull.* **12**, 381–388 (1977).

22. Orishchin, S.V.; Kuz'ma, Y. B. Cr(W)-Ni-P ternary systems. *Inorg. Mater.* **20**, 360–365 (1984).

23. Li, J., Yan, M., Zhou, X., Huang, Z. & Xia, Z. Mechanistic Insights on Ternary Ni 2 − x Co x P for Hydrogen Evolution and Their Hybrids with Graphene as Highly Effi cient and Robust Catalysts for Overall Water Splitting. **26**, 6785–6796 (2016).

24. Liu, J. *et al*. Colloidal Ni2-xCoxP nanocrystals for the hydrogen evolution reaction. *J. Mater. Chem. A* **6**, 11453–11462 (2018).

25. Zhang, T. B. L. S. S. Synthesis of carbon quantum dot-doped NiCoP and enhanced electrocatalytic hydrogen evolution ability and mechanism. *Chem. Eng. J.* **351**, 186–194 (2018).

26. Liu, S. *et al*. Ru decorated with NiCoP : an efficient and durable hydrogen evolution reaction electrocatalyst in both acidic and alkaline conditions †. 13153–13156 (2017). doi:10.1039/c7cc08340h

27. Ma, B., Yang, Z., Chen, Y. & Yuan, Z. Nickel cobalt phosphide with three-dimensional nanostructure as a highly efficient electrocatalyst for hydrogen evolution reaction in both acidic and alkaline electrolytes. **12**, 375–380 (2019).

28. Kwong, W. L., Lee, C. C. & Messinger, J. Scalable Two-Step Synthesis of Nickel – Iron Phosphide Electrodes for Stable and E ffi cient Electrocatalytic Hydrogen Evolution. *J. Phys. Chem. C* **121**, 284-292 (2017).

29. Xu, H., Wei, J., Zhang, K., Shiraishi, Y. & Du, Y. Hierarchical NiMo Phosphide Nanosheets Strongly Anchored on Carbon Nanotubes as Robust Electrocatalysts for Overall Water Splitting. *ACS Appl. Mater. Interfaces* **10**, 29647–29655 (2018).

30. Mu, J., Li, J., Yang, E. & Zhao, X. Three-Dimensional Hierarchical Nickel Cobalt Phosphide Nanoflowers as an Efficient Electrocatalyst for the Hydrogen Evolution Reaction under Both Acidic and Alkaline Conditions. *ACS Appl. Energy Mater.* **1**, 3742–3751 (2018).

31. Luo Yu Ishwar Kumar Mishra Yunlong Xie Haiqing Zhou Jingying Sun Jianqing Zhou Yizhou Ni Dan Luo Fang Yu Ying Yu Shuo Chen Zhifeng Ren. Ternary Ni2(1-x)Mo2xP nanowire arrays toward efficient and stable hydrogen evolution electrocatalysis under large-current-density. *Nano Energy* **53**, 492–500 (2018).

32. Whiffen, V. M. L., Smith, K. J. & Straus, S. K. Applied Catalysis A : General The influence of citric acid on the synthesis and activity of high surface area MoP for the hydrodeoxygenation of 4-methylphenol. "*Applied Catal. A, Gen.* **419**–**420**, 111–125 (2012).

33. Rodriguez, J. A., Kim, J.-Y., Hanson, J. C., Sawhill, S. J. & Bussell, M. E. Physical and Chemical Properties of MoP, Ni $_2$ P, and MoNiP Hydrodesulfurization Catalysts: Time-Resolved X-ray Diffraction, Density Functional, and Hydrodesulfurization Activity Studies. *J. Phys. Chem. B* **107**, 6276–6285 (2003).

34. Diana C. Phillips, Stephanie J. Sawhill, R. S. and M. E. B. Synthesis , Characterization , and Hydrodesulfurization Properties of Silica-Supported Molybdenum Phosphide Catalysts. *J. Catal.* **273**, 266–273 (2002).

35. Rashkov, R., Arnaudova, M., Avdeev, G., Zielonka, A. & Jannakoudakis, P. NiW / TiO x composite layers as cathode material for hydrogen evolution reaction. *Int. J. Hydrogen Energy* **34**, 2095–2100 (2009).

36. Yuancai Ge, Shang-Peng Gao, Pei Dong, Robert Baines, Pulickel M. Ajayan, M. Y. and J. S. Insight into the hydrogen evolution reaction of nickel dichalcogenide nanosheets: activities related to non-metal ligands. *Nanoscale* **9**, 5538–5544 (2017).

37. Zhang, X., Meng, F., Mao, S., Ding, Q. & Shearer, M. J. Amorphous MoS x Cl y electrocatalyst supported by vertical graphene for e ffi cient electrochemical and photoelectrochemical hydrogen generation. *Energy Environ. Sci.* **8**, 862–868 (2015).

38. Xiao-yu Yan , Samrat Devaramani , Jing Chen , Duo-liang Shan , Dong-dong Qin, Q. M. and X. L. Self-supported rectangular CoP nanosheet arrays grown on a carbon cloth as an efficient electrocatalyst for the hydrogen evolution reaction over a variety of pH values. *New J. Chem* **41**, 2436-2442 (2013).

39. Carlos Valero-Vidal, Isaac Herraiz-Cardona, Valentín Pérez-Herranz, A. I.-M. Stability of 3D-porous Ni/Cu cathodes under real alkaline electrolyzer operating

conditions and its effect on catalytic activity. *Appl. Catal. B Environ.* **198**, 142–153 (2016).

40. Xiaoping Daia, Kangli Dua, Zhanzhao Li Hui Sun, YingYang, W. Z. and X. Enhanced hydrogen evolution reaction on few–layer MoS2 nanosheets–coated functionalized carbon nanotubes. *Int. J. Hydrogen Energy* **40**, 8877–8888 (2015).

41. Peng Xiao, Mahasin Alam Sk, Larissa Thia, Xiaoming Ge, Rern Jern Lim, Jing-Yuan Wang, K. H. L. and X. W. Molybdenum phosphide as an efficient electrocatalyst for the hydrogen evolution reaction. *Energy enviromental Sci.* **7**, 2624-2629 (2014).

42. Chen, X. *et al*. Molybdenum phosphide : a new highly efficient catalyst for the electrochemical hydrogen evolution reaction. *Chem. Commun.* **50**, 11683–11685 (2014).

43. Lewis MacDonald, Jessica C. McGlynn, Nicola Irvine, Ihfaf Alshibane, Leanne G. Bloor, Benjamin Rausch, J. S. J. H. and L. C. Using earth abundant materials for the catalytic evolution of hydrogen from electron-coupled proton buffers. *Sustain. Energy Fuels* **1**, 1782–1787 (2017).

44. Cheng, R. *et al*. Synthesis and characterization of high surface area molybdenum phosphide. **316**, 160–168 (2007).

45. Wang, R. & Smith, K. J. Applied Catalysis A : General Hydrodesulfurization of 4 , 6-dimethyldibenzothiophene over high surface area metal phosphides. **361**, 18-25 (2009).

46. Ahmed Galal, S. A. D. and R. A. A. Hybrid organic/inorganic films of conducting polymers modified with phthalocyanines. II. EIS studies and film characterization. *J. Solid State Electrochem.* **11**, 531–542 (2007).

47. Bharathi Konkena, Kai junge Puring, Ilya Sinev, Stefan Piontek, Oleksiy Khavryuchenko, Johannes P. Dürholt, Rochus Schmid, Harun Tüysüz, Martin Muhler, W. S. and U.-P. A. Pentlandite rocks as sustainable and stable efficient electrocatalysts for hydrogen generation. *Nat. Comun.* **7**, 1–8 (2016).

48. Xia Long, Guixia Li, Zilong Wang, HouYu Zhu, Teng Zhang, Shuang Xiao, W. G. & Yang, and S. Metallic Iron–Nickel Sulfide Ultrathin Nanosheets As a Highly Active Electrocatalyst for Hydrogen Evolution Reaction in Acidic Media. *J. Am. Chem. Soc.* **137**, 11900–11903 (2015).

5 Electrocatalytic properties of nitride compounds

Synopsis

The aim of this work was to investigate the potentiality of ternary nitrides as novel hydrogen evolution reaction catalysts. Few nitrides has been reported and yet their performances have always showed to be poorer than other materials, which they have been compared. Moreover, only one ternary nitride has been reported so far, which performances are anyhow incremented by blending the material with carbon. In this chapter, the ternary nitride Ni_2Mo_3N was synthesized by a modified Pechini method obtaining a black crystalline powder in bulk form. The material obtained overperforms all the nitrides in bulk form reported in literature achieving in acidic media an overpotential of 130 mV at 10 mAcm^{-2}. The performances were however poorer in basic media obtaining an overpotential at 10 mAcm^{-2} of only 348 mV in a 1M KOH solution. Speculation has been done about the nature of the Ni_2Mo_3N activity finding on the metallic Nickel nature a possible reason. However, DFT calculation should be carried out to investigate the reason for this high activity. Finally, stability tests in acidic media showed that sample performance decreases over time from 130 mV to 171 mV after 10 hours while remaining still the best nitrides in bulk form reported.

5.1 Introduction

Transition metal nitrides are substantially more challenging to synthesise (especially in nanostructured form) than chalcogenides and phosphides discussed in Chapter 3 and 4. This is due to extremely strong triple bond in nitrogen. Therefore, synthetic procedure often requires access to ammonia gas which is rarely available in chemical labs due to environmental and safety concerns. However, recent reports[1,2] have demonstrated that more benign and easily accessible N_2 / H_2 mixes can be used for preparation of nitrides. Despite this advancement, the bottleneck still remains and very few nitrides active for HER have been reported up to date (Table 5.1). The initial research on electrocatalytically active nitrides stems from the early work on Ni-Mo-N material prepared on carbon support using ammonia synthesis.[3] The product of this reaction was poorly defined (morphologically and structurally) material with Ni / Mo ratio determined at 1:4.7. However, it showed a fairly good performance in 0.1M $HClO_4$

reaching an overpotential of 220 mV at 5 mA cm^{-2}. Quite interestingly the diffraction pattern of this NiMoN$_x$ showed the presence of Ni$_2$Mo$_3$N impurity. However, no attempts have been reported since then to identify whether the catalytic performance could be driven by Ni$_2$Mo$_3$N. In addition a relatively (comparatively with NiMoN$_x$) crystalline product of MoN supported on C was also prepared at similar reaction conditions and showed marginally worse performance compared with the Ni-doped analogue.

Table 5. 1 Electrochemical properties of selected nitrides for HER in acidic media

Reported material description	η at 10 mA cm^{-2} (acidic media)	Tafel slope, mV dec^{-1}	Ref.
NiMoN$_x$ / C nanosheet	220 mV (0.1M HClO$_4$) at 5 mA cm^{-2}	36	3
MoN / C nanosheet	250 mV (0.1M HClO$_4$) at 5 mA cm^{-2}	55	3
Co$_{0.6}$Mo$_{1.4}$N$_2$	200 mV (0.1M HClO$_4$)		4
MoN Exfoliated	290 mV (0.5M H$_2$SO$_4$)	90	5
MoN Bulk	300 mV (0.5M H$_2$SO$_4$) at 1 mA cm^{-2}		
γ- Mo$_2$N	300 mV (0.1M HClO$_4$)		6
Mo$_2$N / CNT-Graphene	186 mV (0.5M H$_2$SO$_4$)	72	7
γ- Mo$_2$N	381 mV (0.5M H$_2$SO$_4$)	108	8
Templated MoN carbon cage	62 mV (0.5M H$_2$SO$_4$)	54	9
MoN bulk	258 mV (0.5M H$_2$SO$_4$)	134	9
Nanostructured MoN carbon	128 mV (0.5M H$_2$SO$_4$)	52	10

However, there were some differences in Tafel slopes between MoN (55 mV dec^{-1}) and NiMoN$_x$ (36 mV dec^{-1}). For intermediate value of 36 mV dec^{-1} reported both Heyrovsky (2) theoretical value of slope 2RT/3F ≈ 40 mV dec^{-1} and Tafel (4) theoretical value of slope RT/2F ≈ 30 mV dec^{-1} processes could be rate limiting steps in HER (for ease of representation H$_3$O$^+$ replaced with H$^+$):

$$M + H^+ + e^- \rightarrow MH_{ads}$$ Volmer reaction is fast   (1)

$$MH_{ads} + H^+ + e^- \rightarrow M + H_2$$ Heyrovsky reaction is slow   (2)

$$M + H^+ + e^- \rightarrow MH_{ads} \qquad \text{Volmer reaction is fast} \qquad (3)$$

$$2MH_{ads} \rightarrow 2M + H_2 \qquad \text{Tafel reaction is slow} \qquad (4)$$

This indicates that adsorption of hydrogen is unhindered and high coverage is expected even at low currents densities. The authors chosen Tafel reaction as underlying mechanism of the reaction suggesting that the $NiMoN_x$ acts similar to Pt (a classical catalyst where Tafel mechanism observed).

In the follow up paper[4] the authors proposed the hexagonal $Co_{0.6}Mo_{1.4}N_2$ (which is isostructural with MoN crystallizing in the WC-structure type) as new electrocatalyst. The material prepared using ammonolysis of $CoMoO_4$ precursor was initially identified as $CoMoN_2$. The composition was later reassigned to $Co_{0.6}Mo_{1.4}N_2$ based on the results of neutron diffraction studies. The resulting product has demonstrated a relatively good performance reaching *ca.* 200 mV at 10 mA cm^{-2}. However, the performance of the catalyst changed dramatically (with overpotential raising to ca. 270 mV at 10 mA cm^{-2}) when it was tested in a freestanding form without addition of carbon paste.

Due to the layered structure of the hexagonal MoN a sonication-assisted exfoliation protocol was suggested to help to increase the surface area and the availability of active sites.[5] However, the exfoliated products only achieved the overpotential of *ca.* 290 mV at 10 mA cm^{-2} in 0.5 M H_2SO_4 showing the underperformance when compared with the MoN / C reported in [Ref. 3]. On the other hand, exfoliation led to a significant improvement (before the exfoliation MoN tested was not able to achieve the current densities of 10 mA cm^{-2}). When compared with sulphides and phosphides discussed in previous chapters this work on hexagonal MoN contains the only computational study of nitrides in the context of HER. The DFT calculations on MoN showed that this hexagonal nitride has a metallic character (in line with experimental observations)[11] which can be favourable for HER. Although no calculation were made to instigate the nature of the catalytic sites; the authors speculated that due to the structure of MoN consisting of edge-sharing {Mo_6N} octahedra, *e.g.* the surface is terminated by Mo atoms and therefore they are the catalytic sites. This, however, seems to conflict with the analysis of the crystal structure of MoN.[12] The latter study showed that depending on N-content the structure consists of a combination of {N_6Mo} trigonal prisms and {N_6Mo} octahedra, *e.g.* the surface is terminated by N atoms.

Recent work on the template synthesis of MoN by ammonolysis of MoO_2 encapsulated within a porous cage may provide an interesting protocol since this hybrid material showed BET surface area of 244 m^2 g^{-1}.[9] This enormous surface area has led to the incredibly low overpotential of 62 mV and the Tafel slope of 54 mV dec^{-1}. In the same vein, nanostructuring and blending with carbons has been demonstrated to be a leading cause of the good performance, *e.g.* nanostructured MoN with 125 mV and the Tafel slope of 51 mV dec^{-1} was reported recently.[10]

Cubic Mo_2N has been suggested as a viable alternative to the hexagonal MoN discussed above. In a rather unusual procedure requiring reaction between ammonium molybdate tetrahydrate $((NH_4)_6Mo_7O_{24}\cdot 4H_2O)$ and soybeans it is possible to obtain a multiphase sample consisting of Mo_2C and Mo_2N which showed pretty good catalytic performance reaching 180 mV at 10 mA cm^{-2}.[6] However, when the authors tested Mo_2C and Mo_2N separately the observed overpotentials were ca. 220 and 300 mV respectively at 10 mA cm^{-2} in 0.1M $HClO_4$. It should be mentioned that both catalyst were prepared as composites with carbon black. Therefore, it remains unclear whether Mo_2N was free from MoC_x impurities. Blending Mo_2N with carbon nanotubes and graphene tend to produce low crystalline material (as evidenced by relatively broad peaks in the X-ray diffraction pattern of the cubic Mo_2N) with quite good performance reaching 186 mV at 10 mA cm^{-2} in 0.5 M sulphuric acid. However, when Mo_2N was tested as a free-standing rather than composite material it showed substantially higher overpotential of 381 mV at 10 mA cm^{-2} in 0.5 M sulphuric acid. The authors attributed poor performance to Tafel slopes of 100 mV dec^{-1} suggesting relatively high free energy of adsorption at the surface of the catalyst.

From the studies above it seems that carbon is an essential part for the good performance of the catalyst while all freestanding materials underperforming the hybrids. However, it is still unclear why there is such a difference between bulk and carbon-functionalized MoN. The question whether it is the nitrogen or molybdenum that is responsible for the catalytic behaviour still remains unresolved. From this perspective a search for alternative nitrides which can show a good performance in bulk form may provide a better route towards the development of nitrides as competent catalysts for HER. One material, Ni_2Mo_3N stands out as it appears to have a surface terminated with metal atoms rather

than nitrogen and therefore it may be better suited for understanding the mechanism of HER on nitrides than MoN.

5.1.1 Structure, properties and synthesis of Ni_2Mo_3N

The cubic Ni_2Mo_3N (a = 6.634 Å) structure belongs to filled ß-Mn structure-type, also known as the Al_2Mo_3C structure-type.[13,14] Generally, the structure of this nitride can be described as an interpenetrating network of nickel atoms (Figure 4.1 a) and edge-sharing distorted $\{NMo_6\}$ octahedra (Figure 4.2 b). Apart from Ni_2Mo_3N three other ternary nitrides (Co_2Mo_3N, Pd_2Mo_3N and Pt_2Mo_3N)[15,16] and several quaternary nitrides ($FeNiMo_3N$, $FePtMo_3N$, $FePdMo_3N$, $FeRhMo_3N$ and $CoNiMo_3N$)[1,17] have been reported to show this structure type. Unlike, MoN and isostructural compounds the structure of the Ni_2Mo_3N suggests that the surface is terminated by metal atoms. This is further supported by XPS analysis with Mo 3d and Ni 2p spectra showing a binding energy of 852.58 eV corresponding to Ni in zero oxidation state.[18] Therefore, It would be interesting to compare this compounds with others on a Volcano plot to better understand how the HER activity changes accordingly with the different material composition. As mentioned before, the Volcano plot correlation is generally only valid for metals, alloys[19] and compounds, which display metal-terminated surfaces. From this perspective Ni_2Mo_3N appears to be a good target for catalytic performance and the opportunity to compare with relevant alloys would be quite interesting. In addition, Ni_2Mo_3N has been reported to be stable in ambient air which further suggests that it could be a competent and practical electrocatalyst.[14] Furthermore, it shows metallic conductivity displaying a remarkably low resistivity of 5.3 10^{-6} Ohm at room temperature.[14]
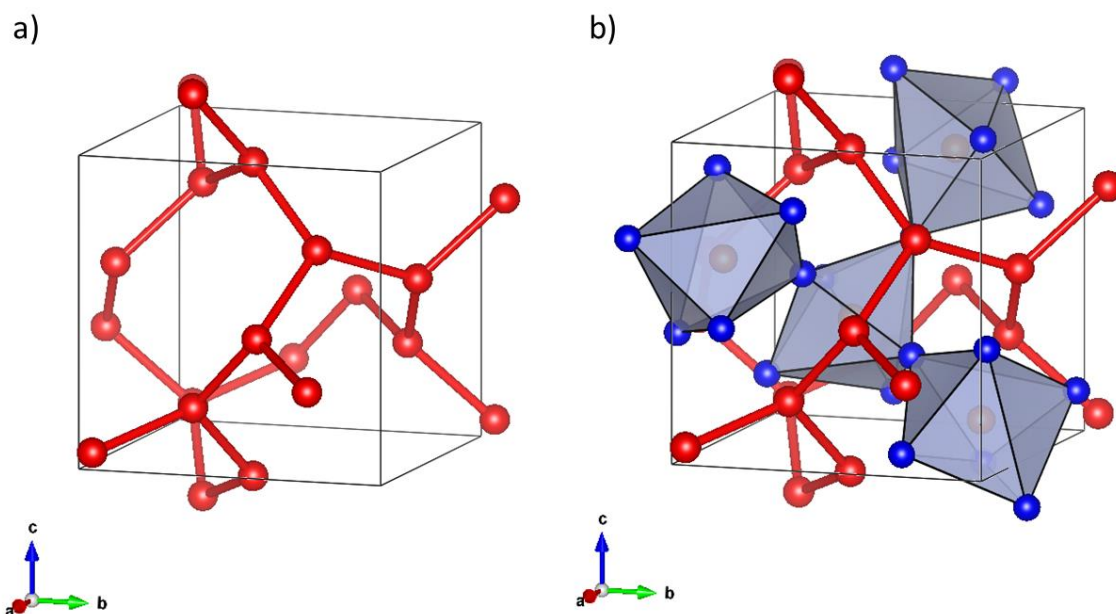
Figure 5-1 Crystal structure of Ni₂Mo₃N showing the network of Ni-atoms and Mo/N omitted for clarity (a) and the network of edge-sharing Mo₆N octahedra within the Ni net (b).

Ni_2Mo_3N is well studied compound as a catalyst for hydrodesulfurization[20] and ammonia synthesis[2,21] as well as for hydrogenation of polyaromatic compounds.[22,23] As a result there are several common synthetic routes for synthesis of Ni_2Mo_3N including ammonolysis of metal oxides;[24,25,26] reaction between $NiCl_2$, Mo and NaN_3 in an autoclave,[27] ammonolysis of Mo and Ni adducts in CH_3CN described in the literature.[2] Among these methods the use of commercially available and relatively benign (from a safety point of view) N_2/H_2 mixtures with metal oxides[28,29] probably presents the most effective way for synthesis of Ni_2Mo_3N.[1] Therefore, this approach was chosen for synthesis of Ni_2Mo_3N prepared in this work.

5.2 Experimental methods:

5.2.1 Synthesis of Ni₂Mo₃N

Reagents: $Ni(NO_3)_2$ (Janssen Chimica), $(NH_4)_6Mo_7O_{24}$ (Fluka Analytical, puriss. p.a., ACS reagent, ≥ 99.0%) and $C_6H_8O_7 H_2O$ (Sigma Aldrich, ACS reagent, ≥ 99.0%).

A nickel molybdenum oxide precursor was prepared by a modified protocol using the Pechini method described in [Ref. 1]. The reagents: nickel nitrate hexahydrate and ammonium molybdate tetrahydrate were dissolved in aqueous solution

acidified by 10% of nitric acid followed by addition of citric acid monohydrate on stirring. The clear solution was then, left to evaporate at 70 °C until a transparent-green gel was formed. The gel was finally calcinated in air at 500 °C (heating rate 60 °C min^{-1}) for 2 hours to obtain grey foam oxide precursor. The precursor was placed into a silica reactor tube, sandwiched between two silica wool pieces, and inserted into the centre of the furnace reactor. Finally, the reaction was carried out in a H$_2$/N$_2$ gas mixture (in a ratio of 3:1, supplied by BOC, H$_2$ 99.998%, N$_2$ 99.995%) flow at 700°C (heating rate of 10 °C min^{-1}) for 3 hours followed by natural furnace cooling to ambient.

5.2.2 Electrochemical characterization

A Biologic SP 150 in a three electrodes configuration at room temperature carried out most of the electrochemical analysis of Ni$_2$Mo$_3$N. The reference electrode used for the measurement was an Ag/AgCl (NaCl 3M) while a Pt wire was used as a counter electrode. The working electrode was a Glassy carbon electrode (0.071 cm^2 surface area), where the testing material was deposited by drop casting 30 µL of a DMF/Nafion ink (GC preparation and cleaning is already described on paragraph 4.2.1.1).

The Pt measurement was done using the same configuration with the use of Pt wire as a WE and a carbon felt as a CE. Finally, all the potential were reported on the NHE scale by using the equation: (NHE) = E(Ag/AgCl) + 0.209 V.

The HER and the Tafel slope measurement were carried out by using the *linear sweep voltammetry* technique with a scan rate of 2 mVs^{-1} on an acidic media of 0.5M H$_2$SO$_4$. The Ohmic resistance was corrected for each measurement. The HER activity was also tested in basic media using a solution 1 M of KOH and modifying the applied potential by the Nerst equation.

The ESCA measurement was performed on a non-Faradaic region by scanning the material with the CV scan technique between 0.155 V to 0.250 V vs NHE for different scan rate and then plotting the potential obtained for 0.209 V

The *electrochemical impedance spectroscopy* (EIS) measurement were carried out in a range of 200 Hz to 1Hz on an AC mode with an amplitude of 10 mV. The sample was probed on a range between - 200 mV to - 450 mV by increasing the potential of 50 mV at each measurement. The data obtained were than fitted by a simplified Randles circuit model using a parallel arrangement of a resistor R and a constant

phase element (CPE) in series with another resistor. Stability measurements were conducted in acidic media by CV scan and *Cromoamperometric* (CP) technique. The CV scan were performed between 0.2 to -0.3 V vs NHE with a scan rate of 100 mV s^{-1}. On the contrary, CP technique tested the sample stability by applying constant current of 0.071 mA overtime and stirring the solution during the measurement.

Gas chromatography (GC) was carried out using an Agilent Tecnologies 7890A GC apparatus coupled with the Chromoamperometric measurement to ensure a constant production of H_2 at the current density of 10 mA cm^{-2} over time. The material was tested with two electrode closed inside an airtight cell using a GC electrode as a WE and a Pt wire as a CE and Reference. During the electrolysis, the gas present on the headspace was collected using a syringe and injected on the 30 metre long 0.320 nm GC column at constant intervals. The carrier gas used for the column was Ar and the apparatus was calibrated with a range of volume % in argon supplied by CK Gas Products Limited (UK).

The expected number of moles of gas were calculated for the H_2 molecule by dividing the charge passed by 2F where F is the Faraday constant. The expected volume percentage was than obtained by taking the volume of 1 mole of an ideal gas at room temperature and pressure it to 24L. The Faraday efficiency was than calculated by the ratio of the gas volume % and the ones obtained by gas chromatography.

5.2.3 Characterization

5.2.3.1 Powder x-ray diffraction

The XRD pattern was collected by a Panalytical XPert-pro diffractometer (Cu$_{K\alpha}$ radiation corresponding to λ= 1.54178 Å wavelength). The XRD measurement was carried out on a 2θ range of 10 to 50 for 25 minutes on a Brags-Bretano configuration. The diffraction pattern of Ni_2Mo_3N was compared with the one already present on the ICSD database.

5.2.3.2 Scanning Electron Microscopy (SEM)

The instrument used to collect the SEM images and the EDX measurement was a Philips XL30 ESEM with an attached Oxford Instruments x-act EDX detector. The instrument was calibrated with a Cu foil standard before to start the measurements. The sample was prepared by depositing the powder on a black rounded carbon tape and then covered it by a thin layer of gold using spluttering to make it more conductive. The images were collected at 100×, 800× and 4000× magnification while the EDX spectroscopy was obtained by scanning three points for two minutes each area at 4000x magnification.

5.3 Results and discussions

5.3.1 Structural characterisation by PXRD

The initial oxide precursor exhibits a PXRD pattern consisting of a predominately mixture of $NiMoO_4$ and MoO_3 as previously reported in the literature (Figure 5.2).[1] The reduction of these oxides at 700 °C in H_2/N_2 mixture yields a black metallic looking material with a XRD pattern showing an excellent agreement with the pattern of Ni_2Mo_3N phase (Figure 5.3). The minor impurities are recognisable as two minor peaks that are associated with Mo_3Ni_2 alloy.

To test the crystal structure and compare the results with data from the literature, LeBail refinements of the PXRD data using a structural model within the $P4_132$ space group was carried out to estimate the unit cell parameters of the prepared product. The results are shown on Figure 5.4 and are in a good agreement between simulated and experimental profiles, which evinced to converge to the model of ß-Mn structure. The unit cell parameter a = 6.63100(7) Å (Table 5.2) is marginally smaller than previously reported a = 6.634 Å, suggesting that even if there is non-stoichiometry it is quite minor and is probably due to the impurity. The Ni_2Mo_3 alloy was not included into refinement due to fairly broad reflections observed for this phase.
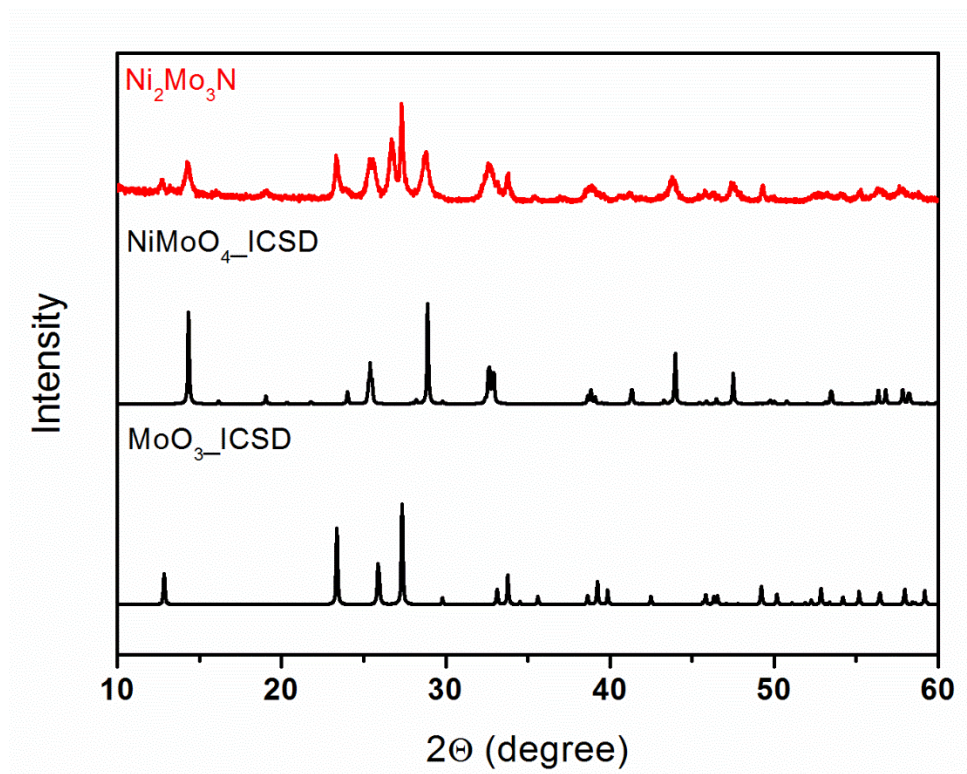
Figure 5-2 XRD pattern of the oxide precursor (used for synthesis of Ni_2Mo_3N) and corresponding simulated patterns of $NiMoO_4$ and MoO_3.
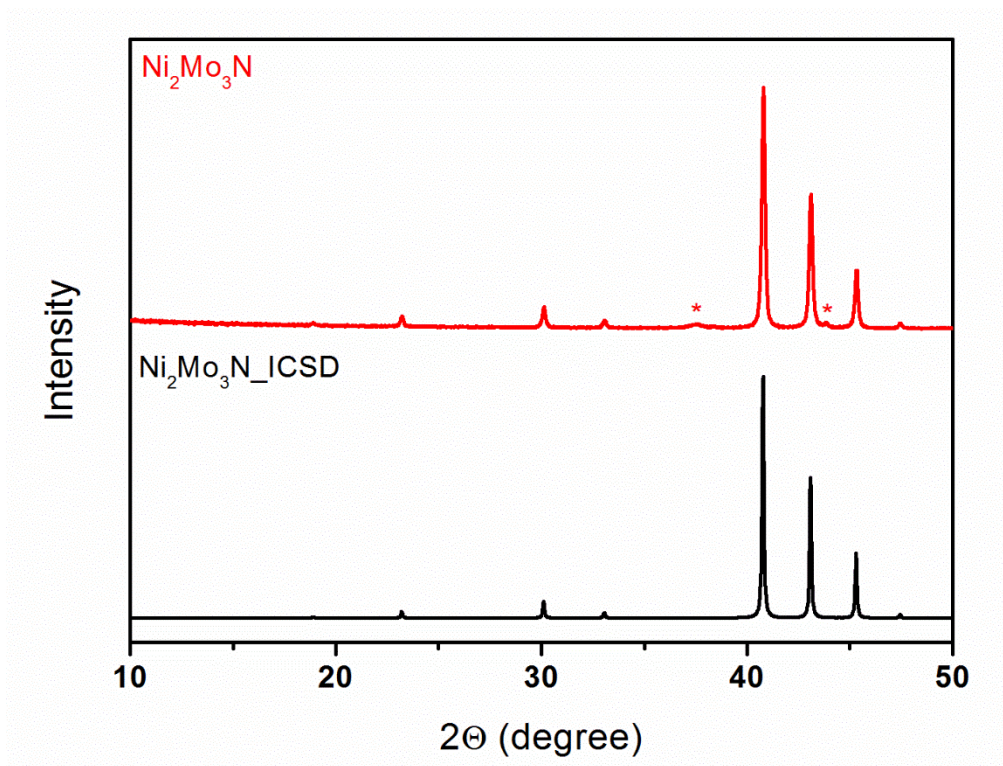
Figure 5-3 PXRD pattern of Ni_2Mo_3N prepared by reaction with H_2/N_2 gas mixture at 700 °C and corresponding simulated pattern of Ni_2Mo_3N. Stars mark the position of the reflections assigned to the Mo_3Ni_2 impurity.
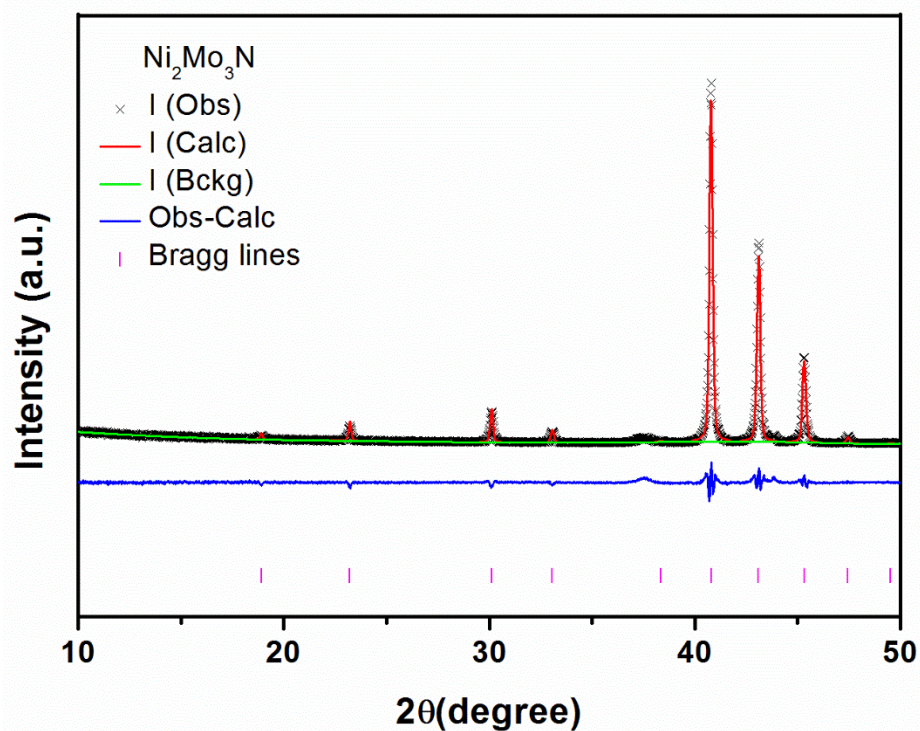
Figure 5-4 LeBail refinement of Ni₂Mo₃N PXRD data. Measured data are shown as crosses, the calculated profile is shown by a solid line through the measured data. The difference profile is shown along the bottom of the plot. Vertical bars represent the reflection positions for the phase.

Table 5. 2 Refinement parameters from XRD data of Ni₂Mo₃N phase.

Sample	Ni₂Mo₃N
Collection temperature	Room temperature
Crystal system	Cubic
Space group	$P4_132$
Unit cell dimension/ Å	6.63100(7)
volume/Å³	291.566(9)
Observations, parameters	2393
R_{wp}	0.1452
R_p	0.0989
Chi²	3.017

5.3.2 Electrochemical investigation of Ni₂Mo₃N

The HER performances of Ni₂Mo₃N products were first tested in 0.5 M H₂SO₄ solution. All experiments were performed on two different batches of Ni₂Mo₃N samples in order to ensure the reliability of the measurements. For comparison,

the measurements on a Pt wire were carried out as controls under identical conditions. The mass loading of the catalyst used to coat the GC electrode was of 3.4 mg cm^{-2}. As expected, the Pt showed a very low potential which is consistent with previous studies.[30,31]

Ni$_2$Mo$_3$N exhibits an overpotential of 130 mV±20 at the current density of 10 mA cm^{-2}. This value is lower than all the free-standing nitrides tested in bulk form reported in literature and even outperform ones in nanostructured form (Table 5.1).

Moreover, the activity of Ni$_2$Mo$_3$N in bulk form confirms the speculation by Zhu *et al.* that Ni$_2$Mo$_3$N might be the possible active phase in the catalyst based on NiMoN$_x$/C nanosheets.[3]
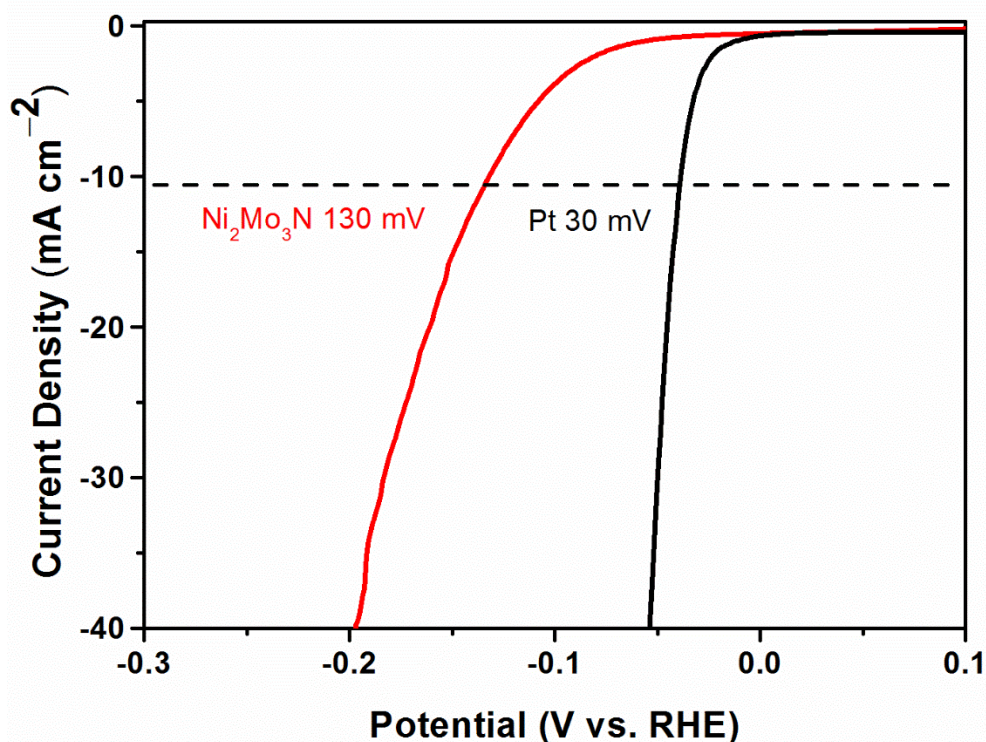
Figure 5-5 Polarization curve of Ni$_2$Mo$_3$N obtained by LSV in acidic media 0.5 M H$_2$SO$_4$ between 0.2 to -0.3 V vs NHE with a scan rate of 2 mV s^{-1}.

A characterization of the HER kinetics was done by plotting the potential obtained from the LSV scan *vs.* the logarithm of the current density. The current density between 5 mA cm^{-2} and 15 mA cm^{-2} was used to obtain the linear fit to define the Tafel slope.

As expected, the commercial Pt shows a slope of 31 mV dec^{-1} in accordance with what is reported in literature and confirming a Volmer-Tafel mechanism.[32,33] The Ni$_2$Mo$_3$N slope exhibits a value of 69 mV dec^{-1} indicating a kinetics following the

Volmer-Heyrovsky mechanism where the rate determining step might be associated to the Heyrovsky half-reaction.
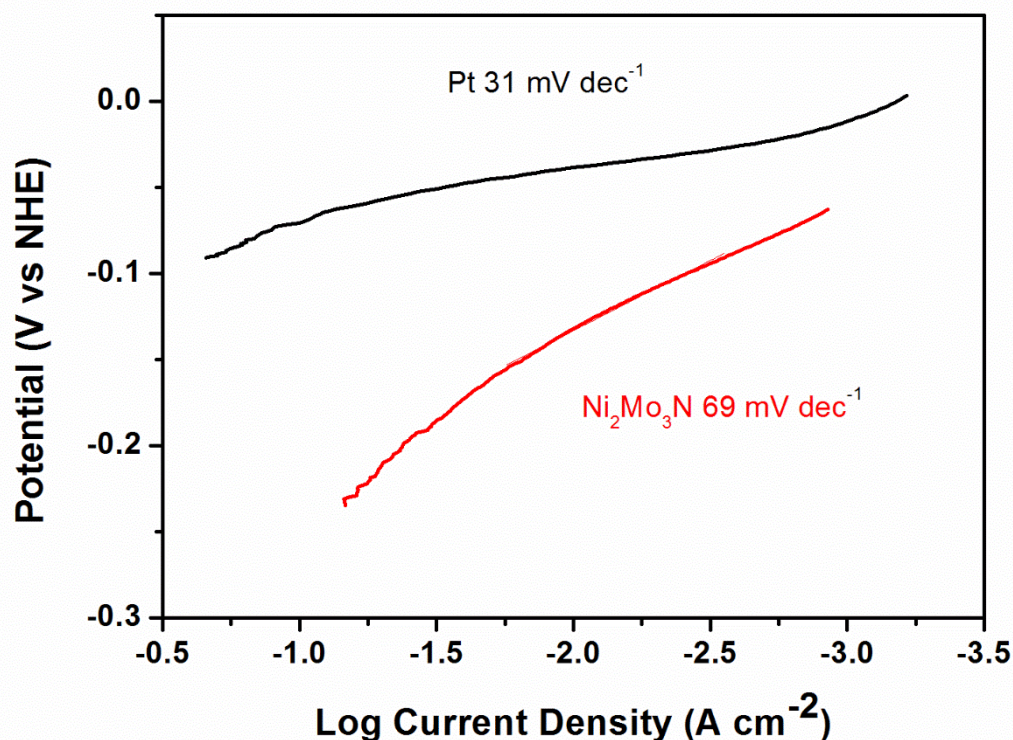
Figure 5-6 Tafel slope obtained from the LSV scan in acidic media.

5.3.2.1 Electronic impedance spectroscopy measurement (EIS)

To further understand the HER mechanism, electron impedance spectroscopy measurements were carried out in acidic media by measuring the Nyquist plots that are discussed on the following paragraph. The data were collected in a frequency range from 200 kHz to 1 Hz on an AC mode with an amplitude of 10 mV. All the data were than fitted using a simple equivalent circuit showed on the insert in Figure 5.7.

The EIS measurements were carried out by using different probing potentials. As the overpotential used to probe the system increases on its module, the diameter of the semicircle associated to the time constant (CPE-R) decreases (see Figure 5.7). This reflects the response of the system to an applied potential and addresses this time constant at the HER kinetic. The value of R indicates the charge transfer resistance, R_{ct}, and the higher its value the more the HER kinetics occur efficiently at that potential. The CPE is the constant phase element related to the double layer capacitance used for the behaviour model of an imperfect capacitor.[34]

In certain cases, the Nyquist shows the presence of a lower semicircle at higher frequencies, which can be associated either to the response to the hydrogen absorption on the surface or to the porosity of the material.[35] A small semicircle could also be identified in our measurements for the potential of 400 mV and 450 mV. Those measurements were then fitted with the model associated to the porous material[36] or to hydrogen absorption.[37] Unfortunately, both those models were not able to describe our system properly giving a bad overlap between the model and the measurement with worst chi-square value than the ones obtained with the standard model. For this reason, it was decided to consider this contribution as minor to the measurement and to neglect it.
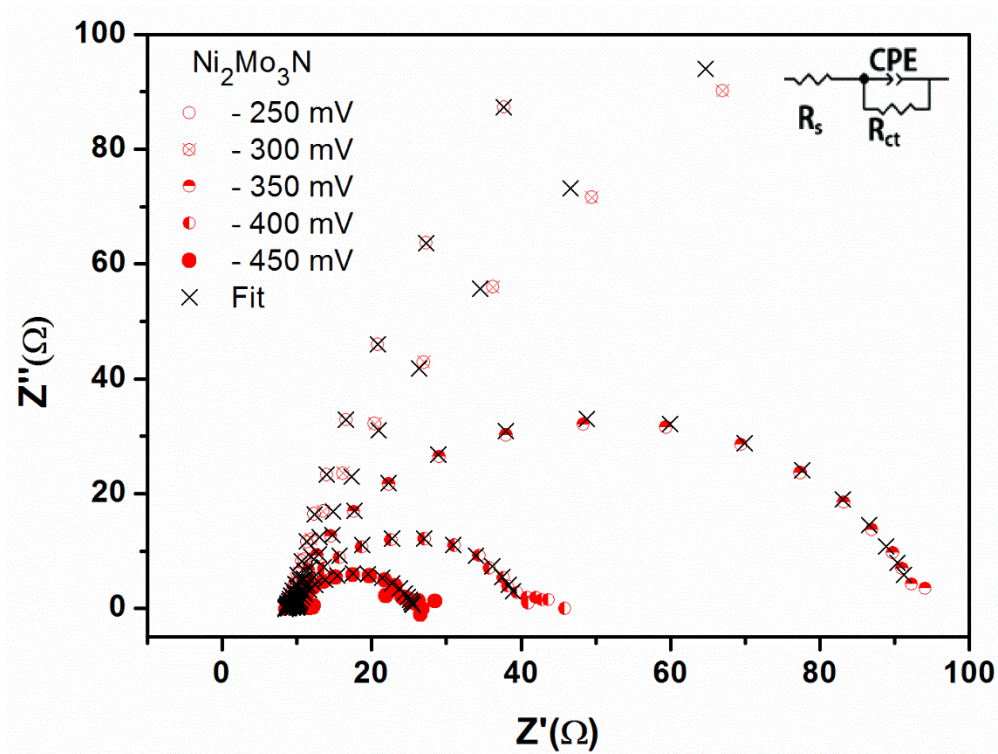
Figure 5-7 Nyquist plot obtained by AC mode with different voltage signals in a frequency range between 200kHz to 1Hz.

Table 5. 3 Fitting of the electronic impedance of Ni_2Mo_3N data obtained by using the Randles circuit model insert in Figure 5.7 consisting of a resistor (R_s) in series with a parallel arrangement of a resistor (R_{ct}) and a constant phase element (CPE).

Voltage signal applied	250 mV	300 mV	350 mV	400 mV	450 mV
R_s solution resistance (Ω)	9.1±0.2	8.9±0.2	9.4±0.4	9.9±0.4	10.0±0.5
R_{ct} charge transfer resistance (Ω)	1235±456	447.2±3.7	83.7±0.6	30.2±0.6	15.6±1.1
CPE Ω^{-1} s^n or cm-2 or $F\ s^{n-1}$	1.6 E^3±0.2 E^{-3}	1.3 E^{-3}±12.3 E^{-6}	0.9 E^{-3}± 68.5 E^{-6}	0.7 E^{-3}±0.2 E^{-3}	0.7 E^{-3}±0.5E^{-3}
x^2 chi-square	1.84	2.62	11.74	1.94	5.40

To confirm the major role of the charge transfer kinetic on the HER of Ni_2Mo_3N, the Tafel slope was calculated from the EIS measurements by plotting the $log(1/R_{ct})$ versus the different probing potentials as previously done in other studies.[8,38] The Tafel slope calculated in this way was of 70 mV dec^{-1}, which agrees with the value obtained from the LVS measurement (Figure 5.6). This indicates that the contribution occurring at higher frequency and associated to the mass transfer resistance is in general negligible for this system.
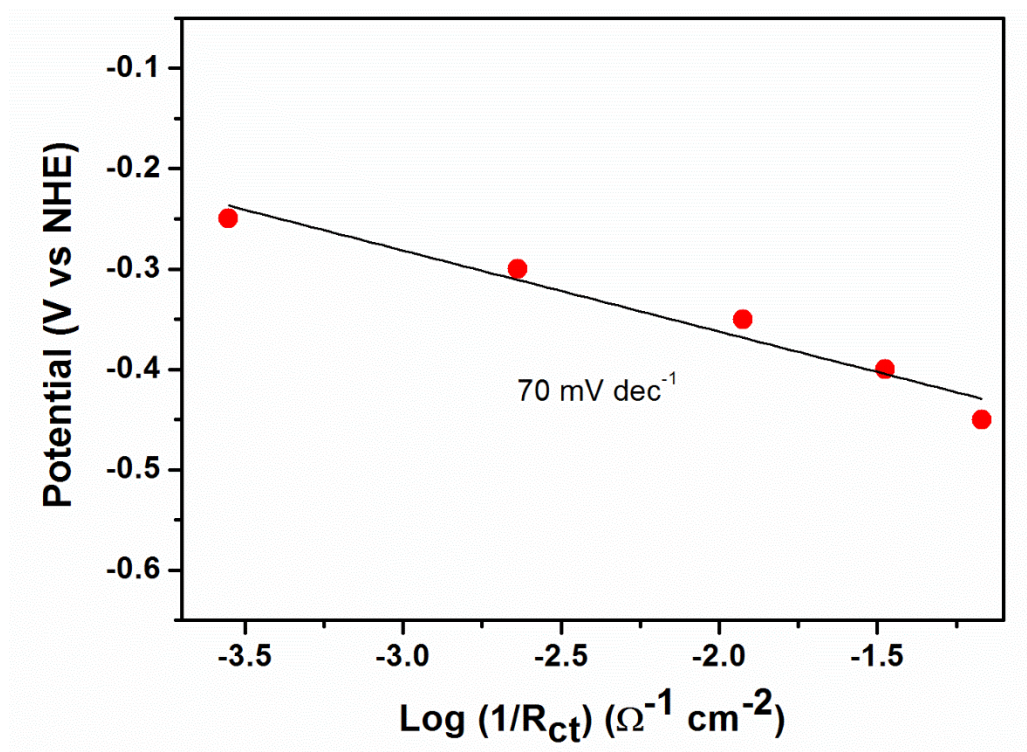
Figure 5-8 Tafel slope calculated with the use of the logarithm of the charge transfer resistance reverse (1/R_{ct}) as a function of the probing over potential.

5.3.2.2 Electrochemical active surface area (ESCA)

ESCA measurements are often used as an indication of the exposed active site density in the catalyst. A high ESCA value corresponds to a major presence of active sites on the surface. The measurement was collected by different CV scans in a non-Faradaic region at different scan rates (Figure 5.9). The Figure 5.10 was then obtained by plotting the 0.209 V vs NHE value for each scan rate.

As already said, the ESCA of a material is proportional to the double layer capacitance C_{dl}. A value of ESCA can be calculated from C_{dl} by following the reaction:

$$ESCA = \frac{C_{dl}}{C_s} \qquad\qquad (5.1)$$

Where C_s is the specific capacitance of a smooth planar surface with a surface area of 1 cm^2.[39] This value is very difficult to obtain and it is typically estimated to be between 15-50 µF cm^{-2}.[40] A smooth and metallic electrode is estimated to have a Cs of 20 µF cm^{-2} [Ref [35]], however, most of the papers assume a Cs value

of 40 µF cm^{-2} [Ref [39]]. The double layer capacitance was calculated from the slope of the linear fit ($C_{dl} = dj/dv$) and then dividing the value by two.

The ESCA obtained for Ni$_2$Mo$_3$N was compared with the ones obtained for MoNiP prepared with the addition of citric acid (Chapter 4). From Figure 5.10 it can be seen that Ni$_2$Mo$_3$N displays an active surface area comparable with the one obtained for MoNiP. The ESCA of Ni$_2$Mo$_3$N is, however, slightly smaller with a value of 87.2 cm^2 compared with the 112.5 cm^2 of MoNiP. It should be noted that both ESCA measurements were carried out with the same catalyst loading on the GC electrode and therefore the data were not normalized to the mass of the catalyst. For Ni$_2$Mo$_3$N, the relatively high surface area might be explained with a material mainly in bulk form but with the presence of some areas with a more jagged morphology (see SEM below).
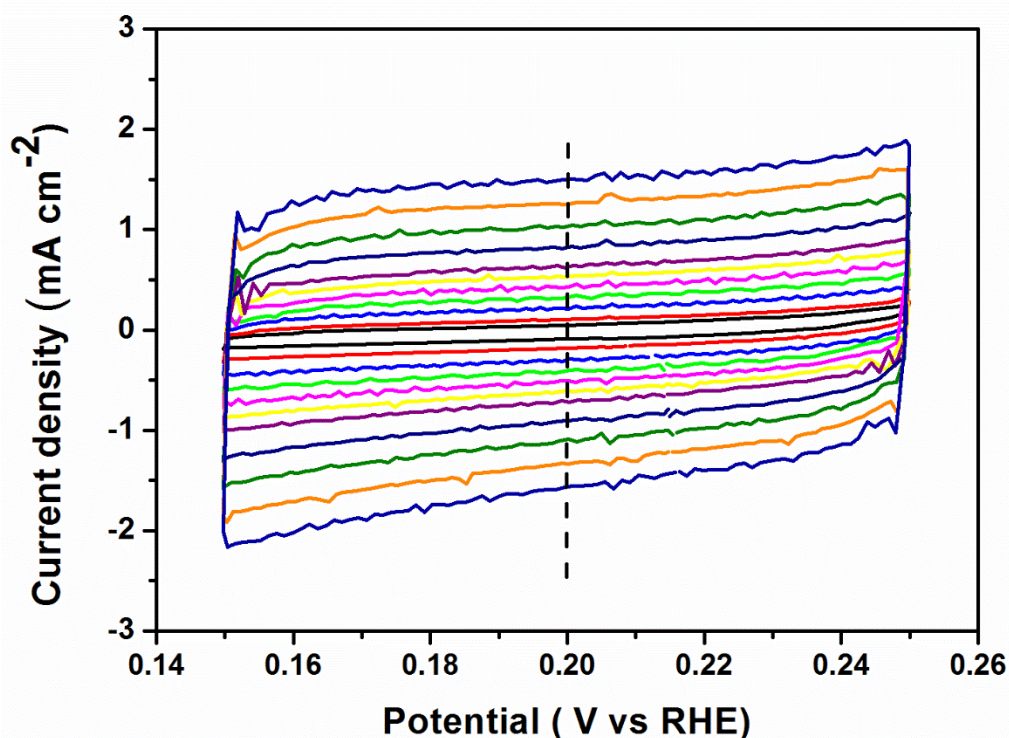
Figure 5-9 Measurement of the current density of a CV scan carried out between -0.155 V to 0.250 V vs NHE on an acidic solution of 0.5M H$_2$SO$_4$.
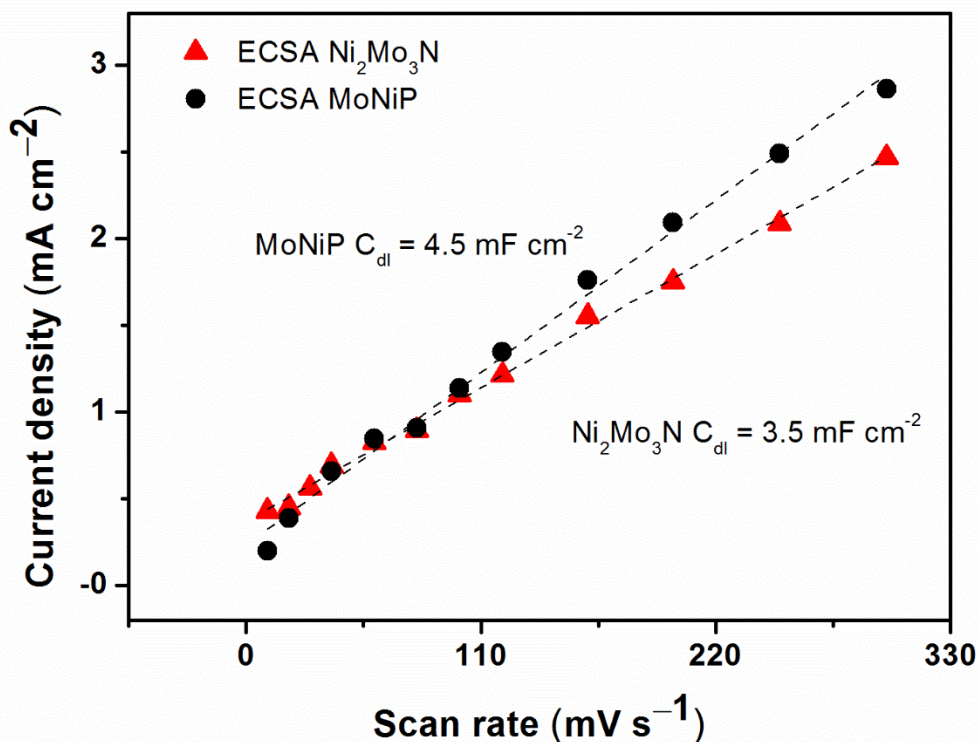
Figure 5-10 The current density at 0.209 V vs RHE for different scan rates.

Table 5. 4 Comparison between the double layer capacitance of Ni_2Mo_3N and MoNiP.

Sample	C_{dl} (mF/ cm^2)	ESCA (cm^2)
Ni_2Mo_3N	3.5 ± 0.1	87.5
MoNiP	4.5 ± 0.2	112.5

5.3.2.3 Stability test

Durability is an important factor for the catalyst performance. Long term stability of Ni_2Mo_3N material was investigated through continuous cyclic voltammetry of the material on glassy carbon substrate in a voltage range of 0.209 to -0.300 V *vs*. RHE at a constant rate of 100 mV s^{-1} for 1000 cycles in 0.5 M H_2SO_4. The stability test with potential cycling in Figure 5.11 shows an unchanged polarization curve after the test suggesting that Ni_2Mo_3N is a stable HER electrocatalyst in acidic condition.
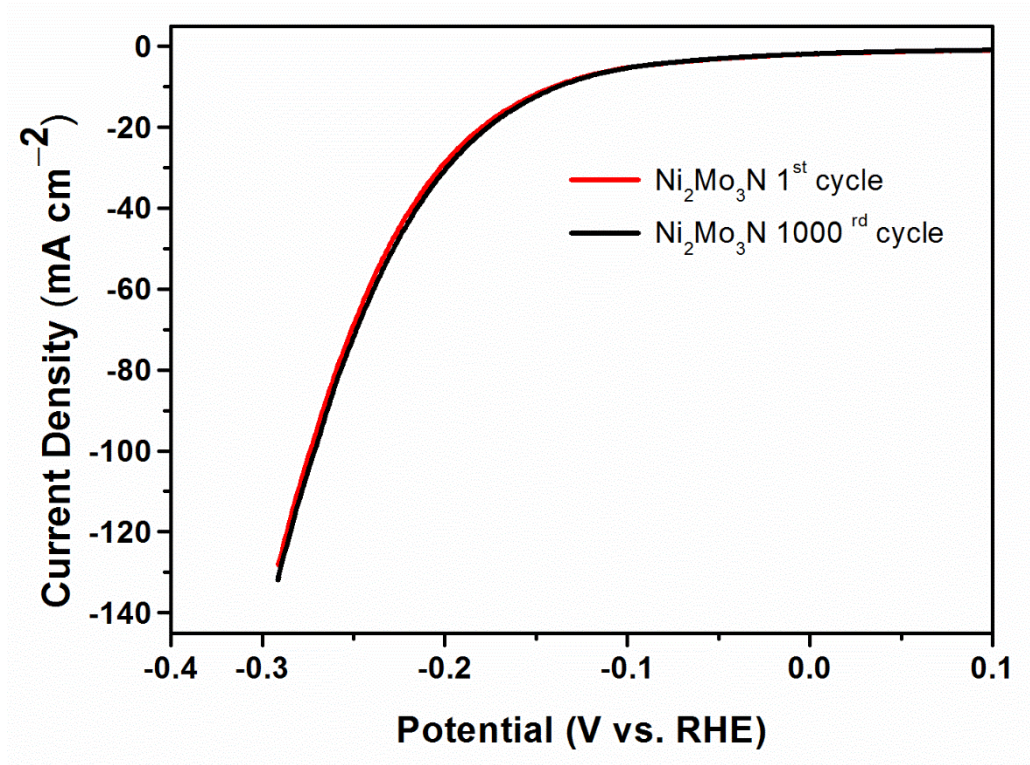
Figure 5-11 CV test between 0.209 to -0.300 V versus RHE at scan rate of 100 mV s⁻¹ for 1000 cycles.

Galvanostatic measurements were also carried out with a constant current density of 10 mA cm⁻² to probe the capability of the material to hold a constant current over time. Unfortunately, the material did not manage to hold the potential at 130 mV and it was observed almost immediately a drop of the potential to 166 mV. The material kept this potential constant for circa 10 hours for than drop again to 171 mV after other 10 hours.
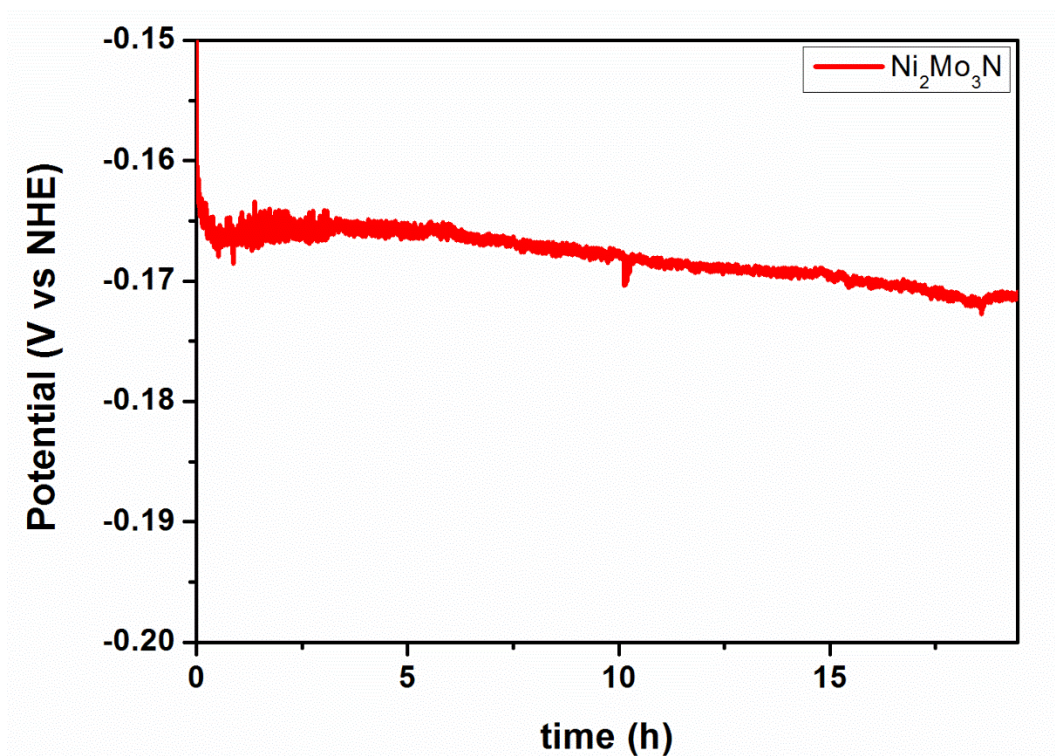
Figure 5-12 Chronoamperometric (glavanostatic) response of Ni_2Mo_3N recorded at the current density of 10 mA cm^{-2}.

5.3.2.4 Gas chromatography (GC) measurements

The galvanostatic measurement (shows in Figure 5.12 above) was also used to determine the hydrogen production and its yield using the same technique previously described in Chapter 3.

The Galvanostatic measurement was performed in an airtight cell and the hydrogen production was detected by gas chromatography with direct injection of the gas present on the headspace. Figure 5.13 shows that the hydrogen production has a Faradaic yield of 85% indicating that protons were the majority species being reduced at the cathode.
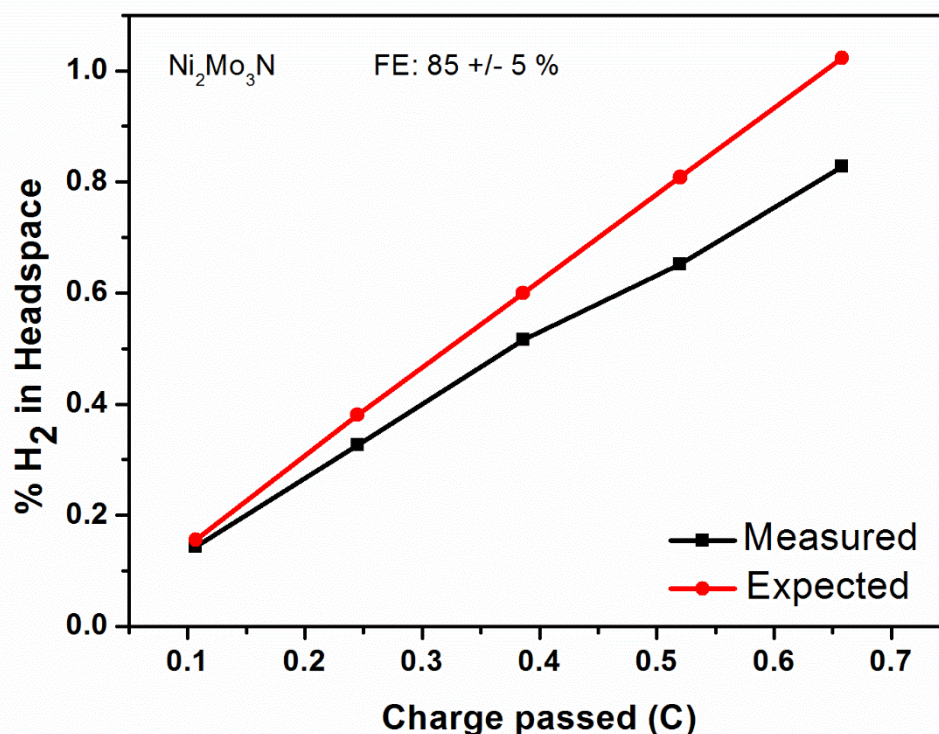
Figure 5-13 Percentage of Hydrogen detected on the headspace of the airtight cell at different time interval by gas chromatography analysis. The hydrogen was produced by applying a constant current of 0.71 A over time. The red line indicated the expected yield while the black like indicated the detected yield at that particular amount of charge passed.

5.3.2.5 Reactions in Basic Media

The Ni_2Mo_3N was also tested for the HER reaction in basic media. The tests were carried out with the same experimental setup in a solution of 1M KOH and the potential corrected accordingly with the Nerst equation (Figure 5.14). The overpotential needed to deliver a current density 10 mA cm^{-2} was of 348 mV showing a poorer performance of this material in basic condition. The linear portion of the Tafel plot was fit to the Tafel equation yielding a slope of 148 mV dec^{-1}. This value clearly indicates a Volmer–Heyrovsky mechanism with clearly the Volmer as a rate determining step.
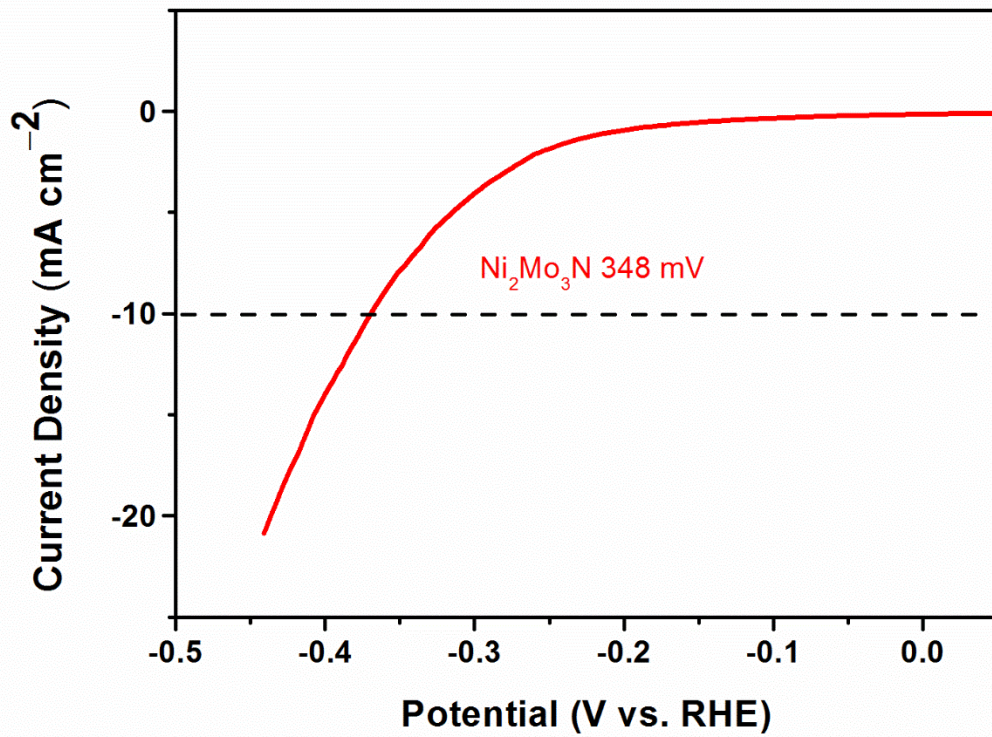
Figure 5-14 CV scan of Ni$_2$Mo$_3$N in 1M KOH between 0.209 and -0.45 V vs RHE. The scan was made with a scan rate of 100 mV s^{-1}.
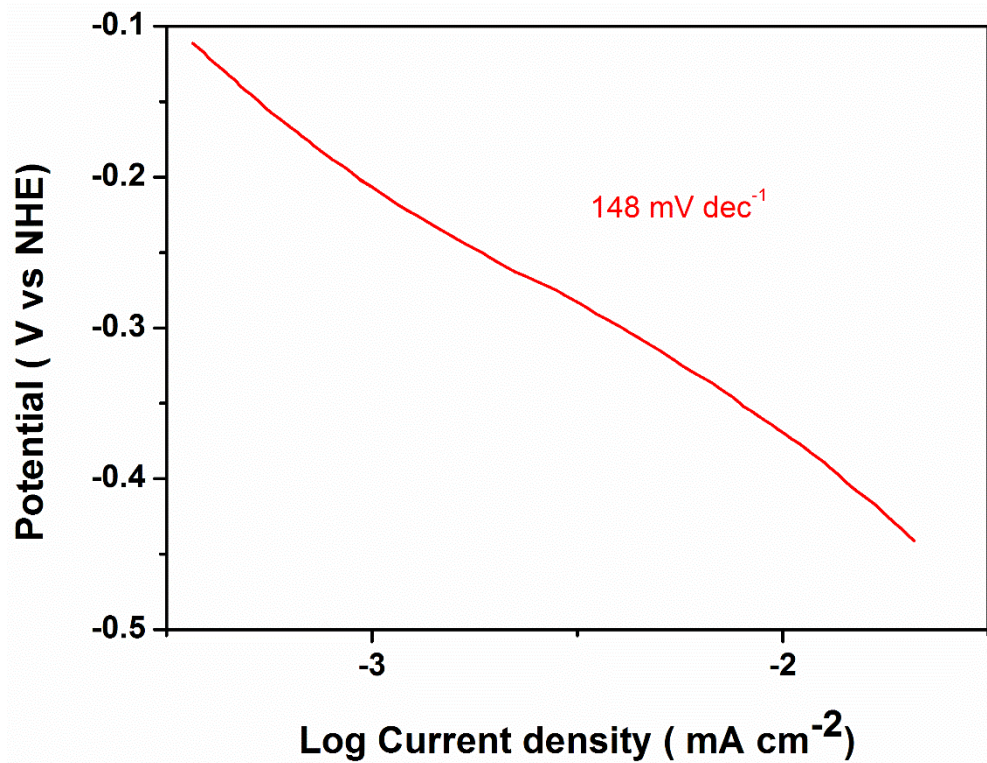
Figure 5-15 Tafel slope obtained from the CV scan in basic media

5.3.3 Scanning electron Microscopy

SEM was used to probe into the microstructure of the prepared materials (Figure 5.16). The low magnification shows homogeneous powder without any evidence for specific microstructure. The long fibre-like structures visible in images are due to tiny impurities coming from the silica wool used as plugs during the thermally controlled synthesis of the nitride. Higher magnification images shows a homogenous and jagged surface at both the magnifications 800X and 4000x. This morphology might be responsible of the quite high electrochemical active surface area recorded from the ESCA and of the small additional contribute to the EIS measurement at higher frequency.
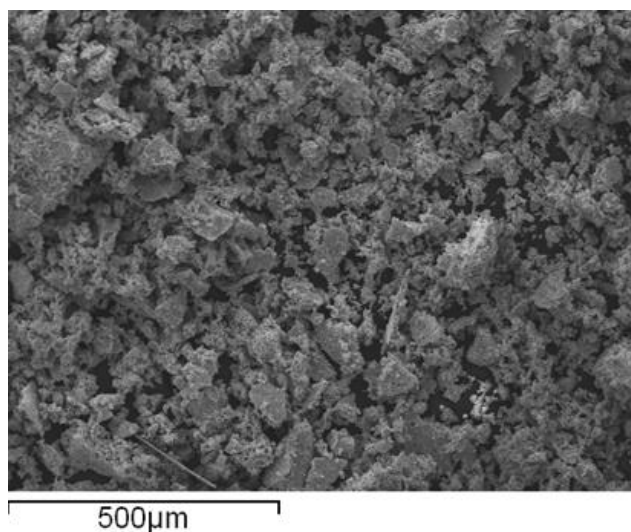
Figure 5-16 Low magnification SEM images of Ni_2Mo_3N powders to give an overview of the sample.

The SEM images confirm that the product is generally homogeneous and presents an excellent opportunity to develop Ni_2Mo_3N into highly stable and efficient electrocatalyst since the overall performances are substantially higher than most of the state-of-the-art composite nitrides listed in the Table 5.1. In addition to SEM the composition of the Ni_2Mo_3N was probed by the EDX. The results of the analysis are summarized in the Table 5.5.

From the EDX measurements, it can be notice that all the areas share a similar composition, which exhibits a presence of the nitrogen inside the sample higher than the one expected. This might be explained from the reported possibilities of nitride materials to lost or absorb nitrogen within their structure.[1]
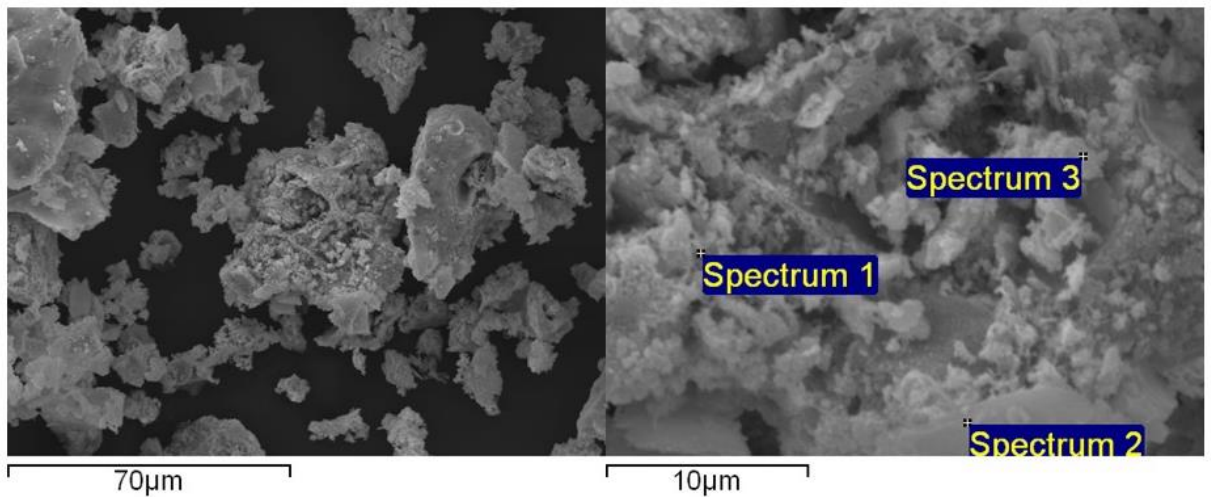
Figure 5-17 High magnification SEM images of Ni$_2$Mo$_3$N powders and the points used for collection of EDX spectra.

Table 5. 5 Results of the EDX analysis of Ni$_2$Mo$_3$N. The data were collected by probing tree point of each area and then making an average of the resulting values.

Atoms	Subtotal Mass%	Subtotal Mass % Theoretical.
N	9.59±4.52	3.34
Mo	64.42±5.29	68.66
Ni	25.98±4.33	28.00

5.4 Conclusions

For the first time relatively phase pure and stoichiometric Ni_2Mo_3N was tested as a novel electrocatalyst for HER in acidic and alkaline media. It showed remarkably low overpotential of 130 ± 20 mV for a free-standing material. In comparison with few-examples of nitrides available in literature, this is excellent performance considering no additives or composing carbonaceous matrix has been employed in this work. The kinetics of the HER reaction may follow the Volmer-Heyrovski mechanism based on the Tafel slope of *ca*. 70 mV dec^{-1} independently confirmed by the LSV and impedance experiments. The ECSA measurements indicated that Ni_2Mo_3N shows the active surface similar to the NiMoP reported in the previous chapter but significantly outperforming this material in terms of OVP values. The morphology of the material assessed by SEM does not show any evidence for extremely high surface area or porous structure (something that might have provided with the abundance of catalytic sites to drive a good performance). Therefore, the electrocatalytic activity of this material probably stems from its unique crystal structure, which contains quite unusual Ni chains. However, it is unclear to what extent this structural feature is responsible for the performance. DFT calculations are required to identify which site is actually responsible for the performance. This is extremely important in the context that Ni_2Mo_3N is not particularly good electrocatalyst in basic media contrary to the MoNiP, which showed a relatively good performance.

5.5 Bibliography

1. N. Bion *et al.* The role of preparation route upon the ambient pressure ammonia synthesis activity of Ni 2 Mo 3 N. *"Applied Catal. A, Gen.* **504,** 44–50 (2015).
2. D. Mckay, J. S. J. Hargreaves, J. L. Rico, J. L. Rivera and X. Sun The influence of phase and morphology of molybdenum nitrides on ammonia synthesis activity and reduction characteristics. *J. Solid State Chem.* **181,** 325–333 (2008).
3. W.-F. Chen, K. Sasaki, C. Ma, A. I. Frenkel, N. Marinkovic, J. T. Muckerman, Y. Zhu and R. R. Adzic Hydrogen-Evolution Catalysts Based on Non-Noble Metal Nickel – Molybdenum Nitride Nanosheets. *Angew. Chemie - Int. Ed.* 6131–6135 (2012). doi:10.1002/anie.201200699
4. B. Cao, G. M. Veith, J. C. Neuefeind, R. R. Adzic and P. G. Khalifah Mixed Close-Packed Cobalt Molybdenum Nitrides as Non-noble Metal Electrocatalysts for the Hydrogen Evolution Reaction. *J. Am. Chem. Soc.* **135,** 19186–19192 (2013).
5. J. Xie, S. Li, X. Zhang, J. Zhang, R. Wang, H. Zhang, B. Pan and Y. Xie Atomically-thin molybdenum nitride nanosheets with exposed active surface sites for efficient hydrogen evolution. *Chem. Sci.* **5,** 4615–4620 (2014).
6. W-F Chen, S. Iyer, S Iyer; K. Sasaki, C-H Wang, J.T. Muckerman and E Fujita Biomass-derived electrocatalytic composites for hydrogen evolution. *Energy Environ. Sci.* **6,** 1818–1826 (2013).
7. D. H. Youn, S. Han, J. Y. Kim, J. Y. Kim, H. Park, S. H. Choi and J. S. Lee Highly Active and Stable Hydrogen Evolution Electrocatalysts Based on Molybdenum Compounds on Carbon Nanotube–Graphene Hybrid Support. *ACS Nano* **8,** 5164–5173 (2014).
8. L. Ma, L. R. L. Ting, V. Molinari, C. Giordano and B. S. Yeo Efficient hydrogen evolution reaction catalyzed by molybdenum carbide and molybdenum nitride nanocatalysts synthesized via the urea glass route. *j Mater. Chem. A* **3,** 8361–8368 (2015).
9. Y. Zhu, G. Chen, X. Xu, G. Yang, M. Liu, and Z. Shao Enhancing Electrocatalytic Activity for Hydrogen Evolution by Strongly Coupled Molybdenum Nitride@Nitrogen-Doped Carbon Porous Nano-OctahedronsNo. *ACS Catal.* **7,** 3540–3547 (2017).
10. J. Xiong, W. Cai, W. Shi, X. Zhang, J. Li, Z. Yang, L. Feng and H. Cheng Salt-templated synthesis of defect-rich MoN nanosheets for boosted hydrogen evolution reaction. *J. Mater. Chem. A* **5,** 24193–24198 (2017).
11. K. Makise, F. Ichikawa, T. Asano and B. Shinozaki Field-tuned superconductor–insulator transitions and Hall resistance in thin polycrystalline MoN films. *J. Phys.* **30,** (2018).
12. A. Y. Ganin, L. Kienle, G. V. Vajenine Synthesis and characterisation of hexagonal molybdenum nitrides. *J. Solid State Chem.* **179,** 2339–2348 (2006).
13. N. Mo and N.A.N Ternary Nitride, I. Ni 2 Mo 3 N: A New Ternary Interstitial Nitride with a Filled -Manganese Structure **4,** 6451-6453 (1998).
14. K. S. Weil, P. N. Kumta and J. Grins Revisiting a Rare Intermetallic Ternary Nitride , Ni 2 Mo 3 N : Crystal Structure and Property Measurements. *J. Solid State Chem.* **35,** 22-35 (1999).
15. A. El-Himri, F. Sapiña, R. Ibanez and A. Beltran Pd2Mo3N: a new molybdenum bimetallic interstitial nitride. *J. Mater. Chem.* **11,** 2311–2314 (2001).
16. A. El-Himri, D. Marrero-López and P. Nunez Pt2Mo3N and PdPtMo3N: new interstitial nitrides prepared from freeze-dried precursors. *J. Solid State Chem.* **177,** 3219–3223 (2004).
17. T. J. Prior, S. E. Oldham, V. J. Couper, and P. D. Battle Ferromagnetic Nitrides

with the Filled ß-Mn Structure: Fe2-xMxMo3N (M = Ni, Pd, Pt). *Chem. Mater*. **17,** 1867–1873 (2005).

18. S. F. Zaman, L. A. Jolaoso, S. Podila, A. A .Al-Zahrani, Y. A. Alhamed, H. Driss, M. M. Daous and L. Petrov Ammonia decomposition over citric acid chelated γ-Mo2N and Ni2Mo3N catalysts. *Int. J. Hydrogen Energy* **43,** 17252–17258 (2018).

19. J. K. Nørskova, T. Bligaarda, A. Logadottir, J. R. Kitchin, J. G. Chen, S. Pandelov and U. Stimming Trends in the Exchange Current for Hydrogen Evolution. *J. Electrochem. Soc*. **3,** J23–J26 (2005).

20. B. Diaz, S. J. Sawhill, D. H. Bale, R. Main and S. Korlann, R. Self and M. E. Bussel Hydrodesulfurization over supported monometallic, bimetallic and promoted carbide and nitride catalysts. *Catal. today* **86,** 191–209 (2003).

21. C. J. H. Jacobsen Novel class of ammonia synthesis catalysts. *Chem. Commun.* **0,** 1057–1058 (2000).

22. W. Li, Z. Wang, M. Zhang and K. Tao Novel Ni2Mo3N/zeolite catalysts used for aromatics hydrogenation as well as polycyclic hydrocarbon ring opening. *Catal. today* **6,** 656–660 (2005).

23. H. Wang, W. Li, M. Zhang and K. Tao A novel Ni2Mo3N/MCM41 catalyst for the hydrogenation of aromatics. *Catal. today* **100,** 73–75 (2005).

24. S. Korlann, B. Diaz, and M. E. Bussel Synthesis of Bulk and Alumina-Supported Bimetallic Carbide and Nitride Catalysts. *Chem. Mater*. **14,** 4049–4058 (2002).

25. Z-Q Wang, Y-L Ma, M-H Zhang, W. Li and K.-Y. Tao A novel route to the synthesis of bulk and well dispersed alumina-supported Ni2Mo3N catalystsvia single-step hydrogen thermal treatment. *J. Mater. Chem.* **18,** 4421–4425 (2008).

26. H. Wang, Z. Wu, J. Kong, Z. Wang and M. Zhang Synthesis of transition metal nitride by nitridation of metastable oxide precursor. *J. Solid State Chem.* **194,** 238–244 (2012).

27. L. Wang, W. Xi, Q. Cheng, K. Zhang and H. Qin, T. Mei, A. Zheng and Q. Zhou A Solid-state Approach to the Synthesis of the Ternary Nitride Ni2Mo3N. *Chem. Lett*. **47,** 20-22 (2017).

28. J. S. J. Hargreaves, D. Mckay A comparison of the reactivity of lattice nitrogen in Co3Mo3N and Ni2Mo3N catalysts. *J. Mol. Catal. A Chem.* **305,** 125–129 (2009).

29. L. Kong, J. Wu, B. Lu, Q. Li and T. Xiong Midscale Preparation and Characterization of Transient Metal Nitride Catalyst. *Ind. Eng. Chem. Res.* **47,** 1779–1783 (2008).

30. H.A. Gasteiger, J. E. Panels and S. G. Yan Dependence of PEM fuel cell performance on catalyst loading. *J. Power Sources* **127,** 162–171 (2004).

31. K. C. Neyerlin, Wenbin Gu, Jacob Jorne and H. A. Gasteiger Study of the Exchange Current Density for the Hydrogen Oxidation and Evolution Reactions. *J. Electrochem. Soc*. **157,** B631–B635 (2007).

32. N. M. Marković*, B. N. Grgur and P. N. Ross Temperature-Dependent Hydrogen Electrochemistry on Platinum Low-Index Single-Crystal Surfaces in Acid Solutions. *J. Phys. Chem. B* **101,** 5405-5413 (1997).

33. A. B. Anderson and Y. Cai Calculation of the Tafel Plot for H2 Oxidation on Pt(100) from Potential-Dependent Activation Energies. *J. Phys. Chem. B* **108,** 19917–19920 (2004).

34. A. Damian and S. Omanovic Ni and Ni Mo hydrogen evolution electrocatalysts electrodeposited in a polyaniline matrix. *J. Power Sources* **146,** 464–476 (2006).

35. D. Delgado, M. Minakshi and D.-J. Kim Electrochemical Impedance Spectroscopy Studies on Hydrogen Evolution from Porous Raney Cobalt in Alkaline Solution. *Int. J. Electrochem. Sci* **10,** 9379-9394 (2015).

36. C. Hitz, A. Lasia Experimental study and modeling of impedance of the her on

porous Ni electrodes. *J. Electroanal. Chem.* **500,** 213–222 (2001).

37. R. Cret,u, A. Kellenberger and N. Vaszilcsin Enhancement of hydrogen evolution reaction on platinum cathode by proton carriers. *SciVerse Sci.* **38,** 11685–11694 (2013).

38. H. Vrubel, T. Moehl, M. Gratzel and X. Hu Revealing and accelerating slow electron transport in amorphous molybdenum sulphide particles for hydrogen evolution reaction. *Chem. Commun.* **49,** 8985–8987 (2013).

39. H. Deng, C. Zhang, Y. Xie, T. Tumlin, L. Giri, S. P. Karna and J. Lin Laser Induced MoS2/Carbon Hybrids for Hydrogen Evolution Reaction Catalysts. *J. Mater. Chem. A* **4,** 6824–6830 (2016).

40. I. Vincent and D. Bessarabov Electrochemical Characterization and Oxygen Reduction Kinetics of Cu-incorporated Cobalt Oxide Catalyst. *Int. J. Electrochem. Sci* **11,** 8002 – 8015 (2016).

6 Conclusion and future work

This thesis investigated alternatives to noble metals as hydrogen evolution reaction electrocatalysts in order to make hydrogen production an ecological alternative. Each examined material was optimised in its synthesis to enhance its electrochemical performance and to make it more appealing for further industrial development.

A Co doped metal sulphide was successfully produced by hydrothermal synthesis on a transparent conductive FTO. This material had an increased number of active sites due to the Cobalt doping, which increases the terminal S-edge site activity together with the number of defects due to the presence of thiourea as a source of sulphur within the reaction. The conductive surface also improved the material's performance by increasing the conductivity. This synthesis allowed the preparation of films with different thickness by scaling down the reagent's concentration, opening the possibility of a direct solar-to-hydrogen application.

The obtained black films had a stoichiometric composition of $Co_2Mo_9S_{26}$, which was estimated from the atomic absorption spectroscopy and CHN analysis.

The typical MoS_2 like structure was identified by Raman spectroscopy analysis, where the prepared films showed the presence of the active modes A_{1g} and $E^1_{2g.}$ Those two peaks were separated by 29 cm^{-1}, indicating that the synthesised material was in bulk form. Moreover, the spectra showed the absence of other active modes related to impurities like CoS_x and MoO_x, indicating a rather monophasic nature of the material. In XPS measurements, the material showed a uniform composition of the elements across the whole surface, with an oxidation state for Molybdenum and Sulphur of +4 and -2, respectively, and in agreement with the MoS_2 structure.

The film thickness was determined with atomic force microscopy together with UV-VIS spectroscopy. The thickest substrate was measured to be 300±50 nm, while the one showing translucent properties was in the order of 150±50 nm. As expected, the transmittance decreased with increasing film thickness. The XRD pattern between 10 and 60 2θ highlighted the preservation of the FTO crystalline structure and the presence of only a broad low diffraction angle peak corresponding to the 2H phase of MoS_2. This broad peak present in the XRD pattern could be explained by scanning electron microscopy images showing a disordered structure due to a misalignment of the layers along the c axis. The films were

tested for hydrogen evolution reaction in acid, basic and neutral media. The best performances was noted with the 300 nm film in acidic media, where an overpotential of 265±8 mV at the current density of 10 mA cm-2 could be reached. . The Tafel slope for this material was measured to be 64 mV dec^{-1}, highlighting a possible Volmer-Heyrovsky mechanism for this film. Unfortunately, the translucent 150 nm film reached only an overpotential of 300 nm with a Tafel slope of 85 mV dec-1.

The material's performance was worse in neutral media, where the 150 nm film at the current density of 10 mA cm^{-2} reached only an overpotential of 460 mV. The performances of the films were not possible to measure in basic media due to the strong instability of the films.

Gas analysis was conducted on the best performing film (300 nm thick $Co_2Mo_9S_{26}$) by applying a constant overpotential of 250 mV in acidic media over an extended period to detect hydrogen production. The yield of the reaction was 89± 6%, but the film showed low stability over time, indicating the need to carry out more studies to further stabilise it before any possible industrial applications.

Compounds isostructural to Ni_2P belonging to the $Mo_xNi_{(2-x)}P$ series were synthesised in bulk form using the solid solution method followed by a time programmed reduction. By this strategy, it was possible to tune the structure with the selective addition of molybdenum on the (0002) phase. The change in composition was observable on the X-Ray diffraction pattern where the peaks associated to planes (11-21), (20-21) and (21-30) left-shifted with the progressive increase of the molybdenum within the structure. Moreover, a linear growth of the unit cell with increasing molybdenum content could be observed. The synthesis of $Mo_xNi_{(2-x)}P$ compounds was only possible for a Ni/Mo ratio larger or equal to one, and for other solid solutions only a mixture of different phases containing MoP was possible. Due to the persistent presence of phase impurities like MoP, $Ni_{11}P_5$ and Mo_3P, citric acid in a ratio of 13:10 with the phosphate source was added to the starting solution to function as stabiliser. The resulting compounds were of a pure phase, highlighting the success of this strategy.

The compounds were tested using an ink deposited by drop-casting on a glassy carbon substrate, whose conductivity helped to improve the overall performance. Electrochemical characterization showed a progressively enhanced HER performance in acid media with the addition of the molybdenum within the

structure. The best performance could be reported for MoNiP, whose overpotential was measured to be 241 mV at the current density of 10 mA cm^{-1}. The material exhibited a Tafel slope of 53 mV dec^{-1} indicating a possible Heyrovsky mechanism.

The electrochemical surface area (ESCA) measurements highlighted the significantly higher surface area of MoNiP as potential reason for the better electrochemical performance of this material. Galvanostatic measurements of MoNiP, $Mo_{0.6}Ni_{1.3}P$ and MoP (used as for comparison as it is a known HER electrocatalyst) were carried out in order to probe the material stability at the constant current of 0.71 mA. All the materials showed constant performances, which only slightly decreases over 48 hours, highlighting their potential for possible industrial applications. The compounds showed good performances in basic media as well, which could make them suitable as bimodal catalysts. However, those compounds did not show the same trend in basic pH as in acid pH, as their overpotentials were very similar and within the experimental error. This result might hint towards a different HER mechanism in acidic media.

Although MoNiP showed promising performances and stability, further attempts should be carried out in order to increase the catalytic surface area and therefore increase the number of active sites potentially involved in the hydrogen evolution reaction. For example, increasing the ratio of citric acid within the solid solution could be a way to increase the surface area. Moreover, since the solid state reaction parameters used (long time and high temperature) have the down side of decreasing the surface area, it could be useful to repeat the study to optimise those parameters using the precursor containing the citric acid.

The ternary nitride Ni_2Mo_3N synthesised by a modified version of the Pechini method showed great catalytic performance, which was never observed before for nitrides in bulk form. The synthesised material showed a fairly pure crystalline phase in the x-ray pattern with the presence of Mo_3Ni_2 as the only minor impurity. In acid media, Ni_2Mo_3N hits an overpotential of 130 mV±8 at the reference current density of 10 mA cm^{-2} with a Tafel slope of 69 mV dec^{-1}.

EIS measurements further confirmed the Tafel slope values, suggesting a possible Volmer-Heyrovsky mechanism. ESCA measurements showed a fairly high exposure of active sites for a material in bulk form, which agrees with the jagged surface displayed on SEM images. Moreover, despite the higher surface area of NiMoP

compared to Ni$_2$Mo$_3$N as determined by ESCA measurements, Ni$_2$Mo$_3$N shows better electrochemical performances, indicating that its active sites are intrinsically more active.

Speculation about the reasons for such high activity could be based on the conductive Nickel metallic nature reported by XPS measurements that enhances the electrical conductivity of the material. The stability of the material was probed by extensive CV scan measurements together with Galvanostatic measurements. As a result, while the performances stay unchanged after 1000 CV scan cycles, in the Galvanostatic test the overpotential experienced an immediate drop from 130 mV to 160 mV to then remain constant for over 10 hours. The Galvanostatic measures were coupled with the use of a gas chromatographer to detect the effective H$_2$ yield, which was estimated to be 85± 6 %.

This promising result highlights that more experimental and theoretical studies should be carried out to investigate new ternary nitrides and their performance. In particular, DFT calculations will be useful to better identify the active sites of those materials. Moreover, the addition of carbon in the ink preparation could be seen as an alternative option to enhance the electrical conductivity without risk the production of side products like carbides.

Finally, other synthetic routes aimed to nanostructure Ni$_2$Mo$_3$N and potentially increase the catalytic activity could be undertaken in order to further improve the electrochemical performance.

Figure 6.1 compares the materials discussed in this work integrated into a Volcano plot with other materials commonly reported in the literature.[1] In the Co$_2$Mo$_9$S$_{26}$ material, the Cobalt doping substitutes the Sulphur within the structure to enhance the activity on the edge by decreasing the Gibbs energy from 0.18 to 0.1 eV. This active site then becomes comparable in activity to the most active Mo-edge (Gibbs energy of 0.08 eV), improving the overall catalytic performance.[2] DFT calculations carried out on the P-capping (0001) Ni$_2$P plane showed a Gibbs value of 0.1 eV for a structure with molybdenum doping on the (0002) plane.[3] This value was compared in Figure 6.1 with the most reported value in the literature for the Ni$_2$P (0001) plane.[4] By comparing these two values, it can be seen that the non-direct doping on the (0001) plane has indeed an effect on the electrochemical reactivity of the material, and more studies should be carried out to better

understand the reason of this increased activity. Finally, the Ni_2Mo_3N material reached a Gibbs value of only -0.6 eV, which makes the hydrogen absorption for this material less efficient than the other materials studied in this thesis.[5] However, the high exchange current density seems to compensate for this lack of efficiency, explaining the good performances reported experimentally.
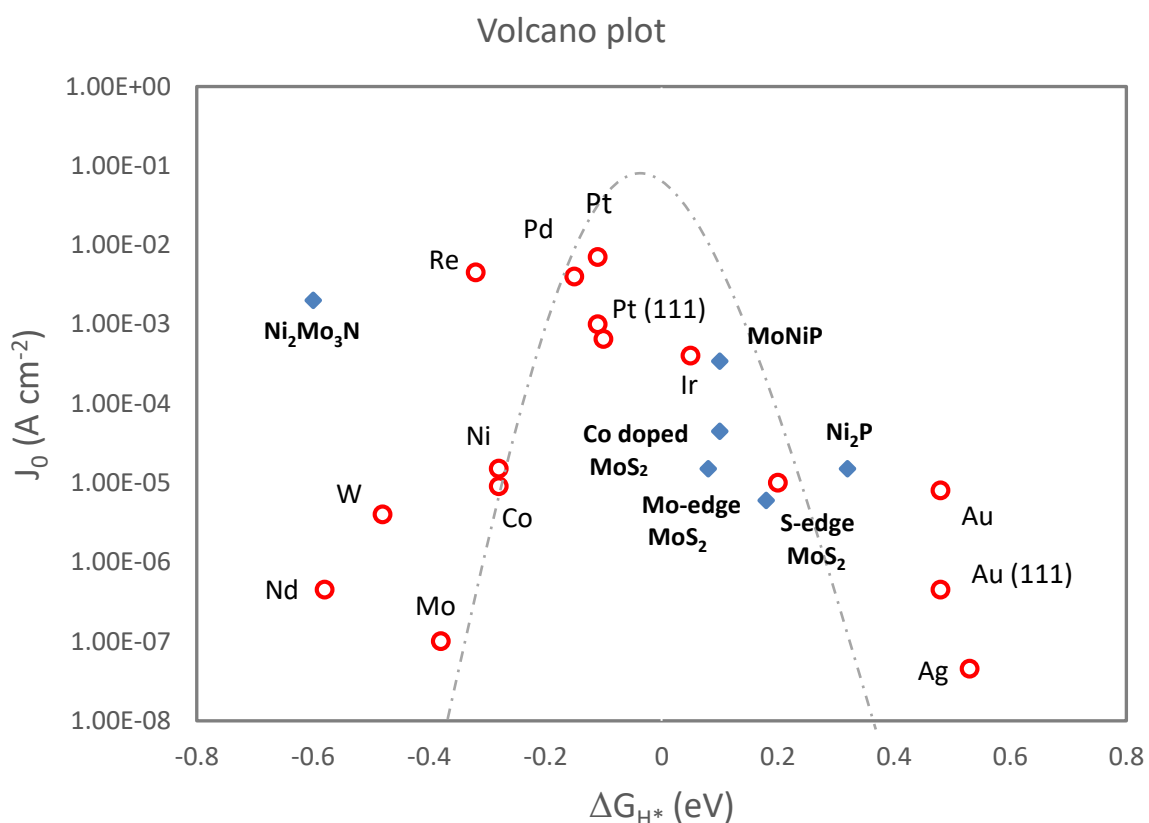

Figura 6-1 Plot comparing the materials discussed in this thesis. The free energy values are taken from DFT calculations previously reported in literature[1,2,3,5] while the exchange current density values are extrapolated from the intercepts of the Tafel plots reported in the previous chapters.

Overall, all the presented materials were successfully synthesised in a fairly pure phase with the presence of only minor impurities. In accordance with the literature, the synthesised compounds exhibited good catalytic activity in acid media and lower performance in basic media. The addition of heteroatoms within the structure presented an effective way to improve the catalytic activity in acid media for all the studied compounds. Finally, all the reported synthesis were easy to perform and required the use of cheap reagents, encouraging further investigations aimed for future industrial applications.

6.1 Bibligraphy

1. J. K. Nørskov, T. Bligaard, A. Logadottir, J. R. Kitchin, J. G. Chen, S. P. and U. S. Trends in the Exchange Current for Hydrogen Evolution. *J. Electrochem. Soc.* **3**, J23–J26 (2005).

2. Merki, D., Vrubel, H., Rovelli, L., Fierro, S., & Hu, X. (2012). Fe, Co, and Ni ions promote the catalytic activity of amorphous molybdenum sulfide films for hydrogen evolution. *Chemical Science*, *3*(90 C), 2515. https://doi.org/10.1039/c2sc20539d

3. Lauri Partanen, M. H. and K. L. (2019). Hydrogen adsorption trends on various metal-doped Ni2P surfaces for optimal catalyst design. *Phys. Chem. Chem. Phys.*, *21*, 184–191.

4. Liu, P., Rodriguez, A. & York, N. Catalysts for Hydrogen Evolution from the [NiFe] Hydrogenase to the Ni 2 P (001) Surface : The Importance of Ensemble Effect. 14871–14878 (2005). doi:10.1021/ja0540019

5. Zhou, P., Lv, X., Gao, Y., Liang, Z., Liu, Y., Wang, Z., Wang, P., Zheng, Z., Dai, Y., & Huang, B. (2020). Synthesis of novel cubic Ni2Mo3N and its electronic structure regulation by vanadium doping towards high-efficient HER electrocatalyst. *Electrochimica Acta*, *337*, 135689. https://doi.org/10.1016/j.electacta.2020.135689

7 Annex: Rietveld refinement for Chapter 4

7.1 Rietveld refinement of phosphides prepared by TPR at 850 °C for 11 hours in a 5% H_2 / 95% Ar gas mixture.

Table 7. 1 Rietveld refinement data from XRD data of the product MoP.

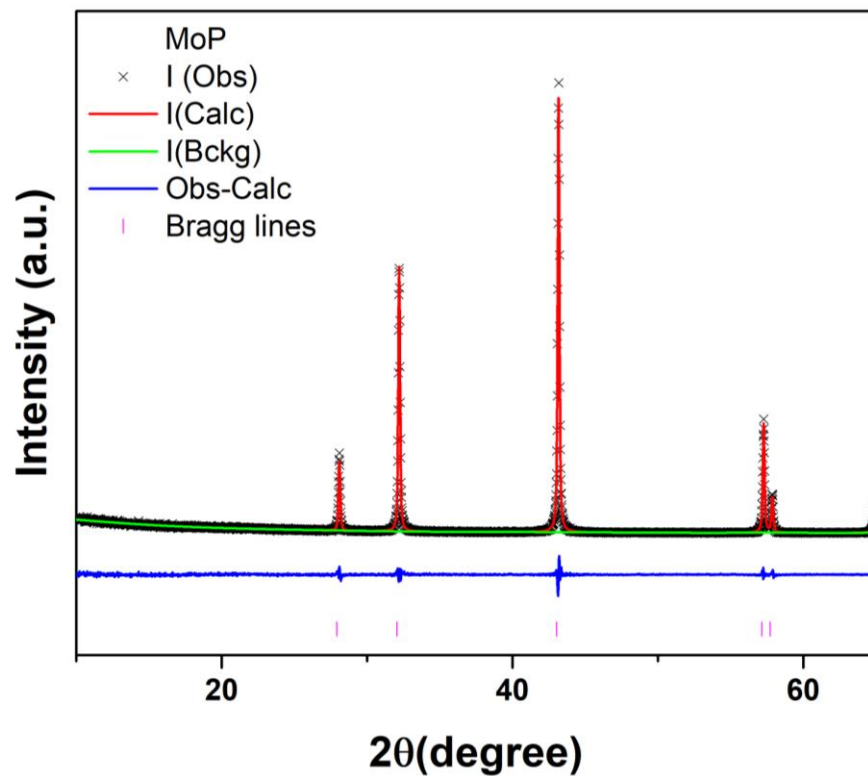| Sample	MoP without citric acid
Collection temperature	Room temperature
Crystal system	hexagonal
Space group	P -6 m 2
Unit cell dimension MoP :	
a/A= b/A	3.2166(1)
c/A	3.1899(2)
alpha/°	90.000
beta/°	90.000
gamma/°	120.000
volume/A^3	28.583(2)
Observations, parameters	3349
R_{wp}	0.1312
R_p	0.1039
Chi^2	1.803

Figure 7-1 Plot from the Rietveld refinement against XRD data. (Back cross: experimental profile; red line: calculated profile; blue line: difference profile; tick marks: bragg reflections for the MoP.)

Table 7. 2 Selected Rietveld refinement data from XRD data of the product MoNiP.

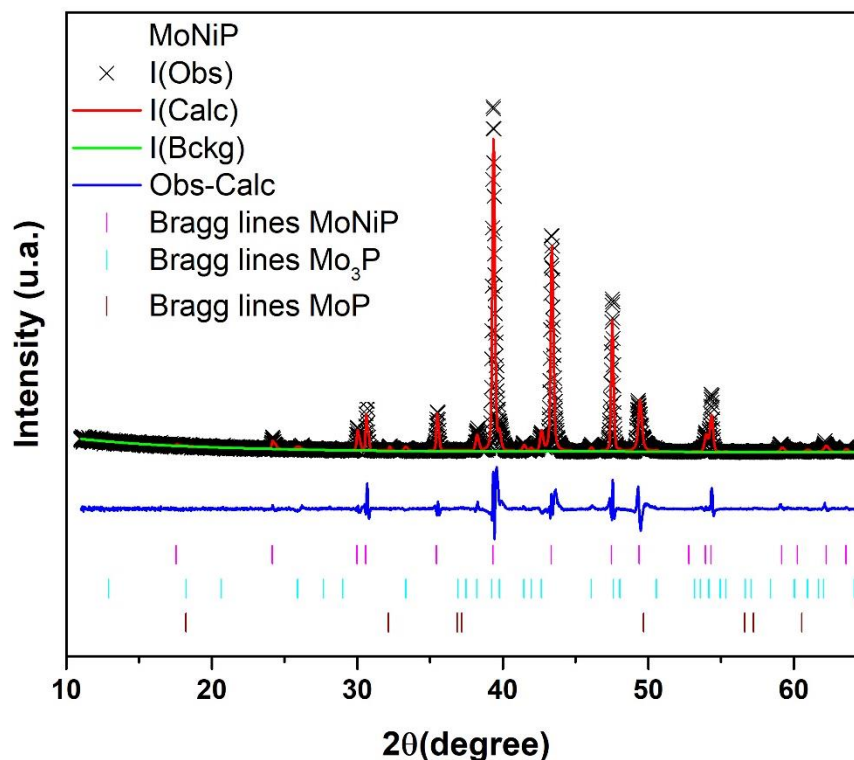| Sample	MoNiP
Collection temperature	Room temperature
Crystal system	hexagonal
Space group	P -6 2 m
Unit cell dimension:	
a/A=b/A	5.8533(1)
c/A	3.6923(1)
alpha/°	90
beta/°	90
gamma/°	120
volume/A^3	109.558(5)
Observations, parameters	3290
R$_{wp}$	0.2289
R$_p$	0.1616
Chi^2	6.329

Figure 7-2 Plot from the Rietveld refinement against XRD data. (Back cross: experimental profile; red line: calculated profile; blue line: difference profile; tick marks: bragg reflections for the MoNiP).

Table 7. 3 Selected Rietveld refinement data from XRD data of the product $Mo_{0.5}Ni_{1.5}P$.

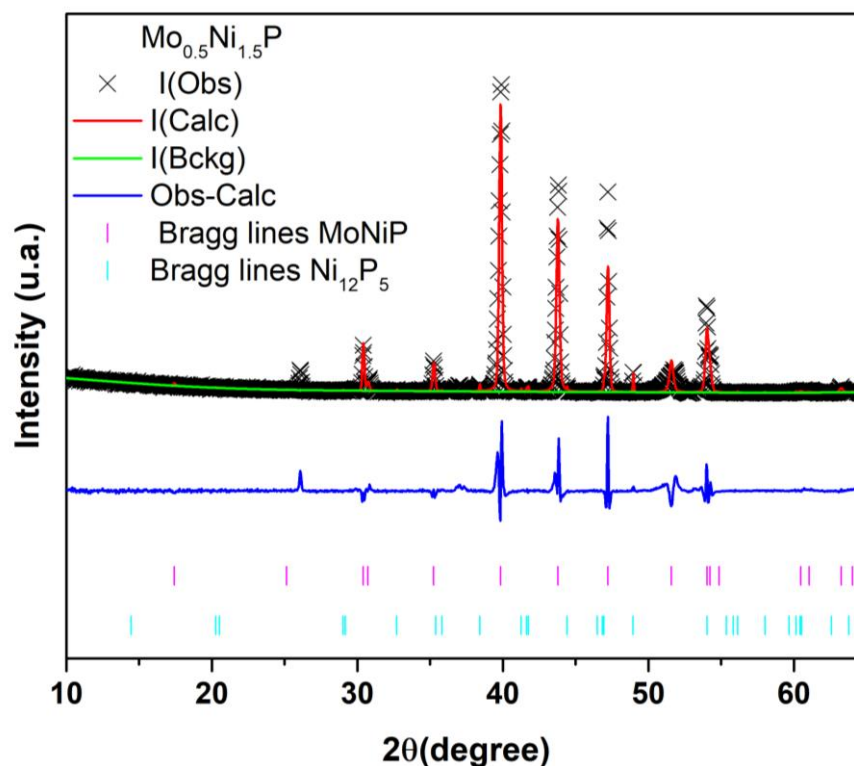| Sample	$Mo_{0.5}Ni_{1.5}P$ without citric acid
Collection temperature	Room temperature
Crystal system	Hexagonal
Space group	P -6 2 m
Unit cell dimension:	
a/A=b/A	5.8744(2)
c/A	3.5401(3)
alpha/º	90
beta/º	90
gamma/º	120
volume/A³	105.522(5)
Observations, parameters	1645
R_{wp}	0.2671
R_p	0.1931
Chi^2	7.635

Figure 7-3 Plot from the Rietveld refinement against XRD data. (Back cross: experimental profile; red line: calculated profile; blue line: difference profile; tick marks: bragg reflections for the $Mo_{0.5}Ni_{1.5}P$)

Table 7. 4 Refinement parameters from XRD data of Mo$_{0.25}$Ni$_{1.75}$P phase.

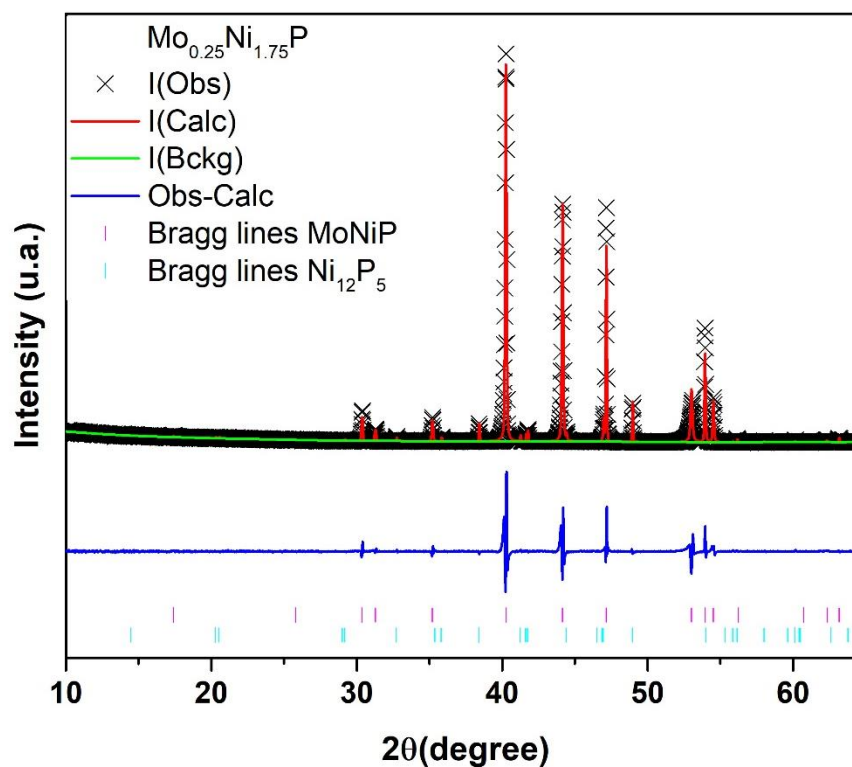| Sample	Mo$_{0.25}$Ni$_{1.75}$P without citric acid
Collection temperature	Room temperature
Crystal system	hexagonal
Space group	P -6 2 m
Unit cell dimension:	
a/A=b/A	5.88292(5)
c/A	3.45190(7)
alpha/°	90
beta/°	90
gamma/°	120
volume/A^3	103.461(2)
Observations, parameters	3291
R$_{wp}$	0.2068
R$_p$	0.1411
Chi^2	9.060

Figure 7-4 Rietveld profile fit for Mo$_{0.25}$Ni$_{1.75}$P. Measured data are shown as crosses, the calculated profile is shown by a solid line through the measured data. The difference profile is shown along the bottom of the plot. Vertical bars represent the reflection positions for the phase.

Table 7. 5 Rietveld refinement data from XRD data of Ni$_2$P.

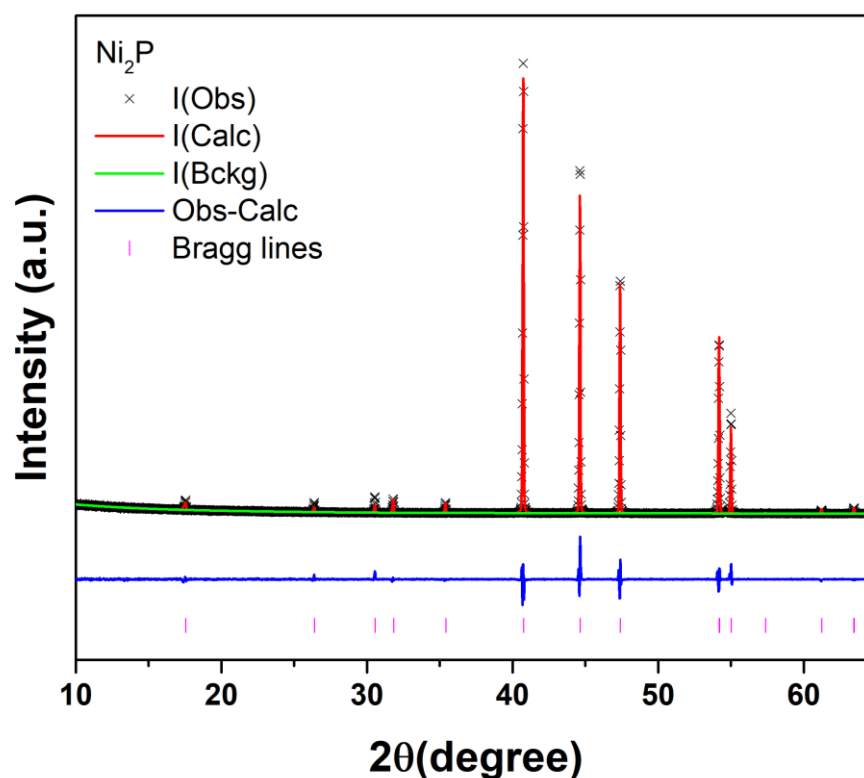| Sample	Ni$_2$P without citric acid
Collection temperature	Room temperature
Crystal system	hexagonal
Space group	P -62 m
Unit cell dimension:	
a/A=b/A	5.86883(1)
c/A	3.38990(8)
alpha/^{o}	90.000
beta/^{o}	90.000
gamma/^{o}	120.000
volume/A^3	101.116(6)
Observations, parameters	3291
R$_{wp}$	0.1419
R$_p$	0.1026
Chi^2	2.400

Figure 7-5 Plot from the Rietveld refinement against XRD data. (Back cross: experimental profile; red line: calculated profile; blue line: difference profile; tick marks: bragg reflections for the Ni$_2$P).

7.2 Rietveld refinement of MoNiP products prepared by TPR at 850 °C at annealing time of 22 and 33 hours.

Table 7. 6 Rietveld refinement data from XRD of MoNiP prepared by TPR at 850 °C for 22 hours.

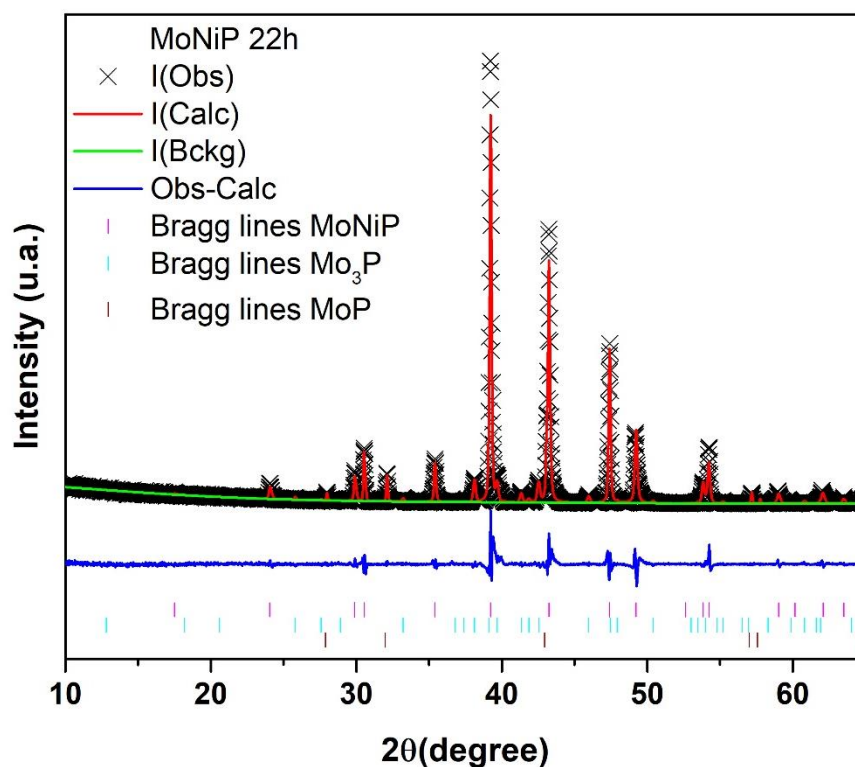| Sample	MoNiP TPR at 850 °C for 22 hours
Collection temperature	Room temperature
Crystal system	Hexagonal
Space group	P -6 2 m
Unit cell dimension:	
a/A=b/A	5.85483(9)
c/A	3.6989(1)
alpha/°	90
beta/°	90
gamma/°	120
volume/A^3	109.810(3)
Observations, parameters	3290
R$_{wp}$	0.1820
R$_p$	0.1258
Chi^2	4.163

Figure 7-6 Plot from the Rietveld refinement against XRD data of MoNiP prepared by TPR at 850 °C for 22 hours. (Back cross: experimental profile; red line: calculated profile; blue line: difference profile; tick marks: bragg reflections for the MoNiP)

Table 7. 7 Refinement parameters from XRD data of MoNiP phase synthesized by TPR at 850 °C for 33 hours.

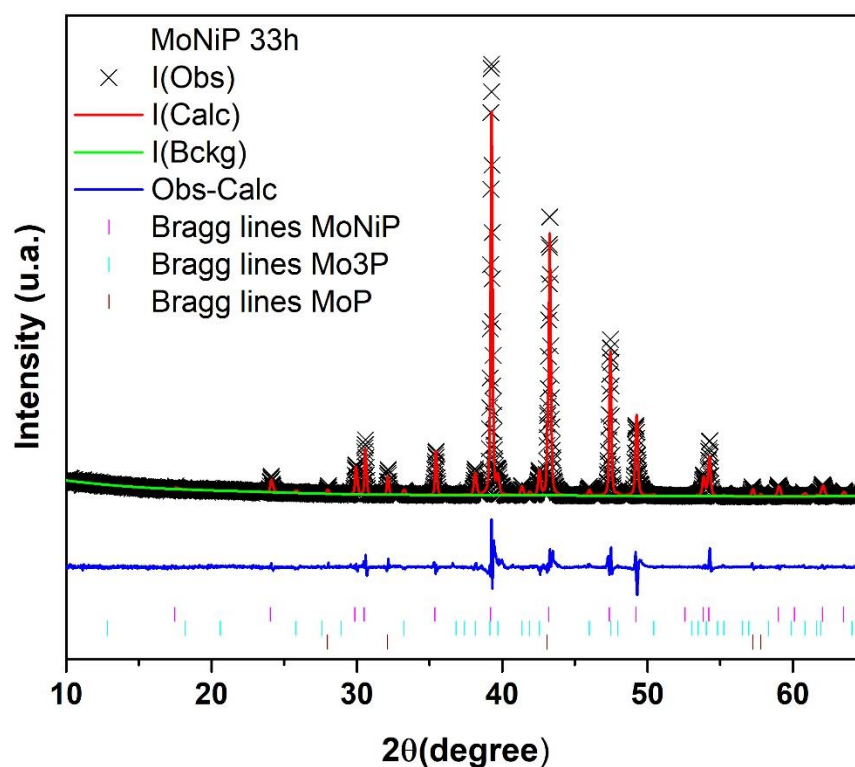| Sample	MoNiP TPR at 850 °C for 33 hours
Collection temperature	Room temperature
Crystal system	hexagonal
Space group	P -6 2 m
Unit cell dimension:	
a/A = b/A	5.8582(3)
c/A	3.7022(2)
alpha/°	90
beta/°	90
gamma/°	120
volume/A^3	110.036(1)
Observations, parameters	3290
R$_{wp}$	0.1855
R$_p$	0.1265
Chi^2	4.220

Figure 7-7 Plot from the Rietveld refinement against XRD data of MoNiP prepared by TPR at 850 °C for 33 hours. (Back cross: experimental profile; red line: calculated profile; blue line: difference profile; tick marks: bragg reflections for the MoNiP)

7.3 Rietveld refinement of phosphides prepared with the use of citric acid in a molar ratio with the phosphorous of 13:10 and reduced by TPR at 850 °C for 11 hours in a 5% H₂ / 95% Ar gas mixture.

Table 7. 8 Refinement parameters from XRD data of MoP phase.

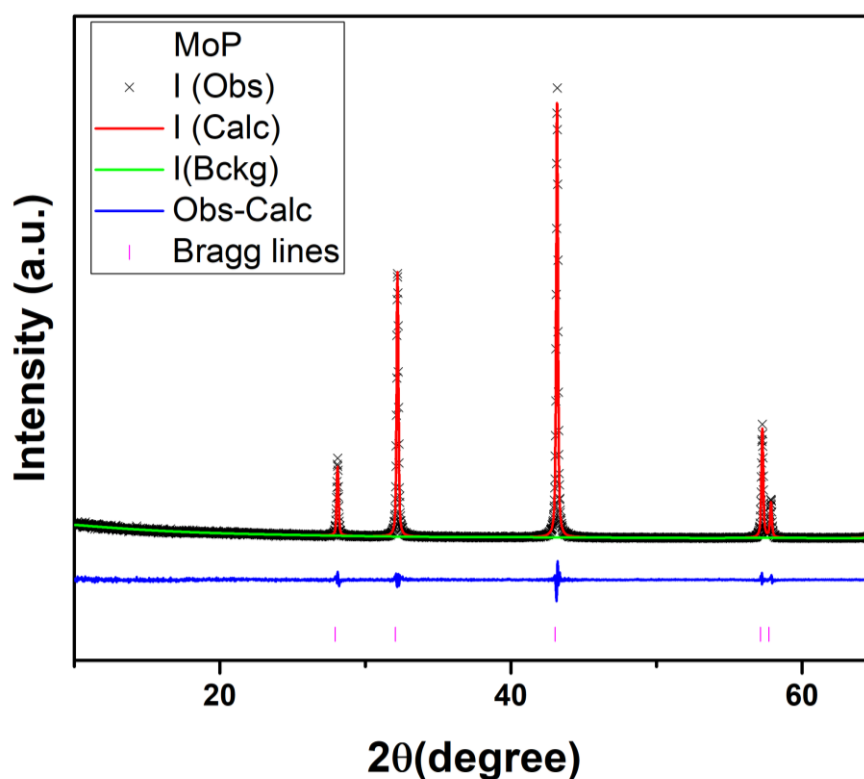| Sample	MoP
Collection temperature	Room temperature
Crystal system	hexagonal
Space group	P -6 2 m
Unit cell dimension:	
$a/A = b/A$	3.22133(3)
c/A	3.19116(5)
alpha/°	90
beta/°	90
gamma/°	120
volume/A^3	28.678(2)
Observations, parameters	3288
R_{wp}	0.1367
R_p	0.0892
Chi^2	1.36

Figure 7-8 Rietveld profile fits for MoP. Measured data are shown as crosses, the calculated profile is shown by a solid line through the measured data. The difference profile is shown along the bottom of the plot. Vertical bars represent the reflection positions for the phase.

Table 7. 9 Refinement parameters from XRD data of MoNiP phase.

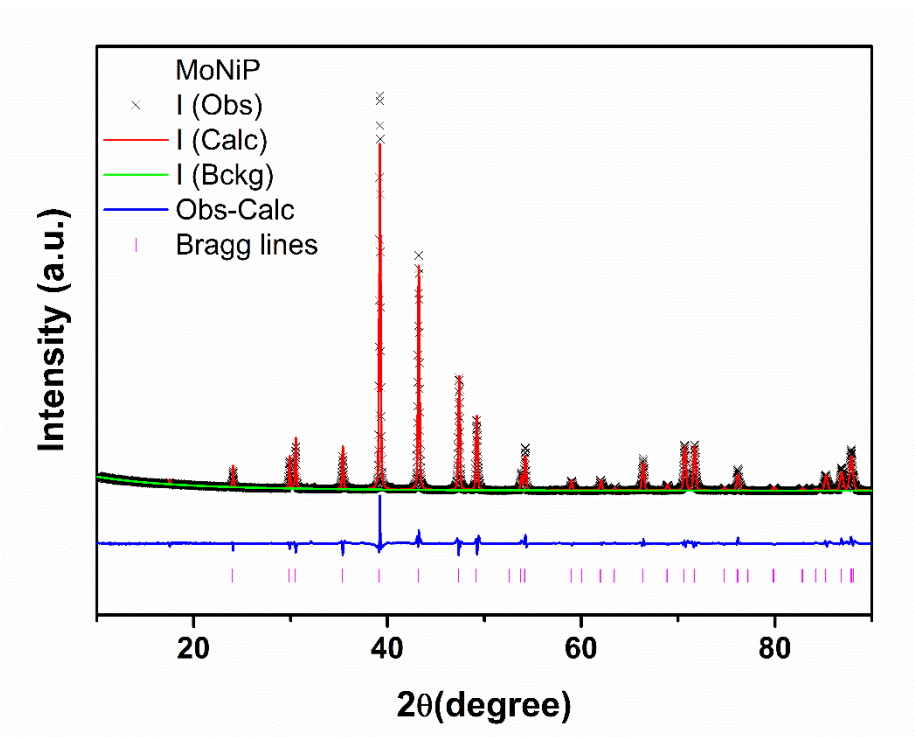| Sample	MoNiP
Collection temperature	Room temperature
Crystal system	hexagonal
Space group	P -6 2 m
Unit cell dimension:	
a/A = b/A	5.85937(7)
c/A	3.70152(8)
alpha/º	90
beta/º	90
gamma/º	120
volume/A^3	110.056(4)
Observations, parameters	3291
R$_{wp}$	0.1524
R$_p$	0.1068
Chi^2	2.586

Figure 7-9 X-ray diffraction profile for NiMoP. Observed (×), calculated (red line), background (green line) and difference (lower blue line) Tick marks show the reflection positions for the phase.

Table 7. 10 Refinement parameters from XRD data of $Mo_{0.6}Ni_{1.3}P$ phase.

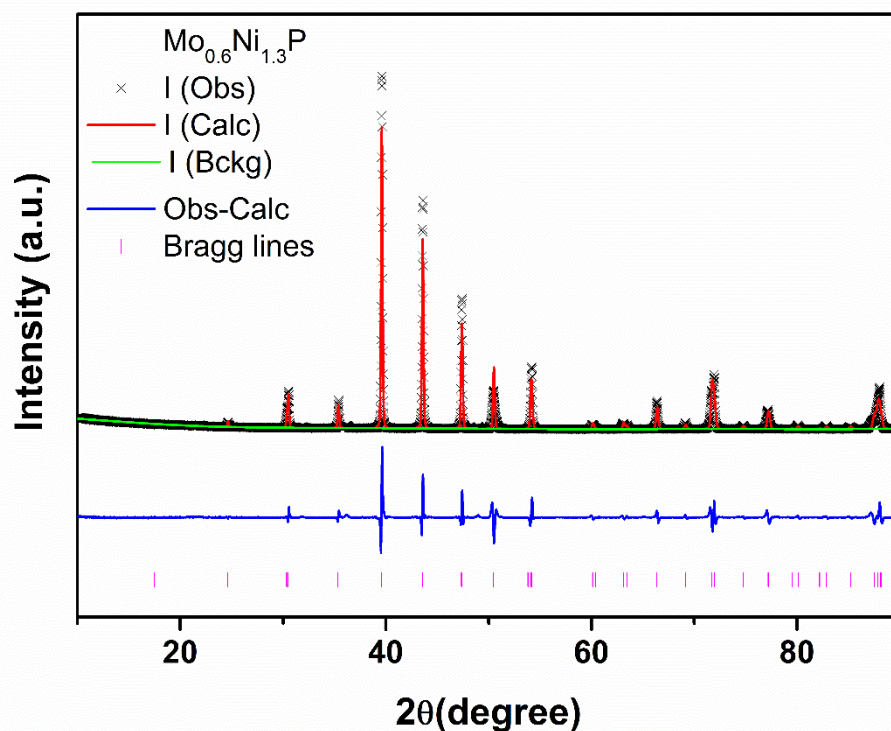| Sample	$Mo_{0.6}Ni_{1.3}P$
Collection temperature	Room temperature
Crystal system	hexagonal
Space group	P -6 2 m
Unit cell dimension:	
a/A = b/A	5.8572(1)
c/A	3.6132(1)
alpha/°	90
beta/°	90
gamma/°	120
volume/A^3	107.355(4)
Observations, parameters	3124
R_{wp}	0.3983
R_p	0.2573
Chi^2	1.931

Figure 7-10 Rietveld profile fits for $Mo_{0.6}Ni_{1.3}P$. Measured data are shown as crosses, the calculated profile is shown by a solid line through the measured data. The difference profile is shown along the bottom of the plot. Vertical bars represent the reflection positions for the phase

Table 7. 11 Selected Rietveld refinement data from XRD data of the product Ni$_2$P

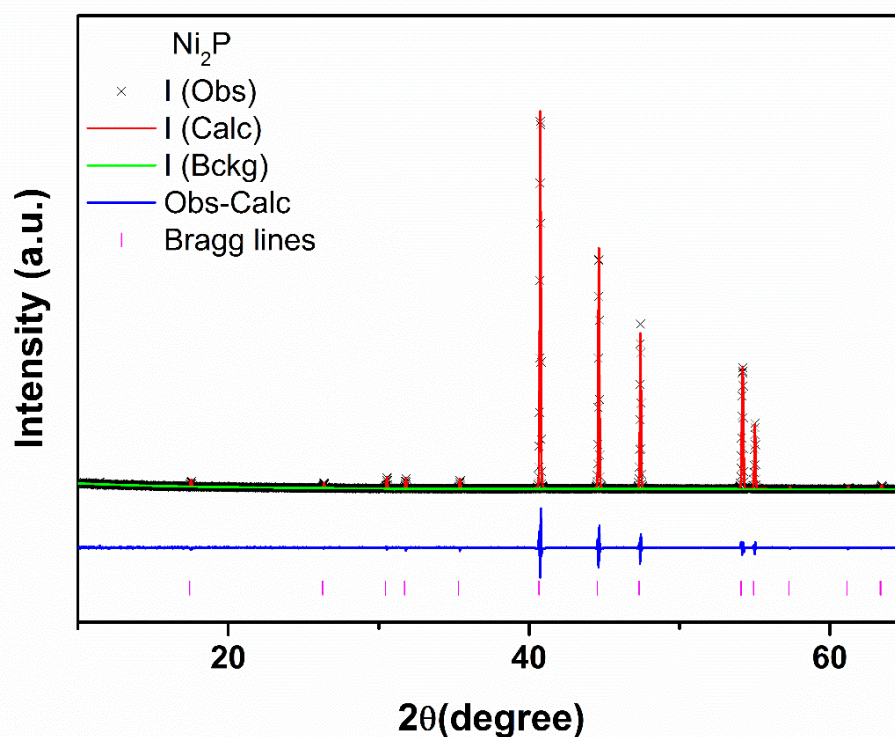| Sample	Ni$_2$P
Collection temperature	Room temperature
Crystal system	hexagonal
Space group	P -6 2 m
Unit cell dimension:	
a/A = b/A	5.86490(3)
c/A	3.38922(3)
alpha/º	90
beta/º	90
gamma/º	120
volume/A^3	100.961(1)
Observations, parameters	3290
R$_{wp}$	0.1744
R$_p$	0.1250
Chi^2	2.593

Figure 7-11 Rietveld profile fits for Ni$_2$P. Measured data are shown as crosses, the calculated profile is shown by a solid line through the measured data. The difference profile is shown along the bottom of the plot. Vertical bars represent the reflection positions for the phase.